Variability in neuromotor control of the musculoskeletal system dynamics

-

A stochastic modelling approach

Bart Christiaan van Veen

Supervisors

Prof. Marco Viceconti

Dr. Claudia Mazzà

A thesis submitted in partial fulfilment of the requirements for the degree of
Doctor of Philosophy

Insigneo Institute for *in silico* Medicine

Department of Mechanical Engineering

Faculty of Engineering

The University of Sheffield

November 2018

I always wondered if I would ever get the opportunity to write 'This page was intentionally left blank'.

SUMMARY

Pain, injuries or diseases might affect how we (are able to) coordinate movement. Therefore, an in-depth understanding of motor control, human movement dynamics and how pathologies affect movement coordination is essential to inform clinical practice that aims to improve the quality of movement in patients and therewith their quality of life. Musculoskeletal models allow for efficient simulations of human movement dynamics to predict the forces in muscles and joints in a non-invasive manner. However, assumptions on motor control are required to solve Bernstein's problem of muscle redundancy: the large number of muscles relative to the number of joints requires the controller, our central nervous system, to choose how each muscle contributes to the forces that result in the intended movement. For healthy people, it seems reasonable to assume that we control our muscles following an optimality principle: to minimize the amount of metabolic energy spent on the task. However, a disease, pain or instability are likely to influence a patient's control strategy; muscle control might be less optimal and more, or less, variable, depending on a person's ability or need to control force production. Therefore, the general aim of this thesis was to explore the variability in motor control of the musculoskeletal dynamics during walking through a stochastic modelling approach.

Firstly, I discussed the theoretical framework to model human movement dynamics and the current efforts to verify and validate musculoskeletal models, with the aim to quantify the errors in their predictions. Secondly, I aimed to explore the influence of motor control on the mechanical load experienced by the joints of the lower limb during level walking. An optimization approach to motor control showed that alternative motor control strategies have the potential to reduce the loading in the knee and the hip, but not in the ankle, during level walking. These results suggest that neuromuscular rehabilitation can be targeted as a conservative treatment when the mechanical load on joints is a determinant of the onset and/or progression of a disease. However, these alternative motor control strategies come at a cost of a moderate increase in the loading at non-targeted joints. Subsequently, the assumption of a lightly sub-optimal motor control strategy to predict knee contact forces, through a stochastic approach to model motor control, captured the measured intra-subject variability in these forces during multiple gait cycles of a patient with a knee replacement. Therefore, the assumption of sub-optimal control can predict a range of plausible joint contact forces, representative of the uncertainty in terms of measurement inaccuracies, modelling errors and inherent variability, which is likely to contain the true force. However, if a higher accuracy of predicted muscle and joint contact forces is required or in case of severely sub-optimal motor control, I believe the only solution is to include an explicit model of motor control. A refined mechanistic model would

allow for the differentiation between hierarchical levels of motor control, as proposed by Bernstein, such as the involuntary spinal control and the cognition-driven anticipatory control.

ACKNOWLEDGEMENTS

Firstly, I am grateful to my supervisors for their guidance throughout this journey.

Marco, thank you for having been the Yoda of my PhD. If only we could have fitted more discussions in a meeting. Your love for quotes made me add one to the end of this thesis, inspired by your rigour.

Claudia, your support during the past years means a lot to me. I learned to appreciate your skill to untangle my complicated reasonings and organise them into understandable stories.

I would like to thank Saulo for the opportunity to visit the Medical Device Research Institute at Flinders University in Adelaide as part of my project. Saulo, your continuous questioning of the application of my work annoyed me until I realized what I could learn from it.

I am thankful to what has been my home for the past years. Sheffield, and particularly Insigneo, you consist of wonderful people who I share beautiful memories with. I will especially miss the gunfights, the metal bars and the phone drums of C+13.

Finally, I would like to thank the people who are most important to me.

To my best friends, thank you for knowing when to be(er) there for me. Wieks, bedankt dat je al jarenlang regelmatig checkt hoe t met me gaat.

Mam, pap, Cas en 'Kleine', jullie onvoorwaardelijke steun is ongelofelijk belangrijk voor me. Bedankt voor jullie bezoeken aan Sheffield en bedankt dat ik altijd thuis kan komen. Mam, jouw bezoek aan Australie is een ontzettend dierbare herinnering.

Bap, bedankt voor je eindeloze geduld en al je hulp. Zonder jou had ik het nooit gered. Je hebt lang moeten wachten, maar het is voorbij: We gaan fietsen!

TABLE OF CONTENTS

CONFERENCE PRESENTATIONS

van Veen B.C., Martelli S., Mazzà C., Somersalo E., Calvetti D., Viceconti M. Variability in neuromotor control of the musculoskeletal system dynamics: a stochastic modelling approach. 21st Congress of the International Society of Electrophysiology and Kinesiology (ISEK), July 2016, Chicago, IL, USA.

van Veen B.C., Martelli S., Mazzà C., Somersalo E., Calvetti D., Viceconti M. A measure of similarity between optimal and sub-optimal muscle force production in gait. Virtual Physiological Human (VPH) Conference, September 2016, Amsterdam, Netherlands.

van Veen B.C., Lamberto G., Mazzà C., Viceconti M. Can alternative muscle recruitment strategies reduce the force transmitted through lower limb joints? 26th Congress of the International Society of Biomechanics (ISB), July 2017, Brisbane, Australia.

van Veen B.C., Modenese L., Mazzà C., Viceconti M. Alternative muscle recruitment strategies have potential to increase accuracy of joint reaction force estimations in musculoskeletal models. 8th World Congress of Biomechanics (WCB), July 2018, Dublin, Ireland.

ABBREVIATIONS

DoF	-	Degree of freedom
PCSA	-	Physiological cross-sectional area
UCM	-	Uncontrolled manifold
MRI	-	Magnetic resonance imaging
CoM	-	Centre of mass
MTU	-	Musculotendinous unit
CNS	-	Central nervous system
PNS	-	Peripheral nervous system
NMJ	-	Neuromuscular junction
CE	-	Contractile element
DE	-	Damping element
SEE	-	Series elastic element
PEE	-	Parallel elastic element
l_o^M	-	Optimal muscle fibre length
SISO	-	Single input-single output
EMG	-	Electromyography
RF	-	Radiofrequency
JCF	-	Joint contact force
API	-	Application programming interface
RMS	-	Root-mean-square
BW	-	Bodyweight
GRF	-	Ground reaction force
FLV	-	Force-length-velocity
EMD	-	Electromechanical delay
RMSE	-	Root-mean-square error
R^2	-	Coefficient of determination

GENERAL INTRODUCTION

Many of us are lucky enough to take coordinated movement during activities of daily life for granted. When we drink from a glass or walk through a field, we are unlikely to consider the complexity of the task. We might be more aware of its difficulty when we try to avoid spilling a hot drink or when we try to avoid falling while walking on a slippery surface. Alternatively, we might wonder at the unfathomable skill of an elite sports athlete, dancer or circus artist. However, how often do we think about the movement of individual body segments or, even more abstract, the contribution of each individual muscle to those movements? Coordinated motion of the human body is highly complex and unstable, especially in tasks that involve balance, such as walking. Nevertheless, we take thousands of steps a day in a continuously changing environment and every single step is slightly different from the other steps, as we might have noticed when a blister on our heel hurt more with one step than with the other. Motor coordination and movement performance also change over a longer time scale: we both learn how to walk and start to struggle to walk with age. Also, pain, injuries or diseases might affect how we (are able to) coordinate movement: one might avoid certain movements to prevent or reduce the pain in an inflamed joint or injured muscle, one might tense muscles during walking to compensate for instability of the knee joint after an anterior cruciate ligament rupture, or the signals from the central nervous system might not reach the muscles due to a neurological disease like multiple sclerosis. An in-depth understanding of motor control, human movement dynamics and how pathologies affect movement coordination is essential to inform clinical practice that aims to improve the quality of movement in patients and therewith their quality of life.

Information about the neural drive, the contribution of individual muscles and the resulting forces experienced by the joints involved in human movement is valuable to study motor control. However, access to these kinds of data is limited due to ethical concerns or technical limitations. For example, force sensors that measure the forces in the hip or knee can be placed in a joint replacement, but for obvious ethical reasons these highly invasive interventions are only performed in end-stage osteoarthritic patients. Musculoskeletal models allow for efficient simulations of human movement dynamics to predict the forces in muscles and joints; these models can be identified through non-invasive measurement techniques such as motion capture and medical imaging. Therewith, musculoskeletal models provide a powerful approach to study motor control.

One of the many open questions in the study of motor control relates to the principles of muscle redundancy and optimal control: the large number of muscles relative to the number of joints requires the controller, our central nervous system, to choose how each muscle contributes to the forces that result in the intended movement (Bernstein, 1967). For healthy people, it seems reasonable to assume that we control our muscles following an optimality principle: When we walk, we use a strategy of muscle activation to minimize the amount of metabolic energy spent on the task. However, one could

argue that we aim for 'good enough' control rather than optimal control as "an organism uses trial-and-error learning to acquire a repertoire of sensorimotor behaviours that are known to be useful, but not necessarily optimal" (Loeb, 2012). This principle of 'good enough', or sub-optimal control, partially explains the observed kinematic variability in repeated tasks, but kinematic variability has been argued to serve a purpose: variability in directions that are independent to task performance does not have to be controlled and could potentially provide stability to sudden changes or perturbations (Scholz and Schöner, 1999). This theory of an uncontrolled manifold can equally be applied to the control of muscles.

The general aim of this thesis was to explore the variability in motor control of the musculoskeletal dynamics during walking through a stochastic modelling approach: The first chapter provides a brief overview of the physiological elements involved in human movement; The second chapter focuses on the theoretical framework for simulations of human movement dynamics by discussing the largest and most common assumptions made in musculoskeletal models; The third chapter presents an overview of the current efforts to verify and validate these models and aims to quantify the uncertainty of the predictions made by musculoskeletal models; The fourth chapter aims to quantify the effect of muscle activation strategies on the forces experienced by the joints of the lower limb during level walking; The fifth chapter explores the limitations of optimal control to model pathological gait through a stochastic approach to motor control. Muscle recruitment that is optimal from the perspective of energy expenditure might be undesirable or even impossible to reach due to pain or impaired motor control in patients.

CHAPTER 1

-

ELEMENTS OF HUMAN MOVEMENT PHYSIOLOGY

This section is aimed to briefly introduce the anatomical and physiological components involved in human movement production and to provide a context to refer to later in this text.

1.1 The musculoskeletal system

The skeleton is the supporting structure of the human body, which protects internal organs, anchors muscles and allows body segments to move with respect to each other (*Figure 1.1*). Its main components are bone and cartilage material. A bone is a rigid organ due to its high content of mineralized tissue and provides structure to the body segments. Cartilage, a substance less stiff than bone, is found throughout the body, providing structure to for example the nose and the ears, but also covering the articular surfaces of bones.
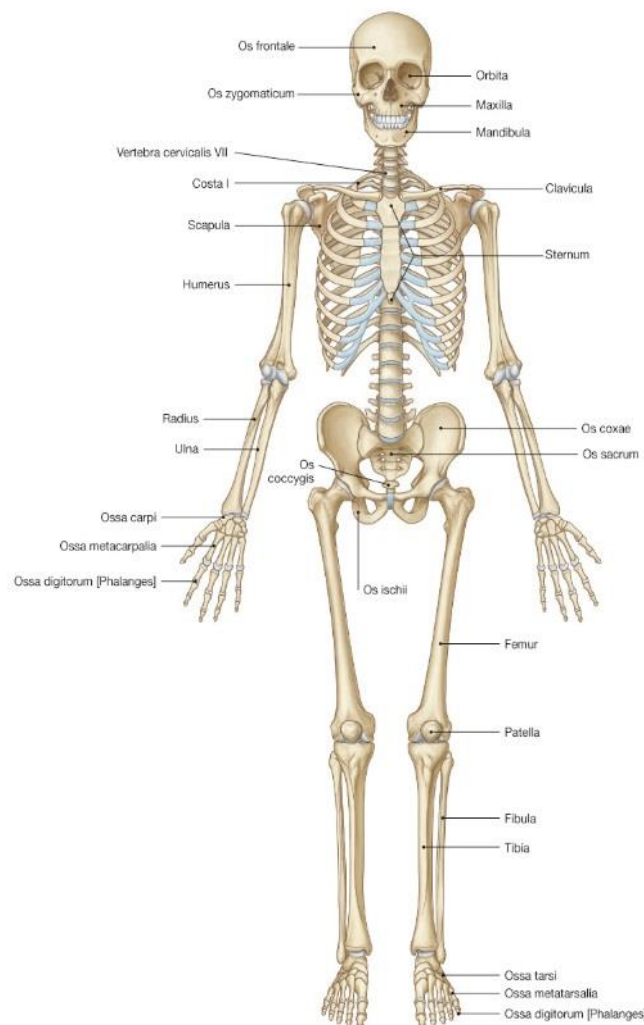
Figure 1.1: Human skeleton.

Joints are the links where the ends of two, or more, bones meet and can be classified according to the level of articulation they allow for: synarthroses are immovable, amphiarthroses are slightly movable and diarthroses, or synovial joints, are freely movable articulations (Gray, 1918). The bony surfaces of diarthroses are covered by articular cartilage, connected by ligaments and filled with synovial fluid to allow for a nearly frictionless articulation of bones with respect to each other. Diarthroses can be subdivided into different classes based on the permitted motion; hinge, pivot, ellipsoidal, saddle, ball-and-socket and gliding joints (*Figure 1.2*). These joints allow free movement in given directions, or degrees of freedom (DoFs), while they resist movement in other directions, due to opposing forces in ligaments and bony structures. The hinge and pivot joints allow for uniaxial rotation around the transverse and longitudinal axis, respectively. Both the ellipsoidal and saddle joints allow for flexion-extension and abduction-adduction movements but resist rotation around the longitudinal axis. Ball-and-socket joints allow the distal bone to rotate around any axes that share a common origin. Gliding joints, as the name implies, do not allow rotational movements, but only allow translational movements, as these joints typically consist of the apposition of the planar surfaces.
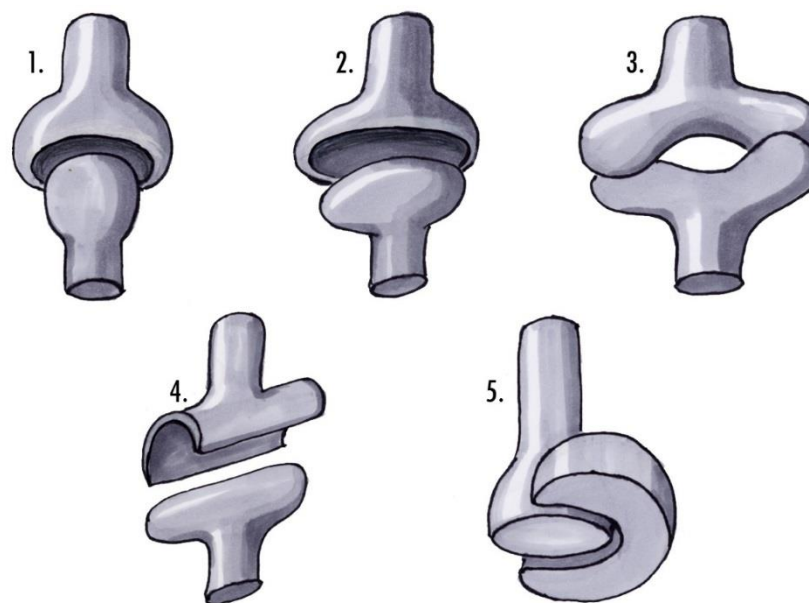
Figure 1.2: 1. Ball-and-socket joint, 2. Ellipsoidal joint, 3. Saddle joint, 4. Hinge joint, 5. Pivot joint. Image by Produnis, distributed under a CC BY-SA 3.0 license.

1.2 Anatomical terminology

Anatomical terminology provides a vocabulary to describe the anatomical location of physiological elements and unambiguously define movement categories. Anatomical locations are described relative either to the centre of the body or to each other and the terminology therefore consists of antonyms (*Figure 1.3*):

- Medial-lateral: Towards or away from the midline of the body.
- Superior-inferior: Towards the head or towards the toes.
- Anterior-posterior: Towards the front or back of the body.
- Proximal-distal: Along a limb, towards or away from the trunk.
- Plantar-dorsal: Towards the palmar or backside of the foot or hand.
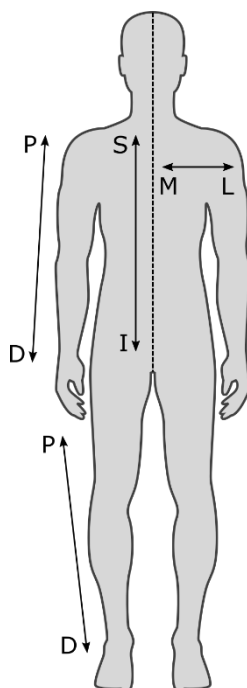
Figure 1.3: Anatomical directions: medial (M) − lateral
(L), inferior (I) − superior (S), proximal (P) − distal (D).

Three planes can be described along the two-dimensional sections of the human body in anatomical position: the frontal, sagittal and transverse plane. Joint motion can generally be categorized as a relative rotation of segments around one of the three axes originating from the intersections of these planes: the transverse, anterior-posterior and longitudinal axis (*Figure 1.4*). Flexion-extension is defined as rotation at the joint around the transverse axis, abduction-adduction occurs around the anterior-posterior axis and internal-external rotation is a rotation around the longitudinal axis.
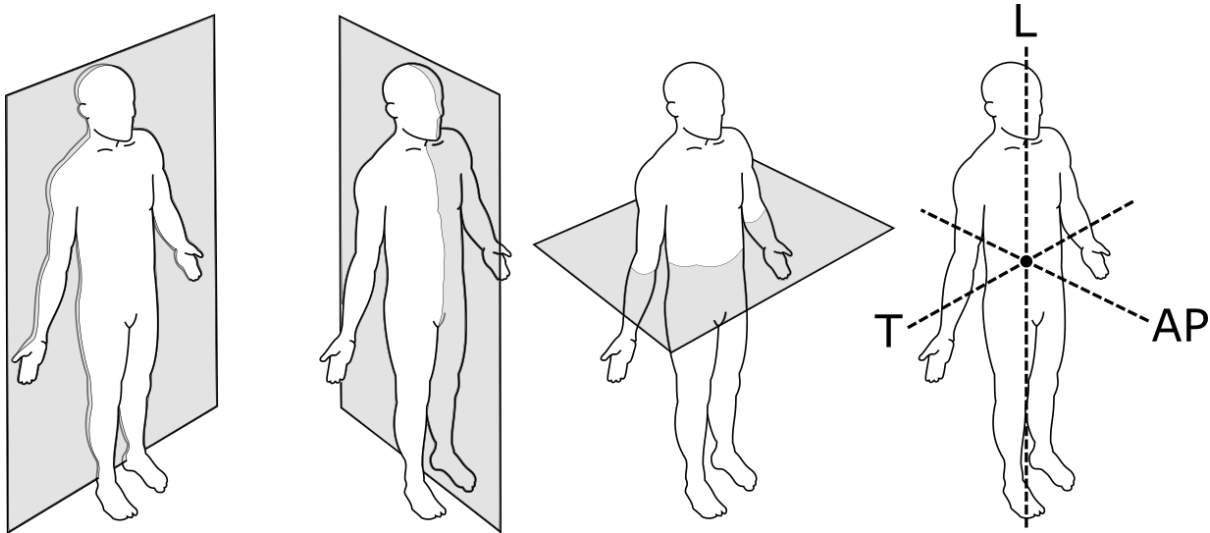
Figure 1.4: Frontal (left), sagittal (middle, left) and transverse (middle, right) planes and the corresponding three axes originating from the intersection of those planes (right): the longitudinal (L), transverse (T) and anterior-posterior (AP) axis.

1.3 Skeletal muscle physiology

The skeletal muscles move, or actuate, the skeleton by producing forces that act on the bones. These myotendinous units consist of active and passive elements. The passive elements, or tendon units, are built up from fibrous connective tissue and typically anchor the functional element to the bones. The active element of a myotendinous unit consists of a highly ordered structure of contractile elements. The contractile proteins actin and myosin make up for about 80% of the total protein content of a muscle. A cylindrically shaped bundle of 100 to 400 filaments forms a myofibril, located in the sarcoplasm and connected to the sarcolemma, or cellular membrane, of the multinucleated muscle fibre cell. A layer of connective tissue, the endomysium, wraps around each muscle fibre and groups of 10 to 100 fibres are in turn wrapped by the slightly thicker perimysium to form fascicles. The epimysium eventually covers the whole muscle and is connected to the tendon unit (Jones et al., 2004). This highly ordered structure does not only allow the length of the muscle to change, but also facilitates force generation.

1.3.1 Motor unit activation and recruitment

One alpha motor neuron, located in the ventral horn of the spinal cord, innervates multiple muscle fibres. A motor neuron and the fibres it innervates together are called a *motor unit*. A contraction of the muscle fibres is initiated when an action potential reaches a muscle fibre. An action potential is a fast depolarization of the membrane potential, travelling down the axon of the motor neuron. A single

action potential will lead to a twitch response in all the muscle fibres of the motor unit. A twitch is a short contraction (20-100 ms to build up tension, depending on the fibre type, as measured in humans by small force transducers in the tendon (Buchthal and Schmalbruch, 1970)) followed by complete relaxation (typically more than four times longer than contraction time). A single action potential originating at the motor neuron will lead to a twitch response in all the muscle fibres of the motor unit. If a sequential action potential reaches a muscle fibre before tension from the previous twitch has disappeared, tension will add up. The force produced by the motor unit will increase with increasing action potential frequency until a plateau is reached at 50-100 Hz. This tetanic activation will lead to the highest possible force the motor unit is able to produce in its specific configuration.

Under isometric conditions, when the length of the muscle fibre is constant, motor units are recruited following a size principle: The smaller motor units that include less and slower muscle fibres are recruited first, while the larger motor units that include more and faster muscle fibres are recruited later. This allows not only for a smooth increase in force with increasing activation, but also for a higher resistance against fatigue as the smaller, more fatigue-resistant motor units are recruited first (Henneman et al., 1965).

1.3.2 Force-length dependency

The sliding-filament theory explains the physiological mechanism that allows for length change in the contractile element of a muscle (Huxley and Niedergerke, 1954; Huxley and Hanson, 1954). The development of phase contrast and interference microscopy allowed for the visualization of the actin and myosin filaments in isolated myofibrils. The geometrical structure of these filaments, arranged in sarcomeres, allows them to slide along each other. A sarcomere is defined to stretch from one Z-line to the next Z-line, where the ends of the thin actin proteins from neighbouring sarcomeres link together. The opposite ends of actin within one sarcomere are interlaced with thick myosin proteins that join at the M-line, the middle of the myosin filament (*Figure 1.5a*).

The development of electron microscopy allowed for higher resolution images of actin and myosin filaments, confirming the cross-bridge theory that suggested an interaction between the interlaced actin and myosin filaments. The theory explains how a sarcomere, and consequently a muscle, can produce a contractile tension through cyclic attachments and detachments of myosin cross bridges (Huxley, 1957). This interconnection mechanism forms the muscle's contractile element and explains why muscles can only pull and not push.

The amount of force produced by a muscle during a tetanic contraction depends on its length and contraction velocity. The amount of overlap between the thin and thick filaments explains this force-

length dependency. At the optimal length, the muscle can produce its *maximum isometric force*: the force resulting from a tetanic contraction under isometric conditions when a maximum overlap between actin and myosin filaments exists. In a shorter muscle, the sarcomeres are compressed, and folds in the actin filaments prevent the attachment of cross-bridges, leading to a reduction in tetanic force. In a longer muscle, the sarcomeres are stretched and less overlap between filaments exists. Therefore, less cross bridges can be formed compared to a sarcomere at its optimal length and again the tetanic force production is reduced (Gordon et al., 1966) (*Figure 1.5b-c*).
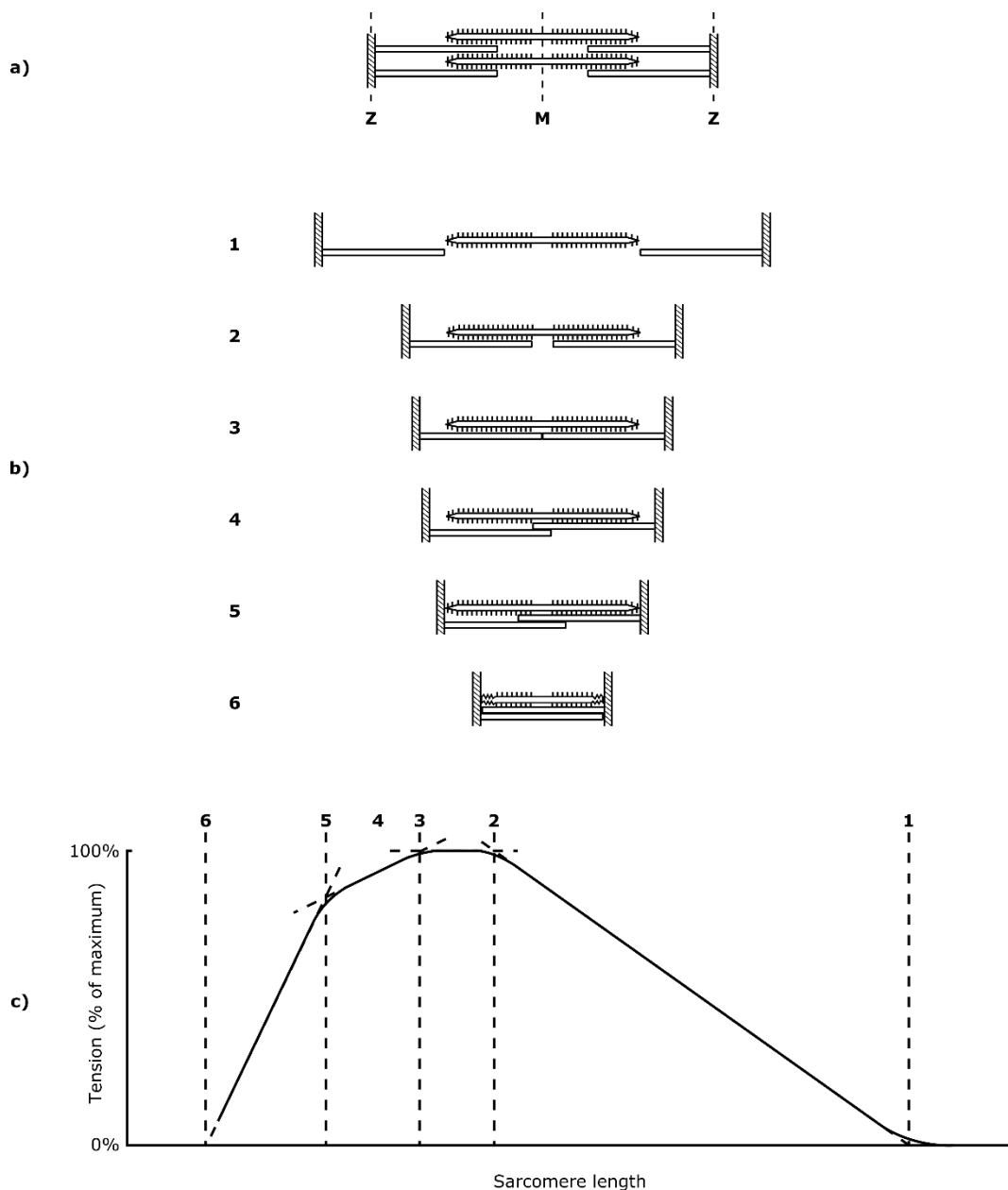

Figure 1.5: a) Sarcomere myosin and actin filaments with Z and M lines; b) Scenarios with increasing level of overlap between actin and myosin filaments; c) Tension-length curve of a sarcomere. The overlap at the numbers correspond to the numbered scenarios in b). Images adapted from Gordon et al. (1966).

Additionally, the stretch of muscle beyond a certain length leads to a passive, activation-independent, tension that increases exponentially with the extension (Jewell and Wilkie, 1958). At these greater muscle lengths the cell membranes, the connective tissues surrounding the muscle fibres, and the titin elements, that connect myosin filaments to the Z-line, are stretched; this mechanism is referred to as the muscle's parallel elastic element.

When a muscle contracts under isometric conditions it stretches the connective tissues in series with the contractile tissue. As the muscle length is constant, the stretch in the series connective tissue can only occur if the contractile tissue shortens by an equal amount. This internal shortening influences the time course of force development in dynamic situations. The force-length characteristics of the serial elastic element can be determined through an experiment where one end of an isolated muscle is instantly released. Before the release, the muscle is stimulated and kept at a constant length until the tension has built up. The muscle's response to the release includes an almost instantaneous change in length of which the duration is dependent on the tension difference pre- and post-release. During the short time of near-instantaneous length change, the contractile tissue is assumed not to be able to shorten, while it still produces tension (Winter, 2009).

1.3.3 Force-velocity dependency

During isometric contractions, the sarcomere length is constant but when active fibres shorten or lengthen their tetanic force also depends on the contraction velocity. During a concentric contraction, when sarcomeres shorten, the tetanic force reduces with increasing velocities because fewer cross bridges form, cross bridges are, on average, less stretched and a proportion of cross bridges will be in a position where they oppose movement, due to their slow detachment compared to the contraction velocity. The relation between the tensile force and the shortening velocity was adequately described by Hill as a hyperbola, based on his work on the thermodynamics of tetanic contractions in frog Sartorius muscles (Hill, 1938):

$$(F + a)(v + b) = b(F_o + a)$$
1.1

where F is the tensile force, F_o is the maximum isometric tensile force, v is the shortening velocity, a is the constant coefficient of shortening heat and b is a constant depending on a, F_o and v_o, the maximum shortening velocity when $F_o = 0$.

Both the force-length and force-velocity dependency, as described above on the sarcomere level, translate to the muscle level: The force-length-velocity relationship of a muscle is shown in *Figure 1.6*.
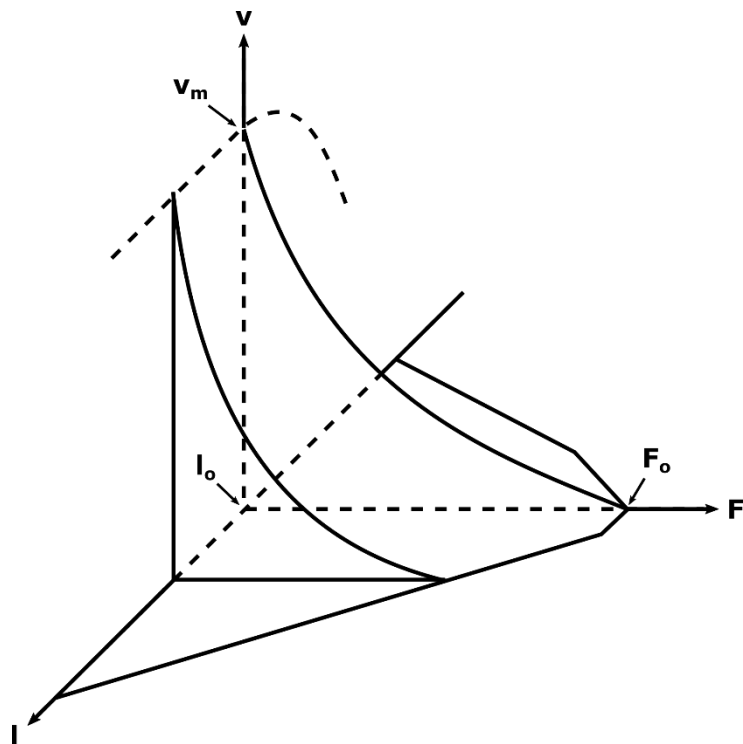
Figure 1.6: Three-dimensional illustration of the muscle force-length-velocity relationship during isometric and concentric contractions for maximum activation. Muscle force (F), contraction velocity (v), muscle length (l), maximum isometric force (F_o) at optimal length (l_o) and maximum shortening velocity (v_m). Image adapted from Mashima et al. (1984).

During an eccentric contraction, when sarcomeres lengthen, the tetanic force increases with increasing lengthening velocities because the cross bridges are more stretched than during isometric contractions. Uncertainty exists about the shape of the eccentric force-velocity curve, but the force increase has been shown to be less during isovelocity, eccentric contractions than during isotonic eccentric contractions leading to a maximal force plateau ranging from 1.1 F_o to 1.8 F_o (Joyce et al., 1969; Mashima, 1984; Mashima et al., 1972).

1.3.4 Musculotendon dynamics

On a muscle level, the orientation of fibres with respect to the tendinous tissue is another important factor influencing the force producing capacity of a muscle. In general, the more fibres are arranged in parallel, the stronger the muscle is because the individual fibre forces add up. Logically, in muscles with an equal volume, a stronger muscle has shorter fibres, but more fibres in parallel, than a weaker muscle. Consequently, the stronger muscle is able to produce more force over a shorter range of muscle lengths, while the weaker muscle is able to produce less force over a longer range of lengths. Based on fibre orientation, muscles can be classified as fusiform or pennate muscles. In fusiform muscles, the fibres run parallel to the muscle length, while in pennate muscles, the fibres run at a

certain *pennation angle* to the aponeurosis, a sheet-like fibrous tissue providing a wide attachment area for fibres. The physiological cross-sectional area (PCSA), as opposed to the anatomical cross-sectional area, is the area of the cross section of a muscle perpendicular to the length of its fibres. Under the assumption of an invariant tetanic stress, the PCSA of a muscle at rest is frequently used as an indicator of muscle strength, even though fibre type, quality and the number of fibres per area also influence the muscle's maximal isometric force.

1.4 The basis of motor control

Motor control research explores how the nervous system interacts with other body parts and the environment to produce purposeful, coordinated movements (Latash, 2012); how are we able to control simultaneous, as opposed to sequential movement, movement of joints to produce smooth, timely, flexible and robust motions? An important aspect to answer how the central nervous system controls our muscles is the understanding, and inclusion, of the physiological elements involved.

Neurons, or nerve cells, receive, process and transmit information within the brain and between the brain and peripheral organs through electrochemical signals. Neurons exchange these signals between each other or pass them to a target cell at either electrically or chemically activated connections, called synapses. Ultimately, a received signal, if strong enough, causes a supra-threshold depolarization of a neuron's membrane potential that initiates an action potential. An action potential consists of a standardized depolarization and sequential repolarization of the membrane potential and typically travels from a dendrite or the cell's soma along the axon towards a synapse with another neuron or a target effector cell. Neuronal signals travel from the central nervous system along so-called *efferent pathways* to reach the innervated muscle fibres along and along *afferent pathways* to transfer information from the many sensory receptors in the human body to the central nervous system. Examples of sensory receptors involved in motor control are the joint proprioceptors, muscle spindles and Golgi tendon organs. Joint proprioceptors provide information on the orientation of joints, muscle spindles feedback information on fibre length and velocity and Golgi tendon organs send signals roughly correlated with muscle force.

The complexity of motor control arises from the integration of sensory feedback into the planning of control signals sent to the muscles that appropriately deal with the complexity of the motor system. In his studies of blacksmiths hitting a chisel with a hammer, Bernstein observed a smaller variability in the trajectories of the tip of the hammer than in the trajectories of the individual joints (Bernstein, 1967; Latash, 2012). This observation highlights what Bernstein classified as the problems of movement control: How to choose a trajectory from a multitude of available trajectories?; How to

14

deal with the excess of degrees of freedom of the motor system?; How to control for the errors in the original control command? Bernstein proposed the sensory corrections principle as an explanation of how the central nervous system deals with errors in motor performance (Feigenberg, 2014). This principle of closed-loop feedback highlights the importance of constant and complete information from sensory receptors. The second problem, known as motor redundancy, can be observed on different levels: On a joint level, as shown by Bernstein's hammer task, an infinite number of combinations of joint angles leads to the same endpoint position, while on a muscle level an infinite number of combinations of muscle forces leads to the same joint movement. Bernstein suggested that synergies reduce the problem of muscle redundancy as muscles are controlled as 'choirs' (Feigenberg, 2014), allowing one signal to control a group of muscles synchronously. For different tasks, a small number of synergies was able to explain a high percentage of the variance in the original dataset. However, this variable reduction was not typically able to account for the motor redundancy completely, supporting the principle of abundance which suggests that an abundant system is able to combine accuracy with stability and flexibility of motor performance (Latash, 2012). From the previous, the following question arises: How is the variability in degrees of freedom controlled during a movement? The uncontrolled manifold (UCM) hypothesis tries to answer this question by assigning variability to two directions (Scholz and Schöner, 1999). The first direction, the UCM, is defined by the configurations of DoFs that do not influence the hypothesized control variable, while the other direction is perpendicular to the UCM. A higher variability along the UCM compared to its perpendicular component would indicate that the hypothesized variable is indeed controlled when performing a motor task. The minimum intervention principle expands the reasoning of the UCM hypothesis. In simplified form, the principle states that the motor system should make no effort to correct deviations from average behaviour unless those deviations interfere with task performance (Todorov and Jordan, 2002). Following this principle, motor control has been suggested to be a stochastic process, as long as the variability appears in the redundant control space without affecting the motor goal (Viceconti, 2011).

Recent studies have argued that the human motor system is potentially not as redundant as the motor redundancy problem implies. Firstly, one could question whether humans have an overcomplete musculature or that the tasks performed in a laboratorial environment are underspecified (Loeb, 2000)? The description of tasks in an experimental setup would imply an abundance of muscles compared to the kinematic degrees of freedom, but those descriptions are oversimplified and ignore task demands that reduce redundancy. In addition, in daily life motor tasks have even more complex demands. Secondly, it has been argued that muscle redundancy does not imply robustness to muscle dysfunction as simulated muscle loss lead to a reduction in index finger force production (Kutch and

Valero-Cuevas, 2011). Although these studies suggest that the motor system might be less redundant than expected, in tasks without a demand to be the highest, quickest or strongest, motor redundancy is observed and the central nervous system successfully manages to control these abundant DoFs. Therefore, the exploration of possible muscle force patterns underlying sub-maximal tasks, including gait, might lead to interesting insights into the variability of neuromotor control.

CHAPTER 2

-

MODELLING HUMAN MOVEMENT DYNAMICS

2.1 The idealisation process

2.1.1 Transient continuum deformation

A continuum is assumed to consist of continuously distributed matter that entirely fills the space it contains; the inter-atomic space and the cracks and discontinuities on a microscopic scale are ignored. Due to its far larger space scale, human movement can be accurately modelled as the transient motion and deformation of a heterogeneous continuum from an initial steady state to a new steady state. Since the average adult human body consists for 50-60% of water (Guyton and Hall, 2006), we can assume that a human-body continuum contains both solid and fluid phases. Continuum mechanics can effectively model the motion and deformation of both phases in mathematical terms. However, the resulting mathematical model is extremely complex; a system of partial differential equations describes the transient motion and deformation of such a multiphase continuum but does not admit an analytical solution (imagine the complexity of the geometrical description and the accompanying boundary value problems). Even numerical methods such as finite element analysis involve dramatic complexity and computational costs due to the heterogeneous, multiphasic, non-linear, and transient nature of the problem.

Therefore, a practical approach to model human movement dynamics requires that we heavily simplify the mathematical problem through a series of idealisations. In the following section, I list the most important idealisations, their experimental evidences, and their limits of validity.

2.1.2 Rigid multibody dynamics

During passive motion, such as a cadaver propelled in a ballistic flight motion, we can neglect the contractions of muscles and only external forces act on the human body. In such passive conditions, the spatial configuration that the body assumes at each instant of time is imposed by the spatial configuration of the skeleton. Thus, a body moves as its underlying skeleton moves; we can study the motion of the human body by modelling the motion of the skeleton and assume that the rest of the body (internal organs, soft connective tissues, internal fluids, etc.) contributes to the motion only as passive inertial masses attached to the skeleton. Within the skeleton itself, most of the deformation observed during motion is concentrated in specific regions called *joints*. If we ignore the deformation of bones, and only consider the deformation of joints, the moving human body can be idealised as a *rigid mechanism*: a set of infinitely rigid bodies of which each element is wrapped by a passive inertial mass and linked to other elements by joints. These assumptions allow us to model human movement with a very mature mathematical approach known as *rigid multibody dynamics*.

The assumption of infinitely rigid bones implies that the loading conditions of the specified task do not deform the bones. A study on cadaveric femora reported that an axial loading of 800 N displaced the femoral head by 0.5-0.6 mm (Cristofolini et al., 1996). With a peak force at the hip during level walking of 2-3 times the body weight (Bergmann et al., 2010), we would neglect changes in the location of the hip joint centre of 1-2 mm by assuming infinitely rigid bones. This inaccuracy lies well within the limits of the experimental methods used to quantify human movement. However, in tasks that involve much higher forces this assumption might not remain valid. For example, measured hip forces during a stumble reached up to 11,000 N (Bergmann et al., 2010), which implies changes in the hip joint centre location of 6-8 mm; depending on the scope of the analysis, this error might not be acceptable anymore.

Body segment dimensions can be obtained from different sources, depending on their availability; scaling of a generic dataset, anthropometric measurements and segmentation of medical images, such as computed tomography or magnetic resonance imaging (MRI), all provide information on segment dimensions, but at increasing levels of accuracy. For each segment, a local reference frame can be constructed from a set of known anatomical landmarks. The location of these landmarks can be obtained through virtual palpation. These segment local reference frames can conveniently be defined following the standards for anatomy-based joint coordinate systems (Wu et al., 2002). Furthermore, the mass matrix of the musculoskeletal system must be defined to allow our dynamics model to be solved. Each segment is assumed to have a fixed mass lumped at its centre of mass (CoM) and the segments' moments of inertia about the CoM are assumed to be constant throughout the movement (Winter, 2009). Average values for the segmental mass characteristics, based on population studies, can be obtained as a function of body mass and height (Drillis et al., 1964). We can make a more accurate approximation of the segments' inertial properties when the segmented volumes of bone and soft tissue and their corresponding densities are available.

2.1.3 Joint idealisation

Classic treatments of rigid body dynamics assume that the rigid elements are connected by idealised joints that present no stiffness in the unconstrained directions, and infinite stiffness in the constrained directions. The validity of these assumptions, and any other assumption in the model, should be assessed by asking the question: 'What is the maximum level of idealization I can afford without compromising the accuracy of my model in predicting what I care for?' (Viceconti, 2011). The extent of joint stiffness in an unconstrained direction is related to its coefficient of friction. The coefficient of kinematic friction for human synovial joints is around 0.003 (Jewett and Serway, 2007). A comparison to the ice-on-ice friction coefficient of 0.03 indicates the extremely low waste of energy into heat in

human joint articulation. The assumption of frictionless articulation is therefore unlikely to significantly influence the model's prediction.

In all friction experiments, Coulomb's Law of Friction (the coefficient of kinetic friction is independent of the sliding velocity) is assumed to be valid. However, the mechanical behaviour of human synovial joints is viscoelastic in the sense that its stiffness depends on the velocity with which the joint is deformed (Valle et al., 2006). Even if the effect of viscosity would increase the coefficient of friction for human synovial joints ten times, the resulting frictional forces would still be negligible compared to the other internal and external forces involved in human movement.

In a three-dimensional Euclidean space, the position and orientation of two segments with respect to each other can be fully described by three translations and three rotations. Ideal joints provide no resistance to motion in some of these directions, the DoFs, while infinite rigidity is assumed in the remaining directions. However, human joints need to ensure a complex combination of stability and flexibility and the joint stiffness, its passive resistance against movement, depends on the orientation and velocity, both in the 'free' and 'constrained' directions. Typically, a sharp rise in stiffness is observed at the extreme orientations and even the constrained directions allow for a narrow range of motion with low resistance, called joint laxity. Besides joint orientation, a change in coordinate velocity changes the viscous contribution to movement resistance. One could argue that joint accelerations during the typical tasks of interest, such as gait, are low and therefore neglecting the viscous behaviour of the joint articulation is valid. However, at higher accelerations this assumption needs to be re-evaluated. In general, assumptions on joint idealization are valid in some circumstances but not in others and one needs to take note of the principle of limited validity when expanding the application of 'validated' models.

The *gait2392* model, one of the most commonly used musculoskeletal models, serves as a good example on joint idealisation (Delp et al., 1990). The hip is modelled as a ball-and-socket joint, the knee as a planar joint with prescribed translation between the tibia and the femur, depending on the flexion-extension angle, and the ankle and the subtalar joint as hinge joints. The justification of representing the knee as a planar joint was the small amount of axial rotation, which only becomes present near full extension, compared to the flexion-extension range of motion (Yamaguchi and Zajac, 1989). However, joint laxity in the ab-adduction and internal-external rotation directions have been reported to range from 2° to 8° and 10° to 26°, respectively, with increasing knee flexion angle (Markolf et al., 1976). Moderate axial loads up to 300 N did not influence the rotation laxity, as was shown in a later study that also reported higher values for rotation laxity (Blankevoort et al., 1988). Even though higher axial loads in the order of magnitude of bodyweights, comparable to the loads in weight bearing activities, might reduce laxity, these studies suggest that significant movement outside

the sagittal plane is possible in the knee. More recently, the knee joint in the *gait2392* model has been expanded to include prescribed internal-external rotation and ab-adduction values dependent on knee flexion (Arnold et al., 2010). Even though, this assumption takes the 'screw-home' movement during knee extension into account (Hallén and Lindahl, 1966), the potential influence of muscle forces on joint orientation in the constrained directions is still neglected. The accuracy of the off-plane kinematic data and the ratio between the joint stiffness and the expected forces and torques experienced by the joint during the movement of interest are other factors that might influence the choice to include or exclude certain degrees of freedom. Despite the potential oversimplification, the validity of a planar knee model, and of any level of idealization for any joint, remains to be assessed by its influence on the accuracy of the prediction.

In addition to the definition of the degrees of freedom at the joints, movement of the musculoskeletal system with respect to the inertial, or ground, reference frame is typically allowed by a free joint, allowing for three translational and three rotational DoFs, between the pelvis and inertial reference frame. The parameters that uniquely describe the location and orientation of a multibody system at any given point in time are called the generalized coordinates $\vec{q}(t)$. In case of musculoskeletal models, the generalized coordinates can therefore be divided into two groups: the six coordinates that describe the location and orientation of the pelvis with respect to the ground reference frame and the coordinates at the joints. The coordinates at the joints are commonly chosen to correspond with the allowed degrees of freedom. If all the DoFs are independent, the number of generalized coordinates is equal to the minimal number of parameters required to uniquely define the system's configuration.

2.1.4 Muscle lumped-parameter models

Rigid multibody dynamics models allow for the analysis of the forces propagated through the joints during movement and muscle forces make up for the largest part of these joint contact forces (Winter, 2009). So far, we assumed the human body behaved as a passive mass, moved only by the action of external forces, while the human body can in reality move autonomously through the contraction and relaxation of complex tissue structures known as *musculotendinous units* (MTU). Force generation in these structures results from the extremely complex interaction of the central nervous system (CNS), the peripheral nervous system (PNS), the excitation-activation dynamics at the neuromuscular junction (NMJ), the sarcomere contraction, the spatial arrangement of sarcomere fibres, and the connections of these fibres to the skeleton through tendons, aponeuroses, and other connective tissues.

Several idealisations are considered to handle the muscles' anatomical complexity and therewith to model the role of MTUs in human movement dynamics. Firstly, MTUs are assumed to connect only to

the skeleton and not to other connective tissues or to each other. Peter Huijing at the Vrije Universiteit Amsterdam showed that this assumption is not true and his work provided a quantification of such myofascial force transmission (Huijing et al., 1998; Huijing and Baan, 2003, 2001); for murine skeletal muscles with the anatomical structure typical of those relevant for locomotion, this effect is in the order of 10-15 %. We also neglect the transverse forces that layers of muscles exchange as they increase in volume during shortening.

Secondly, the collection of three-dimensional, complexly deforming MTUs is reduced to a set of one-dimensional, lumped-parameter actuators. For fusiform muscles the errors introduced by this idealisation are modest; the pennation angle between the muscle fibre direction and the line of action can be accounted for in the MTU formulation. However, for muscles with a more complex geometry, and different components that contribute to different movements, multiple one-dimensional actuators are required to retain sufficient accuracy (Valente et al., 2012).

Lastly, the controlled is assumed to be separable from the controller: the set of one-dimensional actuators representing the MTUs is assumed to be separable from the CNS-PNS-NMJ complex including all the afferent signals from the muscles, tendons, and other connective tissues to the CNS.

In simulations of human movement dynamics, the musculotendon models typically include only the essential mechanical properties to predict the forces along the tendon acting on the bony structures to the required level of accuracy. These essential properties can be included by 'linking together idealized mechanical elements arranged to create a composite lumped-parameter model that mimics the behaviour of the actual physiological system under a set of well-defined conditions' (Yamaguchi, 2001a). The essential properties to include in our muscle models are the previously mentioned contractile and passive viscoelastic properties, describing the force-length-velocity relationship during muscle contractions. The following section describes the elements that are generally included in muscle models that are aimed to represent physiological phenomena observed in tetanic contractions of isolated muscles or muscle fibres. These observations generally refer to a single sarcomere, of which all within a muscle are assumed to be identical. This assumption reduces the muscle model to a superimposition of the behaviour of one single sarcomere onto the behaviour of the whole muscle. Various musculotendon dynamics models have been presented in the literature, but most, if not all, are based on the muscle model proposed by Hill (Hill, 1938). Hill-type muscle models consist of an active, or contractile, element (CE) and a passive structure that is representative of the viscoelastic properties of the muscle. The behaviour of this passive structure depends on the arrangement and properties of the idealized mechanical elements included, typically springs and viscous dampers. The CE is arranged in parallel with a damping element (DE). An elastic element (SEE) is added in series to

the CE and DE, while another elastic element (PEE) is added in parallel to these three elements (*Figure 2.1*) (Yamaguchi, 2001a).
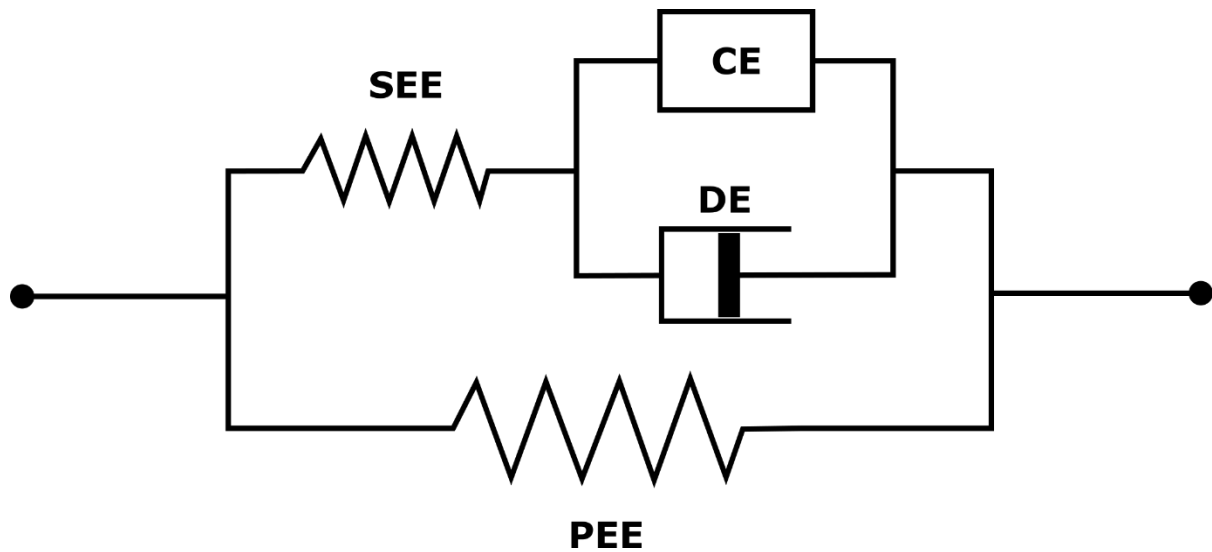
Figure 2.1: Hill's muscle model with a contractile element (CE), damping element (DE), series elastic element (SEE) and parallel elastic element (PEE). Image adapted from Yamaguchi (2001).

The CE represents the length dependency of the active muscle force. The force-producing capacity of the CE reduces when the muscle is shortened or lengthened from its optimal length (l_o^M) and reaches zero at fibre lengths around 0.5 l_o^M and 1.5 l_o^M, respectively. The PEE accounts for the activation-independent force produced during the stretch of a muscle fibre and is assumed to behave as a massless, exponential spring:

$$F_k = kx \qquad\qquad 2.1$$

where F_k is the magnitude of the force along the spring, k is the spring constant, and x is the spring deformation. The spring is slack at fibre lengths smaller than l_o^M, but its deformation is equal to the muscle's deformation at greater lengths, leading to an increase in tension. k can include an exponential term to account for the exponential increase of force with increasing x. The SEE is a second massless spring element that allows for the nearly instantaneous length change observed during the quick release experiments in isolated muscles. The length of the contractile element cannot change instantaneously, because of the damper element works in parallel to the CE. The DE behaves as an ideal damper, allowing the viscous fluid in the cylinder to pass slowly when shortened or lengthened:

$$F_b = b\dot{x} \qquad\qquad 2.2$$

where F_b is the force along the damper, b is the viscous damping constant, and $\dot{x}$ is the change of deformation over time. The velocities of the DE and CE maintain the same direction due to their parallel arrangement, resulting in a force resisting the change in fibre length. Therefore, a concentric contraction of the fibre leads to a force in the DE opposing the velocity of the CE, while during an eccentric contraction the force in the DE works with the CE force. The CE and DE placed in parallel result in a net increase of contractile force, compared to the isometric force, during eccentric contractions and a net decrease of contractile force during concentric contractions.

A large heterogeneity of muscle parameters exists between subjects and between muscles. Not all these parameters can be measured for each specific muscle, due to ethical, cost and time reasons. By scaling only the essential parameters, a single input-single output (SISO) generic muscle model can be adjusted to a specific muscle (Zajac, 1989). Such models allow for 'emphasizing the interactions among body segments and muscles, rather than the secondary and tertiary properties of any muscle' in studies of human coordination. Four further assumptions on our muscle model are required to extend the model to a musculotendon dynamics model suitable to be included in musculoskeletal simulations of movement. Firstly, a muscle consists of many fibres arranged in parallel and their forces are assumed to add up. The fibre model could be expanded to a muscle model with multiple parallel fibres to account for the heterogeneity observed in for example muscle fibre length. However, for practical reasons most muscle models contain one strong muscle fibre that is assumed to be representative of the population of muscle fibres. Secondly, muscle fibres run at an angle with the tendinous tissue which needs to be compensated for to obtain the force along the line of action of the muscle:

$$F^M = \cos(\alpha)\left(F_a^M + F_p^M\right) \qquad \text{2.3}$$

where F^M is the force along the line of action of the muscle, α is the pennation angle, and F_a^M and F_p^M are the active muscle fibre forces, respectively. Thirdly, the tendinous tissue is added as another elastic element in series to the muscle model:

$$F^M = F^T = k_T x^T \qquad \text{2.4}$$

where F^T is the force along the tendon, k_T is the stiffness coefficient of the tendon, and x^T is the deformation of the tendon. Stress-strain properties as well as the strain in the tendon when the muscle force is at its maximal isometric value have been assumed to be tendon independent, leaving the tendon slack length to be the only parameter to scale (Zajac, 1989). Lastly, the level of muscle

activation must be included. In most musculotendon models, the activation ranges from zero to one and serves as a linear scale factor of the force produced by the active component of the muscle:

$$F_a^M = F^{CE}(a(t), \dot{x}^{CE}, l_o^M, F_o^M) \hspace{3cm} 2.5$$

where F^{CE} is the force produced by the contractile element which is dependent on $a(t)$, the activation at time t, $\dot{x}^{CE}$, the rate of change in contractile element length, l_o^M, the optimal muscle fibre length, and F_o^M, the maximal isometric force.

As mentioned previously, a muscle's maximal isometric force is typically estimated from its PCSA, taken from a cadaveric average or medical images, and its tetanic stress. A range of experimentally measured values from 35 to 137 N/cm² has been reported for the tetanic stress, which has also been argued to be a muscle-dependent property (Buchanan, 1995). In the most commonly used musculoskeletal models, however, the tetanic stress is set to 61 N/cm² and assumed to be equal among muscles (Arnold et al., 2010; Delp et al., 1990): PCSA values were taken from cadavers and a relatively high value for the tetanic stress was chosen to compensate for the loss of muscle volume in elderly compared to young people.

In most musculoskeletal models, a myotendinous unit is assumed to be a linear actuator that only transmits forces to bones at its origin and insertion. Many of the limitations introduced by this assumption are beyond the scope of this study, but the complexity of human musculature introduces some relevant difficulties to the definition of muscular lines of action: a muscle might have multiple origins or insertions, different regions of one muscle might contribute to different movement directions, fibre pennation angles might vary across a muscle and a muscle's geometry is likely to be influenced by the surrounding bones, muscles and other structures. Possible solutions to these issues are the discretization of one muscle into multiple separate actuators and the a priori definition of via points or wrapping surfaces that guide the geometry paths. A muscle atlas from a generic model can be mapped onto the subject-specific skeleton using affine transformation or guidance from medical images. Ultimately, the geometry path determines the effectiveness with which a muscle force produces a torque at the spanned joint. Muscle moment arms are important variables to verify musculoskeletal models through a qualitative comparison with cadaveric studies. The perturbation method, commonly used in cadaveric studies, defines the moment arm as the change in muscle length with respect to a change in joint angle (An et al., 1983):

$$B_{ij}(\vec{q}) = \frac{\partial L_j(\vec{q})}{\partial q_i} \hspace{3cm} 2.6$$

where B_{ij} is the moment arm of muscle j with respect to generalized coordinate i, L_j is the length of muscle j, and $\vec{q}$ is the vector of generalized coordinates. In computational studies, the perturbation method might lead to violations of the constraints on the DoFs and involves difficulties with the linearization of complex muscle paths. The generalized force method, which is also derived from the principle of virtual work, overcomes these issues (Sherman et al., 2013):

$$B_{ij}(\vec{q}) = \frac{\partial \tau_i(\vec{q})}{\partial s_j} \qquad\qquad 2.7$$

where τ_i is the torque at coordinate i, and s_j is the tension along muscle j.

2.1.5 Motor control as an optimal process

A central question within studies of motor control is how the central nervous system chooses one solution from the many viable solutions, as discussed in Bernstein's work on the theory of motor redundancy. In the literature, different authors approached the problem from very different perspectives, including reductionist, optimization, and explorative approaches. For example, a reductionist approach of muscle synergies predefines synchronous neural input to groups of muscles aiming to reduce the number of controls to the number of degrees of freedom. The optimization approach 'searches for an allowable combination of controls that produce the 'best' one according to some predefined criterion' (Yamaguchi, 2001a). Latash argued that 'motor programs and control variables are a poor man's way of describing a system, whose physics are unknown' (Latash, 2012). Indeed, optimal control theory only provides a phenomenological representation of the process, which, while effective in predicting some of its manifestations, does not provide a detailed mechanistic representation. One of the main difficulties with this approach is how to formulate a physiologically justifiable cost function, or how to quantify how good a control strategy is; How to define such an optimization criterion that considers physiologically relevant variables like energy expenditure, muscle exertion, pain and fatigue? The optimization approach has resulted in physiologically plausible estimations of muscle forces during healthy gait (Crowninshield and Brand, 1981) and the approach allows for the exploration of muscle abundance and the flexibility of the human motor system. Both the possibilities and limitations of the optimization approach to study motor control will be discussed in the following chapters in full detail, but we can already anticipate one of the main conclusions of this thesis: while optimal control models might work well in healthy adults, this approach shows reduced accuracy and some inherent limitations when used to model the movement of children, elderly people or patients.

2.2 Subject-specific model identification

The following paragraph introduces the typical experimental data to identify subject-specific model parameters and that allow an optimization approach to model the dynamics of human movement.

2.2.1 Gait analysis

Motion capture aims to record human motion and several techniques, such as goniometry, inertial measurements and stereo photogrammetry, are used for this purpose. Optical systems measure the location of skin-attached markers in the lab environment. Through spatial calibration of the cameras with respect to each other, the three-dimensional location of a marker can be reconstructed from the individual two-dimensional images. In a system with passive markers, the cameras are sensitive to the infrared light they emit which the markers reflect. A properly defined marker set allows for the reconstruction of segment orientation and the amount and location of the markers depend on the modelling procedure. Typically, three or more markers are attached per segment to fully define its orientation. With this technique, errors in segment orientation estimation originate from three different sources: instrumentation, marker placement and skin motion. Instrumentation errors are small relative to the other two types of errors. The use of ultrasound techniques or the recording of anatomical markers in the medical images, used to obtain bone geometries, can reduce marker placement errors. The largest source of error, however, is the movement of the skin with respect to the underlying bones. To reduce this error, a distinction is made between anatomical markers and technical markers; the former are attached to the skin over predefined bony landmarks that can be identified through manual palpation; the latter are attached to the skin at locations where movement with respect to the bones during motion tasks is minimal. Generally, the anatomical markers are used to define a static pose from a trial where the participant is asked to stand still, while the technical markers are used to reconstruct the segment orientations during motion trials. One of the possible procedures to estimate joint kinematics will be discussed later.

In case of gait, the forces exchanged with the floor can be measured simultaneously to the skin-marker trajectories with force-sensitive platforms that are mounted in the floor. Different types of instrumentation, such as piezoelectric sensors or strain gauges, exist, but the principle remains the same: the forces at the origin and the moments around the axes of the platform reference frame are measured, which allows for the reconstruction of the point of application of the forces at the platform's surface. Due to this reconstruction, the estimates of the point of application are highly sensitive to noise, especially at the low signal-to-noise ratios during initial contact and toe-off. A force

threshold, a cut-off value for lower forces, and a low-pass filter are commonly applied to reduce instrumentation errors.

2.2.2 Electromyography

Surface electromyography (EMG) allows for the recording of electrical activity of skeletal muscles with electrodes applied to the skin over the muscle centre. In bipolar recordings, a potential difference between two electrodes originates from the action potential dipoles that move along the muscle fibre membranes. Even though EMG recordings are representative of muscle activation, the relation with muscle force is not straightforward due to measurement errors and the non-linear relationship between a muscle's electrical activation and force production. Movement artefacts, crosstalk from other muscles, material properties of the tissues between the muscle and the electrodes and heterogeneity of muscle fibre size are just a few factors that trouble EMG signals. A bandpass filter, signal rectification and a low-pass filter are sequentially applied to obtain EMG envelopes, which are indicative of muscle on- and offsets. Further interpretation of EMG in terms of activation amplitude and force prediction requires many assumptions and is beyond the scope of this study.

2.2.3 Magnetic resonance imaging

Magnetic resonance imaging is an imaging technique based on the spin of hydrogen protons in water molecules and their response to applied magnetic fields. An MRI scanner applies three different magnetic fields: a strong, static magnetic field to align the spin orientation, a radiofrequency (RF) field that excites the spin to a direction perpendicular to the static field and gradient fields to define spatial information. Contrast in the images is obtained through two relaxation measures that depend on the density of water molecules in a tissue: T1-weighted images depend on the time it takes for hydrogen spins to align with the static field after the RF field has been removed and T2*-weighted images depend on the dephasing of hydrogen spins from their alignment with the perpendicular RF field after being excited.

Segmentation of bones from the MRI images provide segment geometries and can inform the orientation of rotation axes through the fitting of geometrical shapes, such as spheres and cylinders, to the joint surfaces. The volumes of soft tissue, such as the skin and muscles, are also visible on MRI images and can therefore inform the estimation of the segment mass properties and the orientation of muscle geometry paths.

2.2.4 Inverse kinematics

Kinematics is the study that describes the motion of points, bodies and systems of bodies without considering the internal and external forces involved. An accurate description of the motion is valuable in the study of dynamics that aims to relate the forces to the positions, velocities and accelerations of the system. Once the musculoskeletal model is identified and the skin marker trajectories are obtained, an inverse approach can be taken to derive the underlying skeletal kinematics from the skin marker motions.

Static tasks do not suffer from relative skin-bone motion and are used to identify the position of the technical markers with respect to the segment reference frames. A global optimization method is used to obtain the generalized coordinates that minimize the difference between the positions of the virtual and experimental anatomical markers (Lu and O'Connor, 1999). The positions of both the technical and anatomical virtual markers in the segment reference frames are then adjusted such that their positions in the global reference frame match those of the experimental markers. The same optimization technique can then be used to identify the trajectories of the generalized coordinates during a dynamic task, such as walking, running and squats. In contrast to the estimation of the static pose, the difference between positions of the virtual and the experimental technical markers now contributes to the optimization criterion. For each dynamic trial, the trajectories of generalized coordinates $\vec{q}(t)$ fully describe the orientation and position of each segment of the musculoskeletal system at each time point.

2.3 Inverse dynamics

When we decide to move, our central nervous system signals our neurons to activate our muscles; the activation of our muscles leads to the production of forces that accelerate our joints and move our body segments in space over time. As mentioned above, rigid multibody dynamics provides a powerful approach to model these dynamics of the musculoskeletal system: The location and orientation of the musculoskeletal system is fully determined by the generalized coordinates $\vec{q}(t)$, the change in configuration of the system over time is described by the generalized velocities, $\dot{\vec{q}}(t)$, and accelerations, $\ddot{\vec{q}}(t)$. Following Newton's and Euler's second laws of motion, all the forces acting on a rigid body with constant mass describe the acceleration of its centre of mass and its angular acceleration. These laws of motion can be conveniently expanded to the dynamics of a rigid multibody system using Lagrange's method, describing the relationship between the generalized accelerations and the forces acting on a system articulated by n degrees of freedom:

$$M(\vec{q})\ddot{\vec{q}}(t) = \vec{T}(t) + \vec{C}\big(\vec{q}(t),\dot{\vec{q}}(t)\big) + \vec{G}\big(\vec{q}(t)\big) + \vec{E}\big(\vec{q}(t),\dot{\vec{q}}(t)\big) \qquad \text{2.8}$$

where M is the $n \times n$ mass matrix and $\vec{T}$ is the $n \times 1$ vector of forces and moments of force acting at the generalized coordinates and $\vec{C}$, $\vec{G}$ and $\vec{E}$ are the $n \times 1$ vectors of the centrifugal, the gravitational and the external forces, respectively. As with the generalized coordinates, the components of $\vec{T}$ can be divided into two groups according to the type of coordinate it acts on: The forces and moments at the joint coordinates represent the net result from the forces in the muscles and the ligaments, while the residual forces and moments act on the coordinates that specify the location and orientation of the pelvis with respect to the inertial reference frame. The residual forces and moments represent the inconsistencies between the mass distribution, the joint kinematics and the measured ground reaction forces and the forces and moments exerted on the pelvis by the contralateral limb and/or the upper-body segment that are potentially ignored.

We can aim to solve this set of equations in a forward or inverse manner depending on the type of questions we want our model to answer and on the type of experimental data that is available. A forward dynamics approach explores the motion output as a function of the muscular force input and therefore allows us to answer 'what if …?' questions. However, two additional requirements complicate the application of a forward approach: Firstly, the ground reaction forces are an output of the model and therefore a foot-ground contact model is required. Secondly, the activation or force patterns for all muscles are required as an input, but a non-invasive technique to measure those forces or activations is currently not available. Muscle excitation patterns have been estimated from calibrated EMG data to drive musculoskeletal motion (Lloyd and Besier, 2003), but such methods require many assumptions and are difficult to validate. In the inverse approach, the orientations, velocities and accelerations, $\vec{q}(t)$, $\dot{\vec{q}}(t)$ and $\ddot{\vec{q}}(t)$, are assumed to be known and the equations of motion are solved for the generalized torques, $\vec{T}(t)$. An estimation of the generalized coordinates can be obtained through the previously explained inverse kinematics technique, while values for the generalized velocities and accelerations can be obtained by differentiation of the orientations with respect to time (*Figure 2.2*). Given the known musculoskeletal anatomy, the known kinematics and the known forces exchanged with the environment, the muscle forces must satisfy the following instantaneous equilibrium:

$$\vec{T}(t) = B(\vec{q},t)\vec{F}^M(t) \qquad \text{2.9}$$

where B is a $n \times m$ matrix of muscle moment arms, and $\vec{F}^M$ is a vector of m muscle forces. With this

set of equilibrium equations, inverse dynamics provides a modelling approach to explore the possible muscle force patterns that underlie the known motion and result in the contact forces experienced by the joints. The inverse approach is commonly referred to as a quasi-static approach, because the dynamic equilibrium can be solved independently for each time point after the generalized accelerations are determined.
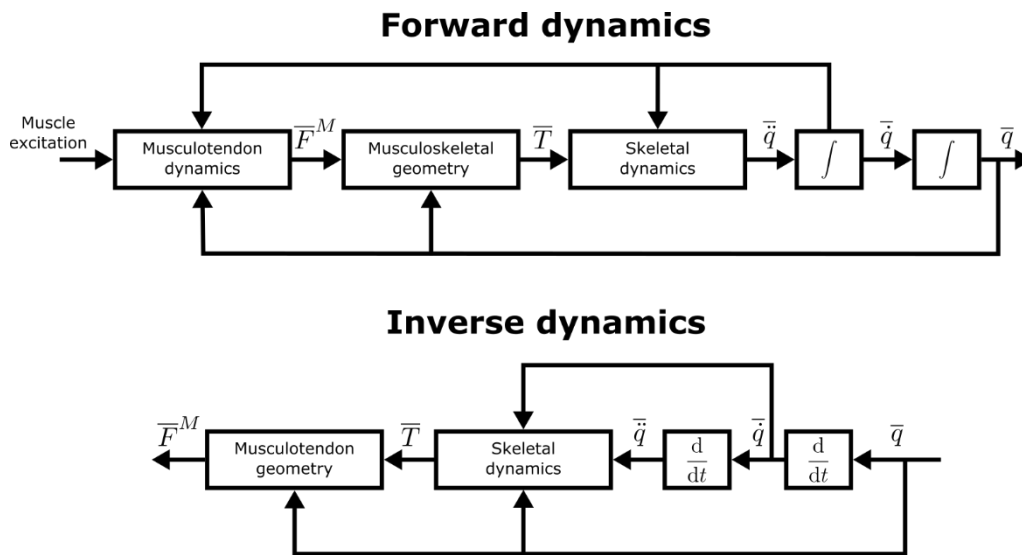

Figure 2.2: Block representation of the forward dynamics (top) and inverse dynamics (bottom) approach to solve the muscle redundancy problem. Generalized coordinates, velocities and accelerations ($\vec{q}$, $\dot{\vec{q}}$ and $\ddot{\vec{q}}$, respectively), generalized torques ($\vec{T}$) and muscle forces ($\vec{F}^M$). Image adapted from Viceconti (2011).

2.4 Static optimization

The concept of muscle redundancy implies that an infinite amount of muscle forces exists that balance the generalized torques in *Equation 2.9*. The central nervous system chooses one control pattern from many possibilities to make the musculoskeletal system execute the intended motion. One approach to solve this muscle load-sharing problem, typical in inverse dynamics simulations, is to assume that our central nervous system solves an optimization problem where a muscle activation pattern is selected by minimizing an objective function J:

$$
\begin{aligned}
\min \quad & J(\vec{F}^M) \\
\text{subject to} \quad & \vec{T}(t) = B(\vec{q}, t)\vec{F}^M\ (t) \\
& \vec{0} \leq \vec{F}^M \leq \vec{F}^M_{max}(t)
\end{aligned}
\qquad 2.10
$$

where $\vec{F}^M_{max}$ is the $n \times 1$ vector of maximal muscle forces given the dynamically solvable equations of

musculotendon dynamics (*Equation 2.5*). A large number of studies explored if an objective function existed of which the minimization would predict a muscle activation pattern that agreed with the activation measured by EMG (Crowninshield and Brand, 1981; Hardt, 1978; Patriarco et al., 1981; Seireg and Arvikar, 1975) (For a complete overview, see (Erdemir et al., 2007)). Eventually, the consensus settled on the summation of muscle activations squared as an objective function that predicted muscle activation patterns in close enough agreement with EMG data. If we ignore the muscle force-length-velocity relationship, the generalized form of this objective function is:

$$J(\vec{F}^M) = \sum_{i=1}^{m} \left(\frac{F_i^M(t)}{\vec{F}_{max,i}^M(t)} \right)^k \qquad 2.11$$

where m is the number of muscles and the exponent $k > 1$. However, such an objective function did not provide a physical explanation of motor control as such. A later study included a sophisticated model of muscular energetics in a forward dynamics approach to simulate level walking: The minimization of the metabolic energy expenditure per unit distance travelled predicted body-segmental displacements, ground reaction forces and muscle activations that were representative of healthy gait (Anderson and Pandy, 2001a). The same authors found that the minimization of the sum of muscle activations squared predicted very similar, but not identical, muscle activation patterns as the energetically optimal solution (Anderson and Pandy, 2001b). From here on, I will refer to optimal control as the minimization of the sum of muscle activations squared, due to its close approximation of the minimization of metabolic energy expenditure. In recent studies, optimal muscle control provided estimates of joint contact forces that were in approximation to the forces measured with instrumented implants (Kinney et al., 2013).

Beyond the aim to obtain a physiologically plausible estimation of muscle forces and the resulting joint contact forces, the optimization approach has also been used to assess the influence of muscle recruitment on axial tibiofemoral forces and to explore feasible muscle activation ranges in walking (DeMers et al., 2014; Simpson et al., 2015). One important limitation of this quasi-static, optimization approach to motor control compared to a forward dynamics approach is the lack of dependency between time points. An instantaneous change in muscle force production is physiologically impossible, but not constrained in this approach. Also, 'frame-by-frame' optimality does not guarantee optimality for an entire movement (Yamaguchi, 2001a).

2.5 Joint contact forces

Once we know the muscle forces, the dynamics of the system are fully described. The equal and opposite forces transmitted at the constrained directions of the joints do not contribute to the generalized accelerations and therefore are not represented in *Equation 2.8*. However, the joint surfaces experience these resultant forces and thus these forces are an important output of musculoskeletal dynamics models when considering possible biomarkers of joint degeneration. Some confusion exists on the correct term for these forces, but I will refer to them as joint contact forces (JCF), as proposed by (Zajac et al., 2002). The contact forces at each joint can be made explicit by solving the force equilibrium equations in a Cartesian coordinate system for each segment in an iterative manner; starting from the most distal segment upon which the ground reaction forces act and continuing in a proximal direction:

$$\vec{F}^j(t) = M_i(\vec{q})\vec{a}_i(t) - \sum \vec{F}^M(t) - \sum \vec{F}^{ext}(t) - \vec{F}^{j+1}(t) \qquad 2.12$$

where $\vec{F}^j$ is the contact force and moment of joint j on the distal segment i, $\vec{a}_i$ is the six-dimensional vector of linear and angular accelerations of segment i, $\sum \vec{F}^{ext}$ is the sum of external forces, including the gravitational force, and $\vec{F}^{j+1}$ is the contact force of joint $j+1$ on its proximal segment i. An example of all the forces acting on the femur is provided in the free-body diagram shown in *Figure 2.3*.

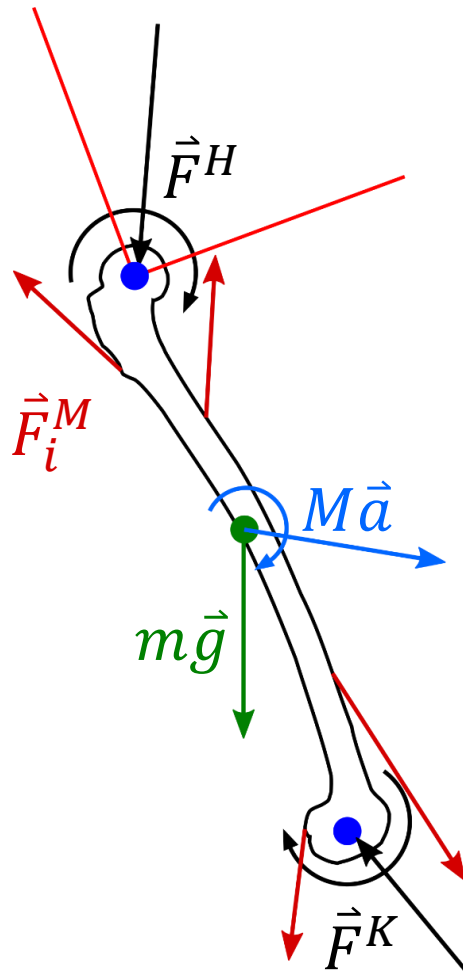*Figure 2.3*: Two dimensional free-body diagram of the femur; the muscle forces ($\vec{F}_i^M$), inertial forces ($M\vec{a}$), gravitational force ($m\vec{g}$) and knee and hip contact forces ($\vec{F}^K$ and $\vec{F}^H$) are shown. The reference frame is located at the centre of the femoral head.

CHAPTER 3

-

VERIFICATION, VALIDATION AND UNCERTAINTY QUANTIFICATION

OF MOVEMENT DYNAMICS

To trust the answer a model provides to a specific research question, we need to know the accuracy of or, conversely, the error in its predictions. We need to quantify the uncertainty in predictions due to the inherent variability in the system of interest and determine the sensitivity of the output to our modelling assumptions. Specifically for musculoskeletal models and simulations of movement, Hicks and colleagues proposed a set of guidelines for model verification and validation (Hicks et al., 2015). These guidelines provide a complete and in-depth overview of best practices; the following section expands on these guidelines and is specifically aimed to quantify the uncertainty in joint contact force predictions and their relation to the prediction of muscle activation patterns.

Hicks and colleagues followed the definitions of verification and validation from the American Society of Mechanical Engineers (Thacker, 2001):

'Verification is the process of determining that a model implementation accurately represents the developer's conceptual description of the model and the solution to the model.'

and

'Validation is the process of determining the degree to which a model is an accurate representation of the real world from the perspective of the intended uses of the model.'

3.1 Solver verification

After we have defined a research questions and a methodological design and before we generate any simulation results with third-party software or in-house developed code, we must verify its implementation. In software development, a test suite provides a collection of test cases that collectively verify the implementation of the code. These test cases typically compare the predictions from the software to analytical benchmarks.

OpenSim is a widely used, open-source code that *allows for computational modelling and simulation of neuromusculoskeletal systems* (Delp et al., 2007; Hicks et al., 2015; Seth et al., 2011), which leverages on the, also open-source, SimBody code to perform the simulations of multibody dynamics (Sherman et al., 2011). Before every release, OpenSim is tested against 29 benchmark problems that cover every aspect of the software's functionality.

Any in-house developed code, described in the remaining sections, leveraged as much as possible on the object-oriented design of the OpenSim-MATLAB application programming interface (API) to allow for efficient software verification (Hicks et al., 2015; Seth et al., 2011). The implementations of the system definition (*Equation 2.10*) and the optimizer to obtain muscle activation solutions (*Equation 2.11*) were verified through comparison with the solution obtained from the OpenSim static

optimization tool when the objective function aimed to minimize the sum of muscle activations squared.

3.2 Model verification: conservation of momentum

The law of conservation of momentum states that the total momentum is constant in a closed system. In other words: for a system that does not interact with its environment, the sum of the mass multiplied by the velocity of each element remains equal. The musculoskeletal system, however, does exchange forces with its surroundings during dynamic tasks and therefore the momentum of the system changes over time. How well an inverse dynamics model captures these changes in momentum is quantified by the residual forces and moments: errors in the estimated kinematics and mass distribution of the musculoskeletal model result in residual forces and moments at the other end of the kinematic chain than where the external forces, or ground reaction forces, apply. Typically, the residual forces are defined to act at the link between the pelvis and the inertial reference frame, or ground.

The guidelines proposed by Hicks and colleagues suggest threshold values that the residual forces and moments should not exceed for the model to accurately simulate the system dynamics: the root-mean-square (RMS) and peak residual forces should not exceed 5 % of the magnitude of the external forces and the RMS and peak residual moments should not exceed 1 % of the body centre-of-mass height multiplied by the magnitude of the external forces. When the values of the original simulations exceed the threshold values, the reduce residual algorithm suggests slight adjustments of the kinematics and segments' mass distribution to minimize the residual forces and moments (Hamner et al., 2010; Kuo, 1998). However, the residual forces and moments should only be minimized when these forces and moments are not compensating for a contralateral limb or upper body that is not represented in the model. Even when the model does contain both lower limbs and an upper body, one could question whether adjustments of the kinematics and mass distributions within the lower limb of interest are preferred. Most likely, the parameter identification and model assumptions for the lower limb are less course than those for the upper body. In simulations of walking, the upper limbs are generally ignored and the upper body is regarded as a single, rigid segment. Incorrect adjustments to the kinematics and mass distribution of the lower limb might be made to compensate for the inaccurate representation of the moving masses of the arms and internal organs. Therefore, the reduce residuals algorithm has not been applied in the following studies, but the residual forces and moments will be reported for each of the models.

3.3 Uncertainty quantification of inverse dynamics models

Inverse dynamics simulations of human level walking require a variety of assumptions and data on the musculoskeletal system. Subsequently, the uncertainty in the model output suffers from these assumptions and a variety of errors in the parameter identification and the measured data.

Soft-tissue artefacts are one of the largest sources of error in the input data for inverse dynamics models: The skin-attached markers move with respect to the bones during dynamic tasks, which introduces errors to the predicted location and orientation of segments over time. These artefacts get as large as 30 mm for markers on the thigh during walking, but are smaller for the markers on the tibia (Cappozzo et al., 1996). One sensitivity study artificially created 500 different sets of marker trajectories for level walking task, representative of the measured soft-tissue artefacts reported in literature (Lamberto et al., 2017). In three different scaled generic musculoskeletal models, the effect on the predicted joint angles and net-joint moments was evident. This effect propagated to the predicted joint contact forces: On average, the soft-tissue artefacts affected the force at the hip by less than one bodyweight (BW) and less than 0.5 BW for the knee and ankle, while maximum values reached as high as 1.5 BW for the hip. The effect on the predicted muscle forces varied across muscles, up to on average of 0.4 BW for the Gluteus Medius muscle, and around 10 % of each muscles' maximum isometric force.

Another sensitivity study focussed on the uncertainties in the identification of bony landmarks (influencing the location of joint axes), muscle geometry paths and maximum muscle tension (Valente et al., 2014). An MRI-based subject-specific model included a ball-and-socket joint at the hip and hinges at the knee and ankle. The sensitivity of the joint angles and net-joint moments to the uncertainties in parameter identification was minimal, but the joint contact forces showed a more pronounced sensitivity: the maximum standard deviation across stance was smaller than 0.3 BW for all joints, but maximum ranges varied from 1.5 BW for the hip and ankle to 2.1 BW for the knee. The maximum standard deviations of the forces in each muscle were smaller than 0.25 BW, with a maximum range of 1.5 BW for the Soleus muscle. These results suggest that the sensitivity of predicted muscle and joint contact forces to parameter identification is likely to be moderate, but a potentially large influence on the joint contact forces could occur in a worst-case scenario. An older study came to similar conclusion when varying the bone attachment points of muscles, but found a larger sensitivity of the hip contact force to these changes (Röhrle et al., 1984).

A third study quantified the sensitivity of model predictions to the uncertainties in the definition of joint axes orientation (Martelli et al., 2015b). The joint locations and axes were defined following the recommendations of the International Society of Biomechanics (Wu et al., 2002). The operator-

dependent variability in virtual palpations of anatomical landmarks defined the uncertainties in the joint reference frames. The ranges of predicted force in each muscle were smaller than 0.35 BW and did not exceed 15% of their maximal force contribution throughout the gait cycle. The ranges of predicted muscle forces were smaller than 0.3 BW for the hip and the ankle joint and smaller than 0.15 BW for the knee joint.

Besides the orientation of joint axes, assumptions on the degrees of freedom in different joint models also affect the model predictions. One study compared the effect of joint models on the predicted muscle and joint contact forces from three different MSK models to the reference model used for the sensitivity analysis of parameter identification mentioned previously (Valente et al., 2015, 2014). The first model included prescribed translation of the tibia with respect to the femur dependent on the knee flexion angle and a universal joint rather than a hinge at the ankle to allow for rotation in the subtalar joint; the second model included a three degree of freedom at the knee; the third model included anatomical ligaments that constrained the knee and ankle joints to function as hinges that allowed for small anterior-posterior and inferior-superior translations prescribed by the knee flexion angle. The differences with the predictions from the reference model in terms of joint contact forces were dependent on the joint model. The mean differences over repeated trials for the first model were smaller than 0.1 BW for the hip and the knee and smaller than 0.2 BW for the ankle, while the maximum difference did not exceed 0.5 BW for any of the joints. The differences of the second model got as large as 0.8 BW for the hip, 2.4 BW for the knee and 1.6 BW for the ankle. The differences of the third model were on average smaller than 0.2 BW for all joints, while the maximum differences did not exceed 1.1 BW for the knee. The differences in activation of the first and third model compared to the reference model were maximally 10-15 % during the stance phase.

The assumption to represent muscles as linear actuators introduces errors in their estimated moment arms and lines of action, especially for muscles with large bone-attachment areas. Therefore, the decision on how to discretize these large muscles into individual compartments, all represented by one linear actuator, is likely to affect the errors in predicted joint contact forces and muscle forces. The effect of an accurate representation of muscles with a large bone-attachment area as separate linear actuators on the resultant force in the centroid of the attachment area was small, but larger for the resultant moments (Valente et al., 2012). This finding is relevant to estimate the effect on the bone surface, but the effect on the predicted muscle and joint contact forces during dynamic tasks, such as level walking, remained unclear. A follow-up study, presented in a doctoral thesis, suggested that during level walking the effect on the peak forces at the hip and knee ranged from 5 to 15 %, while no effect was found at the ankle (Valente, 2013).

The operator-dependent variability in the predicted vertical ankle forces and the forces in muscles that span the ankle within a subject-specific model construction pipeline were dependent on the subject (Hannah et al., 2017). For three different subjects the maximum difference in ankle force between operators ranged from 0.7 to 1.5 BW, while intra-operator variability was 0.3 BW for the subject with the lowest inter-operator variability. The inter-operator variability of predicted muscle forces was highly dependent on the subject and the maximum differences were as large as 73 % of the maximum isometric force for the Gastrocnemius Medialis muscle.

From these studies, we can estimate the uncertainty affecting the predictions of musculoskeletal models, similar to the ones used in the following sections of this work, to be around 1-2 BW for joint contact forces and roughly 10 % of the maximum activation for each muscle. In the following, we will explore this region through variability in motor control and study how well the uncertainty on muscle force predictions overlap with the measured forces across repeated trials, which include both intra-subject variability and all uncertainties affecting the experimental measurements.

3.4 Solution space of the dynamic equilibrium

3.4.1 Introduction

When using an inverse approach to study the dynamics of human movement assumptions on motor control strategies are required. Typically, these assumptions are represented as optimization strategies that are suggested to yield physiologically plausible results. However, the selection of a motor control strategy is likely to be patient specific and influenced by multiple factors. For example, the minimization of energy expenditure has been proposed as a general strategy in healthy gait (Anderson and Pandy, 2001a), but energy expenditure has been shown to increase in pathological gait (Waters and Mulroy, 1999) and the amount of co-contraction observed during gait has been associated with painful joints (Childs et al., 2004; Heiden et al., 2009) and instability (Hirokawa et al., 1991; Hurd and Snyder-Mackler, 2007). This indicates that the minimization of energy expenditure is not always the preferred control strategy. Also, muscle control might be more, or less, variable, depending on a person's ability or need to control force production, for example due to pathologies or pain.

Several alternative approaches have been suggested to explore the solution space of muscle forces that satisfy the dynamic equilibrium (*Equation 2.9*). For example, in one experimental approach surface electromyography was successfully used to predict muscle forces in different knee movement tasks and gait (Lloyd and Besier, 2003; Pizzolato et al., 2015). Another study focussed on the estimation

of joint contact forces by predicting ranges of muscle forces based on variability in EMG (Mirka and Marras, 1993). Despite these interesting applications, an experimental framework to explore the solution space of the dynamic equilibrium is difficult to realise, as variability in experimental measurements only occurs when a task is repeated. Hence, variability will not only occur in the space of muscle force patterns, but will also inherently occur as kinematic variability. The question would be how to separate these sources of variability.

In a more deterministic approach to explore the structure of muscle redundancy, a combination of cadaveric data and computational geometry of the cat hind limb was used (Kutch and Valero-Cuevas, 2011; Valero-Cuevas et al., 2015, 1998). Feasible force sets were determined for each muscle, representing the contribution of a specific muscle to the force produced at the motor endpoint. Many different combinations of individual muscle forces produced identical submaximal forces at the most distal point of the limb (Valero-Cuevas et al., 2015). However, due to both the cadaveric element and the computational expense to obtain an exact solution, it is currently unfeasible to apply this method to a multi-body dynamics model of the human motor system for complex tasks such as walking.

Optimization techniques have been used to assess muscle redundancy in force producing tasks by exploring the borders of the solution space through minimization and maximization of the activation of a single muscle, while the other muscle were free to satisfy the dynamic equilibrium (Sohn et al., 2013). However, this method did not provide any information on the distribution of sub-optimal muscle recruitment strategies within the solution space, while previous studies did account for sub-optimality and showed its relevance to the prediction of spontaneous fractures (Martelli et al., 2011; Viceconti et al., 2012). A later study introduced a probabilistic approach to estimate an even larger set of sub-optimal muscle force patterns (Martelli et al., 2013). These sub-optimal solutions were shown to, on average, correlate well with EMG and span a large range of hip contact forces (Martelli et al., 2015a).

Specifically, this method leverages on Bayesian statistics to define a probability distribution from which muscle force patterns are sampled using a Markov chain Monte Carlo method. The sampled posterior probability distribution of muscle forces is defined by a prior and a likelihood term:

$$\pi\big(\vec{F}^M(t)\big|\vec{T}(t)\big) \propto \pi_{pr}\big(\vec{F}^M(t)\big)\pi\big(\vec{T}(t)\big|\vec{F}^M(t)\big) \qquad 3.1$$

where $\pi_{pr}\big(\vec{F}^M(t)\big)$ is the prior term that represents the constraints on the muscle forces (*Equation 2.10*), $\pi\big(\vec{T}(t)\big|\vec{F}^M(t)\big)$ is the likelihood term that represents the probability of the known generalized torques, $\vec{T}(t)$, given a vector of muscle forces $\vec{F}^M(t)$ and $\pi\big(\vec{F}^M(t)\big|\vec{T}(t)\big)$ is the posterior distribution

that represents the probability of a vector of muscle forces that satisfies the dynamic equilibrium (*Equation 2.8*). The likelihood term $\pi\left(\vec{T}(t)\middle|\vec{F}^M(t)\right)$ consists of a Gaussian distribution along the null space of the moment-arm matrix $B(q,t)$ (*Equation 2.9*). For each time frame, a Markov chain Monte Carlo random-walk method was used to obtain a set of representative samples, or muscle force patterns, from the probability distribution. The algorithm to sample the solution space of muscle force patterns was part of the Metabolica software, implemented in MATLAB (v2017a, The MathWorks, Inc., Natick, MA, USA) (Heino et al., 2010, 2007).

When such a probabilistic approach to obtain sub-optimal muscle force patterns is used to study physiologically plausible motor control, it is important to assess how the set of samples is representative of the entire solution space. On the one hand, in the study that introduced the use of Metabolica in this context, at least one force pattern was sampled for each muscle in which that muscle did not contribute any force at the instant of the gait cycle where the first peak of the hip contact force occurred during level walking (Martelli et al., 2013). This result was later subscribed by an optimization study in which no muscle was specifically required to contribute force at any instant of the gait cycle in treadmill walking (Simpson et al., 2015). On the other hand, in the Metabolica study, no solutions were sampled that reached the muscles' maximum force values for (compartments of) the Gluteus Maximus, the hip adductor, the Semimembranosus, the Vasti, the Gastrocnemius and the Soleus muscles. However, the optimization study showed that only for the Gastrocnemius and the Soleus muscles no force pattern existed, at specific time intervals during the gait cycle, in which these muscles contributed their maximum force. Even though these studies were performed on different participants, these results suggest that the probabilistic method does not always reach the boundaries of the solution space of muscle force patterns. However, the sample size could influence the range of forces that is obtained for each muscle. Therefore, the first aim of this methodological work was to study the effect of the sample size in the probabilistic method, as described above, on the range of muscle forces obtained for a multibody-dynamics simulation of level walking. The second aim of this work was to explore the distribution and the density of samples within the solution space.

3.4.2 Methods

Dynamics simulations

The trajectories of skin marker positions and ground reaction forces of one overground, level walking gait cycle for one healthy participant (male, age: 28 yrs., height: 1.90 m) were included. Details on the experimental data collection are listed in *Appendix A.1* under *p01*. The segment geometries of a generic musculoskeletal model that included 13 DoFs and 92 muscles, were scaled based on the

measured positions of skin markers during a static standing trial (Delp et al., 1990). The generalized coordinates, the generalized torques and the muscle lever arms with respect to the coordinates were estimated using the Opensim inverse kinematics and inverse dynamics tools. The patterns of joint angles and joint moments (normalized to body weight × height) resembled normative patterns (Kadaba et al., 1989). The maximum force each muscle could produce during any instant of the gait cycle was defined by its maximum isometric force, which was scaled according to the ratio of body mass between the participant and the generic model.

Muscle force patterns

The optimization problem in *Equation 2.10* was solved twice for each muscle to obtain the minimum and maximum possible force for each muscle using the following linear objective function:

$$J(\vec{F}) = \vec{w}^T \vec{F}(t) \qquad\qquad 3.2$$

where $\vec{w}$ is a $m \times 1$ vector of weights of each actuator. The first optimization $J_{min}(\vec{F})$ aimed to minimize the force in the targeted muscle actuator: the entries of $\vec{w}$ were set to 0, except for the entry of the targeted muscle which was set to 1. The second optimization $J_{max}(\vec{F})$ aimed to maximize the force in the targeted muscle: the entries of $\vec{w}$ were set to 0, except for the entry of the targeted muscle which was set to -1. MATLAB's linear programming *linprog*, leveraging on the dual-simplex algorithm, was used to solve the problem.

The Metabolica tool was used to generate multiple sets of possible muscle force patterns $\left\{ [\vec{F}(t)]_1, [\vec{F}(t)]_2, \ldots, [\vec{F}(t)]_N \right\}$ from which each sample satisfied *Equation 2.9*. The samples were drawn four times to obtain four sets of different sample sizes: $N = 1 \times 10^5$, $N = 2 \times 10^5$, $N = 3 \times 10^5$ and $N = 1 \times 10^6$. The starting point was the solution to the optimization problem in *Equation 2.10* given the following objective function, where each actuator was treated as an ideal force generator:

$$J_{opt}(\vec{F}) = \sum_{i=1}^{m} \left(\frac{F_i(t)}{F_{o,i}} \right)^2 \qquad\qquad 3.3$$

where $F_{o,i}$ is the maximum isometric force of (muscle) actuator i. MATLAB's quadratic programming *quadprog*, leveraging on the interior-point algorithm, was used to solve the problem.

Quantification of sampled region of muscle force patterns

For each muscle in each of the four sampled sets, the range of the sampled forces was expressed as a ratio with respect to the range of forces found through optimization:

$$r_i(t) = \frac{\left[F_i^M(t)\right]_{max} - \left[F_i^M(t)\right]_{min}}{F_{max,i}^M(t) - F_{min,i}^M(t)} \qquad 3.4$$

where $\left[F_i^M(t)\right]_{max}$ is the maximum force value of muscle i within a set of samples, $\left[F_i^M(t)\right]_{min}$ is the minimum force value of muscle i within a set of samples, $F_{max,i}^M(t)$ is the force value of muscle i from the J_{max} solution and $F_{min,i}^M(t)$ is the force value of muscle i from the J_{min} solution. Values of $r_i(t)$ were defined to fall in between 0 and 1, indicating a not sampled or fully sampled range of forces for muscle i, respectively.

As a measure of similarity, the normalized distance of each sampled force pattern to the J_{opt} solution was defined as:

$$d_k(t) = \sqrt{\sum_{i=1}^{m} \left(\frac{\left[F_i^M(t)\right]_k - F_{opt,i}^M(t)}{F_{o,i}^M}\right)^2} \qquad 3.5$$

where $\left[F_i^M(t)\right]_k$ is the force in muscle i from the sampled force pattern k and $F_{opt,i}^M(t)$ is the force in muscle i from the J_{opt} solution. A distance value of zero indicates a sample that is identical to the J_{opt} solution, while a higher distance value indicates a sampled force pattern that is increasingly different from the J_{opt} solution.

3.4.3 Results

For a sample size of 1×10^5, the force ranges sampled with Metabolica were significantly smaller than the muscle force ranges from the J_{min} and J_{max} solutions for most muscles throughout the gait cycle. At the larger sample sizes, the maximum and minimum possible muscle forces were sampled for most muscles at each instant of the gait cycle (*Figure 3.1*). However, the Metabolica samples did not reach the boundaries of the solution space for the Vasti, the intermediate and posterior compartments of the left Gluteus Maximus and the anterior and posterior compartments of the left Gluteus Medius muscles, typically during the terminal stance (around 50 % of the gait cycle) or terminal swing phase (90-100 % of the gait cycle). In addition, for both the left and right Soleus muscles the sampled force values only reached the boundaries of the solution space at a short time interval during terminal

stance. A further increase in sample size from 2x10^5 to 1x10^6 did not increase the sampled range of forces for any of these muscles at the specified time intervals. Therefore, only the sample size of 2x10^5 was considered when discussing the distance values d_k.

The average distance of the samples from the J_{opt} solution ranged from 4.2 to 4.9 normalized force values throughout the gait cycle and at each time point a bell-shaped frequency distribution was obtained around the average distance value (*Figure 3.2*). The interval of distance values between zero and 3 to 3.5 normalized force values, depending on the time point, was scarcely sampled, while no distance values higher than 6 normalized force values occurred. The samples in this scarcely sampled region were intermediate steps of the random walker in the direction of the densely sampled region around the average distance.
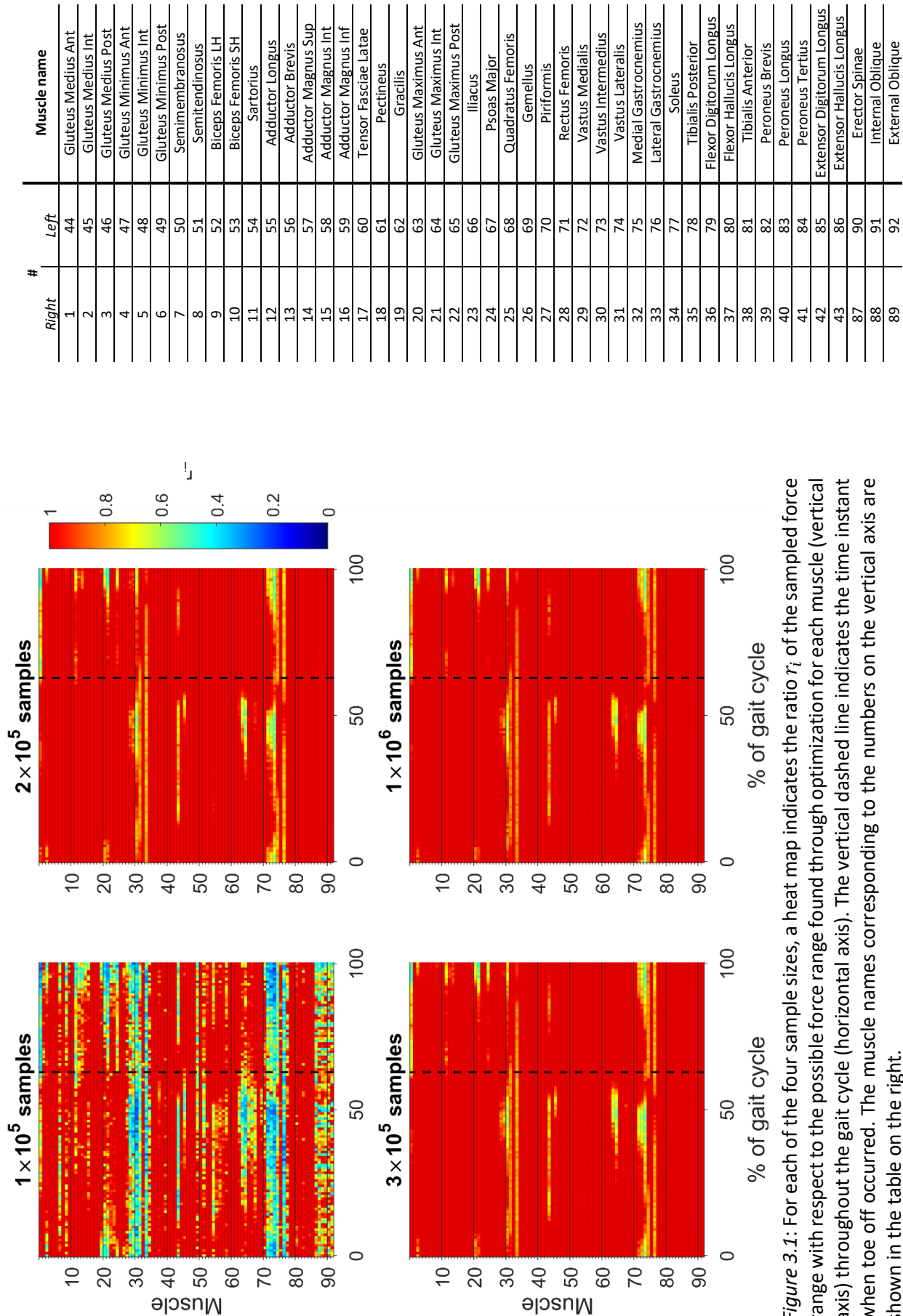
# Right	Left	Muscle name
1	44	Gluteus Medius Ant
2	45	Gluteus Medius Int
3	46	Gluteus Medius Post
4	47	Gluteus Minimus Ant
5	48	Gluteus Minimus Int
6	49	Gluteus Minimus Post
7	50	Semimembranosus
8	51	Semitendinosus
9	52	Biceps Femoris LH
10	53	Biceps Femoris SH
11	54	Sartorius
12	55	Adductor Longus
13	56	Adductor Brevis
14	57	Adductor Magnus Sup
15	58	Adductor Magnus Int
16	59	Adductor Magnus Inf
17	60	Tensor Fasciae Latae
18	61	Pectineus
19	62	Gracilis
20	63	Gluteus Maximus Ant
21	64	Gluteus Maximus Int
22	65	Gluteus Maximus Post
23	66	Iliacus
24	67	Psoas Major
25	68	Quadratus Femoris
26	69	Gemellus
27	70	Piriformis
28	71	Rectus Femoris
29	72	Vastus Medialis
30	73	Vastus Intermedius
31	74	Vastus Lateralis
32	75	Medial Gastrocnemius
33	76	Lateral Gastrocnemius
34	77	Soleus
35	78	Tibialis Posterior
36	79	Flexor Digitorum Longus
37	80	Flexor Hallucis Longus
38	81	Tibialis Anterior
39	82	Peroneus Brevis
40	83	Peroneus Longus
41	84	Peroneus Tertius
42	85	Extensor Digitorum Longus
43	86	Extensor Hallucis Longus
87	90	Erector Spinae
88	91	Internal Oblique
89	92	External Oblique

Figure 3.1: For each of the four sample sizes, a heat map indicates the ratio r_i of the sampled force range with respect to the possible force range found through optimization for each muscle (vertical axis) throughout the gait cycle (horizontal axis). The vertical dashed line indicates the time instant when toe off occurred. The muscle names corresponding to the numbers on the vertical axis are shown in the table on the right.
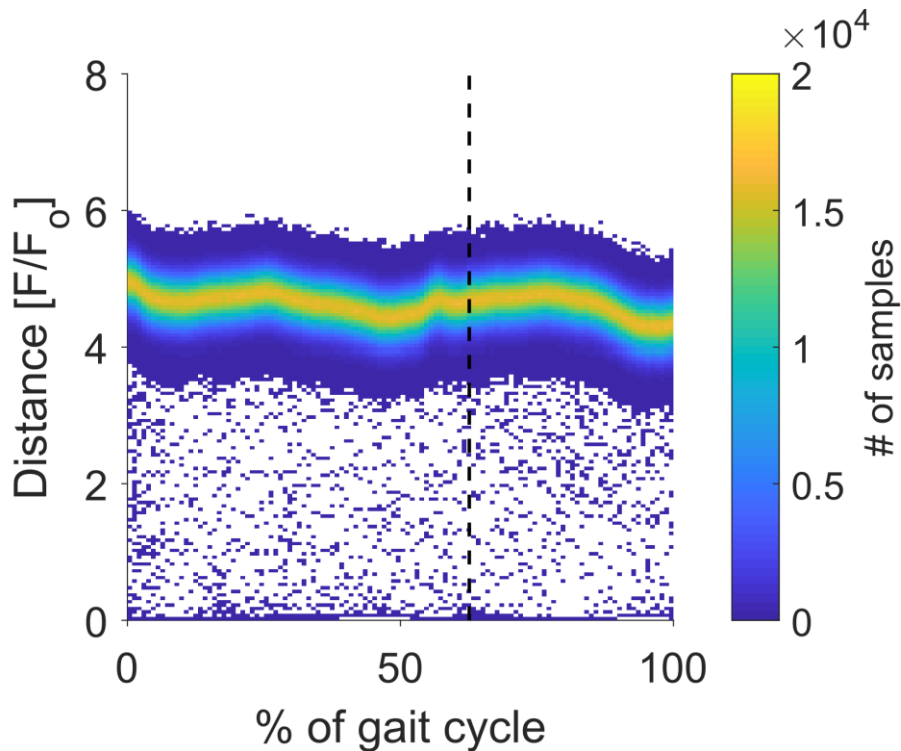
Figure 3.2: The distance d of the sampled muscle force patterns to the J_{opt} solution are shown throughout the gait cycle. The colour of the data points indicates the number of samples at the corresponding distance. The vertical, dashed line indicates the time instant when toe off occurred.

3.4.4 Discussion

The aim of the current methodological work was twofold: Firstly, this work aimed to study the effect of the sample size on the range of obtained muscle forces in a previously published, probabilistic method to calculate sub-optimal muscle force patterns in a multibody-dynamics simulation of level walking. Secondly, this work aimed to explore the distribution and the density of those sampled muscle force patterns within the solution space.

The difference in sampled muscle force ranges obtained with a sample size of 1×10^5 and 2×10^5 suggests that an insufficiently large sample size results in an underrepresentation of the possible sub-optimal force patterns. The number of samples to include, likely dependent on the size of the system (the number of degrees of freedom and muscles), can be evaluated by assessing the influence of a stepwise increase in sample size on the sampled range of forces for each muscle, as presented here.

In a previous study, the sampled force range of, among other muscles, the intermediate compartment of the Gluteus Maximus, the Vasti and the Soleus muscles did not span from zero to its corresponding maximum isometric force (Martelli et al., 2013). In this work, the sampled forces for these muscles did not reach the boundary forces for which the dynamic equilibrium could still be satisfied, determined following the methodology of a previous optimization study (Sohn et al., 2013). A further five times

increase in sample size, from 2×10^5 to 1×10^6 samples, did not evidently change the sampled force ranges. These results suggest that the probabilistic estimation of sub-optimal muscle force patterns with Metabolica needs to be accompanied by or confirmed with results from optimization techniques when the entire solution space of possible muscle force patterns is of interest.

Only a relatively small number of samples nearby the J_{opt} solution, in terms of distance in the normalized force space, was obtained. These samples were all obtained as intermediate steps of the random-walk method from the starting point to the densely sampled region. Therefore, this behaviour of the sampler results in a non-uniform representation of the solution space. These results suggest that the boundaries on the muscles' maximum force should be narrowed around a specific region of interest to obtain a representative set of muscle force patterns that resembles light sub-optimality with respect to an assumed control strategy.

In conclusion, the sampling technique of Metabolica provides a valuable, probabilistic approach to obtain a large number of muscle force patterns, representative of sub-optimality and variability in motor control, in inverse dynamics simulations of human movement. However, the probabilistic method is not suited for the exploration of the boundaries of motor control and the definition of these limits is likely to be an important factor when aiming to obtain physiologically plausible muscle force patterns.

CHAPTER 4

-

EFFECT OF MUSCLE ACTIVATION STRATEGIES ON JOINT LOADS

4.1 Introduction

Degeneration of the joint surface in diseases like osteoarthritis leads to joint pain, reduces functionality and affects activity in daily life. Biomechanical determinants considerably affect the progression, and possibly drive the onset, of damage to the joint cartilage and the underlying bone; aberrant loading of joints was argued to be an important risk factor of the progression of knee osteoarthritis (Waller et al., 2011). Varus-valgus misalignment and anterior cruciate ligament rupture have been associated with disease development and progression due to their influence on joint loading (Andriacchi et al., 2004; Brouwer et al., 2007; Sharma et al., 2001), while an independent relationship between joint overloading due to obesity and joint degeneration was not established (Felson, 2000; Reijman et al., 2006). Nonetheless, obesity has been identified as a risk factor for both hip osteoarthritis (Cooper et al., 1998) and total hip replacement (Karlson et al., 2003); indeed, increased loading due to obesity amplified degeneration in misaligned knee joints (Felson et al., 2004).

Unloading has been proposed as a conservative treatment to osteoarthritis progression (Lafeber et al., 2006) and interventions focus on weight loss, gait retraining, selective strength training and neuromuscular rehabilitation. The aim of the latter is not to introduce macroscopic kinematic compensations in the gait pattern, but rather to develop subtler neuromotor strategy compensations aimed to reduce the joint loading. Physical interventions, designed to reduce the load transmitted to the affected joint by modifying the neuromuscular recruitment patterns during gait, have a high potential because muscle forces are the primary contributors to joint compressive forces (Winby et al., 2009; Winter, 2009). But, being also the mildest of the interventions, one may wonder if it is reasonable to expect a significant reduction in the force transmitted through a joint by simply modifying the muscular recruitment strategy while preserving the gait kinematics.

Direct measurements of muscle forces and joint loads are invasive and musculoskeletal models offer a valuable non-invasive alternative to investigate the forces transmitted at joints during activities of daily life. A range of plausible muscle recruitment strategies in walking has been proposed (Anderson and Pandy, 2001b; Crowninshield and Brand, 1981; Seireg and Arvikar, 1975), among which the minimization of the sum of muscle activations squared was shown to be equivalent to energetically optimal strategies and is now widely used to estimate muscle forces in simulations of gait (Anderson and Pandy, 2001b). However, the potential of alternative muscle recruitment strategies to unload joints has been studied to a limited extent; A previous optimization study showed that alternative neuromotor control could significantly reduce axial knee loads on the tibia throughout the stance phase of gait (DeMers et al., 2014), while an exploration of possible muscle recruitment strategies in walking suggested that the potential to reduce the hip loads might be limited (Martelli et al., 2011);

The load-reducing potential of alternative muscle recruitment remains unknown for the ankle. Also, the influence of such alternative muscle recruitment strategies on the load in adjacent joints has not been investigated. The current study aimed to fill these gaps and to expand the investigation to a diverse population by answering the following questions: 1) Can alternative muscle recruitment strategies reduce the peak force transmitted at each lower limb joint during level walking?; 2) Is this reduction similar for all four cases studied here, which were selected to represent widely different populations in terms of age, gender and health status?; 3) If a muscle recruitment strategy that significantly reduces the force in one joint exists, what is its influence on the other joints?; 4) Does the joint load-reducing potential of alternative recruitment strategies change with different walking speeds?; 5) How do the activation patterns predicted by different recruitment strategies at the instant of peak joint contact force differ?

4.2 Methods

4.2.1 Experimental data

In order to explore the research questions with sufficient generality, we conducted the same analysis of four different subject-specific musculoskeletal dynamics models, each generated in a different research project, using different modelling approaches, and each referring to a very different subject: one for a healthy participant (*p01*), one for a participant with an instrumented full right knee replacement (*p02;* the sixth Knee Grand Challenge dataset (Fregly et al., 2012)), one for a participant with juvenile idiopathic arthritis (*p03*, part of the *MD-Paedigree* project JIA cohort (EC 7th FP, ICT Programme, Ref. No. 600932)) and one for a participant with osteopenia (*p04,* part of the *MultiSim* cohort (EPSRC Frontier Engineering Awards, Ref. No. EP/K03877X/1))*;* details for all participants in *Table 4.1*). Overground, level-walking trials at a self-selected speed for all participants and at orally instructed slow and fast speeds for *p01* and *p04* were included (*Table 4.2*) in this study.

Table 4.1: Details of participants.

	Gender	Age (yrs.)	Height (m)	Mass (kg)
p01	male	28	1.90	82
p02*	male	N/A	1.72	70
p03	female	16	1.68	83
p04	female	74	1.64	57

* Participant has a total knee replacement in the right limb

51

Table 4.2: Number of available trials (#) and average walking speeds for each participant.

	Self-selected		Slow		Fast	
	#	*Speed ± SD (m/s)*	#	*Speed ± SD (m/s)*	#	*Speed ± SD (m/s)*
p01	6	1.24 ± 0.02	5	1.03 ± 0.05	2	2.43 ± 0.06
p02	6	1.03 ± 0.02	N/A	N/A	N/A	N/A
p03	5	1.32 ± 0.03	N/A	N/A	N/A	N/A
p04	5	1.27 ± 0.03	5	1.14 ± 0.04	5	1.60 ± 0.05

Three-dimensional positions of skin markers and ground reaction forces (GRF) were available for all trials. Technical details of the data collection, specific for each participant, are provided in *Appendix A.1*. A 10 Hz low-pass, zero-lag, 4th order Butterworth filter was applied to the ground reaction force, moment and centre-of-pressure trajectories. For the time frames with a vertical force below 20 N, the force, moment and centre-of-pressure components were set to equal zero. This threshold prevented a low signal-to-noise ratio to influence the accuracy of the centre of pressure reconstructions.

4.2.2 Musculoskeletal models

Model identification

Participant 1 (*p01*)

An eight segment, 19 degree-of-freedom, 92 actuator generic musculoskeletal model was scaled to match the participant's anthropometry based on the ratio between the segment lengths of the generic model and those obtained from the marker trajectories of the static trial (Delp et al., 1990). Details on the methods used to compute the segment lengths from the experimental data can be found in (Lamberto et al., 2017). The back and hip were defined as ball-and-socket joints, the knee was defined as a hinge joint with prescribed anteroposterior and superior-inferior translation and the ankle was defined as a hinge joint.

The maximal isometric forces of the muscles were initially scaled uniformly according to the ratio between the body mass of the participant and the generic model. After the initial muscle force scaling, the model appeared too weak to produce the required generalized torques of the fast walking trials and therefore the maximal isometric forces were increased by a factor 1.5 (Yamaguchi, 2001b).

Participant 2 (*p02*)

A five segment, 11 degree-of-freedom and 43 actuator subject-specific musculoskeletal model of the patient's implanted, right leg was constructed. Segment geometries were provided with the dataset; Bone geometries for the femur, tibia, fibula and patella had been segmented from pre- and post-operative CT scan data; Implant geometries for the femoral component, patellar button, tibial insert and tibial tray had been extracted from point cloud data (Fregly et al., 2012; Lin et al., 2010). Segmental mass, centre-of-mass locations and inertial properties were obtained from the known geometries and densities of soft tissue, bone and implant structures. The pelvis' geometry was obtained from the *Visible Human Dataset* (Spitzer and Whitlock, 1998). The dimensions and mass properties of the pelvis segment were taken from a generic pelvis segment that was scaled according to the body-mass ratio of the generic model and the participant (Delp et al., 1990). The foot segment was obtained from one of the musculoskeletal models constructed from the *MD-Paedigree* dataset and scaled to the patient according to the body-mass ratio.

Analytical shapes were fitted to the joint surfaces of the identified bone geometries (Modenese et al., 2018); a spherical shape was fitted to the femoral head to identify the hip as a ball-and-socket joint and cylindrical shapes were fitted to the femoral condyles and to the talar trochlea to identify the knee and ankle as hinge joints, respectively. The rotation in the sagittal plane and translation of the patellofemoral joint were prescribed by the knee angle, ensuring an articulation of the patellar button along the surface of the femoral component.

The geometrical paths of the 43 muscle actuators were mapped onto the patient-specific bone geometries from a generic model (Delp et al., 1990). The paths of the Quadriceps muscles were adjusted such that they extended through the patella and attached to the tibia (Rajagopal et al., 2016). The maximal isometric forces of the muscles were scaled uniformly according to the ratio between the lower-limb mass of the participant and the generic model. The pennation angles were copied from the generic model.

Participant 3 (*p03*)

A five segment, 12 degree-of-freedom and 42 actuator subject-specific musculoskeletal model of the participant's right leg was used which had previously been constructed following a published pipeline (Modenese et al., 2018): Bone geometries were obtained through segmentation of MRI images and segment inertial properties were estimated with use of the segmented soft-tissue volumes, assigning different densities to bone and soft tissue. Analytical shapes were fitted to the joint surfaces of the identified bone geometries; the hip, knee and ankle joint were defined as in *p02*; spherical shapes were fitted to the talocalcaneal and to the talonavicular articular surfaces to identify the subtalar joint

as a hinge joint with its axis of rotation defined by the line joining the two spheres. The patella was rigidly attached to the tibia.

The geometrical paths of the 42 muscle actuators were mapped onto the patient-specific bone geometries from a generic model (Delp et al., 1990): The atlas of the muscle attachment and via-point locations were mapped to the subject-specific geometry using an affine transformation of registered bony landmarks and sequentially snapped onto the bone surfaces. The maximal isometric forces of the muscles were scaled uniformly according to the ratio between the lower-limb mass of the participant and the generic model. The pennation angles were copied from the generic model.

Participant 4 (*p04*)

A seven segment, 16 degree-of-freedom and 86 actuator subject-specific musculoskeletal model of the participant's two lower limbs was constructed, largely following the model identification methods as explained for *p03*. Two differences exist between the methods: Firstly, no subtalar joint was included and hence the foot was modelled as a single segment. Secondly, mapping of the muscle geometry points was performed using an iterative-closest point method rather than an affine transformation.

Figure 4.1 shows the four different musculoskeletal models used in this study.
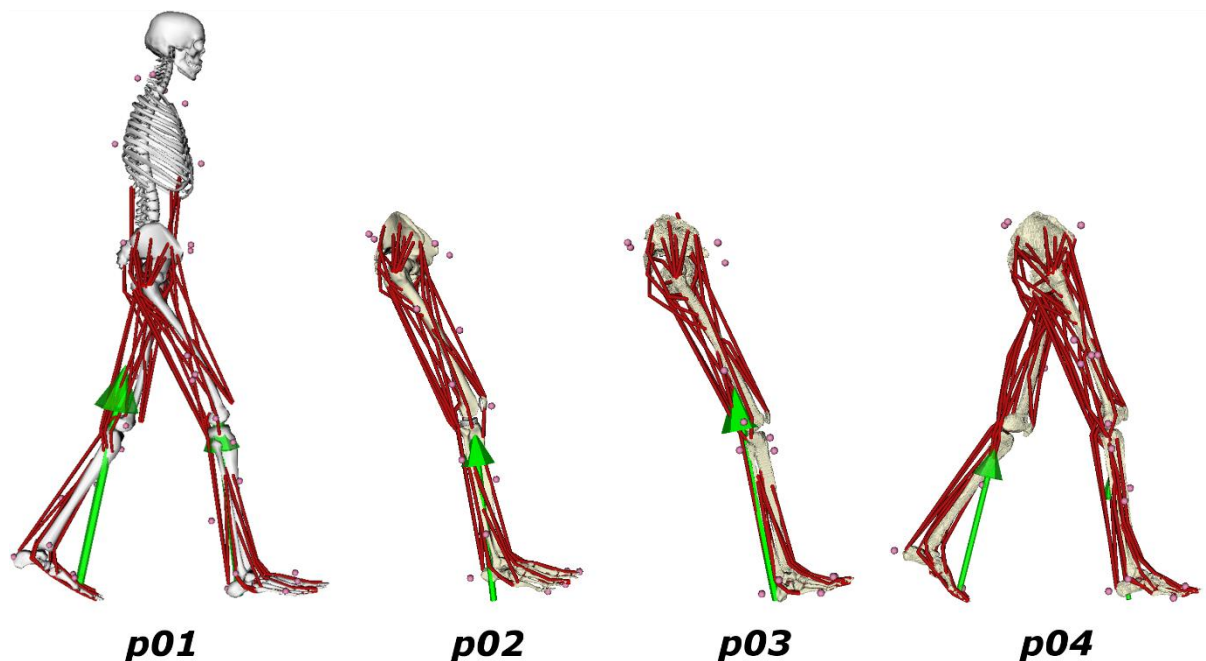
Figure 4.1: The four different models during the loading phase of the gait cycle. The pink markers show the location of the virtual markers on the models. The green arrows represent the ground reaction forces acting on the foot segments of the models.

The force-length-velocity (FLV) relationship of the muscle actuators was not considered for any of the participants. Currently no standardized methods exist to accurately predict this relationship on an individual basis and the translation of the involved muscle properties from isolated physiological experiments to their involvement in whole-body mechanics, where musculotendinous units are idealised as one-dimensional actuators, is unclear.

Inverse kinematics

The generalized coordinates, $\vec{q}(t)$, were obtained by solving the inverse kinematics problem with a global optimization method that minimized the differences between the position of the model's virtual markers and the experimental markers at each time frame using the *inverse kinematics* tool in OpenSim (Delp et al., 2007; Lu and O'Connor, 1999). The trajectories of the generalized coordinates for the full gait cycle are shown in the figures of *Appendix A.2*.

The generalized coordinates were further processed to allow for double differentiation with respect to time to obtain the generalized speeds and accelerations, similar to the implementation in OpenSim; Firstly, the coordinate trajectories were low-pass filtered using a 3rd order inverse impulse response Butterworth filter with a cut-off frequency of 10 Hz. Secondly, a quintic spline was fitted to each trajectory such that the trajectories were expressed as a time-dependent continuous function.

Inverse dynamics

The known generalized coordinates, velocities and accelerations were input to the equations of motion, using the *inverse dynamics* tool in OpenSim, to solve for the unknown torques:

$$\vec{T}(t) = M(\vec{q})\ddot{\vec{q}}(t) - \vec{C}(\vec{q}(t), \dot{\vec{q}}(t)) - \vec{G}(\vec{q}(t)) - \vec{E}(\vec{q}(t), \dot{\vec{q}}(t)) \qquad 4.1$$

The trajectories of the generalized forces and moments $\vec{T}(t)$ for the full gait cycle are shown in the figures of *Appendix A.3*.

4.2.3 Optimization problems

Two different objective functions within a constrained, nonlinear optimization were used to solve the muscle redundancy problem, similar to the problem defined in *Equation 2.10*:

$$\begin{aligned} \min \quad & J(\vec{a}) \\ \text{subject to} \quad & \vec{T}(t) = B(q,t)\big(\vec{a}^T(t)\vec{F}_{max}\big) \\ & \vec{a}_L \leq \vec{a}(t) \leq \vec{a}_U \end{aligned} \qquad 4.2$$

where $\vec{a}$ is the vector of activations with its entries defined as $a_i(t) = F_i(t)/F_{max,i}$, $\vec{F}_{max}$ is the vector of m maximum forces, F_i is the force of actuator i and $\vec{a}_L$ and $\vec{a}_U$ are the lower and upper constraints on $\vec{a}(t)$, respectively.

System definition

Six residual actuators that acted on the three rotational and three translational degrees of freedom of the ground-pelvis joint were appended to the model's set of musculotendinous actuators. These residual actuators compensate for the inconsistencies between the measured ground reaction forces and the mass distribution and joint kinematics and for the forces and moments exerted on the pelvis by the contralateral limb and/or the upper-body segment that are missing in some of the models used in this study.

Therefore, the column vector $\vec{a}$ represents the muscle activations and the activations of the residual actuators, such that $\vec{a}(t) = [\vec{a}^M(t), \vec{a}^R(t)]^T$. The column vector $\vec{F}_{max}$ represents the maximum active, isometric muscle forces and the maximum forces and torques of the residual actuators, such that $\vec{F}_{max} = \left[\vec{F}_{max}^M \; \vec{F}_{max}^R\right]^T$. The values of the residual actuators in the matrix of moment arms, $B(q,t)$, were set to 1, representing ideal moment arms. The constraint on the activation of each residual actuator was set to $[-\infty, \infty]$, ensuring that the residual actuators could produce the required forces, while the activation of muscle actuators could vary between 0 and 1. The variables required to define the optimization problem were obtained using the OpenSim API through MATLAB (v2017a, The MathWorks Inc., Natick, MA, USA).

Objective functions

The first objective function aimed to minimize overall muscle activation and was defined as:

$$J_{act}(\vec{a}) = \sum_{i=1}^{m} (a_i(t))^2 \qquad 4.3$$

where a_i is the activation of actuator i. MATLAB's quadratic programming *quadprog*, leveraging on the interior-point algorithm, was used to solve the problem.

The second objective function, aimed to minimize the magnitude of the joint contact force, was defined as:

$$J_{Fj}(\vec{a}) = w_1 \left(\frac{\left\| \vec{F}^j(\vec{a}, t) \right\|}{\left\| \vec{F}^j_{act}(\vec{a}_{act}, t) \right\|} \right) + w_2 R(\vec{a}, t) \qquad\qquad 4.4$$

where $\left\| \vec{F}^j(\vec{a}, t) \right\|$ is the magnitude of the contact force at joint j acting on its distal segment, $\left\| \vec{F}^j_{act}(\vec{a}_{act}, t) \right\|$ is the magnitude of the contact force given the solution, $\vec{a}_{act}(t)$, of J_{act}, $R(\vec{a}, t)$ is a regularization term and w_1 and w_2 are constant weights that define the relative contribution of both parts to the objective function. MATLAB's nonlinear programming *fmincon*, leveraging on the interior-point algorithm, was used to solve the problem.

For each trial of each participant, the optimization problem was solved once for J_{act} and three times for J_{Fj}; once for the hip (J_{FH}), once for the knee (J_{FK}) and once for the ankle (J_{FA}).

At the time points during the swing phase when $\left\| \vec{F}^j_{act}(\vec{a}_{act}, t) \right\|$ equalled 0 N, no minimization of $J_{Fj}(\vec{a})$ for the corresponding joint was performed: No solution would have been found due to an infinitely high value of the first part of the objective function as a result of a normalization of $\left\| \vec{F}^j(\vec{a}, t) \right\|$ with 0. Therefore, no muscle activation values from the $J_{Fj}(\vec{a}, t)$ solution at these time points were included in any further analyses. The J_{act} solution served as an alternative at these time points, as the resultant contact force at the joint was already minimal for the J_{act} solution.

Regularization term

The regularization term $R(\vec{a})$ was included to prevent the optimization problem from being ill-posed (Tikhonov and Glasko, 1965) and was defined as:

$$R(\vec{a}, t) = \frac{\sum_{i=1}^{m} \left(a_i^{NS}(t) \right)^2}{m} \qquad\qquad 4.5$$

where $a_i^{NS}(t)$ is the activation of the ith muscle that does not span the joint for which the contact force is minimized. The following equally holds for the minimization of the knee and the ankle contact forces, but let us consider the regularization term within the minimization of the hip contact force. The muscles not spanning the hip do not contribute to the objective function directly and without the regularization term, the cost function would be underdetermined. In that case we would not be able to identify a local minimum through nonlinear constrained optimization; the solution could vary along certain dimensions, the activation of the non-spanning muscles, without changing the value of the objective function. This is not to be confused with the occurrence of multiple local minima in the solution space. The ratio of the two weight constants, $w_1 : w_2$, had to be chosen such that the influence

of the regularization term on the solution was minimal: For all trials of *p01*, the minimizations of J_{Fj} were performed for the hip, knee and ankle joint, each with six different weight ratios ranging from 1:1 to 1×10^5:1. The decrease in magnitude of joint contact force showed asymptotic behaviour with the increase in weight ratio. When the weight ratio was increased from 10:1 to 100:1, the joint contact force did not decrease more than 0.002 BW for any joint, averaged over time points and trials, and did not exceed 0.03 BW for any time point in any trial. These results indicated a minimal influence of the regularization term on the obtained solution; the weight ratio was set to 10:1 for all J_{Fj} minimizations.

Initial guess

To ensure the J_{Fj} minimizations resulted in unique solutions, the minimizations for all trials of *p02* were started from 44 different initial guesses. 43 of the initial guesses were obtained by solving a quadratic programming problem with different relative weights to the individual muscle activations:

$$J(\vec{a}) = \frac{1}{2}\,\vec{a}(t)^T H \vec{a}(t) + f^T \vec{a}(t) \qquad\qquad 4.6$$

where H is a $m \times m$ matrix, representative of the quadratic term, and f is a $m \times 1$ vector, representative of the linear term. MATLAB's quadratic programming *quadprog*, leveraging on the interior-point algorithm, was used to solve the problem. For each muscle one minimization was performed where the contribution of that muscle to the quadratic term was set to 0, while the entries in H of the other muscles were set to 1. The contribution to the linear term for the muscle of interest was set to -1, while the entries to f for the other muscles were set to 0. This configuration of relative weights ensured the optimization problem was solved by maximizing the activation in the muscle of interest, while the solution for the remaining muscles followed *Equation 4.3*. In this way, for each time frame of each trial of *p02,* 43 different initial guesses for the J_{Fj} minimizations, distributed over the range of the solution space, were obtained. One additional initial guess was set equal to a $m \times 1$ zero vector, $\vec{0}$. For each joint, all 44 J_{Fj} minimizations converged to the same solution. Therefore, the initial guesses for the minimizations performed for the other participants were set to $\vec{0}$.

4.2.4 Joint Contact Forces

For each solution, the joint contact forces at the hip, knee and ankle were computed following the implementation of joint reaction forces in OpenSim (Steele et al., 2012). The change in peak contact force magnitude at the hip, knee and ankle for each solution of the corresponding JCF minimization ($\vec{a}_{FH}$, $\vec{a}_{FK}$ and $\vec{a}_{FA}$) was quantified as a percentage:

$$r_{Fj} = \frac{(\left\|\vec{F}^j(\vec{a}_{Fj}, t)\right\|_{max} - \left\|\vec{F}^j(\vec{a}_{act}, t)\right\|_{max})}{\left\|\vec{F}^j(\vec{a}_{act}, t)\right\|_{max}} \times 100\% \qquad 4.7$$

where r_{Fj} is the percentage of change in the peak contact force at joint j and $\left\|\vec{F}^j(\vec{a}_{Fj}, t)\right\|_{max}$ is the peak magnitude of contact force at joint j given the solution $\vec{a}_{Fj}$ that minimizes the force transmitted at joint j. The time point at which the peak contact force magnitude occurs in joint j is defined as t_{Fjmax}.

4.3 Results

For all participants and all walking speeds, the peak magnitude of contact force at the hip, knee and ankle was reduced with a muscle recruitment strategy aimed to minimize the loads at the respective joints (J_{Fj}) compared to a recruitment strategy aimed to minimize the sum of muscle activation squared (J_{act}). The reduction of peak force ranged from 7 to 21 % at the hip, from 27 to 49 % at the knee and from 3 to 5 % at the ankle depending on the participant and the walking speed. No significant influence of the walking speed on the joint contact force reduction was found (*Table 4.3*). No consistent pattern across participants was found with respect to a time shift in peak contact force occurrence; for several trials of *p01* the peak hip and knee contact force occurred during early stance, rather than during late stance, when aiming to minimize the loads in the respective joints; for two out of six trials of *p02* the occurrence of peak knee contact force shifted from late to early stance when aiming to minimize the knee load (*Table 4.4*).

The muscle activation patterns that aimed to minimize the load in one joint, when compared to the J_{act} solutions, had a variable effect on the peak magnitude of the contact force in the non-targeted joints (*Table 4.3*); when minimizing the hip load, the peak JCF magnitude in the knee increased, with a range from 20 to 102 %, for *p01*, *p03* and *p04*, while the peak JCF decreased for *p02*. No significant change in peak ankle force was observed for any of the participants at any of the speeds, except for the two fast trials of *p01*, where the peak ankle contact force increased; when minimizing the knee load, the peak JCF magnitude in the hip increased for all participants at all speeds, ranging from 4 to 54 %. A slight increase of 3 to 5 % in peak JCF was observed at the ankle for all the participants at all speeds, except for the trials at a self-selected speed for *p03*, where the ankle load increased by 22 %; when minimizing the ankle load, the peak JCF magnitude in the hip did not change significantly, except for the trials at a self-selected speed, where the hip force increased. The peak magnitude of knee

contact force increased for all participants at all walking speeds, with a range of increase from 33 to 92 %.

In *Table 4.5*, the muscle activations, averaged over the trials at a self-selected walking speed, for both the J_{act} and the J_{Fj} solutions are shown at the time instants t_{Fjmax} of peak contact force in the hip, knee and ankle as predicted by the J_{act} solution. When aiming to minimize the hip contact force magnitude, a change in muscle activation pattern, consistent across the models, was observed: The activation of the Gluteus Minimus compartments and the knee stabilizers increased, while the activation of the Gluteus Medius compartments and the Iliopsoas muscles decreased. For three out of for models, the activation of the Rectus Femoris muscle increased and a shift in activation from the Soleus to the Gastrocnemius muscles occurred. For two models, the Gemellus muscle became involved when aiming to minimize the hip contact force.

When aiming to minimize the knee contact force, a change in muscle activation, consistent across the models, was observed. The activation of the Gluteus Medius (and, to a lesser extent, the Gluteus Minimus) compartments, the Iliopsoas muscles, and the Soleus muscle increased, while the Rectus Femoris muscle, the knee stabilizers and the Gastrocnemius muscles (except for the lateral compartment of *p04*) were switched off. For two models, the Semitendinosus muscle became involved when aiming to minimize the knee contact force. For *p03* the activation of the smaller plantarflexors around the ankle increased. These changes in muscle activation patterns were consistent across models even though the peak loads for the J_{act} solution, in both the hip and the knee joint, occurred predominantly during late stance for *p01* and *p04* and predominantly during early stance for *p02* and *p03*. When aiming to minimize the ankle contact force magnitude, the change in muscle activation, was consistent across models: The activation of the Soleus muscle decreased, while the activation of the Gastrocnemius muscles and the Rectus Femoris muscle (and to a lesser extent the Iliopsoas muscles) increased.

The trajectories over the gait cycle for the contact force magnitudes in all joints and the activation of all muscles can be found in *Appendices A.4 and A.5*, respectively. A table, equivalent to *Table 4.5*, which shows the mean and standard deviation values of muscle activation over the different trials for each muscle of each model, can be found in *Appendix A.6*.

Table 4.3: Mean and standard deviation (SD) values of the peak hip, knee and ankle contact force magnitude ($\|\vec{F}^j\|_{max}$) in bodyweight (BW) for the minimization of activation (J_{act}) and the minimization of the contact force in the corresponding joint (J_{Fj}); The mean and standard deviation values of the change in peak contact force magnitude (r_{Fj}) for each J_{Fj} compared to J_{act} in percentages.

			J_{act}	J_{FH}		J_{FK}		J_{FA}	
			$\|\vec{F}^j\|_{max}$ ± SD (BW)	$\|\vec{F}^j\|_{max}$ ± SD (BW)	r_{Fj} ± SD (%)	$\|\vec{F}^j\|_{max}$ ± SD (BW)	r_{Fj} ± SD (%)	$\|\vec{F}^j\|_{max}$ ± SD (BW)	r_{Fj} ± SD (%)
Hip	Slow	p01	4.1 ± 0.2	3.3 ± 0.2	-19 ± 2	5.2 ± 0.2	27 ± 5	4.1 ± 0.2	-1 ± 0
		p04	4.2 ± 0.2	3.3 ± 0.1	-20 ± 1	4.9 ± 0.2	18 ± 1	4.0 ± 0.2	-3 ± 0
	Self-selected	p01	4.3 ± 0.2	3.6 ± 0.2	-16 ± 3	6.6 ± 0.5	54 ± 11	4.3 ± 0.3	1 ± 6
		p02	4.0 ± 0.2	3.7 ± 0.2	-7 ± 1	4.8 ± 0.3	20 ± 6	4.2 ± 0.5	5 ± 10
		p03	4.2 ± 0.1	3.7 ± 0.1	-11 ± 1	4.4 ± 0.2	4 ± 4	4.2 ± 0.1	0 ± 1
		p04	4.4 ± 0.3	3.5 ± 0.2	-21 ± 1	5.2 ± 0.3	19 ± 0	4.3 ± 0.3	-3 ± 0
	Fast	p01	7.6 ± 0.5	6.8 ± 0.6	-12 ± 2	11.3 ± 0.0	48 ± 10	7.5 ± 0.5	-1 ± 0
		p04	5.4 ± 0.1	4.7 ± 0.2	-14 ± 2	6.5 ± 0.1	21 ± 2	5.3 ± 0.2	-1 ± 1
Knee	Slow	p01	3.2 ± 0.1	5.0 ± 0.6	57 ± 17	1.6 ± 0.2	-49 ± 6	5.9 ± 0.4	85 ± 8
		p04	3.5 ± 0.1	4.9 ± 0.2	40 ± 3	2.0 ± 0.0	-43 ± 1	6.6 ± 0.1	86 ± 2
	Self-selected	p01	3.4 ± 0.1	6.8 ± 0.6	102 ± 11	2.0 ± 0.2	-41 ± 5	5.5 ± 0.1	63 ± 8
		p02	2.2 ± 0.1	2.0 ± 0.1	-8 ± 6	1.6 ± 0.2	-27 ± 7	4.2 ± 0.4	92 ± 20
		p03	3.6 ± 0.2	4.3 ± 0.6	20 ± 14	2.1 ± 0.1	-40 ± 3	5.3 ± 0.1	50 ± 7
		p04	3.7 ± 0.2	5.1 ± 0.1	39 ± 4	2.0 ± 0.1	-47 ± 1	6.9 ± 0.2	86 ± 9
	Fast	p01	5.7 ± 0.7	10.5 ± 0.1	86 ± 20	3.3 ± 0.5	-41 ± 15	7.5 ± 0.6	33 ± 5
		p04	4.0 ± 0.2	5.1 ± 0.2	25 ± 4	2.1 ± 0.1	-47 ± 3	7.0 ± 0.1	73 ± 10
Ankle	Slow	p01	4.6 ± 0.3	4.7 ± 0.3	1 ± 0	4.8 ± 0.3	4 ± 0	4.4 ± 0.3	-4 ± 0
		p04	4.9 ± 0.1	4.9 ± 0.1	0 ± 0	5.1 ± 0.1	4 ± 0	4.7 ± 0.1	-5 ± 0
	Self-selected	p01	4.4 ± 0.2	4.6 ± 0.2	3 ± 3	4.7 ± 0.2	5 ± 0	4.3 ± 0.2	-4 ± 0
		p02	3.2 ± 0.3	3.3 ± 0.2	1 ± 0	3.3 ± 0.3	3 ± 0	3.1 ± 0.2	-5 ± 0
		p03	6.1 ± 0.1	6.0 ± 0.1	0 ± 1	7.4 ± 0.4	22 ± 5	5.8 ± 0.1	-4 ± 0
		p04	5.1 ± 0.2	5.1 ± 0.2	0 ± 0	5.3 ± 0.2	4 ± 0	4.9 ± 0.2	-5 ± 0
	Fast	p01	5.3 ± 0.3	6.9 ± 0.0	30 ± 9	5.6 ± 0.4	5 ± 0	5.2 ± 0.3	-3 ± 0
		p04	5.0 ± 0.1	5.0 ± 0.1	0 ± 0	5.2 ± 0.1	4 ± 0	4.8 ± 0.0	-4 ± 0

Table 4.4: For the hip, knee and ankle joint, the percentage of trials with a peak contact force during the late stance phase of the gait cycle for the J_{act} solution and the J_{Fj} solution of the corresponding joint.

			Hip		Knee		Ankle	
			J_{act}	J_{FH}	J_{act}	J_{FK}	J_{act}	J_{FA}
$\|\vec{F^j}\|_{max}$ during late stance (% of trials)	Slow	p01	100	80	100	20	100	100
		p04	100	100	100	100	100	100
	Self-selected	p01	100	50	100	83	100	100
		p02	0	0	50	17	100	100
		p03	40	20	0	0	100	100
		p04	100	100	100	100	100	100
	Fast	p01	100	100	100	0	100	100
		p04	100	100	100	20	100	100

Table 4.5: Muscle activations at the time of peak hip, knee and ankle contact force magnitude in the J_{act} solution, given for both the J_{act} and the corresponding J_{Fj} solution. Muscle activation values are averaged over trials at self-selected speed and represented by a colour scale (white: no activation, red: full activation). For each muscle, the four rows represent the activation level for the four different participants.

		$a_i(t_{FHmax})$		$a_i(t_{FKmax})$		$a_i(t_{FAmax})$	
		J_{act}	J_{FH}	J_{act}	J_{FK}	J_{act}	J_{FA}
Gluteus Max	Gluteus Maximus Ant						
	Gluteus Maximus Int						
	Gluteus Maximus Post						
Gluteus Med	Gluteus Medius Ant						
	Gluteus Medius Int						
	Gluteus Medius Post						
Gluteus Min	Gluteus Minimus Ant						
	Gluteus Minimus Int						
	Gluteus Minimus Post						
Adductors	Adductor Brevis						
	Adductor Longus						
	Adductor Magnus Sup						
	Adductor Magnus Int						
	Adductor Magnus Inf						
	Pectineus						
Hip ext rotators	Gemellus						
	Piriformis						
	Quadratus Femoris						
Iliopsoas	Iliacus						
	Psoas Major						
Hamstrings	Biceps Femoris LH						
	Biceps Femoris SH						
	Semimembranosus						
	Semitendinosus						
Quadriceps	Rectus Femoris						
	Vastus Intermedius						
	Vastus Lateralis						
	Vastus Medialis						
Knee stabilizers	Gracilis						
	Sartorius						
	Tensor Fasciae Latae						
Plantar flexors-I	Lateral Gastrocnemius						
	Medial Gastrocnemius						
	Soleus						
Plantar flexors-II	Flexor Digitorum L						
	Flexor Hallucis L						
	Peroneus Brevis						
	Peroneus Longus						
	Tibialis Posterior						
Dorsi flexors	Extensor Digitorum L						
	Extensor Hallucis L						
	Peroneus Tertius						
	Tibialis Anterior						

4.4 Discussion

This study was aimed to explore the potential of alternative muscle recruitment strategies to reduce the forces experienced by the joints of the lower limb during level walking through answering the following five research questions: 1) Can alternative muscle recruitment strategies reduce the peak force transmitted at each lower limb joint?; 2) Is this reduction similar for all four cases, representative of four widely different populations, studied here?; 3) If a muscle recruitment strategy that significantly reduces the force in one joint exists, what is its influence on the other joints?; 4) Does the joint load-reducing potential of alternative recruitment strategies change with different walking speeds?; 5) How do the activation patterns predicted by different recruitment strategies at the instant of peak joint contact force differ?

Alternative recruitment strategies reduced the magnitude of peak contact force in the knee, and to a smaller extent in the hip, compared to a strategy that minimized the sum of muscle activation squared (J_{act}), which has been shown to be equivalent to an energetically optimal recruitment strategy (Anderson and Pandy, 2001b); for the trials at a self-selected walking speed, the reduction in peak force magnitude ranged from 0.6 to 1.7 BW in the knee and from 0.3 to 0.9 BW in the hip. In the ankle joint the effects of an alternative recruitment strategy seemed to be minimal as the reduction in peak force magnitude ranged from 0.1 to 0.3 BW. The reduction of peak force at the hip and knee is comparable to the effect of alternative muscle recruitment strategies on the joint contact force found in previous studies (DeMers et al., 2014; Martelli et al., 2011). Also, this study found a similar pattern of reduction in knee force over the gait cycle for *p01, p03* and *p04* compared to a previous study (DeMers et al., 2014): The biggest reduction in knee force occurred during late stance, as shown in *Figure 4.2* for all models for the trials at a self-selected speed.

The potential to reduce joint contact forces through alternative muscle recruitment strategies is measured against an estimated reference, the J_{act} solution. At a self-selected walking speed, this reference of peak magnitude of force in the hip and knee ranged from 4.0 to 4.4 BW and from 3.4 to 3.7 BW (excluding *p02*), respectively. In studies that measured the forces at the hip and knee during level walking through instrumented joint replacements, the peak forces ranged from 2 to 3 BW (Bergmann et al., 2001; Damm et al., 2017; Kutzner et al., 2010), which is significantly lower than the estimated reference peak forces in this study. However, *p01*, *p03* and *p04* were either healthy or did not have a pathology with hip and knee involvement and therefore a notable difference in walking dynamics most likely exists with patients that underwent a full hip replacement. For *p02*, who had an instrumented knee implant, the peak knee forces from J_{act} were similar to the measured values (*Figure 4.2*), supporting the choice to use the J_{act} solutions as a reference. The potential to reduce the

force experienced by the hip, knee and ankle in *p02* followed the patterns of the other models, but was slightly smaller. However, this difference in effect size can likely be attributed to a difference in walking dynamics rather than an overestimation of the reference force values from the J_{act} solutions, as suggested by the difference in self-selected, or preferred, walking speed.
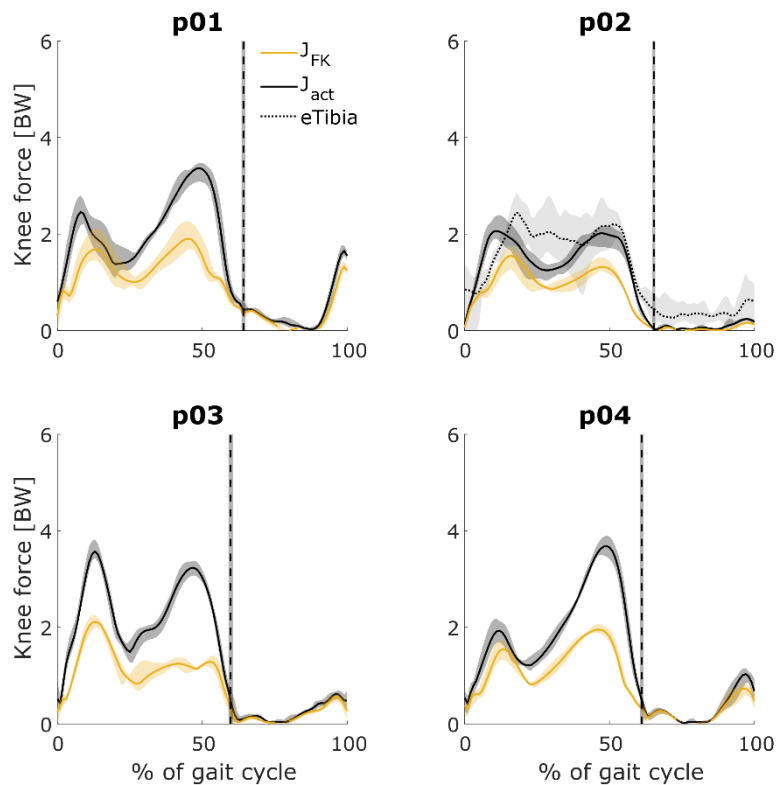
Figure 4.2: Knee contact force trajectories of all participants for the trials at a self-selected walking speed; mean (solid line) and range (shaded area) values of force magnitude are shown in bodyweight (BW) for the J_{act} (black) and J_{FK} (yellow) solutions. For *p02*, the mean and range values as measured by the implant (*eTibia*, dashed) are shown. The vertical dashed line indicates the time instant when toe off occurred.

The four cases presented here were selected to represent widely different populations and a range of methods in musculoskeletal models; the participants showed a big range in age (16 to 74 years old), height (1.64 to 1.90 m), mass (57 to 83 kg) and health status; the musculoskeletal models were identified on different levels of subject specificity, ranging from a scaled generic model (*p01*) to a model with fully personalised musculoskeletal geometry and joint orientation (*p04*). Also, for *p02* a patellofemoral joint was included to represent a more refined knee mechanism, while for *p03* a subtalar joint was included to represent a more refined ankle mechanism. Nonetheless, the potential to reduce contact forces at the hip, knee and ankle was found to be consistent across different four cases. This consistency suggests these results are not subject specific in their general nature, but are determined by the physical limitations that the muscle controls have in each of the lower limb joints.

In general, the results of this study showed an increase of the load in the adjacent joint, when aiming to minimize the force in a particular joint: when aiming to minimize hip force magnitude, the peak force increased in the knee, but not in the ankle; when aiming to minimize knee force magnitude, the peak force in both the hip and, to a lesser extent, the ankle increased; when aiming to minimize the ankle force magnitude, the peak force increased in the knee, but not in the ankle. This shift of load towards adjacent, non-targeted joints was to be expected due to the coupling of the joints through multi-articular muscles. A change in force along a multi-articular muscle, aimed to reduce the load in a targeted joint, has to be compensated for by antagonist muscles at the non-targeted joint in order to maintain the balance in joint moments and will therefore affect the load in non-targeted joints. The effect of this compensation wears off when moving along the kinematic chain further away from the targeted joint. The magnitude of the adverse effects on the load in non-targeted joints, at a self-selected walking speed, was dependent on the joint and varied across participants: the knee load, when minimizing the force in the hip, doubled from 3.4 to 6.8 BW for *p01*, while for *p02* the knee load decreased with 8 %; when minimizing the knee force, the effect on the hip force ranged from hardly any to half a bodyweight; when minimizing the ankle force, a significant increase in knee load occurred for all participants and ranged from 1.7 to 3.2 BW. The magnitude of the adverse effects are potentially sensitive to the capacity of muscles in the model to produce force beyond the minimum required by the dynamic equilibrium. In any case, due to the assumption of independent muscle control, possibly not all adjustment are physiologically possible and therefore this study provides theoretical boundaries to the reduction of joint loads through alternative muscle recruitment strategies and the effect on non-targeted joints.

The absolute values of the contact forces at the different joint increased with the walking speed as expected due to the requirement of larger muscle forces for the increase in segment accelerations. However, no clear effect of walking speed on the potential to reduce joint forces or on the load in non-targeted joints was observed.

The change in muscle activation showed clear patterns depending on the joint in which the force was minimized; the peak force in the hip reduced due to a shift in activation from the Gluteus Medius to the Gluteus Minimus muscle and a decrease in the activation of the Iliopsoas muscles. To maintain the levels of hip adduction moment and hip flexion moment during late stance, the Rectus Femoris, Sartorius and Tensor Fasciae Latae muscles were activated. The bi-articular nature of these muscles led to the observed increase in knee contact force; the peak force in the knee reduced due to a shift in activation from the bi-articular Rectus Femoris and Gastrocnemius muscles to the mono-articular Iliopsoas and Soleus muscles. The required moments around the hip and ankle were not produced by muscles spanning the knee, but by mono-articular muscles with smaller moment arms around the hip

and ankle coordinates which required larger forces. These results were consistent with the findings in a previous study (DeMers et al., 2014); the peak force in the ankle reduced only by a very small amount due to a shift in activation from the Soleus to the Gastrocnemius muscles. An increase in the activation of this bi-articular muscle, spanning the ankle and the knee, increased the force experienced by the knee significantly. For *p03* only, the muscles contributing to the in-/eversion moment at the ankle were involved in all solutions and their activation further increased when minimizing the force at knee. The inclusion of a subtalar joint might therefore be associated to the increased estimated ankle contact force for *p03* compared to the other models. However, the participant was a JIA patient and might therefore have an altered kinematic pattern compared to healthy participants or patients without ankle involvement.

The main limitation of this study is the assumption of independent muscle control and the author acknowledges that future work should include a dependency between the controls of muscle groups. However, as stated above, this study does provide a theoretical boundary to the reduction of joint loads through alternative muscle recruitment strategies. Secondly, the force-length-velocity relationship was not considered when determining the force producing capacity of the muscles. As mentioned before, no standardized method currently exists to accurately predict this relationship for each muscle individually. Furthermore, some muscle groups might be more compliant to a change in length of the musculotendon unit and might show near isometric behaviour during the stance phase of level walking compared to other muscle groups (Lichtwark et al., 2007). Therefore, the author assumed the optimal fibre length to be representative at the instants of peak force in the hip, knee and ankle when no extreme orientations of the joints occurred. Lastly, these results are somehow limited in scope as they assume that the compensation strategy is limited to the neuromuscular control and not to possible changes in joint kinematics. We believe this assumption represents an idealised case, representative of moderately severe compensation strategies, typical of early-stage pathologies.

In conclusion, the results presented in this study suggest that neuromuscular rehabilitation can be targeted to reduce the loading of the affected joint at the knee and the hip. The muscles that are primarily involved in such compensatory strategies have been identified for all joints of the lower limb. These alternative muscle recruitment strategies come at a cost of a moderate increase in the loading at other joints, so the opportunity of neuromuscular rehabilitation must be considered carefully in patients with multiple joints affected. Instead, the ankle joint load can only be reduced by a small amount by simply changing the neuromuscular control.

In the previous chapter, muscle recruitment strategies were identified through mathematical optimization techniques. Even though this approach is representative of these strategies' potential to reduce the metabolic energy cost or to reduce the force acting at the joints of the lower limb during level walking, no variability is included in such assumptions of motor control. Indeed, useful and 'good enough' control strategies, identified through trial and error, have been argued to represent human motor control, rather than strategies identified through optimization (Loeb, 2012). Moreover, we might allow for variability along task-independent directions in repeated movements to ensure stability to perturbations (Scholz and Schöner, 1999). Therefore, the following chapter explores muscle recruitment through a stochastic approach, representative of sub-optimal motor control.

CHAPTER 5

-

LIMITATIONS OF OPTIMAL MUSCLE CONTROL TO MODEL

PATHOLOGICAL GAIT

5.1 Introduction

The relevance of the forces experienced by the articular surface of weight-baring joints during activities of daily life to the onset and progression of joint degenerative diseases, such as osteoarthritis, has been discussed extensively in the literature (see *Section 4.1*) and a framework to understand the in vivo pathogenesis of knee osteoarthritis has previously been proposed (Andriacchi et al., 2004): Changes in joint loading due to traumatic injuries, such as a rupture of the anterior cruciate ligament, or due to aging, have been associated to disease onset, while increased loads have been associated to disease progression. Experimental data on the forces experienced by the joints are typically obtained from a patient population with end-stage osteoarthritis through force sensors in a hip or knee implant. Therefore, accurate predictions of joint contact forces with simulations of musculoskeletal dynamics can provide insight in the joint loads of early-stage patients and healthy controls, are relevant to study treatment effects in a non-invasive manner and could potentially inform clinical practice. Nevertheless, open-source datasets from instrumented joint implants, such as the Knee Grand Challenge dataset, serve as an important validation of simulation studies (Fregly et al., 2012).

Numerous studies used one of the six Knee Grand Challenge (or similar) datasets to validate different approaches to simulate musculoskeletal dynamics and predict knee contact forces, such as the inclusion of more complex and subject-specific joint contact models (Hast and Piazza, 2013; Jung et al., 2016; Kim et al., 2009; Smith et al., 2016; Thelen et al., 2014), force-dependent knee kinematics (Marra et al., 2015) and patient-specific musculoskeletal geometry in a segment-based model (Ding et al., 2016). Experimental data has also been used to argue the importance of the discretization of large muscles into separate compartments and subject-specific muscle parameters in musculoskeletal dynamic simulations when predicting knee contact forces (Moissenet et al., 2016; Serrancolí et al., 2016). All of the studies mentioned previously predicted muscle activation patterns under the assumption of optimal control (from the perspective of metabolic energy expenditure, see *Section 2.4*) that might be valid for healthy gait, but does not necessarily hold for pathological gait (*Section 3.4.1*). Previous studies that allowed for validation with experimental data have included subject-specific approaches to muscle control, such as EMG-driven forward dynamics and muscle synergies, to predict knee contact forces (Razu and Guess, 2018; Walter et al., 2014). However, the assumptions required for the translation from measurements of electrical activation to units of force and the limited information on the activation levels of deep muscles with surface electromyography remain a major limitation.

The influence of sub-optimal muscle control on hip joint loads has been shown previously through a probabilistic approach (Martelli et al., 2013), but the study lacked a direct comparison to experimental measurements. Another approach to study sub-optimal muscle control varied the relative contribution of agonist muscle groups and their individual muscles parametrically to obtain a solution space of possible muscle activations and knee contact forces (Lundberg et al., 2013, 2009). The variability of muscle activations and its influence on the knee contact forces predicted by such a parametric approach was small compared to the probabilistic approach. Most likely, this approach did not include every possible combination of muscle activations and therefore underestimated the influence of accurate models of motor control on joint force predictions.

This study was aimed to explore the limitations of optimal control in predictions of knee contract forces by answering the following questions: 1) Can a subject-specific musculoskeletal dynamics model, built according to the current best practice, predict the measured forces at the knee during level walking? In other words, does at least one muscle activation pattern exist for which the model prediction and the measurements differ less than the measurement precision?; 2) Assuming such a solution exists, how different is it from an optimal control solution in terms of knee contact forces, but also in terms of muscle activation?; 3) How well can this difference be explained by a stochastic component superimposed to the optimal control (consistent with the uncontrolled manifold theory)?

5.2 Methods

The experimental data, the musculoskeletal model, the dynamic simulations and the muscle activation solution that minimized the sum of muscle activations squared (J_{act}, *Equation 4.3*) and the solution that minimized the contact force in the knee (J_{FK}, *Equation 4.4*) solutions for *p02*, as described in the previous chapter, were re-used for this study. The following section describes the additional data and methodology in more detail.

5.2.1 Experimental data

Six trials of level, overground walking, labelled as '*DM_ngait_og*' in the original dataset, were included. The original trial numbers (*3, 4, 5, 6, 7* and *9*) were maintained to allow for comparison across studies.

Instrumented knee implant

The forces and moments acting on the right knee joint were available from a six-axis load cell embedded in the stem of the tibial prosthesis (*eTibia;* (Kirking et al., 2006)). The implant data were originally sampled at 50 Hz but provided after being resampled to 200 Hz using a cubic-spline

interpolation and filtered using a 4th order, low-pass Butterworth filter with a cut-off frequency of 15 Hz. The location and orientation of the load cell's reference frame are shown in *Figure 5.1*.

eTibia Coordinate System (Left Implant)

Coordinate system origin is located at stem center and surface of tray
Coordinate system stays the same for a right implant except that x-axis points medially instead of laterally
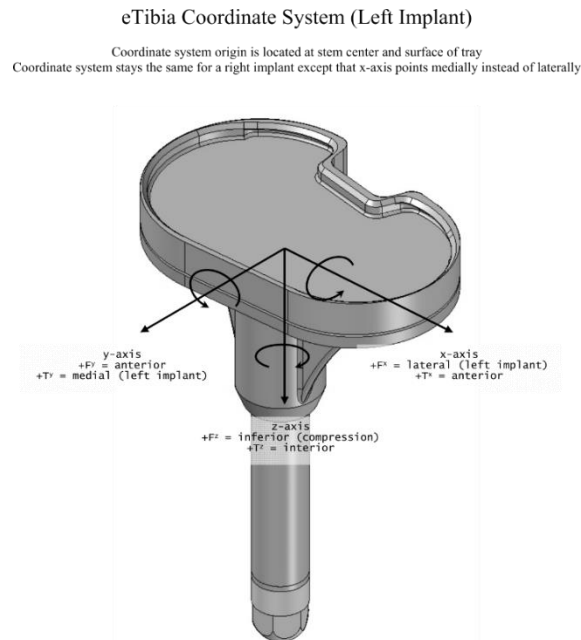
Figure 5.1: The coordinate system fixed in the tibial tray and used to resolve the instrumented implant force and moment measurements. Image from Fregly et al. (2012).

Electromyography

EMG data were available for 15 muscles of the right lower extremity: The Gluteus Maximus, the Gluteus Medius, the Adductor Magnus, the Tensor Fasciae Latea, the Sartorius, the Semimembranosus, the long head of the Biceps Femoris, the Vastus Medialis and Lateralis, the Rectus Femoris, the Gastrocnemius Medialis and Lateralis, the Soleus, the Tibialis Anterior and the Peroneus Longus muscles. Upon visual inspection, the data for the Gluteus Medius and the Vastus Medialis muscles were identified to be of insufficient quality given the signals' small amplitudes. In a study that used the same dataset for EMG-driven forward dynamics simulations, the data for these two muscles and the Biceps Femoris were also excluded for quality reasons (Razu and Guess, 2018). The Biceps Femoris data was of good quality for the trials considered in this study and therefore included in further analyses. Electrode placement was consistent with (Delagi and Perroto, 1980). The data were sampled at 1000 Hz and provided after being high-pass filtered at 30 Hz using a 4th order Butterworth filter. Subsequently, the offset of each signal was removed, a low-pass filter with a cut-off frequency

of 400 Hz was applied and the signals were full-wave rectified. The data were then separately processed to obtain both the envelope trajectories and the EMG onset times: Envelope trajectories were obtained through applying a low-pass filter with a cut-off frequency of 4 Hz; After a low-pass filter with a cut-off frequency of 10 Hz, EMG onset times were defined as the time of the initial frame of a 50 ms sliding window at which the average value of the window exceeded a predefined threshold value (Hodges and Bui, 1996). For each muscle, the threshold value was defined, on a trial-by-trial basis, as three standard deviations increase from the average value of a period of visually-inspected inactivity. All filters were 4th order, zero-lag Butterworth filters and implemented in MATLAB. To allow for a direct comparison of EMG data with muscle activations predicted by musculoskeletal models, given that no activation dynamics was included in the muscle models used in this study, an electromechanical delay (EMD) of 60 ms was taken into account; values for EMD in lower-limb muscles reported in experimental literature varied from 40 to 80 ms (Vos et al., 1990; Zhou et al., 1995).

5.2.2 Musculoskeletal model

To facilitate the comparison of the simulated knee contact force with the measured values from the instrumented knee implant, a knee contact joint was placed in the tibial tray aligned with the origin of the reference frame of the implant (*Figure 5.2*). A massless body linked the articulating knee joint with the knee contact joint, which was in turn linked distally to the tibia segment. All six coordinates of the knee contact joint were locked which assured the original orientation of the massless body and the tibia with respect to each other was maintained; the addition of the knee contact joint allowed for direct comparison of the estimated knee contact force to the measured knee forces. Therefore, any reported knee contact forces predicted by the model in the following sections are resolved around this knee contact joint.
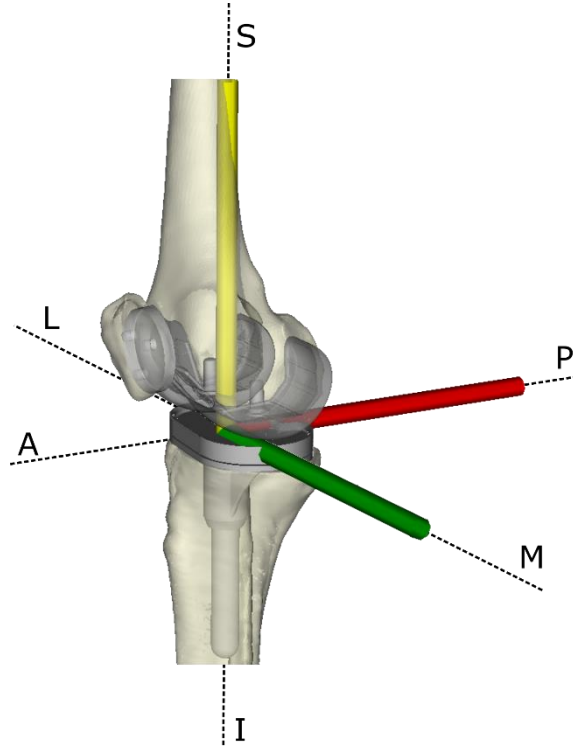
Figure 5.2: The coordinate system (anterior posterior (AP) axis (red), mediolateral (ML) axis (yellow) and superior-inferior (SI) axis (green)) fixed in the locked knee contact joint and used to resolve the simulated joint contact forces and moments.

5.2.3 Muscle activation patterns

Muscle activation patterns were available from the previously defined J_{act} and J_{FK} solutions (*Equations 4.3 and 4.4*, respectively). Additional muscle activation patterns were obtained through two different methods: an additional optimization and the probabilistic approach described in *Section 3.4.1*.

Optimization problem

Muscle activation patterns for all trials were obtained by solving the optimization problem defined in *Equation 4.2*. The following objective function was used, aimed to minimize the difference between the resultant force as measured by the knee implant and the knee resultant force as estimated by the model:

$$J_{Fmatch}(\vec{a}) = w_1 \left(\frac{\left\| \vec{F}_{exp}^K(t) \right\| - \left\| \vec{F}^K(\vec{a}, t) \right\|}{\left\| \vec{F}_{exp}^K(t) \right\|} \right)^2 + w_2 R(\vec{a}, t) \qquad 5.1$$

where $\left\|\vec{F}_{exp}^{K}(t)\right\|$ is the magnitude of the experimental knee resultant force, acting on the tibia segment, as measured by the instrumented knee implant and $\left\|\vec{F}^{K}(\vec{a},t)\right\|$ is the magnitude of the resultant force acting on the tibia in the knee joint as predicted by the musculoskeletal model, $R(\vec{a},t)$ is a regularization term and w_1 and w_2 are constant weights that define the relative contribution of both parts to the objective function. The regularization term $R(\vec{a},t)$ was included to prevent the optimization problem from being ill posed, as some muscles do not contribute directly to the first part of the objective function, and was defined as in *Equation 4.5*. MATLAB's nonlinear programming *fmincon*, leveraging on the interior-point algorithm, was used to solve the problem.

The weight ratio $w_1 : w_2$ was set to 10:1, based on the asymptotic behaviour of the objective function value with an increasing weight ratio, as described in *Section 4.2.3*. To ensure the J_{Fmatch} minimizations resulted in unique solutions, the minimizations for all trials of *p02* were started from 44 different initial guesses as described in *Section 4.2.3*. All 44 J_{Fmatch} minimizations converged to the same solution. Therefore, the initial guesses for the minimizations were set to $\vec{0}$.

Sampling of solution space

The probabilistic approach, as explained in more detail in *Section 3.4.1*, was used to draw a set of possible muscle activation patterns $\{[\vec{a}^M(t)]_1, [\vec{a}^M(t)]_2, \dots, [\vec{a}^M(t)]_N\}$ from the following probability distribution:

$$\pi\big(\vec{a}^M(t)\big|\vec{T}(t)\big) \propto \pi_{pr}\big(\vec{a}^M(t)\big)\pi\big(\vec{T}(t)\big|\vec{a}^M(t)\big) \qquad 5.2$$

where $\pi_{pr}\big(\vec{a}^M(t)\big)$ is the prior term that represents the constraints on the muscle activations, $\pi\big(\vec{T}(t)\big|\vec{a}^M(t)\big)$ is the likelihood term that represents the probability of the known generalized torques, $\vec{T}(t)$, given a vector of muscle activations $\vec{a}^M(t)$ and $\pi\big(\vec{a}^M(t)\big|\vec{T}(t)\big)$ is the posterior distribution that represents the probability of a vector of muscle activations that satisfies the dynamic equilibrium:

$$\vec{T}(t) = B(q,t)\big(\vec{a}(t)^T \vec{F}_{max}\big) \qquad 5.3$$

The constraints on the muscle activations were set to a limit radius around the J_{act} solution:

$$\max\{\vec{a}_{act}(t) - 0.1, \vec{0}\} \leq \vec{a}(t) \leq \min\{\vec{a}_{act}(t) + 0.1, \vec{1}\} \qquad 5.4$$

where $\vec{a}_{act}(t)$ is the vector of muscle activations that resulted from the minimization of J_{act}. The values of the constraints were defined component-wise. The limit radius of 0.1, or 10% of the maximum activation of 1, was chosen to be representative of the uncertainty in predicted muscle activations as quantified in *Section 3.3*. The sample size was set to $N = 1 \times 10^5$, which was assumed to be sufficiently large to obtain a set of muscle activation patterns representative of the allowed solution space, given the results from *Section 3.4*, the narrow constraints on the activation values and the fewer number of generalized coordinates in the model compared to the model presented in *Section 3.4.2*. The sampling was performed with use of Metabolica, implemented in MATLAB (Heino et al., 2010).

In total, three muscle activation patterns were obtained with different objective functions in an optimization approach: J_{Fmatch} tested if an activation pattern existed that allowed the model to accurately predict the measured knee forces; J_{act} represented the activation pattern that minimized the metabolic energy expenditure; J_{FK} represented the activation pattern that minimized the knee contact force. A fourth muscle activation pattern, the J_{met} solution, was selected from the 1×10^5 Metabolica samples as the sampled muscle activation pattern that resulted in the predicted knee force closest to the measured value.

5.2.4 Knee contact forces

The contact forces at the knee joint were computed, leveraging on the implementation in OpenSim through the MATLAB API, for each muscle activation pattern that was obtained as an optimization solution or as a sample from the solution space.

Evaluation of knee contact force prediction

The root-mean-square error (RMSE) was used to quantify the differences between the magnitude of the estimated knee contact forces $\left\| \vec{F}^K(\vec{a}, t) \right\|$ and the measured knee contact forces $\left\| \vec{F}^K_{exp}(t) \right\|$ for each trial:

$$RMSE = \sqrt{\frac{\sum_{t=1}^{T} \left(\left\| \vec{F}^K(\vec{a}, t) \right\| - \left\| \vec{F}^K_{exp}(t) \right\| \right)^2}{T}} \qquad 5.5$$

where T is the total number of time points. The RMSE was chosen as a suitable measure of differences due to its sensitivity to confusing-factors, such as amplitude, amplitude fluctuations, offset and curve shapes (Di Marco et al., 2018).

The coefficient of determination (R^2) was used to quantify the proportion of the variance in the measured knee forces $\left\|\vec{F}_{exp}^K(t)\right\|$ that was explained by the estimated knee forces $\left\|\vec{F}_{est}^K(t)\right\|$ for each trial:

$$R^2 = 1 - \frac{SS_{res}}{SS_{tot}} \qquad\qquad 5.6$$

where the residual sum of squares $SS_{res} = \sum_{t=1}^{T}(\left\|\vec{F}^K(\vec{a},t)\right\| - \left\|\vec{F}_{exp}^K(t)\right\|)^2$, the total sum of squares $SS_{tot} = \sum_{t=1}^{T}(\left\|\vec{F}_{exp}^K(t)\right\| - \overline{\left\|\vec{F}_{exp}^K\right\|})^2$ and $\overline{\left\|\vec{F}_{exp}^K\right\|}$ is the average magnitude of measured knee contact force over all time points.

RMSE and R^2 values were obtained for the J_{act}, J_{FK}, J_{Fmatch} and J_{met} solutions. Both the RMSE and R^2 values were the suggested measures of comparison for the Knee Grand Challenge, so allowed for comparison with previous studies (Fregly et al., 2012).

5.2.5 Sampled regions of muscle activation patterns

Unblinded selection of accurate samples

From the set of 1×10^5 muscle activation patterns obtained with Metabolica at each time point, the muscle activation patterns that predicted a knee contact force within 5 % from the measured value were selected. This subset of samples, Met_{close}, is therefore representative of the range of muscle activations that predicted the knee contact force within measurement uncertainties: a maximum error of 15 N was observed during ex-vivo, dynamic load tests of the knee implant where the force ranged from 200 to 1800 N (Kirking et al., 2006). No samples were included in the Met_{close} set for time points when none of the 1×10^5 samples predicted the measured knee force with 5 % accuracy.

Normalized range of sampled activations

For both the complete set of 1×10^5 muscle activation patterns and the Met_{close} subset, the ratio of the range of sampled activations with respect to the allowed range of activations, as defined by the constraints on the activations of the optimal control solution ± 0.1 (*Equation 5.4*), was defined for each muscle:

$$r_i(t) = \frac{[a_i^M(t)]_{max} - [a_i^M(t)]_{min}}{a_{H,i}^M(t) - a_{L,i}^M(t)} \qquad\qquad 5.7$$

where $\left[a_i^M(t)\right]_{max}$ is the maximum activation of muscle i within a set of samples, $\left[a_i^M(t)\right]_{min}$ is the minimum activation of muscle i within a set of samples, $a_{H,i}^M(t)$ is the constraint to the highest allowed activation value of muscle i and $a_{L,i}^M(t)$ is the constraint to the lowest allowed activation value of muscle i. The ratio $r_i(t)$ was defined to be in between 0 and 1, indicating whether the set of samples (the complete set or the Met_{close} subset) included no samples or the complete allowed range of activations for muscle i, respectively.

5.3 Results

The magnitude of the knee contact force for the J_{Fmatch} solutions matched the measured values for each of the six trials throughout the entire gait cycle, except for small time intervals during the loading response phase (0-10 % of the gait cycle) of trial 3 and 5 and a short time interval during the terminal stance phase (30-50 % of the gait cycle) of trial 9 (*Figure 5.3*). During these time intervals the J_{Fmatch} solution overestimated the knee contact force.

The following pattern in knee contact force prediction was consistent in the J_{act} solutions for all trials: J_{act} underestimated the knee force at initial contact, during the mid-stance phase (10-30% of the gait cycle) and during swing phase (except for the final 8 % of the swing phase in trial 4) and overestimated the knee force during the loading response phase. The differences between the predicted and measured values were less consistent throughout trials for the first peak and during terminal stance: The first peak in predicted knee contact force was lower for trial 4, 6 and 9, while this underestimation in knee force during the transition from loading response to mid-stance phase did not occur for trials 3, 5 and 7; The second peak in predicted knee contact force, during the final part of terminal stance, was lower for trial 3, 5, 7 and 9, while oscillations of the measured knee force around the predicted value were obtained for trial 4, 6 and 9 during terminal stance. The knee contact force for the J_{FK} solutions underestimated the measured values for each trial throughout the gait cycle, except for the same time intervals of the trials when J_{Fmatch} overestimated the knee forces. Even though underestimated in terms of absolute value, the predicted timing of the first peak by the J_{FK} solution shifted towards the measured value compared to the J_{act} solution (*Figure 5.3*).

For each trial, the measured knee contact forces were within the range of forces estimated by the sampled muscle activation patterns for most of the gait cycle, except for a time interval during the loading response phase when all sampled muscle activation patterns overestimated the measured knee force. Also, for trial 4, 6 and 9, all sampled muscle activation patterns overestimated the

measured knee contact force during a time interval in the terminal stance phase, while for trial 6 all samples underestimated the measured knee contact force around 30 % of the gait cycle (*Figure 5.3*).

The RMSE and R^2 values, both for individual trials and averaged over trials, showed a similar pattern in terms of goodness of knee force estimation for the J_{Fmatch}, J_{act} and J_{FK} solutions and the closest sample J_{met} (*Table 5.1*); the RMSE was lowest and the R^2 was highest for the J_{Fmatch} solution, followed by the J_{met} sample. These muscle activation patterns were both obtained in an unblinded manner as the measured knee contact force was required to identify the solutions. From the blinded predictions, the J_{act} solution resulted in lower RMSE and higher R^2 values (0.5 BW and 0.61 on average, respectively) compared to the J_{FK} (0.7 BW and 0.20 on average, respectively).

The activation levels of the main muscles that span the knee for the J_{Fmatch} solutions were consistently lower than the J_{act} solutions for time intervals when the J_{act} solutions overestimated the measured knee contact forces and consistently higher for time intervals when the J_{act} solutions underestimated the measured knee contact forces. In trial 3, a representative example, a reduction in activation of muscles that span the knee was predicted during the loading response phase, while a pattern of co-contraction was predicted by the J_{Fmatch} solution during the mid-stance and terminal stance phases (*Figure 5.4*). In the J_{FK} solutions, the main muscles that span the knee were not activated throughout the gait cycle, except for the Rectus Femoris muscle during the mid-stance phase and the Semitendinosus muscle during the loading response, mid-stance and terminal stance phase (figure for Semitendinosus activation can be found in *Appendix A.7*). The muscle activation to produce the required joint moments around the hip and ankle shifted to the mono-articular muscles as previously shown in *Section 4.3*.

For the largest part of the gait cycle, the muscle activations as predicted by the J_{Fmatch} solutions were within the range of muscle activations as sampled by Metabolica. A mismatch between the sampled activation ranges and the J_{Fmatch} solutions occurred in all trials during the first 10 % of the gait cycle, when the J_{act} solutions underestimated the magnitude of knee contact forces (*Figure 5.4* for trial 3, *Appendix A.7* for other trials).
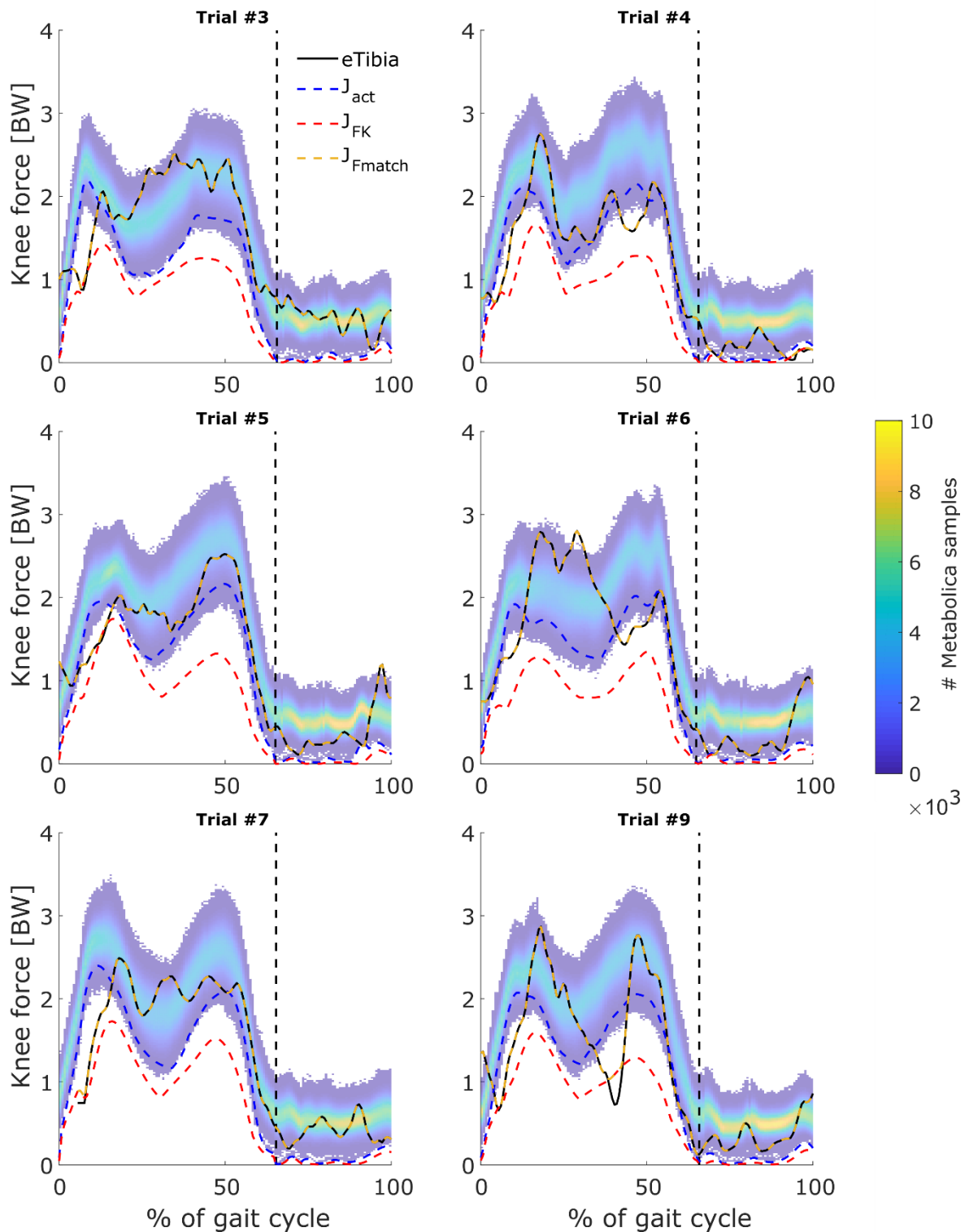
Figure 5.3: Knee contact force trajectories in bodyweight (BW) for all trials; the values from the instrumented implant (eTibia; black, solid), the J_{act} (blue, dashed), J_{FK} (red, dashed) and J_{Fmatch} (yellow, dashed) solutions are shown as lines; the sampled values from Metabolica are shown as a range for which the colour indicates the number of samples that resulted in the corresponding knee force (see colour bar). The vertical dashed line indicates the time instant when toe off occurred.

Table 5.1: Root-mean-square errors (RMSE; in bodyweight (BW)) and coefficients of determination (R^2) for each trial and the mean values over trials for the J_{Fmatch}, J_{act} and J_{FK} solutions and J_{met}, the sample closest to the measured knee force.

	RMSE (BW)							R^2						
	Trial #							Trial #						
	3	4	5	6	7	9	mean	3	4	5	6	7	9	mean
J_{Fmatch}	0.0	0.0	0.0	0.0	0.0	0.1	0.0	1.00	1.00	1.00	1.00	1.00	1.00	1.00
J_{act}	0.7	0.3	0.4	0.6	0.5	0.5	0.5	0.23	0.85	0.76	0.59	0.58	0.65	0.61
J_{FK}	0.8	0.6	0.7	0.9	0.7	0.7	0.7	-0.21	0.50	0.21	0.06	0.25	0.32	0.19
J_{met}	0.1	0.1	0.1	0.1	0.2	0.2	0.1	0.96	0.99	0.99	1.00	0.95	0.96	0.98

Overall, the agreement between activation patterns from the J_{Fmatch} solutions and EMG onset data for muscles spanning the knee changed minimally and non-consistently across muscles when compared to the J_{act} solutions for each trial (*Figure 5.4* for trial 3, *Appendix A.7* for other trials). One difference between the EMG data and the J_{Fmatch} solutions was consistent across trials: the EMG data did not show the predicted inactivity of muscles that span the knee during loading response. Apart from an accurately predicted activation of the Rectus Femoris muscle during the mid-stance phase, the J_{FK} solutions agreed poorly with EMG onset timing.

The muscle activation patterns in the complete set of samples spanned the range allowed by the constraints for most muscles throughout the gait cycle (*Figure 5.5*): only the sampled activation range for the anterior compartment of the Gluteus Medius, the medial Gastrocnemius, the Semitendinosus and the Soleus muscles (and the Gluteus Maximus for some trials during the terminal stance phase) was smaller than the allowed range during parts of the gait cycle. The range of muscle activations in the Met_{close} set was narrower compared to the range of the complete set for most muscles at time points when the measured knee force was close to the boundary of the range of knee forces predicted by the sampled muscle activation patterns. Logically, these narrow ranges occurred at time points adjacent to the intervals where the measured knee force fell outside the range of sampled knee forces due to the sparsity of accurate predictions (*Figure 5.5*). However, besides these time intervals, the activation ranges of the Met_{close} subset were comparable to the ranges of the complete set, indicating a high possible variability in muscle activations that accurately predicted the measured knee contact force.
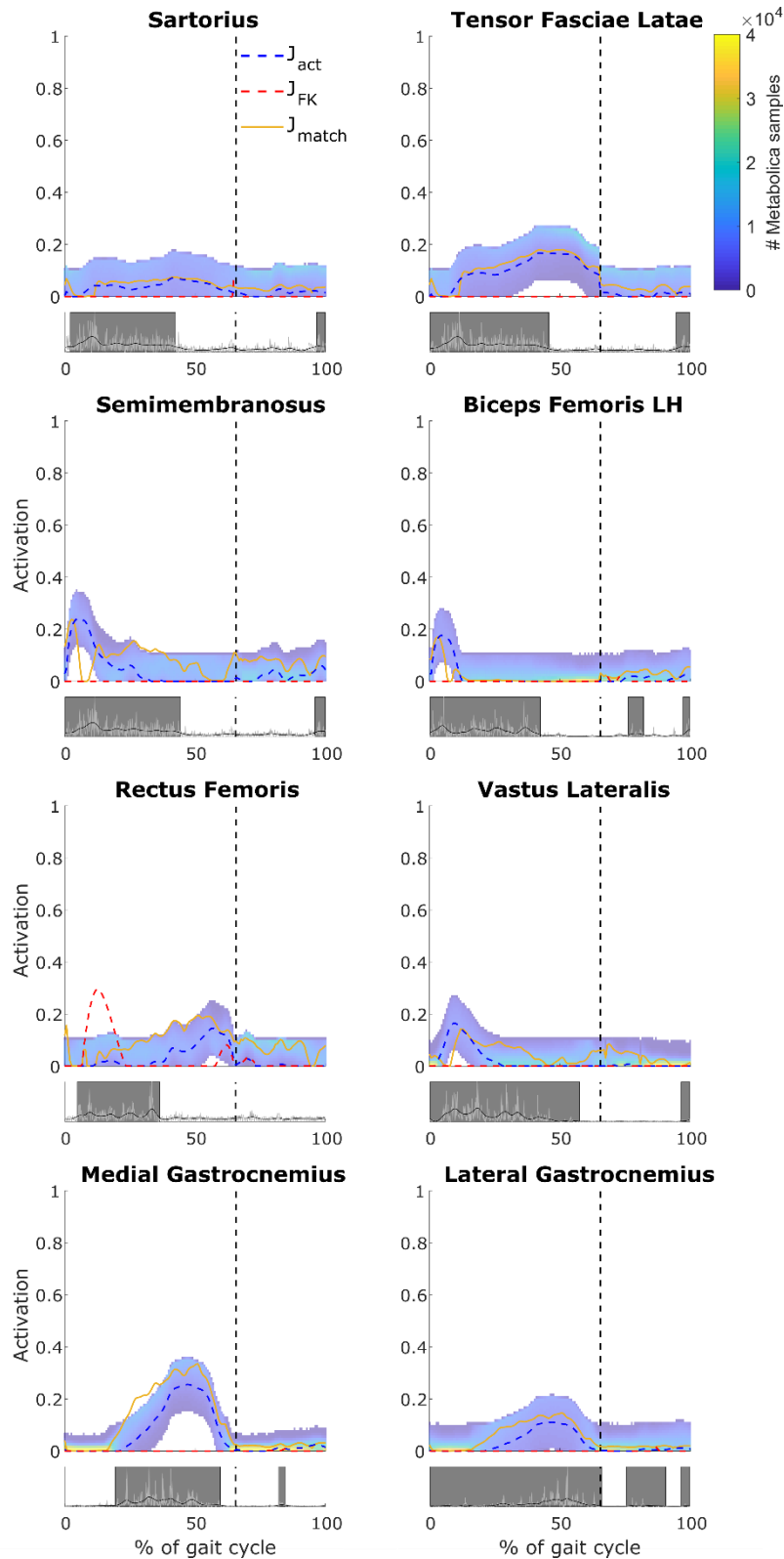
Figure 5.4: Trial 3, the activation patterns of the muscles that span the knee for which EMG data were available. For each muscle, the top graph shows the J_{act} (blue, dashed), J_{FK} (red, dashed) and J_{Fmatch} (yellow, solid) solutions as lines and the sampled muscle activation patterns as a range for which the colour indicates the number of samples (see colour bar); the bottom graph shows the EMG data: the rectified values in light grey, the envelope in black and the onset timing as dark grey boxes. The vertical axis of the bottom graph was normalized to the maximum value in the rectified EMG data. The vertical dashed lines indicate the time instant when toe off occurred.

#	Muscle name
1	Adductor Brevis
2	Adductor Longus
3	Adductor Magnus Sup
4	Adductor Magnus Int
5	Adductor Magnus Inf
6	Biceps Femoris LH
7	Biceps Femoris SH
8	Extensor Digitorum Longus
9	Extensor Hallucis Longus
10	Flexor Digitorum Longus
11	Flexor Hallucis Longus
12	Gemellus
13	Gluteus Maximus Ant
14	Gluteus Maximus Int
15	Gluteus Maximus Post
16	Gluteus Medius Ant
17	Gluteus Medius Int
18	Gluteus Medius Post
19	Gluteus Minimus Ant
20	Gluteus Minimus Int
21	Gluteus Minimus Post
22	Gracilis
23	Iliacus
24	Lateral Gastrocnemius
25	Medial Gastrocnemius
26	Pectineus
27	Peroneus Brevis
28	Peroneus Longus
29	Peroneus Tertius
30	Piriformis
31	Psoas Major
32	Quadratus Femoris
33	Rectus Femoris
34	Sartorius
35	Semimembranosus
36	Semitendinosus
37	Soleus
38	Tensor Fasciae Latae
39	Tibialis Anterior
40	Tibialis Posterior
41	Vastus Medialis
42	Vastus Intermedius
43	Vastus Lateralis
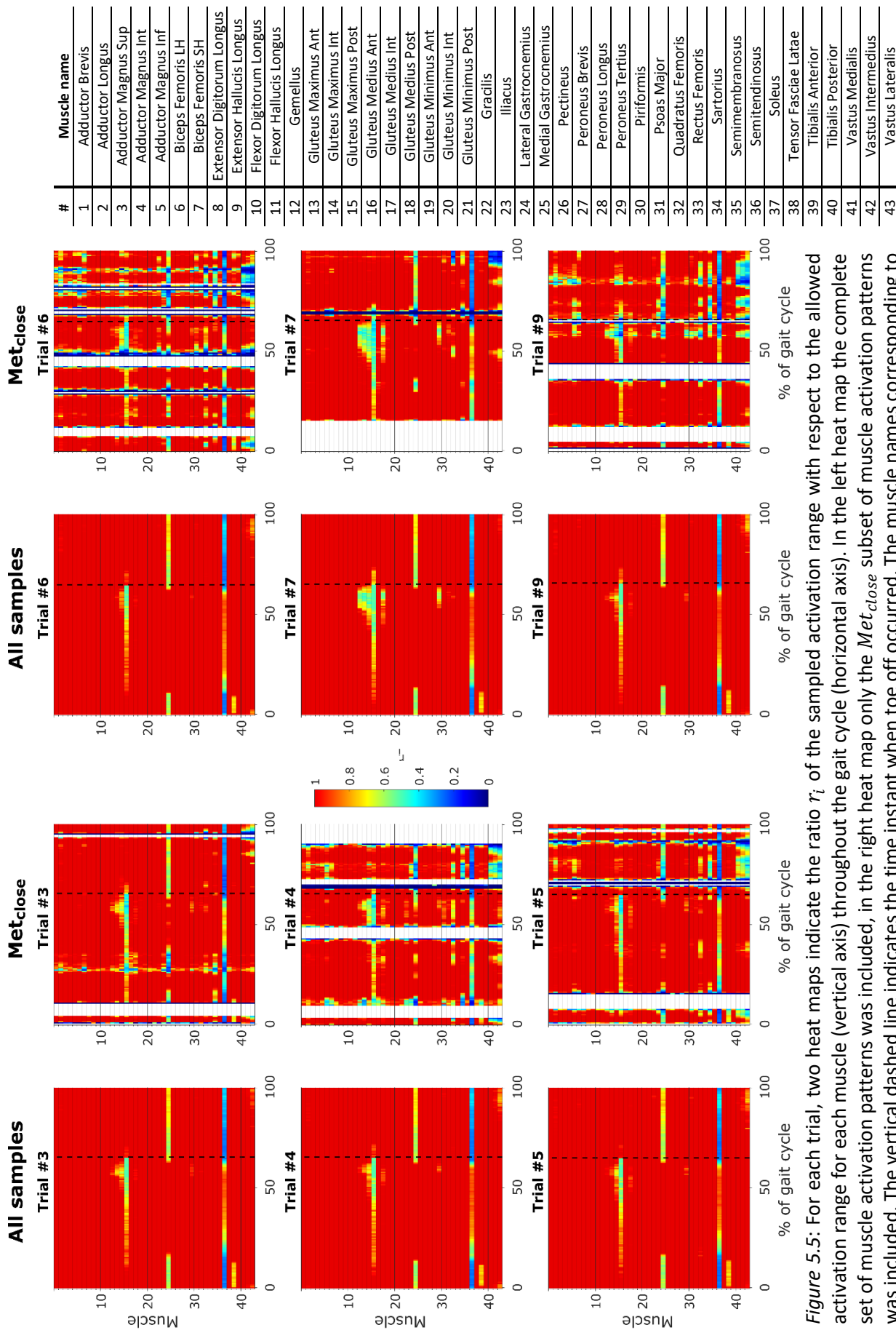
Figure 5.5: For each trial, two heat maps indicate the ratio r_i of the sampled activation range with respect to the allowed activation range for each muscle (vertical axis) throughout the gait cycle (horizontal axis). In the left heat map the complete set of muscle activation patterns was included, in the right heat map only the Met_{close} subset of muscle activation patterns was included. The vertical dashed line indicates the time instant when toe off occurred. The muscle names corresponding to the numbers on the vertical axis are shown in the table on the right. A transparent column indicates that no samples at that time point resulted in knee forces within 5 % from the measured value.

83

5.4 Discussion

This study was aimed to explore the limitations of optimal control in predictions of knee contract forces by answering the following questions: 1) Can a subject-specific musculoskeletal dynamics model, built according to the current best practice, predict the measured forces at the knee during level walking? In other words, does at least one muscle activation pattern exist for which the model prediction and the measurements differ less than the measurement precision?; 2) Assuming such a solution exists, how different is it from an optimal control solution in terms of knee contact forces, but also in terms of muscle activation?; 3) How well can this difference be explained by a stochastic component superimposed to the optimal control (consistent with the uncontrolled manifold theory)?

For each trial, a J_{Fmatch} solution of muscle activations existed for which the knee force tracked the force measured with an instrumented implant; only during a brief time interval during terminal stance in one trial a difference in knee force occurred. The existence of such solutions confirmed that the model, with its idealisations and methods used to identify its input, is capable to exactly describe the observations in multiple repeated trials. Given their uniqueness, the J_{Fmatch} solutions can serve as a reference activation pattern for solutions obtained in an unblinded manner.

The mean RMSE and R^2 values of the J_{act} solutions (0.5 BW and 0.61, respectively) were comparable to the values reported for blinded predictions of the total knee force in various studies that assumed optimal control in simulations of different trials (normal and instructed 'bouncy' and 'smooth' gait) from the same Knee Grand Challenge dataset: 0.4 – 0.8 BW and 0.54 – 0.74, respectively (Ding et al., 2016; Jung et al., 2016; Moissenet et al., 2016; Smith et al., 2016). In each of these studies, the objective functions to obtain muscle activation patterns included a term comparable to J_{act}: the minimization of the sum of muscle activation squared. It should be noted that some of these studies included some form of a contact force term in the objective function (Jung et al., 2016; Moissenet et al., 2016) and for most studies only one or two trials of smooth and bouncy gait were included compared to the six trials of normal, level walking included in this study. Hence, we assumed that the current model, under the assumption of optimal control, performed comparable to other approaches. For one normal gait trial from the dataset used here, an EMG-driven forward dynamics approach showed a slight improvement in predicted total knee force (RMSE: 0.2 BW, R^2: 0.93, (Razu and Guess, 2018)) compared to the highest agreement for a single trial in this study, when assuming optimal control (trial 3; RMSE: 0.3 BW, R^2: 0.85). However, the results for only one trial of normal gait were made available and therefore no comparison could be made with the capability of an EMG-driven approach to capture the large inter-trial variability in experimental knee forces in this dataset. The different muscle activation patterns from the optimal control and the best-match solutions did not

show a notable difference in agreement with the EMG onset timing, which raise questions on the capability of EMG-driven approaches to identify the activation patterns that best match the measured knee forces.

A stochastic approach explored the solution space of sub-optimal muscle activation patterns within a 10 % limit radius from the solution for optimal control, representative of the uncertainty in predicted muscle activations as quantified in *Section 3.3*. For most of the gait cycle in all six trials, this stochastic approach captured the best-match solutions in terms of both knee force and muscle activation: only during limited time intervals during the loading response phase (all trials) and the terminal stance phase (three out of six trials) did the low knee contact force not appear in the set of sub-optimal solutions. The range of sampled knee forces was larger compared to a study that explored sub-optimal muscle control with a parametric approach in a different Knee Grand Challenge dataset (Lundberg et al., 2013). The bias of the probabilistic approach to sample higher knee forces compared to the optimal control solution corresponded to the range of hip forces found in a previous study that used the same approach on a different dataset (Martelli et al., 2013). The large range of muscle activation that resulted in accurate predictions of knee contact forces suggest that the probabilistic approach used here is representative of a 'lightly sub-optimal' or 'good-enough' control that accounts for co-contraction and captures the inter-trial variability in knee forces during most of the gait cycle, while during some time intervals a more explicit representation of the motor control strategy is required. In this specific case, the minimization of the knee force might provide a more accurate prediction during the loading response phase.

The author acknowledges three main limitations of this study: Firstly, even though an instrumented knee implant provides a valuable dataset of measured knee forces to validate our model predictions, the current study included only one participant. The author acknowledges that the current work should be expanded to other datasets within the Knee Grand Challenge competition and preferably to other publicly available datasets that include measured hip forces, such that the generalizability of the current work can be confirmed. Nonetheless, the question how to validate approaches to predict joint contact forces in participants without an instrumented joint implant remains. Secondly, the force-length-velocity relationship was not considered when determining the force producing capacity of the muscles. However, as mentioned before, no standardized method currently exists to accurately predict this relationship for each muscle individually. Furthermore, the predicted levels of activation were relatively low, strengthening the author's belief that the results would not change when the force-length-velocity relationship would be considered. Thirdly, only the resultant force and not the direction of the forces experienced by the knee were considered. Given the relatively large contribution of the axial component to the resultant force and the small mediolateral and anterior-

posterior orientation of the muscle lines of action with respect to the joint during the stance phase, no difference in the obtained results was expected if the directional components of the contact force were included separately. Nonetheless, future work should study the influence of muscle control on the distribution of loads over different compartments of the knee joint.

In conclusion, the results presented in this study underline the importance of muscle control in the prediction of knee forces within a multi-body dynamics approach. A subject-specific musculoskeletal dynamics model, built according to the current best practice, was compatible with the experimentally measured knee forces during level walking. In case of pathological gait, such as studied here, the assumption of optimal motor control was not representative of the considerable level of inter-trial variability. A stochastic approach that assumed an uncontrolled manifold of 10 % around the optimal control solution did capture this variability for most of the gait cycle. In cases when the motor control strategy is severely sub-optimal or when a higher level of accuracy for the predicted joint contact forces is required, the author believes the only solution is to not reduce motor control to an optimization problem and include an explicit model of control.

GENERAL DISCUSSION

AND

FUTURE WORK

The general aim of this thesis was to explore the variability in motor control of the musculoskeletal dynamics during walking through a stochastic modelling approach: Optimal motor control is not representative of inherent variability in repeated tasks and optimality from the perspective of energy expenditure might be undesirable or even impossible in pathological gait.

The first part of this work outlined the processes of verification and validation of musculoskeletal dynamics models that allow for quantification of the uncertainty in the predicted muscle and joint contact forces. Previous studies suggested that the sensitivity of predicted joint contact forces to measurement errors, model parameter identification and joint models was around 1 to 2 BW. The corresponding uncertainty of predicted muscle forces was around 10 % of the maximum isometric force. Exploratory work showed that a previously presented stochastic approach to predict muscle activation patterns has potential to capture sub-optimal control and inherent variability in repeated tasks but is not suited to explore the boundaries of motor control.

The second part of this work explored the boundaries of motor control by aiming to minimize the forces experienced by the lower-limb joints during level walking. Alternative muscle recruitment strategies have the potential to reduce the forces at the hip and knee, but not at the ankle. Muscle recruitment strategies that aim to reduce the force in the hip or knee, might increase the peak contact force in the non-targeted knee or hip, respectively. Therefore, future work should further study the potential of neuromuscular rehabilitation, such as strength training of specific muscle groups and body-awareness approaches, to target preventive reduction of contact forces at the hip and knee, while considering the potential adverse effects on non-targeted joints.

The third part of this work studied the limitations of optimal control in dynamic simulations of pathological gait, specifically in a patient with an instrumented knee implant. Optimal muscle control predicted the measured knee contact force, on average, with a root-mean-square error of 0.5 BW and a correlation coefficient of 0.61; previous studies on the same publicly available dataset that assumed optimal control reported comparable levels of accuracy. A control strategy that aimed to minimize the knee force did not improve the accuracy of the predicted knee force; given the high inter-trial variability in the measured knee force, no single cost function is likely to provide a viable alternative. A stochastic approach to predict muscle activation patterns, representative of the 10 % uncertainty in their prediction (*Section 3.3*), captured the uncertainty and inherent variability of repeated tasks in predicted joint contact forces. Therefore, the assumption of sub-optimal control provides a range of plausible joint contact forces, representative of the uncertainty in terms of measurement inaccuracies, modelling errors and inherent variability, which is likely to contain the true force. The inclusion of a stochastic element in the prediction of muscle activation corresponds with larger frameworks such as 'good enough' control and the uncontrolled manifold theory (Loeb, 2012; Scholz and Schöner, 1999).

Both frameworks highlight the importance of variability in motor control, which is ignored by the assumption of motor control arising from optimization. The stochastic approach, first applied to a musculoskeletal modelling approach by Martelli et al. (Martelli et al., 2013), draws sub-optimal muscle recruitment patterns from a probability distribution along the null space of the force equilibrium equations. This null space represents all combinations of muscle activations that do not alter the resultant net-joint moments, equivalent to the task-independent direction, or uncontrolled manifold, on the level of muscle activation (Scholz and Schöner, 1999). According to the uncontrolled manifold theory, variability along this direction could allow for stability to perturbations. In case of motor control, such perturbations could be noise in the signals from the central nervous system to the muscle fibres or sudden changes in the length of muscle fibres, affecting the afferent information. By limiting the sampled muscle activation to lie within a range from the optimal muscle activation pattern, a level of sub-optimality was introduced to the prediction of muscle control. The stochastic approach to muscle control presented here successfully predicted the inter-trial variability observed in the knee contact force that could not be predicted by kinematic variability alone. Future work should focus on how to quantify the level of sub-optimality in muscle activation in different applications: Pathologies are likely to influence the level of sub-optimality in control strategies due to altered or decreased neural control. Also, modelling errors influence the uncertainty in predicted muscle activation: Validation and quantification of error propagation should therefore be an integrated element when identifying ranges of predicted joint contact forces.

If higher accuracy of predicted muscle and joint contact forces is required or in case of severely sub-optimal motor control, I believe the only solution is to include an explicit model of motor control. A refined mechanistic model would allow for the differentiation between hierarchical levels of motor control, as proposed by Bernstein (Bernstein, 1967), such as the involuntary spinal control and the cognition-driven anticipatory control. The current work has shown that the validity of a sophisticated model of human movement dynamics is highly dependent on the assumptions on motor control. A mechanistic approach would allow for a subject-specific model of motor control, likely to be dependent on the health status of the participants or the environment of the task, and has the potential to improve the accuracy of neuromusculoskeletal models.

A logical approach to include subject-specific motor control would be to include electromyography data in the identification of the control signals that drive the musculoskeletal dynamics. In the inverse dynamics approach muscle synergies, a reduced number of activation signals to groups of muscles identified with EMG data, have prescribed muscle activation patterns. EMG has also been successfully used to define the muscle activation in a forward dynamics approach (Lloyd and Besier, 2003; Pizzolato et al., 2015). In such an EMG-driven approach, the relationship between the measured electric

potential and the force exerted by a muscle is identified through calibration: Typically, both the net-joint moments and the EMG of relevant muscles are recorded simultaneously during simple tasks such as isolated joint flexion or extension. The parameters that predict the force a muscle produces given the measured electric potential are determined from these calibration trials. However, the calibration is indirect as multiple muscles are involved in even the simplest movements and the net-joint moment, rather than the force along each muscle's tendon, serve as the calibration values. Additionally, assumptions on the excitation of deeper muscle tissues are required as these muscles cannot be reached with surface electrodes and wire EMG raises ethical issues in most applications. Nonetheless, an EMG-driven, or EMG-informed, approach could provide a subject-specific muscle activation pattern representative of possible pathological muscle control, as opposed to the assumption of optimal control. This muscle activation pattern could then serve as the muscle activation pattern around which the stochastic approach assumes a level of sub-optimality. The level of sub-optimality could, for example, be representative of the uncertainty in the muscle activation prediction resulting from the EMG-force calibration. However, one could question the difficulty to validate the model predictions qualitatively when EMG is already included in the model definition and measured joint contact forces data are not available.

An explicit model of motor control would allow for truly predictive simulations as not only the effect of the activation of a specific muscle on the segmental accelerations, but also the influence of different levels of motor control on the movement can be determined directly. Motion capture through stereo photogrammetry or wearable sensors, in tasks that are more representative of daily life, and EMG data can serve as independent validation measures for movement dynamics and motor control, respectively. Such an approach to answer 'what if' questions has a large potential to inform research into compensatory strategies targeted by neurorehabilitation.

A second challenge remains to determine the influence of the assumptions on muscle physiology on model predictions. The dependency between time points in a forward dynamics approach, for example, allows to account for the stretch in tendinous tissue that stores energy and keeps muscle fibres around their optimal length. Not only are such mechanisms metabolically advantageous, they are also likely to influence motor control: energy can be released at later time points and tendinous elasticity might be exploited to regulate joint stability. The current inverse approach to optimal motor control, however, ignores these mechanisms.

A relevant question is how task specification determines the variability in predicted muscle activations. Many studies focus on tasks in a simplified setting, such as a motion capture laboratory environment, which is likely to overestimate the redundancy in more demanding tasks of everyday

life (Loeb, 2000). New approaches to study motor control should be developed with their application to more complex tasks in a setting of daily life kept in mind.

In conclusion, motor control in complex motor tasks should be studied with the required level of dynamic accuracy to obtain a solution space representative of the physiological muscle redundancy that motor control must choose a solution from. An inverse dynamics approach suffices in certain applications, but sub-optimality in motor control should be accounted for to provide a range of muscle and joint contact force predictions. However, an explicit model of motor control, implemented in a forward dynamics approach, is required to study the influence of individual elements of the neural system on the movement dynamics in pathological gait.

And so castles made of sand

Melts into the sea

Eventually

       Jimi Hendrix

REFERENCES

An, K.N., Ueba, Y., Chao, E.Y., Cooney, W.P., Linscheid, R.L., 1983. Tendon excursion and moment arm of index finger muscles. J. Biomech. 16, 419–425. https://doi.org/10.1016/0021-9290(83)90074-X

Anderson, F.C., Pandy, M.G., 2001a. Dynamic Optimization of Human Walking. J. Biomech. Eng. 123, 381. https://doi.org/10.1115/1.1392310

Anderson, F.C., Pandy, M.G., 2001b. Static and dynamic optimization solutions for gait are practically equivalent. J. Biomech. 34, 153–161. https://doi.org/10.1016/S0021-9290(00)00155-X

Andriacchi, T.P., Mündermann, A., Smith, R.L., Alexander, E.J., Dyrby, C.O., Koo, S., 2004. A Framework for the in Vivo Pathomechanics of Osteoarthritis at the Knee. Ann. Biomed. Eng. 32, 447–457. https://doi.org/10.1023/B:ABME.0000017541.82498.37

Arnold, E.M., Ward, S.R., Lieber, R.L., Delp, S.L., 2010. A Model of the Lower Limb for Analysis of Human Movement. Ann. Biomed. Eng. 38, 269–279. https://doi.org/10.1007/s10439-009-9852-5

Bergmann, G., Deuretzbacher, G., Heller, M., Graichen, F., Rohlmann, A., Strauss, J., Duda, G.., 2001. Hip contact forces and gait patterns from routine activities. J. Biomech. 34, 859–871. https://doi.org/10.1016/S0021-9290(01)00040-9

Bergmann, G., Graichen, F., Rohlmann, A., Bender, A., Heinlein, B., Duda, G.N., Heller, M.O., Morlock, M.M., 2010. Realistic loads for testing hip implants. Biomed. Mater. Eng. 20, 65–75. https://doi.org/10.3233/BME-2010-0616

Bernstein, N.A., 1967. The Co-ordination and Regulation of Movements. Pergamon Press, Oxford.

Blankevoort, L., Huiskes, R., de Lange, A., 1988. The envelope of passive knee joint motion. J. Biomech. 21, 705–720. https://doi.org/10.1016/0021-9290(88)90280-1

Brouwer, G.M., Tol, A.W. Van, Bergink, A.P., Belo, J.N., Bernsen, R.M.D., Reijman, M., Pols, H.A.P., Bierma-Zeinstra, S.M.A., 2007. Association between valgus and varus alignment and the development and progression of radiographic osteoarthritis of the knee. Arthritis Rheum. 56, 1204–1211. https://doi.org/10.1002/art.22515

Buchanan, T.S., 1995. Evidence that maximum muscle stress is not a constant: differences in specific tension in elbow flexors and extensors. Med. Eng. Phys. 17, 529–536. https://doi.org/10.1016/1350-4533(95)00005-8

Buchthal, F., Schmalbruch, H., 1970. Contraction Times and Fibre Types in Intact Human Muscle. Acta Physiol. Scand. 79, 435–452. https://doi.org/10.1111/j.1748-1716.1970.tb04744.x

Cappozzo, A., Catani, F., Leardini, A., Benedetti, M., Della Croce, U., 1996. Position and orientation in space of bones during movement: experimental artefacts. Clin. Biomech. 11, 90–100. https://doi.org/10.1016/0268-0033(95)00046-1

Childs, J.D., Sparto, P.J., Fitzgerald, G.K., Bizzini, M., Irrgang, J.J., 2004. Alterations in lower extremity movement and muscle activation patterns in individuals with knee osteoarthritis. Clin. Biomech. 19, 44–49. https://doi.org/10.1016/j.clinbiomech.2003.08.007

Cooper, C., Inskip, H., Croft, P., Campbell, L., Smith, G., Mclearn, M., Coggon, D., 1998. Individual Risk factors for Hip Osteoarthritis: Obesity, Hip Injury and Physical Activity. Am. J. Epidemiol. 147, 516–522. https://doi.org/10.1093/oxfordjournals.aje.a009482

Cristofolini, L., Viceconti, M., Cappello, A., Toni, A., 1996. Mechanical validation of whole bone composite femur models. J. Biomech. 29, 525–535. https://doi.org/10.1016/0021-9290(95)00084-4

Crowninshield, R.D., Brand, R.A., 1981. A physiologically based criterion of muscle force prediction in locomotion. J. Biomech. 14, 793–801. https://doi.org/10.1016/0021-9290(81)90035-X

Damm, P., Kutzner, I., Bergmann, G., Rohlmann, A., Schmidt, H., 2017. Comparison of in vivo measured loads in knee, hip and spinal implants during level walking. J. Biomech. 51, 128–132. https://doi.org/10.1016/j.jbiomech.2016.11.060

Delagi, E.F., Perroto, A., 1980. Anatomic Guide for the Electromyographer: The Limbs. Charles C Thomas Publisher, Springfield, Ill.

Delp, S.L., Anderson, F.C., Arnold, A.S., Loan, P., Habib, A., John, C.T., Guendelman, E., Thelen, D.G., 2007. OpenSim: Open-Source Software to Create and Analyze Dynamic Simulations of Movement. IEEE Trans. Biomed. Eng. 54, 1940–1950. https://doi.org/10.1109/TBME.2007.901024

Delp, S.L., Loan, J.P., Hoy, M.G., Zajac, F.E., Topp, E.L., Rosen, J.M., 1990. An interactive graphics-based model of the lower extremity to study orthopaedic surgical procedures. IEEE Trans. Biomed. Eng. 37, 757–767. https://doi.org/10.1109/10.102791

DeMers, M.S., Pal, S., Delp, S.L., 2014. Changes in tibiofemoral forces due to variations in muscle activity during walking. J. Orthop. Res. 32, 769–776. https://doi.org/10.1002/jor.22601

Di Marco, R., Scalona, E., Pacilli, A., Cappa, P., Mazzà, C., Rossi, S., 2018. How to choose and interpret

similarity indices to quantify the variability in gait joint kinematics. Int. Biomech. 5, 1–8. https://doi.org/10.1080/23335432.2018.1426496

Ding, Z., Nolte, D., Kit Tsang, C., Cleather, D.J., Kedgley, A.E., Bull, A.M.J., 2016. In Vivo Knee Contact Force Prediction Using Patient-Specific Musculoskeletal Geometry in a Segment-Based Computational Model. J. Biomech. Eng. 138, 021018. https://doi.org/10.1115/1.4032412

Drillis, R., Contini, R., Bluestein, M., 1964. Body segment parameters; a survey of measurement techniques. Artif. Limbs 8, 44–66.

Erdemir, A., McLean, S., Herzog, W., van den Bogert, A.J., 2007. Model-based estimation of muscle forces exerted during movements. Clin. Biomech. 22, 131–154. https://doi.org/10.1016/j.clinbiomech.2006.09.005

Feigenberg, J.M., 2014. Nikolai Bernstein: From Reflex to the Model of the Future. LIT Verlag, Münster.

Felson, D.T., 2000. Osteoarthritis: New Insights. Part 1: The Disease and Its Risk Factors. Ann. Intern. Med. 133, 635. https://doi.org/10.7326/0003-4819-133-8-200010170-00016

Felson, D.T., Goggins, J., Niu, J., Zhang, Y., Hunter, D.J., 2004. The effect of body weight on progression of knee osteoarthritis is dependent on alignment. Arthritis Rheum. 50, 3904–3909. https://doi.org/10.1002/art.20726

Fregly, B.J., Besier, T.F., Lloyd, D.G., Delp, S.L., Banks, S.A., Pandy, M.G., D'Lima, D.D., 2012. Grand challenge competition to predict in vivo knee loads. J. Orthop. Res. 30, 503–513. https://doi.org/10.1002/jor.22023

Gordon, A.M., Huxley, A.F., Julian, F.J., 1966. The variation in isometric tension with sarcomere length in vertebrate muscle fibres. J. Physiol. 184, 170–192. https://doi.org/10.1113/jphysiol.1966.sp007909

Gray, H., 1918. Anatomy of the Human Body, 20th ed. Lea & Febiger, Philadelphia.

Guyton, A.C., Hall, J.E., 2006. Textbook of Medical Physiology, 11th ed. Elsevier Saunders, Philadelphia.

Hallén, L.G., Lindahl, O., 1966. The "Screw-Home" Movement in the Knee-Joint. Acta Orthop. Scand. 37, 97–106. https://doi.org/10.3109/17453676608989407

Hamner, S.R., Seth, A., Delp, S.L., 2010. Muscle contributions to propulsion and support during running. J. Biomech. 43, 2709–2716. https://doi.org/10.1016/j.jbiomech.2010.06.025

Hannah, I., Montefiori, E., Modenese, L., Prinold, J., Viceconti, M., Mazzà, C., 2017. Sensitivity of a juvenile subject-specific musculoskeletal model of the ankle joint to the variability of operator-dependent input. Proc. Inst. Mech. Eng. Part H J. Eng. Med. 231, 415–422.

https://doi.org/10.1177/0954411917701167

Hardt, D.E., 1978. Determining Muscle Forces in the Leg During Normal Human Walking—An Application and Evaluation of Optimization Methods. J. Biomech. Eng. 100, 72. https://doi.org/10.1115/1.3426195

Hast, M.W., Piazza, S.J., 2013. Dual-Joint Modeling for Estimation of Total Knee Replacement Contact Forces During Locomotion. J. Biomech. Eng. 135, 021013. https://doi.org/10.1115/1.4023320

Heiden, T.L., Lloyd, D.G., Ackland, T.R., 2009. Knee joint kinematics, kinetics and muscle co-contraction in knee osteoarthritis patient gait. Clin. Biomech. 24, 833–841. https://doi.org/10.1016/j.clinbiomech.2009.08.005

Heino, J., Calvetti, D., Somersalo, E., 2010. Metabolica: A statistical research tool for analyzing metabolic networks. Comput. Methods Programs Biomed. 97, 151–167. https://doi.org/10.1016/j.cmpb.2009.07.007

Heino, J., Tunyan, K., Calvetti, D., Somersalo, E., 2007. Bayesian flux balance analysis applied to a skeletal muscle metabolic model. J. Theor. Biol. 248, 91–110. https://doi.org/10.1016/j.jtbi.2007.04.002

Henneman, E., Somjen, G., Carpenter, D.O., 1965. Excitability and inhibitability of motoneurons of different sizes. J. Neurophysiol. 28, 599–620. https://doi.org/10.1152/jn.1965.28.3.599

Hicks, J.L., Uchida, T.K., Seth, A., Rajagopal, A., Delp, S.L., 2015. Is My Model Good Enough? Best Practices for Verification and Validation of Musculoskeletal Models and Simulations of Movement. J. Biomech. Eng. 137, 020905. https://doi.org/10.1115/1.4029304

Hill, A. V., 1938. The Heat of Shortening and the Dynamic Constants of Muscle. Proc. R. Soc. B Biol. Sci. 126, 136–195. https://doi.org/10.1098/rspb.1938.0050

Hirokawa, S., Solomonow, M., Luo, Z., Lu, Y., D'Ambrosia, R., 1991. Muscular co-contraction and control of knee stability. J. Electromyogr. Kinesiol. 1, 199–208. https://doi.org/10.1016/1050-6411(91)90035-4

Hodges, P.W., Bui, B.H., 1996. A comparison of computer-based methods for the determination of onset of muscle contraction using electromyography. Electroencephalogr. Clin. Neurophysiol. Mot. Control 101, 511–519. https://doi.org/10.1016/S0921-884X(96)95190-5

Huijing, P.A., Baan, G.C., 2003. Myofascial force transmission: muscle relative position and length determine agonist and synergist muscle force. J. Appl. Physiol. 94, 1092–1107. https://doi.org/10.1152/japplphysiol.00173.2002

Huijing, P.A., Baan, G.C., 2001. Myofascial Force Transmission Causes Interaction between Adjacent Muscles and Connective Tissue: Effects of Blunt Dissection and Compartmental Fasciotomy on Length Force Characteristics of Rat Extensor Digitorum Longus Muscle. Arch. Physiol. Biochem. 109, 97–109. https://doi.org/10.1076/apab.109.2.97.4269

Huijing, P.A., Baan, G.C., Rebel, G.T., 1998. Non-myotendinous force transmission in rat extensor digitorum longus muscle. J. Exp. Biol. 201, 683–691.

Hurd, W.J., Snyder-Mackler, L., 2007. Knee instability after acute ACL rupture affects movement patterns during the mid-stance phase of gait. J. Orthop. Res. 25, 1369–1377. https://doi.org/10.1002/jor.20440

Huxley, A.F., Niedergerke, R., 1954. Structural Changes in Muscle During Contraction: Interference Microscopy of Living Muscle Fibres. Nature 173, 971–973. https://doi.org/10.1038/173971a0

Huxley, H.E., 1957. The double array of filaments in cross-striated muscle. J. Biophys. Biochem. Cytol. 3, 631–48. https://doi.org/10.1083/jcb.3.5.631

Huxley, H.E., Hanson, J., 1954. Changes in the cross-striations of muscle during contraction and stretch and their structural interpretation. Nature 173, 973–6. https://doi.org/10.1038/173973a0

Jewell, B.R., Wilkie, D.R., 1958. An analysis of the mechanical components in frog's striated muscle. J. Physiol. 143, 515–540. https://doi.org/10.1113/jphysiol.1958.sp006075

Jewett, J., Serway, R.A., 2007. Physics for Scientists and Engineers with Modern Physics, 7th ed. Brooks/Cole, Pacific Grove, California.

Jones, D., de Haan, A., Round, J., 2004. Skeletal Muscle from Molecules to Movement. Churchill Livingstone, Edinburgh.

Joyce, G.C., Rack, P.M.H., Westbury, D.R., 1969. The mechanical properties of cat soleus muscle during controlled lengthening and shortening movements. J. Physiol. 204, 461–474. https://doi.org/10.1113/jphysiol.1969.sp008924

Jung, Y., Phan, C.-B., Koo, S., 2016. Intra-Articular Knee Contact Force Estimation During Walking Using Force-Reaction Elements and Subject-Specific Joint Model 2. J. Biomech. Eng. 138, 021016. https://doi.org/10.1115/1.4032414

Kadaba, M.P., Ramakrishnan, H.K., Wootten, M.E., Gainey, J., Gorton, G., Cochran, G.V.B., 1989. Repeatability of kinematic, kinetic, and electromyographic data in normal adult gait. J. Orthop. Res. 7, 849–860. https://doi.org/10.1002/jor.1100070611

Karlson, E.W., Mandl, L.A., Aweh, G.N., Sangha, O., Liang, M.H., Grodstein, F., 2003. Total hip

replacement due to osteoarthritis: the importance of age, obesity, and other modifiable risk factors. Am. J. Med. 114, 93–98. https://doi.org/10.1016/S0002-9343(02)01447-X

Kim, H.J., Fernandez, J.W., Akbarshahi, M., Walter, J.P., Fregly, B.J., Pandy, M.G., 2009. Evaluation of predicted knee-joint muscle forces during gait using an instrumented knee implant. J. Orthop. Res. 27, 1326–1331. https://doi.org/10.1002/jor.20876

Kinney, A.L., Besier, T.F., D'Lima, D.D., Fregly, B.J., 2013. Update on Grand Challenge Competition to Predict in Vivo Knee Loads. J. Biomech. Eng. 135, 021012. https://doi.org/10.1115/1.4023255

Kirking, B., Krevolin, J., Townsend, C., Colwell, C.W., D'Lima, D.D., 2006. A multiaxial force-sensing implantable tibial prosthesis. J. Biomech. 39, 1744–1751. https://doi.org/10.1016/j.jbiomech.2005.05.023

Kuo, A.D., 1998. A Least-Squares Estimation Approach to Improving the Precision of Inverse Dynamics Computations. J. Biomech. Eng. 120, 148. https://doi.org/10.1115/1.2834295

Kutch, J.J., Valero-Cuevas, F.J., 2011. Muscle redundancy does not imply robustness to muscle dysfunction. J. Biomech. 44, 1264–1270. https://doi.org/10.1016/j.jbiomech.2011.02.014

Kutzner, I., Heinlein, B., Graichen, F., Bender, A., Rohlmann, A., Halder, A., Beier, A., Bergmann, G., 2010. Loading of the knee joint during activities of daily living measured in vivo in five subjects. J. Biomech. 43, 2164–2173. https://doi.org/10.1016/j.jbiomech.2010.03.046

Lafeber, F.P., Intema, F., Van Roermund, P.M., Marijnissen, A.C., 2006. Unloading joints to treat osteoarthritis, including joint distraction. Curr. Opin. Rheumatol. 18, 519–525. https://doi.org/10.1097/01.bor.0000240366.54960.a1

Lamberto, G., Martelli, S., Cappozzo, A., Mazzà, C., 2017. To what extent is joint and muscle mechanics predicted by musculoskeletal models sensitive to soft tissue artefacts? J. Biomech. 62, 68–76. https://doi.org/10.1016/j.jbiomech.2016.07.042

Latash, M.L., 2012. Fundamentals of Motor Control. Academic Press.

Lichtwark, G.A., Bougoulias, K., Wilson, A.M., 2007. Muscle fascicle and series elastic element length changes along the length of the human gastrocnemius during walking and running. J. Biomech. 40, 157–164. https://doi.org/10.1016/j.jbiomech.2005.10.035

Lin, Y.-C., Walter, J.P., Banks, S.A., Pandy, M.G., Fregly, B.J., 2010. Simultaneous prediction of muscle and contact forces in the knee during gait. J. Biomech. 43, 945–952. https://doi.org/10.1016/j.jbiomech.2009.10.048

Lloyd, D.G., Besier, T.F., 2003. An EMG-driven musculoskeletal model to estimate muscle forces and

knee joint moments in vivo. J. Biomech. 36, 765–776. https://doi.org/10.1016/S0021-9290(03)00010-1

Loeb, G.E., 2012. Optimal isn't good enough. Biol. Cybern. 106, 757–765. https://doi.org/10.1007/s00422-012-0514-6

Loeb, G.E., 2000. Overcomplete musculature or underspecified tasks? Motor Control 4, 81-3; discussion 97-116.

Lu, T.-W., O'Connor, J.J., 1999. Bone position estimation from skin marker co-ordinates using global optimisation with joint constraints. J. Biomech. 32, 129–134. https://doi.org/10.1016/S0021-9290(98)00158-4

Lundberg, H.J., Foucher, K.C., Wimmer, M.A., 2009. A parametric approach to numerical modeling of TKR contact forces. J. Biomech. 42, 541–545. https://doi.org/10.1016/j.jbiomech.2008.11.030

Lundberg, H.J., Knowlton, C., Wimmer, M.A., 2013. Fine Tuning Total Knee Replacement Contact Force Prediction Algorithms Using Blinded Model Validation. J. Biomech. Eng. 135, 021015. https://doi.org/10.1115/1.4023388

Markolf, K.L., Mensch, J.S., Amstutz, H.C., 1976. Stiffness and laxity of the knee--the contributions of the supporting structures. A quantitative in vitro study. J. Bone Joint Surg. Am. 58, 583–94.

Marra, M.A., Vanheule, V., Fluit, R., Koopman, B.H.F.J.M., Rasmussen, J., Verdonschot, N., Andersen, M.S., 2015. A Subject-Specific Musculoskeletal Modeling Framework to Predict In Vivo Mechanics of Total Knee Arthroplasty. J. Biomech. Eng. 137, 020904. https://doi.org/10.1115/1.4029258

Martelli, S., Calvetti, D., Somersalo, E., Viceconti, M., 2015a. Stochastic modelling of muscle recruitment during activity. Interface Focus 5, 20140094. https://doi.org/10.1098/rsfs.2014.0094

Martelli, S., Calvetti, D., Somersalo, E., Viceconti, M., Taddei, F., 2013. Computational tools for calculating alternative muscle force patterns during motion: A comparison of possible solutions. J. Biomech. 46, 2097–2100. https://doi.org/10.1016/j.jbiomech.2013.05.023

Martelli, S., Taddei, F., Cappello, A., van Sint Jan, S., Leardini, A., Viceconti, M., 2011. Effect of sub-optimal neuromotor control on the hip joint load during level walking. J. Biomech. 44, 1716–1721. https://doi.org/10.1016/j.jbiomech.2011.03.039

Martelli, S., Valente, G., Viceconti, M., Taddei, F., 2015b. Sensitivity of a subject-specific musculoskeletal model to the uncertainties on the joint axes location. Comput. Methods

Biomech. Biomed. Engin. 18, 1555–1563. https://doi.org/10.1080/10255842.2014.930134

Mashima, H., 1984. Force-velocity relation and contractility in striated muscles. Jpn. J. Physiol. 34, 1–17. https://doi.org/10.2170/jjphysiol.34.1

Mashima, H., Akazawa, K., Kushima, H., Fujii, K., 1972. The force-load-velocity relation and the viscous-like force in the frog skeletal muscle. Jpn. J. Physiol. 22, 103–20. https://doi.org/10.2170/jjphysiol.22.103

Mirka, G.A., Marras, W.S., 1993. A Stochastic Model of Trunk Muscle Coactivation During Trunk Bending. Spine (Phila. Pa. 1976). 18, 1396–1409. https://doi.org/10.1097/00007632-199318110-00003

Modenese, L., Montefiori, E., Wang, A., Wesarg, S., Viceconti, M., Mazzà, C., 2018. Investigation of the dependence of joint contact forces on musculotendon parameters using a codified workflow for image-based modelling. J. Biomech. 73, 108–118. https://doi.org/10.1016/j.jbiomech.2018.03.039

Moissenet, F., Chèze, L., Dumas, R., 2016. Influence of the Level of Muscular Redundancy on the Validity of a Musculoskeletal Model. J. Biomech. Eng. 138, 021019. https://doi.org/10.1115/1.4032127

Patriarco, A.G., Mann, R.W., Simon, S.R., Mansour, J.M., 1981. An evaluation of the approaches of optimization models in the prediction of muscle forces during human gait. J. Biomech. 14, 513–525. https://doi.org/10.1016/0021-9290(81)90001-4

Pizzolato, C., Lloyd, D.G., Sartori, M., Ceseracciu, E., Besier, T.F., Fregly, B.J., Reggiani, M., 2015. CEINMS: A toolbox to investigate the influence of different neural control solutions on the prediction of muscle excitation and joint moments during dynamic motor tasks. J. Biomech. 48, 3929–3936. https://doi.org/10.1016/j.jbiomech.2015.09.021

Prinold, J.A.I., Mazzà, C., Di Marco, R., Hannah, I., Malattia, C., Magni-Manzoni, S., Petrarca, M., Ronchetti, A.B., Tanturri de Horatio, L., van Dijkhuizen, E.H.P., Wesarg, S., Viceconti, M., 2016. A Patient-Specific Foot Model for the Estimate of Ankle Joint Forces in Patients with Juvenile Idiopathic Arthritis. Ann. Biomed. Eng. 44, 247–257. https://doi.org/10.1007/s10439-015-1451-z

Rajagopal, A., Dembia, C.L., DeMers, M.S., Delp, D.D., Hicks, J.L., Delp, S.L., 2016. Full-Body Musculoskeletal Model for Muscle-Driven Simulation of Human Gait. IEEE Trans. Biomed. Eng. 63, 2068–2079. https://doi.org/10.1109/TBME.2016.2586891

Razu, S.S., Guess, T.M., 2018. Electromyography-Driven Forward Dynamics Simulation to Estimate In

Vivo Joint Contact Forces During Normal, Smooth, and Bouncy Gaits. J. Biomech. Eng. 140, 071012. https://doi.org/10.1115/1.4038507

Reijman, M., Pols, H.A.P., Bergink, A.P., Hazes, J.M.W., Belo, J.N., Lievense, A.M., Bierma-Zeinstra, S.M.A., 2006. Body mass index associated with onset and progression of osteoarthritis of the knee but not of the hip: The Rotterdam Study. Ann. Rheum. Dis. 66, 158–162. https://doi.org/10.1136/ard.2006.053538

Röhrle, H., Scholten, R., Sigolotto, C., Sollbach, W., Kellner, H., 1984. Joint forces in the human pelvis-leg skeleton during walking. J. Biomech. 17, 409–424. https://doi.org/10.1016/0021-9290(84)90033-2

Scholz, J.P., Schöner, G., 1999. The uncontrolled manifold concept: identifying control variables for a functional task. Exp. Brain Res. 126, 289–306. https://doi.org/10.1007/s002210050738

Seireg, A., Arvikar, R.J., 1975. The prediction of muscular load sharing and joint forces in the lower extremities during walking. J. Biomech. 8, 89–102. https://doi.org/10.1016/0021-9290(75)90089-5

Serrancolí, G., Kinney, A.L., Fregly, B.J., Font-Llagunes, J.M., 2016. Neuromusculoskeletal Model Calibration Significantly Affects Predicted Knee Contact Forces for Walking. J. Biomech. Eng. 138, 081001. https://doi.org/10.1115/1.4033673

Seth, A., Sherman, M., Reinbolt, J.A., Delp, S.L., 2011. OpenSim: a musculoskeletal modeling and simulation framework for in silico investigations and exchange. Procedia IUTAM 2, 212–232. https://doi.org/10.1016/j.piutam.2011.04.021

Sharma, L., Song, J., Felson, D.T., Cahue, S., Shamiyeh, E., Dunlop, D.D., 2001. The role of knee alignment in disease progression and functional decline in knee osteoarthritis. JAMA 286, 188–95. https://doi.org/10.1001/jama.286.2.188

Sherman, M.A., Seth, A., Delp, S.L., 2013. What is a Moment Arm? Calculating Muscle Effectiveness in Biomechanical Models Using Generalized Coordinates, in: 9th International Conference on Multibody Systems, Nonlinear Dynamics, and Control. ASME. https://doi.org/10.1115/DETC2013-13633

Sherman, M.A., Seth, A., Delp, S.L., 2011. Simbody: multibody dynamics for biomedical research. Procedia IUTAM 2, 241–261. https://doi.org/10.1016/j.piutam.2011.04.023

Simpson, C.S., Sohn, M.H., Allen, J.L., Ting, L.H., 2015. Feasible muscle activation ranges based on inverse dynamics analyses of human walking. J. Biomech. 48, 2990–2997. https://doi.org/10.1016/j.jbiomech.2015.07.037

Smith, C.R., Vignos, M.F., Lenhart, R.L., Kaiser, J., Thelen, D.G., 2016. The Influence of Component Alignment and Ligament Properties on Tibiofemoral Contact Forces in Total Knee Replacement. J. Biomech. Eng. 138, 021017. https://doi.org/10.1115/1.4032464

Sohn, M.H., McKay, J.L., Ting, L.H., 2013. Defining feasible bounds on muscle activation in a redundant biomechanical task: practical implications of redundancy. J. Biomech. 46, 1363–1368. https://doi.org/10.1016/j.jbiomech.2013.01.020

Spitzer, V.M., Whitlock, D.G., 1998. The visible human dataset: The anatomical platform for human simulation. Anat. Rec. 253, 49–57. https://doi.org/10.1002/(SICI)1097-0185(199804)253:2<49::AID-AR8>3.0.CO;2-9

Steele, K.M., DeMers, M.S., Schwartz, M.H., Delp, S.L., 2012. Compressive tibiofemoral force during crouch gait. Gait Posture 35, 556–560. https://doi.org/10.1016/j.gaitpost.2011.11.023

Thacker, B.H., 2001. ASME Standards Committee on Verification and Validation in Computational Solid Mechanics.

Thelen, D.G., Won Choi, K., Schmitz, A.M., 2014. Co-Simulation of Neuromuscular Dynamics and Knee Mechanics During Human Walking. J. Biomech. Eng. 136, 021033. https://doi.org/10.1115/1.4026358

Tikhonov, A.N., Glasko, V.B., 1965. Use of the regularization method in non-linear problems. USSR Comput. Math. Math. Phys. 5, 93–107. https://doi.org/10.1016/0041-5553(65)90150-3

Todorov, E., Jordan, M.I., 2002. Optimal feedback control as a theory of motor coordination. Nat. Neurosci. 5, 1226–1235. https://doi.org/10.1038/nn963

Valente, G., 2013. Subject-specific musculoskeletal models of the lower limbs for the prediction of skeletal loads during motion. Alma Mater Studiorum – Università di Bologna.

Valente, G., Martelli, S., Taddei, F., Farinella, G., Viceconti, M., 2012. Muscle discretization affects the loading transferred to bones in lower-limb musculoskeletal models. Proc. Inst. Mech. Eng. Part H J. Eng. Med. 226, 161–169. https://doi.org/10.1177/0954411911425863

Valente, G., Pitto, L., Stagni, R., Taddei, F., 2015. Effect of lower-limb joint models on subject-specific musculoskeletal models and simulations of daily motor activities. J. Biomech. 48, 4198–4205. https://doi.org/10.1016/j.jbiomech.2015.09.042

Valente, G., Pitto, L., Testi, D., Seth, A., Delp, S.L., Stagni, R., Viceconti, M., Taddei, F., 2014. Are Subject-Specific Musculoskeletal Models Robust to the Uncertainties in Parameter Identification? PLoS One 9, e112625. https://doi.org/10.1371/journal.pone.0112625

Valero-Cuevas, F.J., Cohn, B.A., Yngvason, H.F., Lawrence, E.L., 2015. Exploring the high-dimensional structure of muscle redundancy via subject-specific and generic musculoskeletal models. J. Biomech. 48, 2887–2896. https://doi.org/10.1016/j.jbiomech.2015.04.026

Valero-Cuevas, F.J., Zajac, F.E., Burgar, C.G., 1998. Large index-fingertip forces are produced by subject-independent patterns of muscle excitation. J. Biomech. 31, 693–703. https://doi.org/10.1016/S0021-9290(98)00082-7

Valle, M.S., Casabona, A., Sgarlata, R., Garozzo, R., Vinci, M., Cioni, M., 2006. The pendulum test as a tool to evaluate passive knee stiffness and viscosity of patients with rheumatoid arthritis. BMC Musculoskelet. Disord. 7, 89. https://doi.org/10.1186/1471-2474-7-89

Viceconti, M., 2011. Multiscale Modeling of the Skeletal System. Cambridge University Press, Cambridge. https://doi.org/10.1017/CBO9781139049627

Viceconti, M., Taddei, F., Cristofolini, L., Martelli, S., Falcinelli, C., Schileo, E., 2012. Are spontaneous fractures possible? An example of clinical application for personalised, multiscale neuro-musculo-skeletal modelling. J. Biomech. 45, 421–426. https://doi.org/10.1016/j.jbiomech.2011.11.048

Vos, E.J., Mullender, M.G., van Ingen Schenau, G.J., 1990. Electromechanical delay in the vastus lateralis muscle during dynamic isometric contractions. Eur. J. Appl. Physiol. Occup. Physiol. 60, 467–471. https://doi.org/10.1007/BF00705038

Waller, C., Hayes, D., Block, J.E., London, N.J., 2011. Unload it: the key to the treatment of knee osteoarthritis. Knee Surgery, Sport. Traumatol. Arthrosc. 19, 1823–1829. https://doi.org/10.1007/s00167-011-1403-6

Walter, J.P., Kinney, A.L., Banks, S.A., D'Lima, D.D., Besier, T.F., Lloyd, D.G., Fregly, B.J., 2014. Muscle Synergies May Improve Optimization Prediction of Knee Contact Forces During Walking. J. Biomech. Eng. 136, 021031. https://doi.org/10.1115/1.4026428

Waters, R.L., Mulroy, S., 1999. The energy expenditure of normal and pathologic gait. Gait Posture 9, 207–231. https://doi.org/10.1016/S0966-6362(99)00009-0

Winby, C.R., Lloyd, D.G., Besier, T.F., Kirk, T.B., 2009. Muscle and external load contribution to knee joint contact loads during normal gait. J. Biomech. 42, 2294–2300. https://doi.org/10.1016/j.jbiomech.2009.06.019

Winter, D.A., 2009. Biomechanics and Motor Control of Human Movement. John Wiley & Sons, Inc., Hoboken, NJ, USA. https://doi.org/10.1002/9780470549148

Wu, G., Siegler, S., Allard, P., Kirtley, C., Leardini, A., Rosenbaum, D., Whittle, M., D'Lima, D.D., Cristofolini, L., Witte, H., Schmid, O., Stokes, I., 2002. ISB recommendation on definitions of joint coordinate system of various joints for the reporting of human joint motion—part I: ankle, hip, and spine. J. Biomech. 35, 543–548. https://doi.org/10.1016/S0021-9290(01)00222-6

Yamaguchi, G.T., 2001a. Dynamic Modeling of Musculoskeletal Motion. Springer US, Boston, MA. https://doi.org/10.1007/978-0-387-28750-8

Yamaguchi, G.T., 2001b. Appendix B: Human Lower Extrimities Muscle Parameters, in: Dynamic Modeling of Musculoskeleton Motion. Springer US, Boston, MA, pp. 243–246. https://doi.org/10.1007/978-0-387-28750-8

Yamaguchi, G.T., Zajac, F.E., 1989. A planar model of the knee joint to characterize the knee extensor mechanism. J. Biomech. 22, 1–10. https://doi.org/10.1016/0021-9290(89)90179-6

Zajac, F.E., 1989. Muscle and tendon: properties, models, scaling, and application to biomechanics and motor control. Crit. Rev. Biomed. Eng. 17, 359–411. https://doi.org/10.1016/j.pcad.2015.11.006

Zajac, F.E., Neptune, R.R., Kautz, S.A., 2002. Biomechanics and muscle coordination of human walking. Part I: introduction to concepts, power transfer, dynamics and simulations. Gait Posture 16, 215–32. https://doi.org/10.1016/S0966-6362(02)00068-1

Zhou, S., Lawson, D.L., Morrison, W.E., Fairweather, I., 1995. Electromechanical delay in isometric muscle contractions evoked by voluntary, reflex and electrical stimulation. Eur. J. Appl. Physiol. Occup. Physiol. 70, 138–145. https://doi.org/10.1007/BF00361541

APPENDICES

A.1 Experimental data

Participant 1 (p01)

Ethical approval for the data collection was provided by the University Research Ethics Committee at the University of Sheffield. Skin marker trajectories were captured at 100 Hz with an 8-camera motion capture system (MX, Vicon Motion Systems Ltd, Oxford, UK). The ground reaction forces were measured at 1000 Hz with two strain-gauge force platforms (Bertec Corp., Columbus, OH, USA).

Participant 2 (p02)

The dataset was provided through the Knee Grand Challenge (Fregly et al., 2012). The marker trajectory data were originally sampled at 120 Hz, but provided after being resampled to 200 Hz using a cubic-spline interpolation and filtered using a 15 Hz low-pass, 4th order Butterworth filter. The ground reaction force data were originally sampled at 3840 Hz, but provided after being resampled to 1200 Hz using a cubic-spline interpolation and filtered using a 100 Hz low-pass, 4th order Butterworth filter.

Participant 3 (p03)

The data were previously collected as part of the MD-Paedigree project (EC 7th FP, ICT Programme, Ref. No. 600932) and details on the data collection were published earlier (Prinold et al., 2016). Skin marker trajectories were captured at 100 Hz with a 6-camera motion capture system (Smart-DX, BTS S.p.A., Milan, Italy). The ground reaction forces were measured at 1000 Hz with two piezoelectric force platforms (Kistler Group, Winterthur, Switzerland).

Participant 4 (p04)

The data were provided as part of the MultiSim project (EPSRC Frontier Engineering Awards, Ref. No. EP/K03877X/1) for which the data collection was approved by the NHS research ethics committee. Skin marker trajectories were captured at 100 Hz with a 12-camera motion capture system (Vantage 5, Vicon Motion Systems Ltd, Oxford, UK). The ground reaction forces were measured at 1000 Hz with two piezoelectric force platforms (Kistler Group, Winterthur, Switzerland).

Specifications of the skin markers included for the different participants can be found in *Table A.1.1*.

Table A.1.1: The skin markers and their anatomical locations for the different datasets

Acronym	Location	p01	p02	p03	p04
C7	Spinous process of the 2nd thoracic vertebrae	x			
T10	Spinous Process of the 10th thoracic vertebrae	x^M			
SHO	Acromioclavicular joint	x^M			
CLAV	Anterior, superior aspect of sternum	x^M			
STRN	Xiphoid process of sternum	x			
RASI	Right anterior, superior iliac spine	x^M			
LASI	Left anterior, superior iliac spine	x	x	x	x
RPSI	Right posterior, superior iliac spine	x	x	x	x
LPSI	Left posterior, superior iliac spine	x	x	x	x
THI	Lateral aspect of thigh - on wand	x	x	x	x
TC1	First marker of technical cluster on thigh				x^M
TC2	Second marker of technical cluster on thigh	x^M	x^M	x^M	x^M
TC3	Third marker of technical cluster on thigh	x^M	x^M		x^M
KNE	Lateral femoral epicondyle	x^M	x^M		x^M
MFC	Medial femoral epicondyle	x	x^S	x	x^S
SC1	First marker of technical cluster on shank	x^S		x^S	x^S
SC2	Second marker of technical cluster on shank	x^M	x^M	x^M	x^M
SC3	Third marker of technical cluster on shank		x^M		
TIB	Lateral aspect of shank - on wand		x^M		
HFB	Lateral aspect of the head of the fibula	x^M			x
MMA	Medial malleolus of right ankle			x	x
ANK	Lateral malleolus of right ankle	x^S	x^S	x^S	x^S
HEE	Posterior aspect of the calcaneus or equivalent on shoe - at approximate toe height	x	x^S	x	x^S
TOE	In between second and third metatarsal heads/above second metatarsal head or equivalent on shoe - aligned with RHEE	x	x	x	x
D1M	Medial aspect of the first metatarsal head	x^M	x	x	x
D5M	Lateral aspect of the fifth metatarsal head	x			x^S
TTB	Tibial tuberosity	x		x^S	x^S

^{S}: Static trials only, ^{M}: Movement trials only

A.2 Trajectories of generalized coordinates
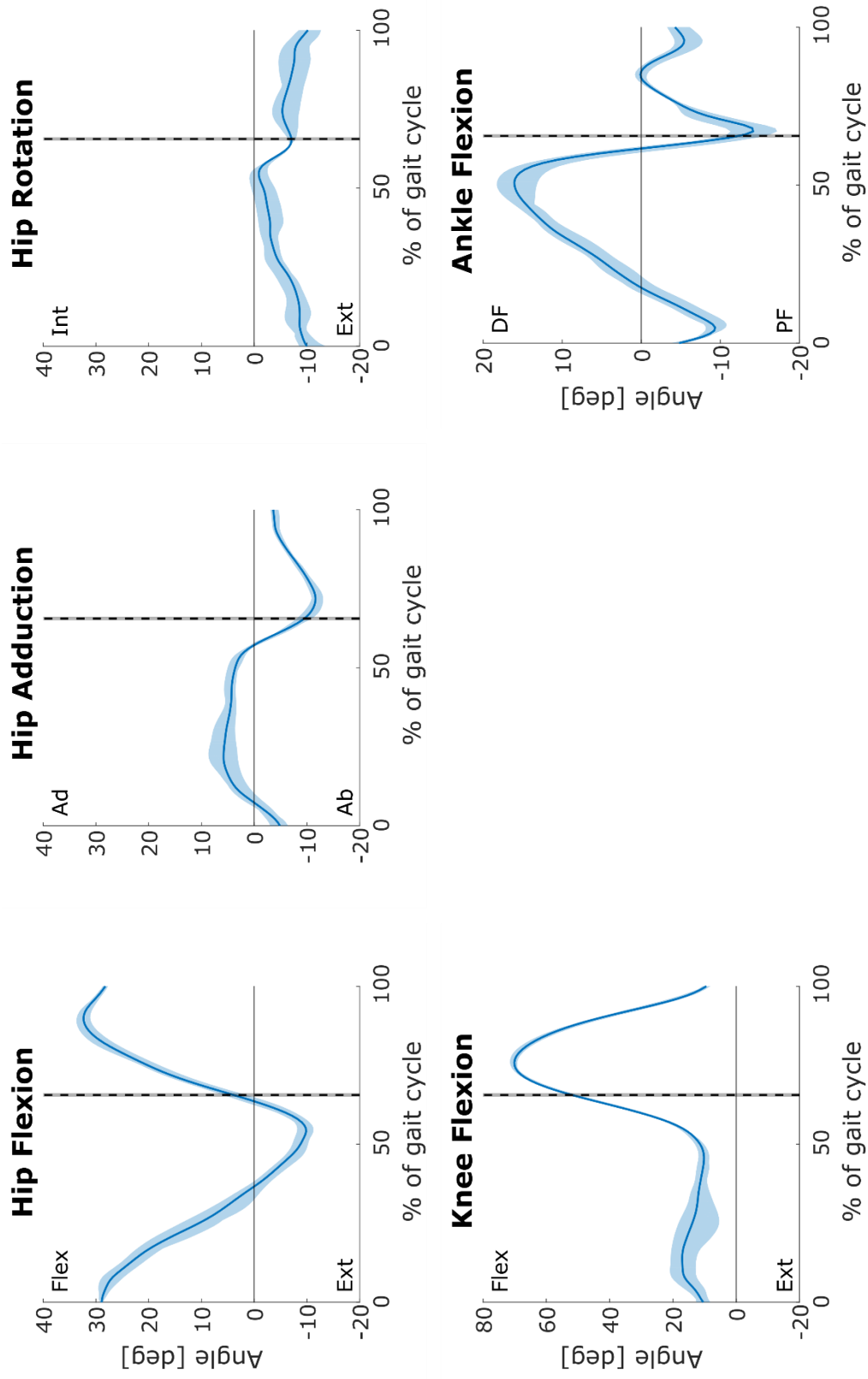
Figure A.2.1: Generalized coordinate trajectories of *p01* for the trials at a slow walking speed; mean (solid line) and range (shaded area) values are shown in degrees.
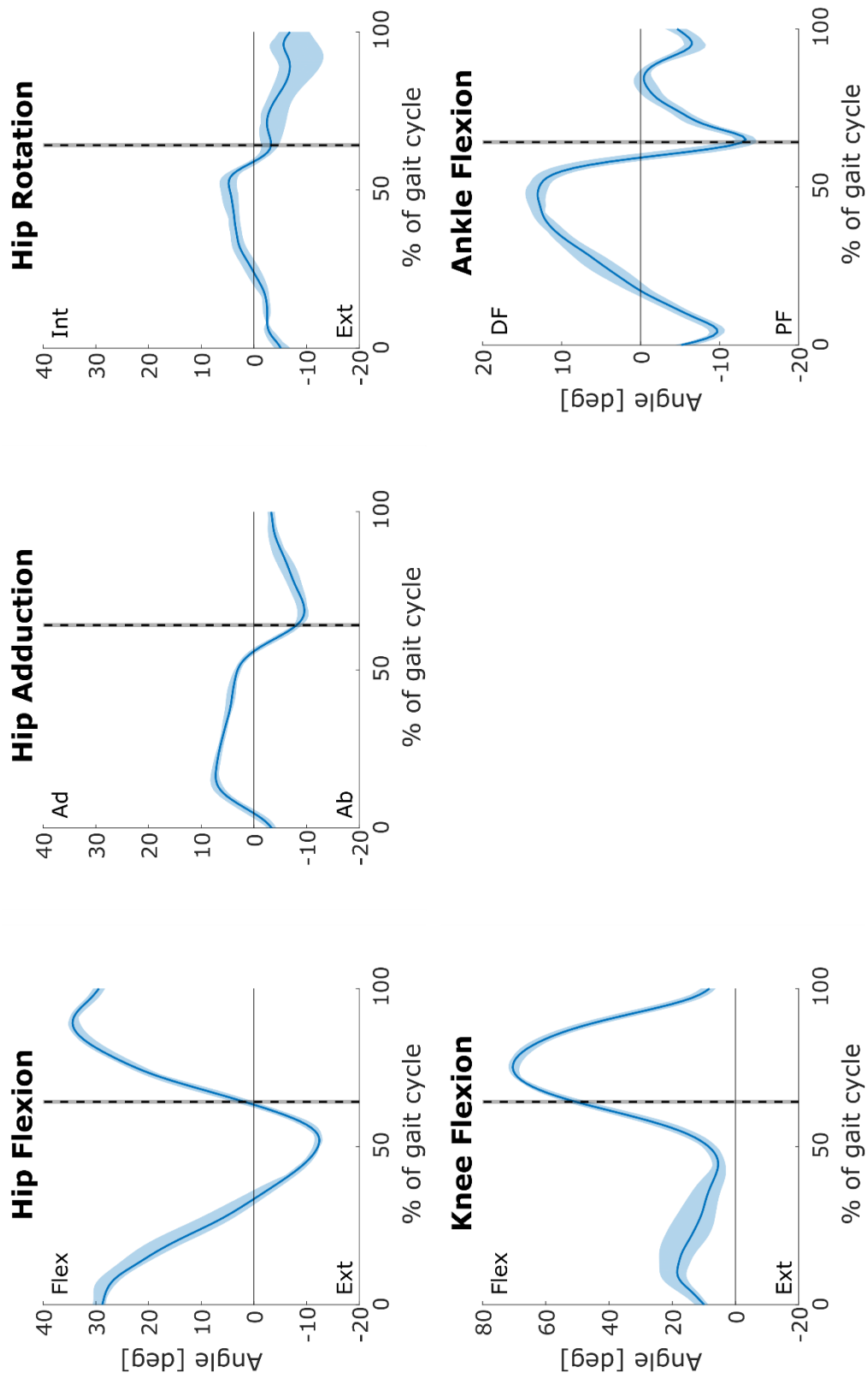
Figure A.2.2: Generalized coordinate trajectories of *p01* for the trials at a self-selected walking speed; mean (solid line) and range (shaded area) values are shown in degrees.
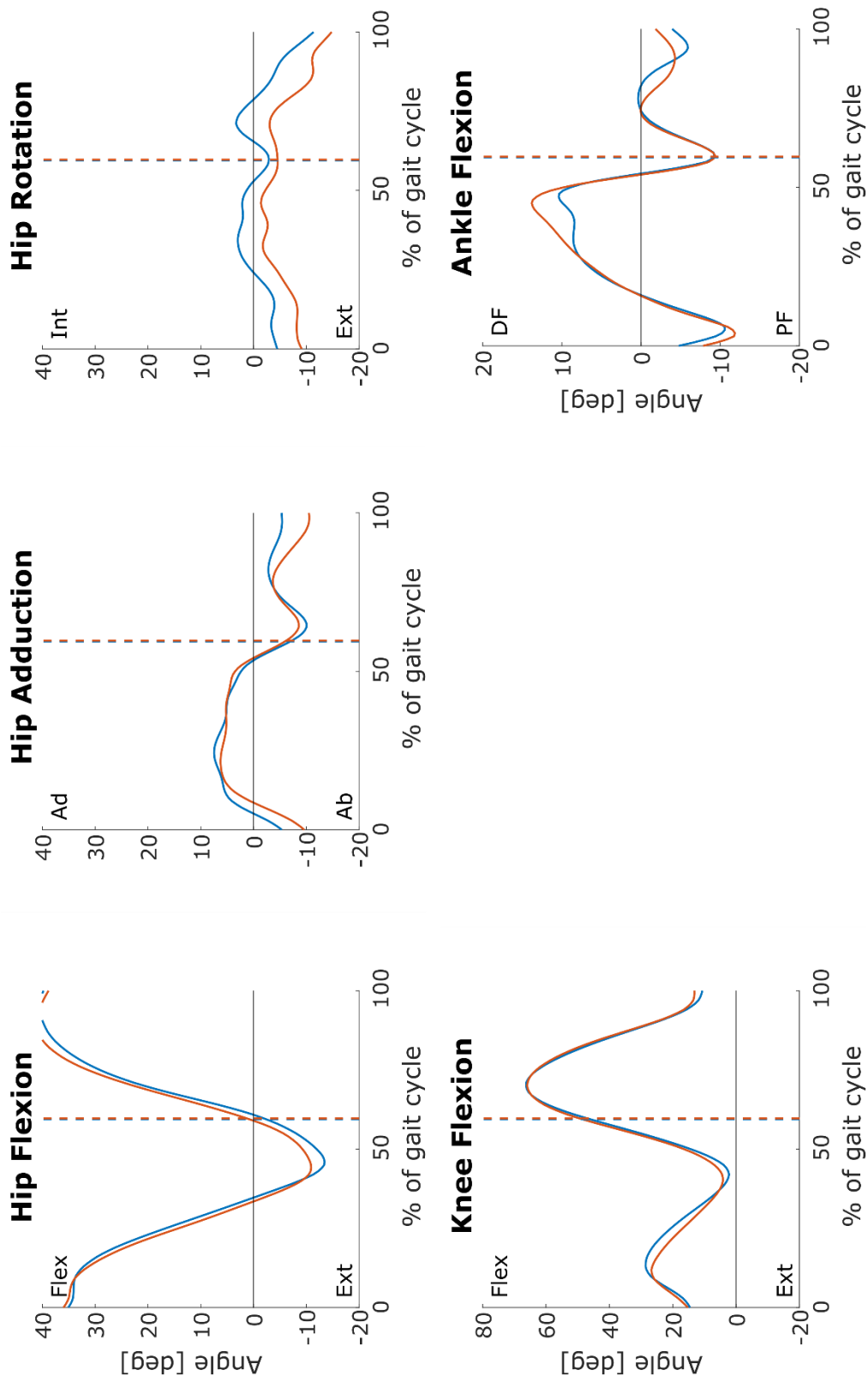
Figure A.2.3: Generalized coordinate trajectories of *p01* for the trials at a fast walking speed values are shown in degrees.
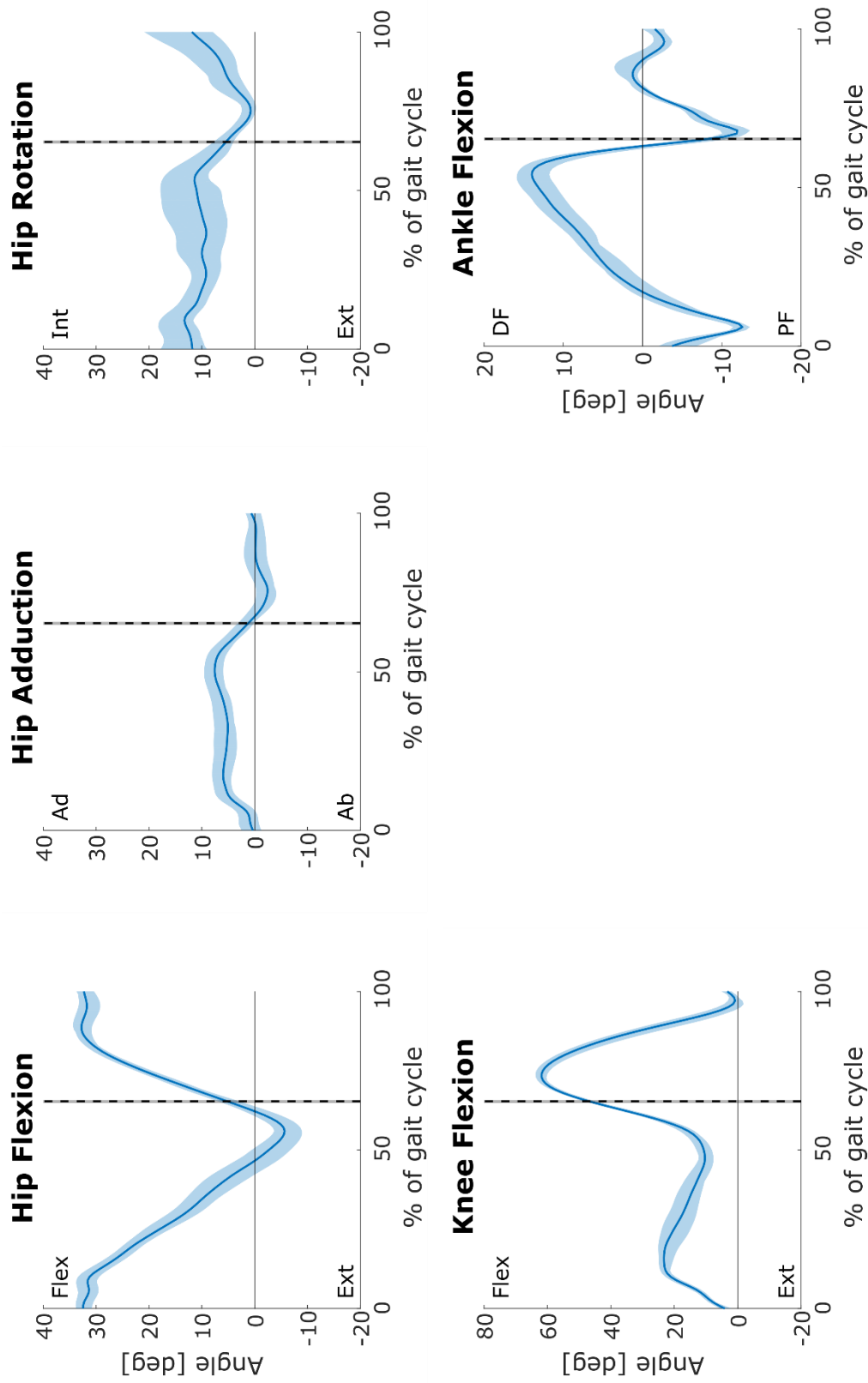
Figure A.2.4: Generalized coordinate trajectories of *p02*; mean (solid line) and range (shaded area) values are shown in degrees.
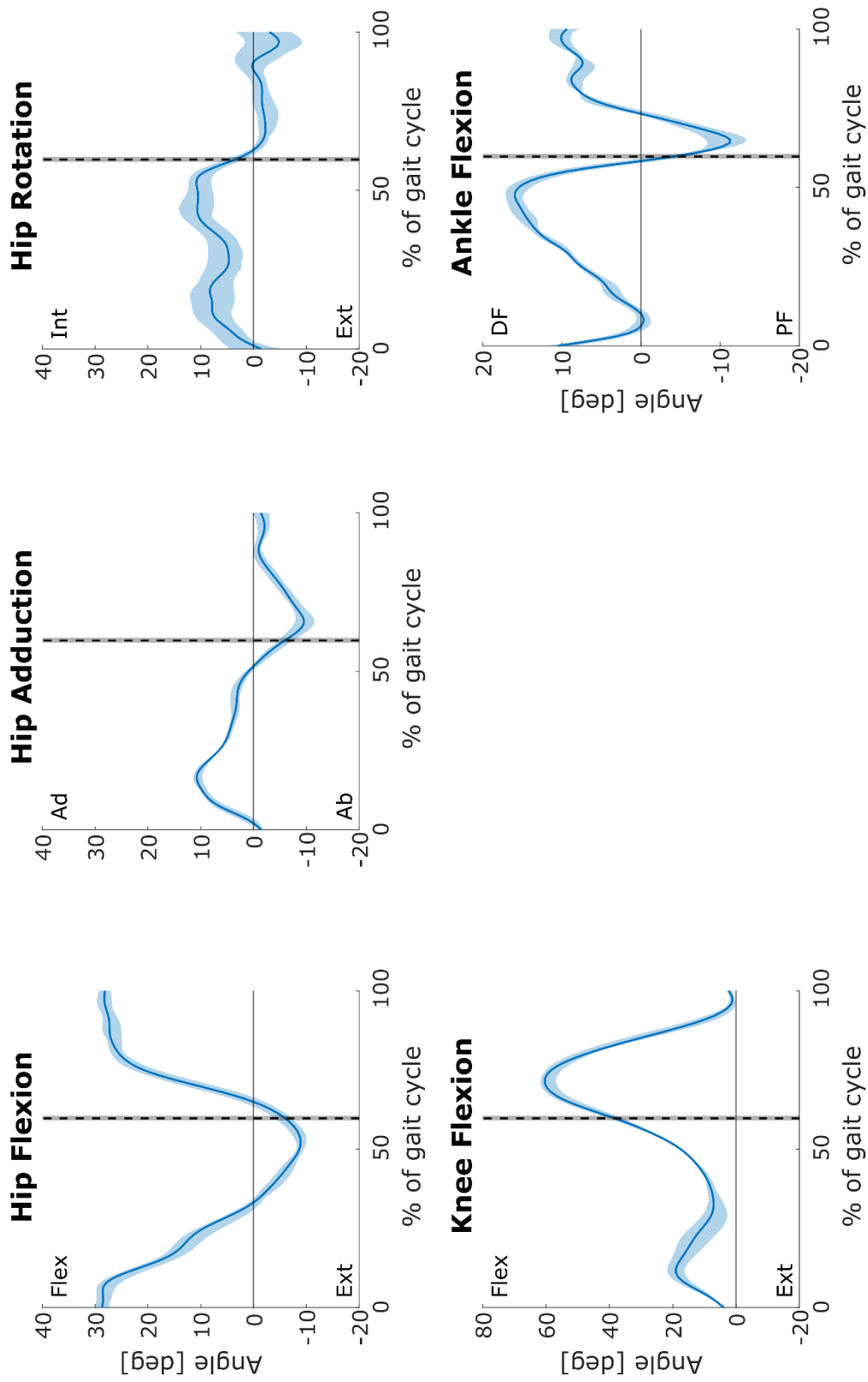
Figure A.2.5: Generalized coordinate trajectories of *p03*; mean (solid line) and range (shaded area) values are shown in degrees.
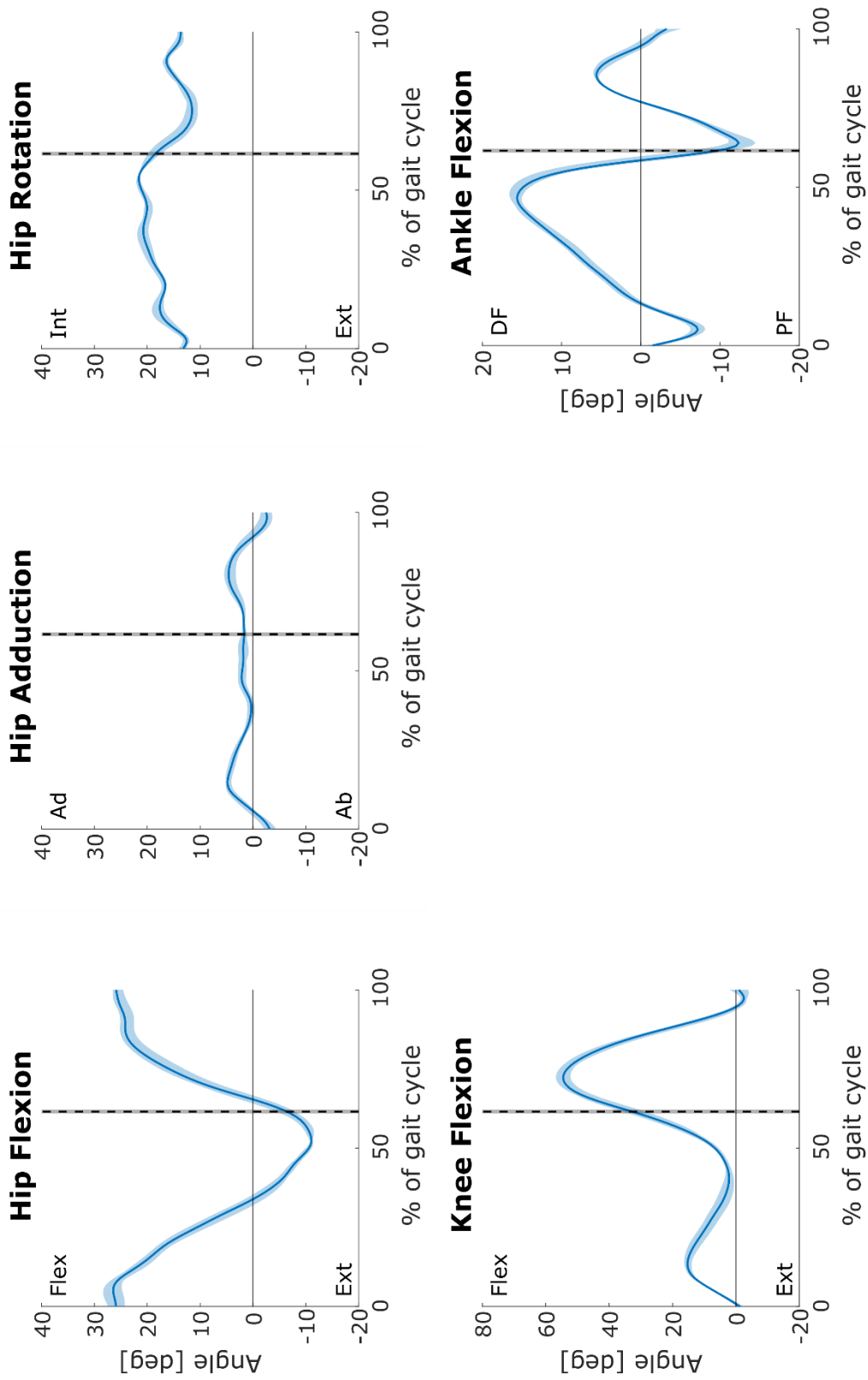
Figure A.2.6: Generalized coordinate trajectories of *p04* for the trials at a slow walking speed; mean (solid line) and range (shaded area) values are shown in degrees.
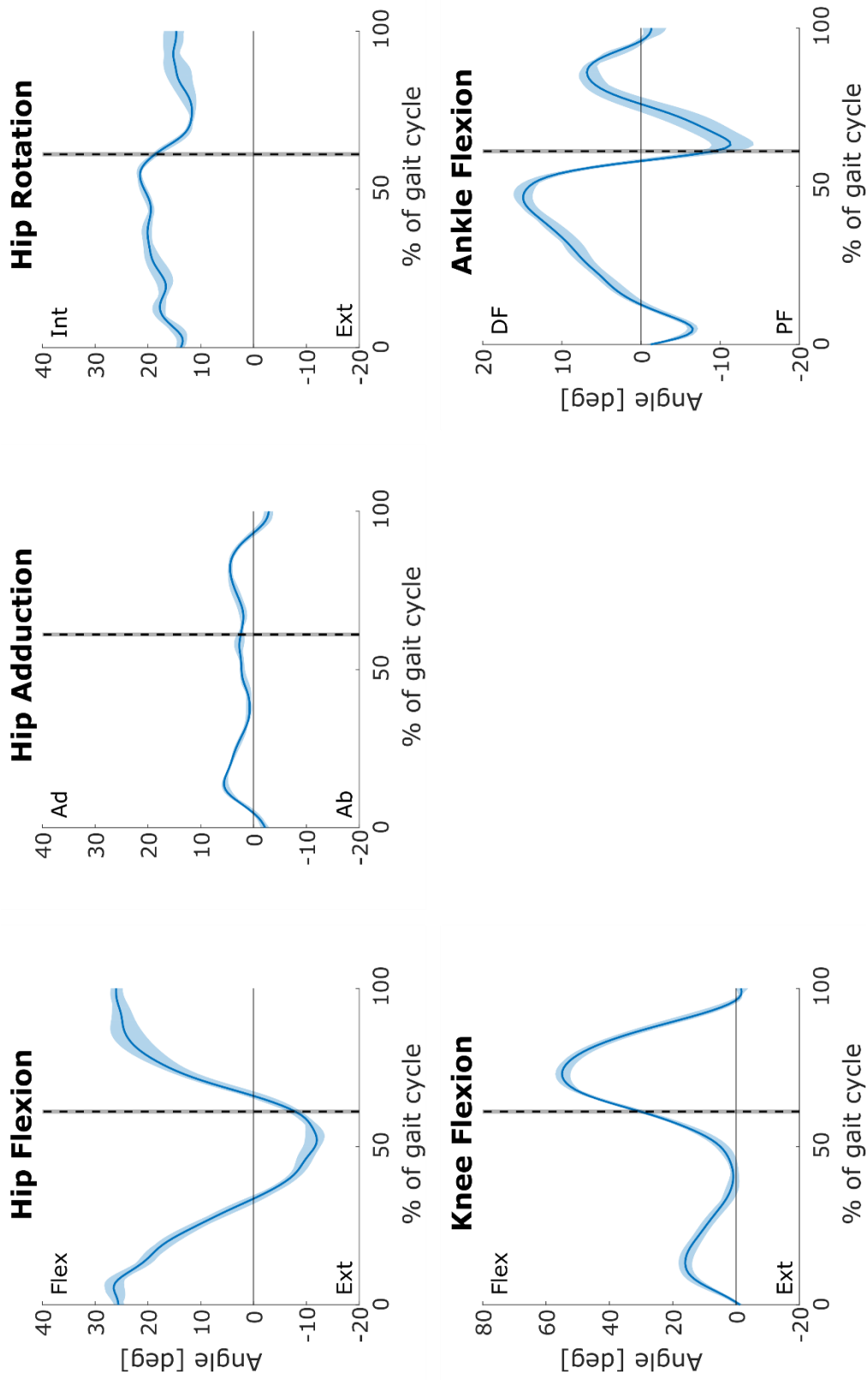
Figure A.2.7: Generalized coordinate trajectories of *p04* for the trials at a self-selected walking speed; mean (solid line) and range (shaded area) values are shown in degrees.
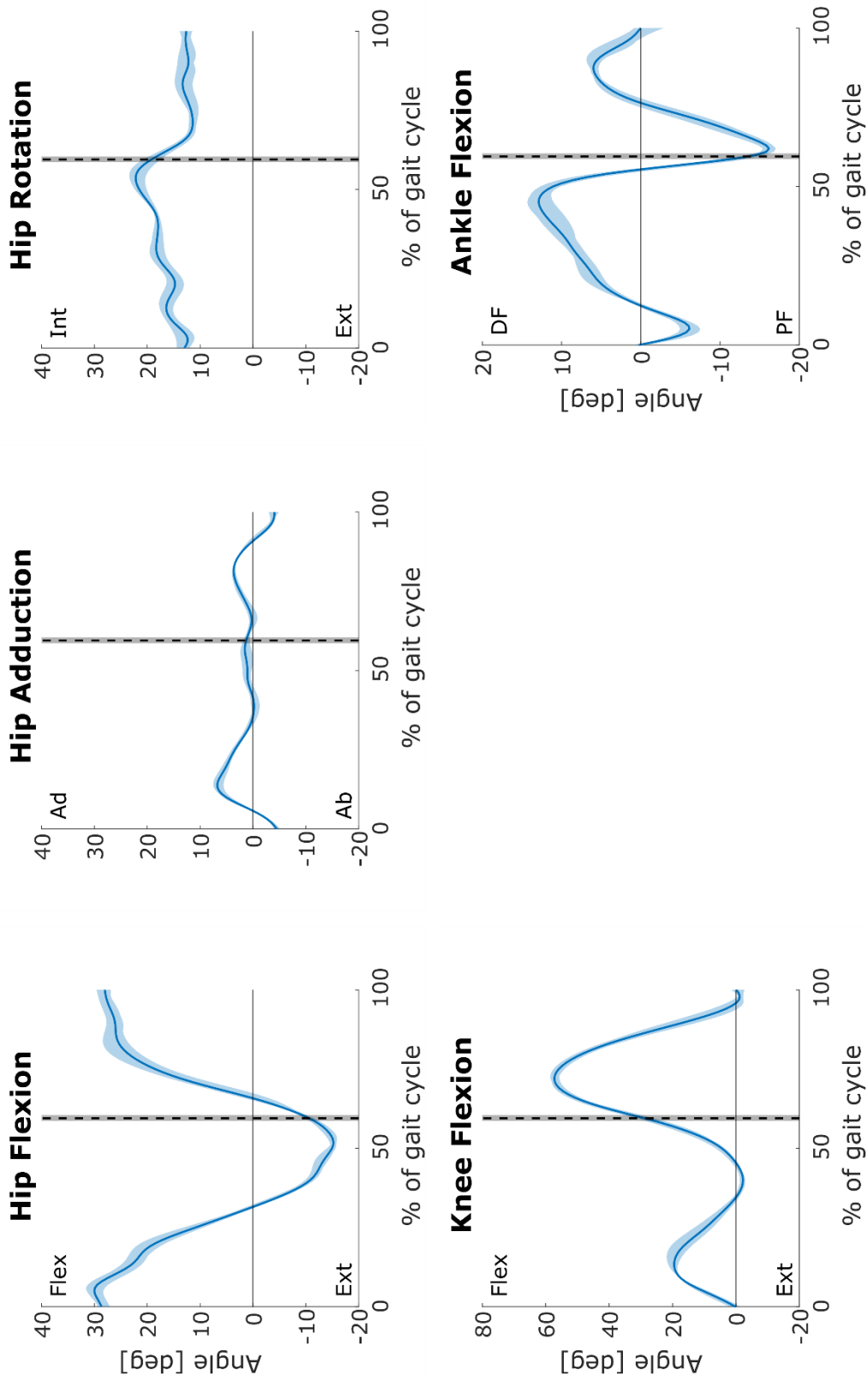
Figure A.2.8: Generalized coordinate trajectories of *p04* for the trials at a fast walking speed; mean (solid line) and range (shaded area) values are shown in degrees.
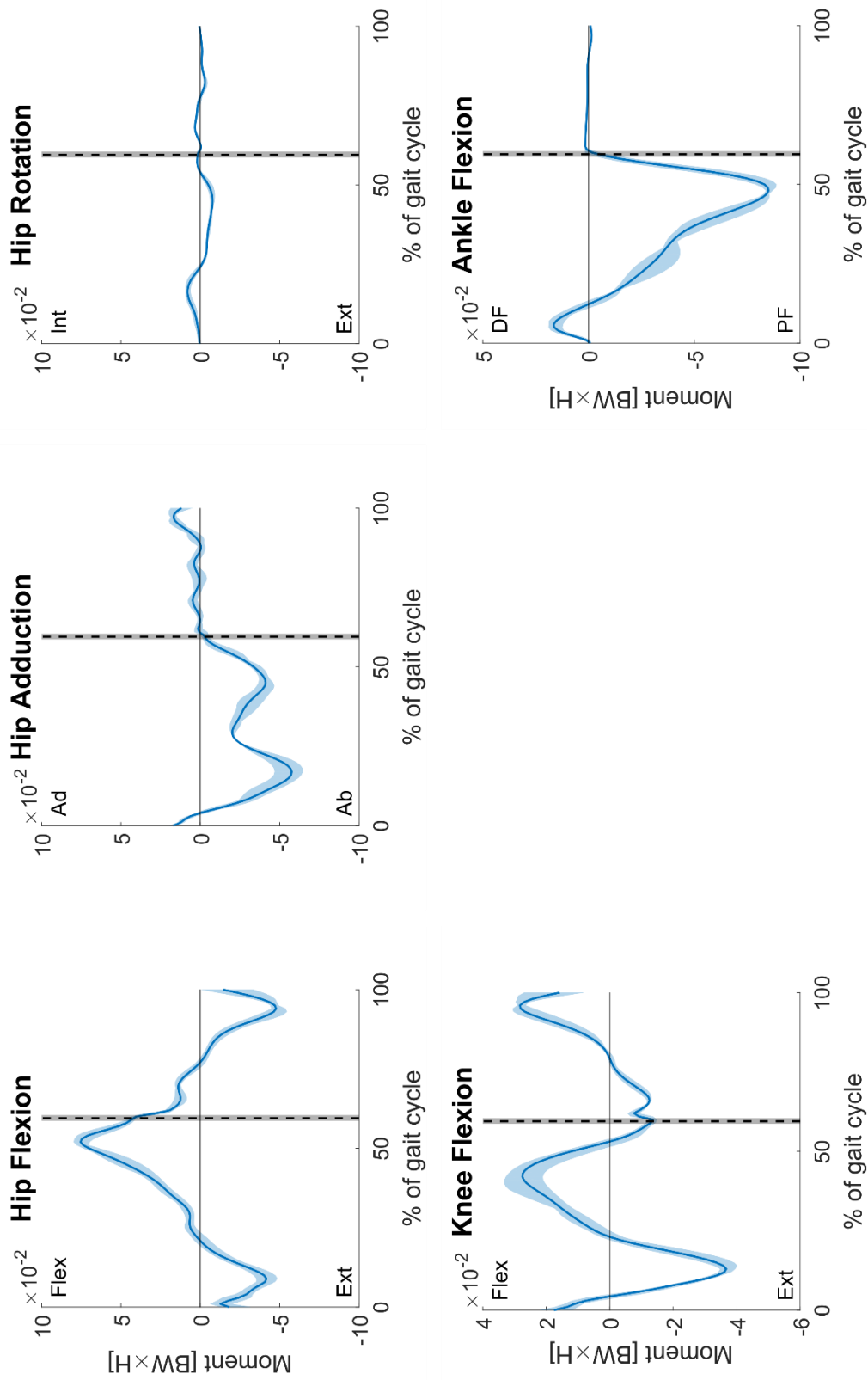
A.3 Trajectories of generalized torques
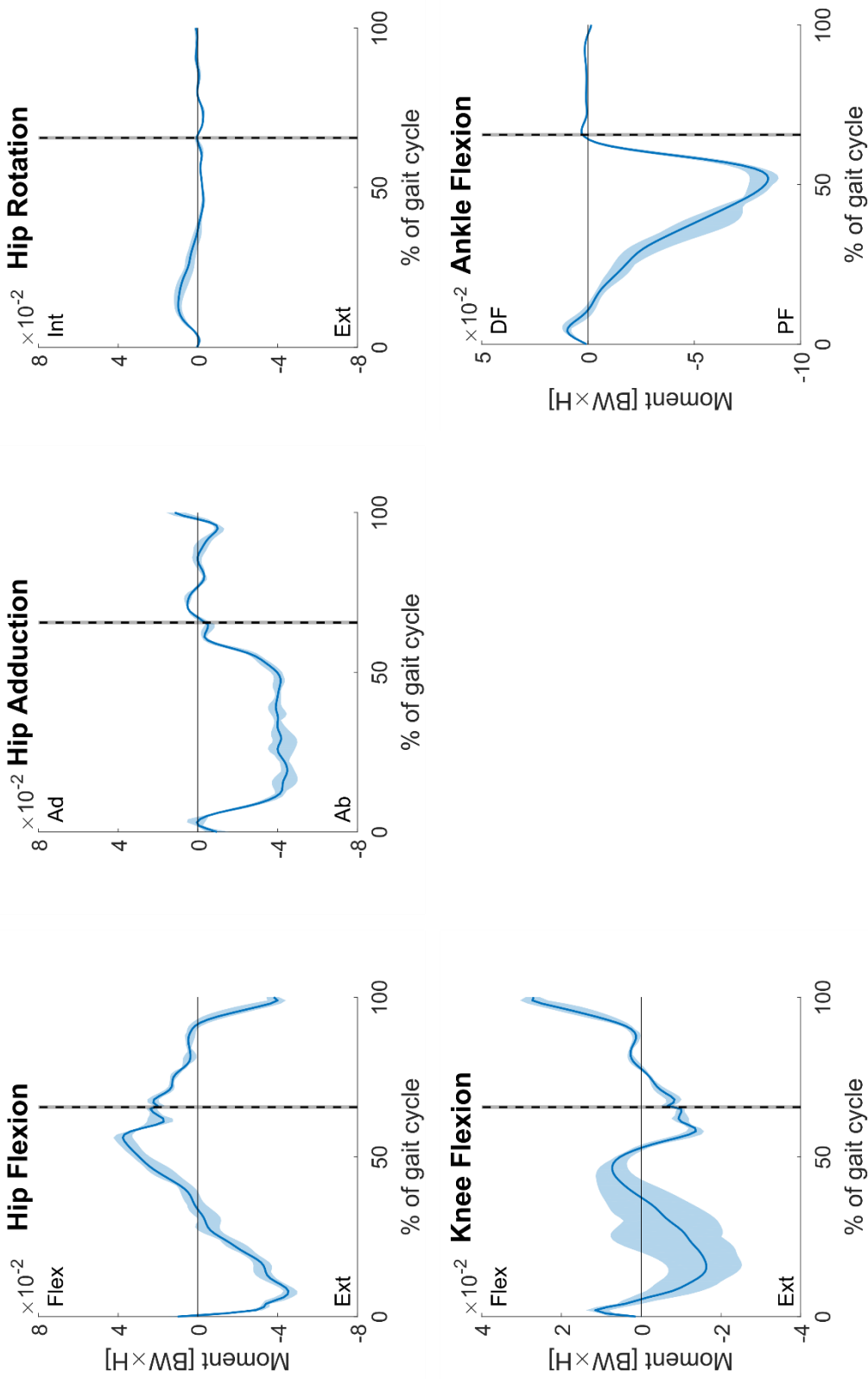
Figure A.3.1: Generalized moment trajectories at the hip, knee and ankle of *p01* for the trials at a slow walking speed; mean (solid line) and range (shaded area) values are shown in bodyweight × height (BW×H).
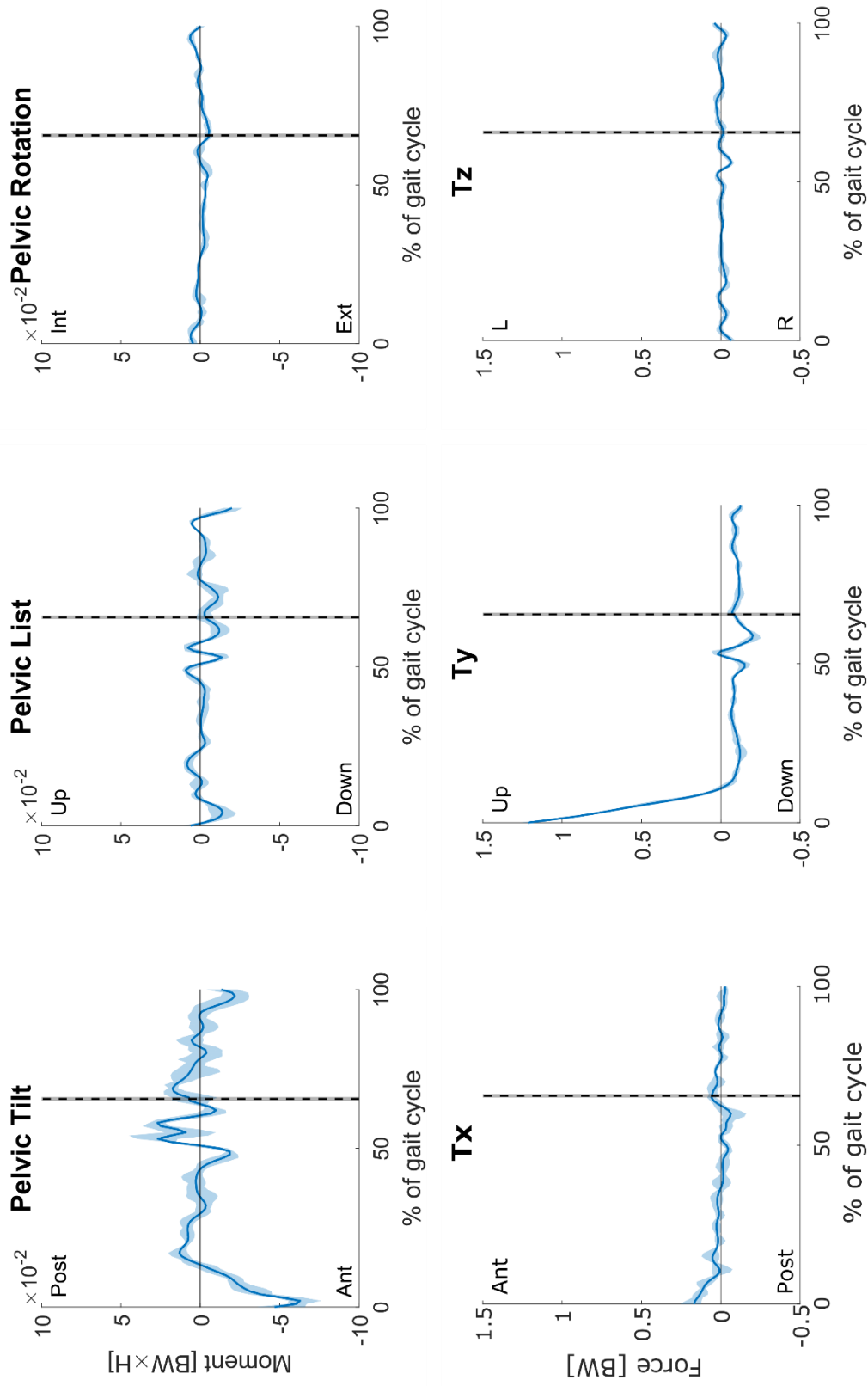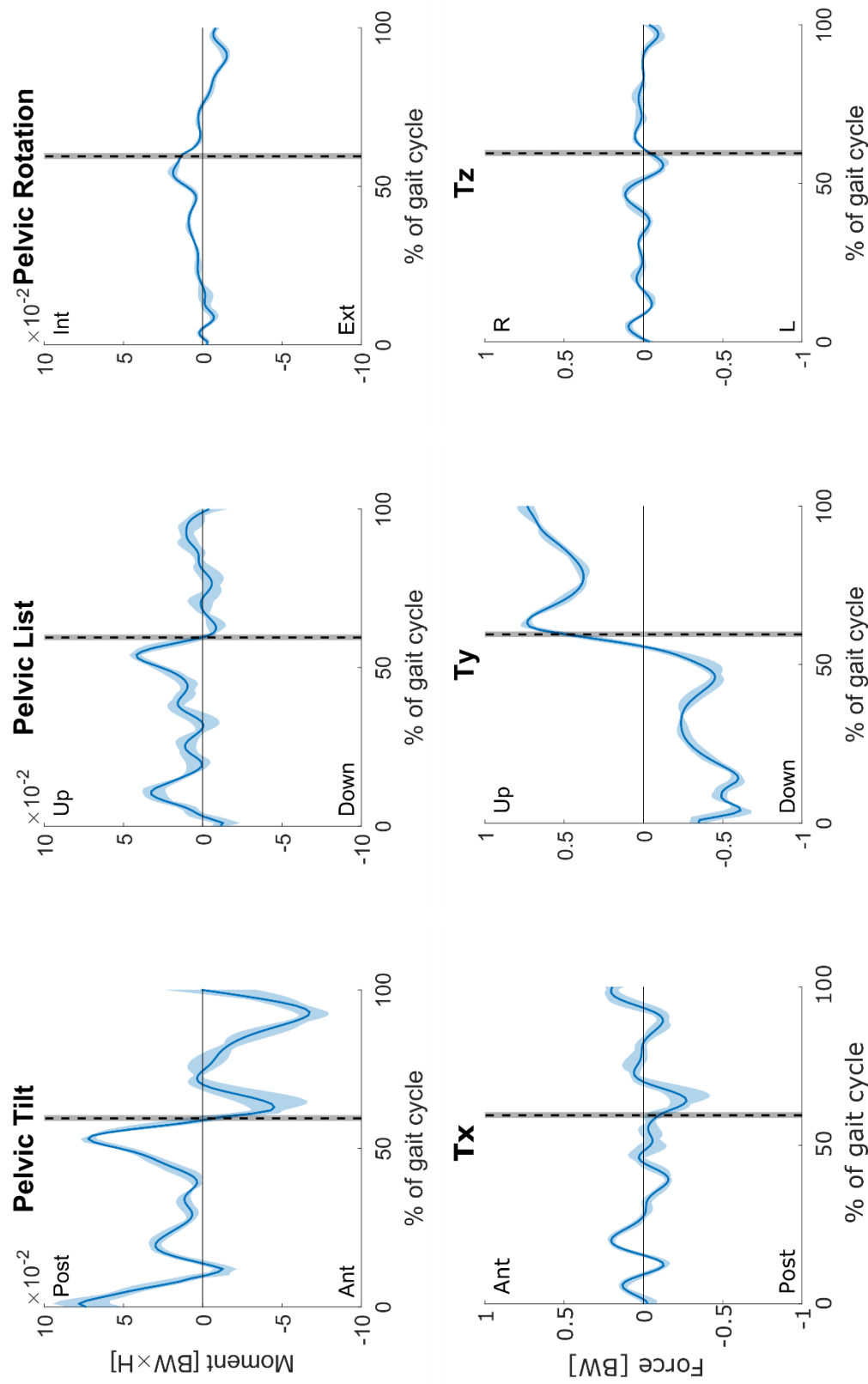
Figure A.3.2: Generalized moment and force trajectories at the ground-pelvis joint of *p01* for the trials at a slow walking speed; mean (solid line) and range (shaded area) values are shown in bodyweight × height (BW×H) for moments and bodyweight (BW) for forces.
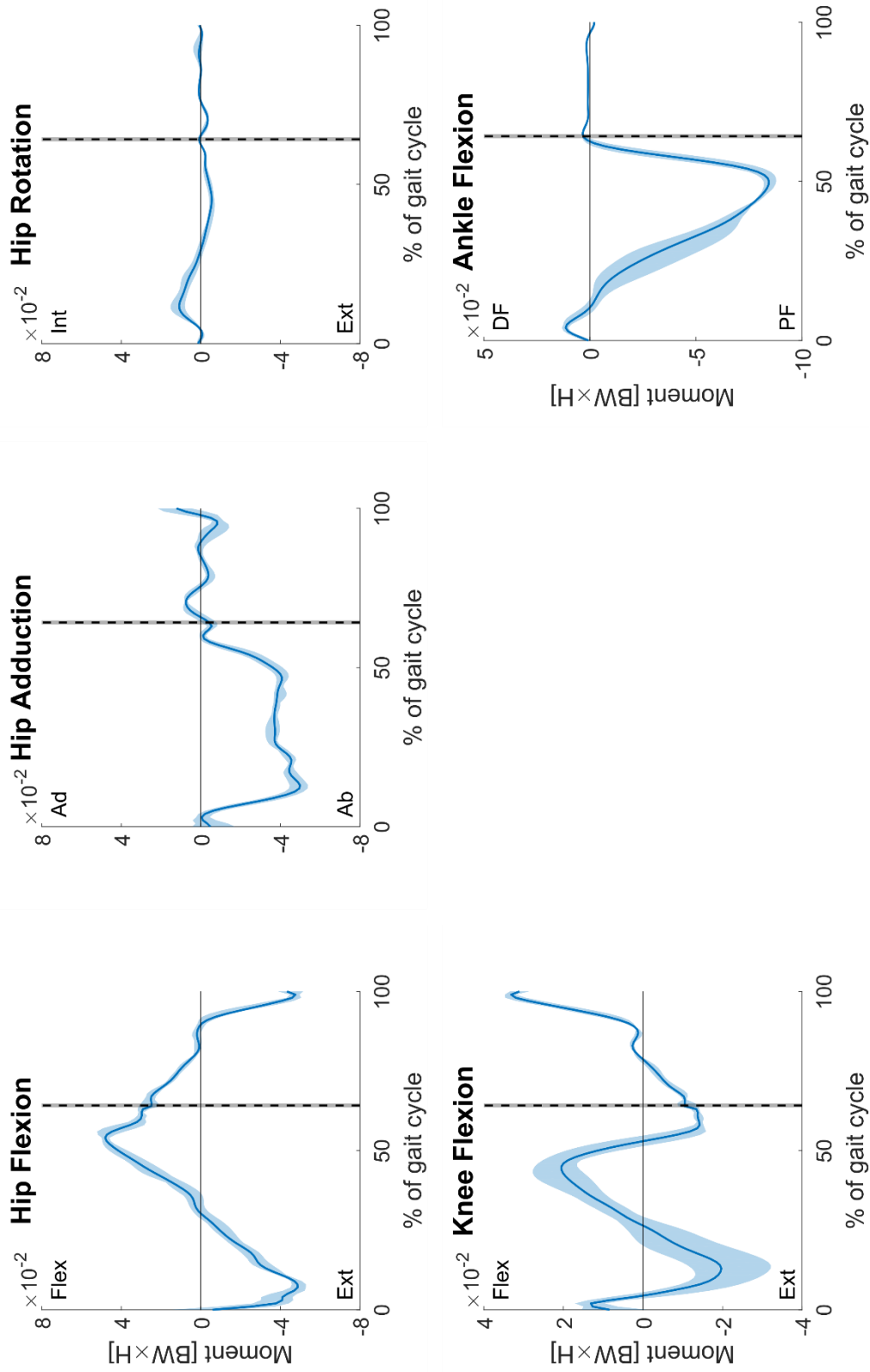
Figure A.3.3: Generalized moment trajectories at the hip, knee and ankle of *p01* for the trials at a self-selected walking speed; mean (solid line) and range (shaded area) values are shown in bodyweight × height (BW×H).
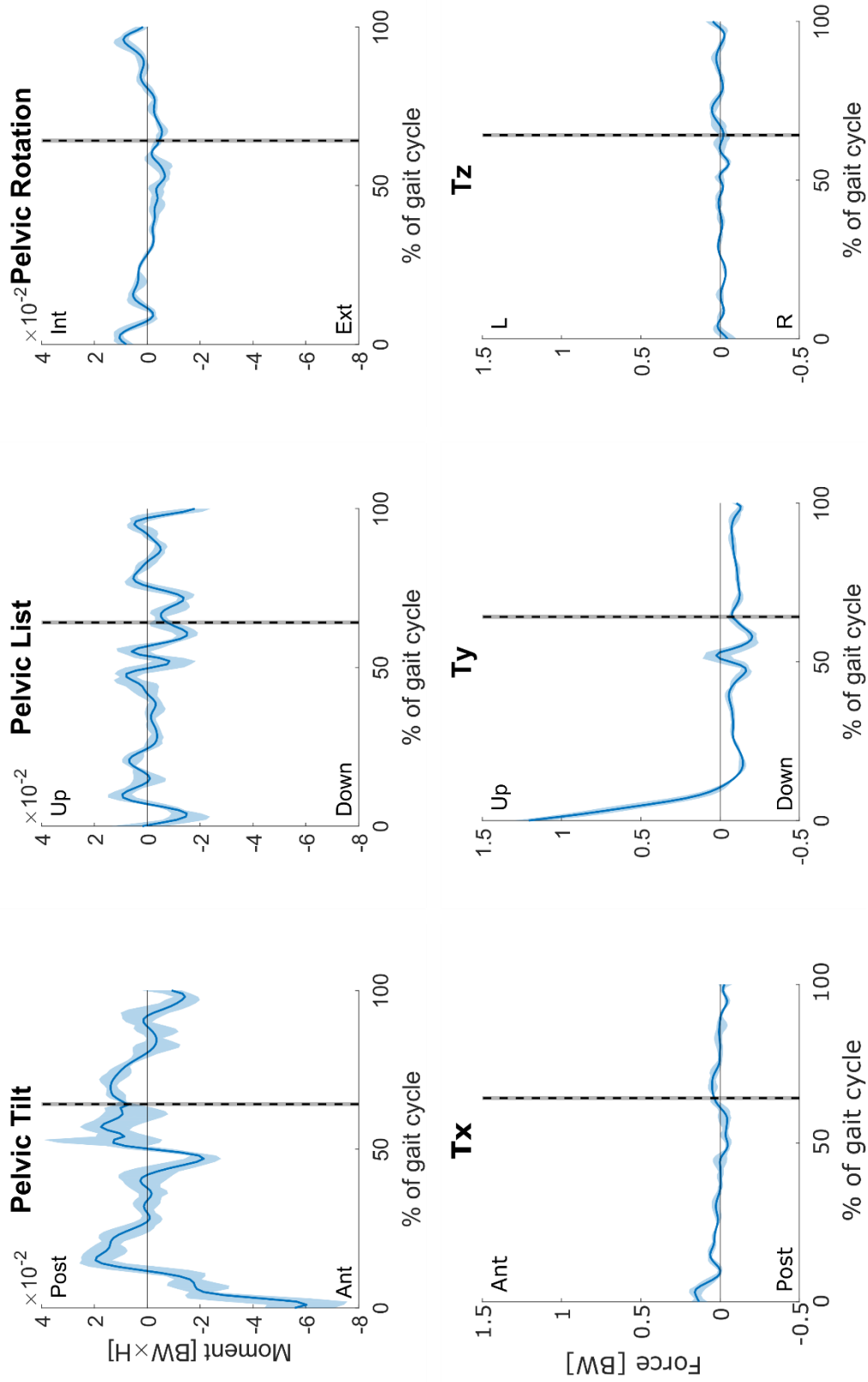
Figure A.3.4: Generalized moment and force trajectories at the ground-pelvis joint of *p01* for the trials at a self-selected walking speed; mean (solid line) and range (shaded area) values are shown in bodyweight × height (BW×H) for moments and bodyweight (BW) for forces.
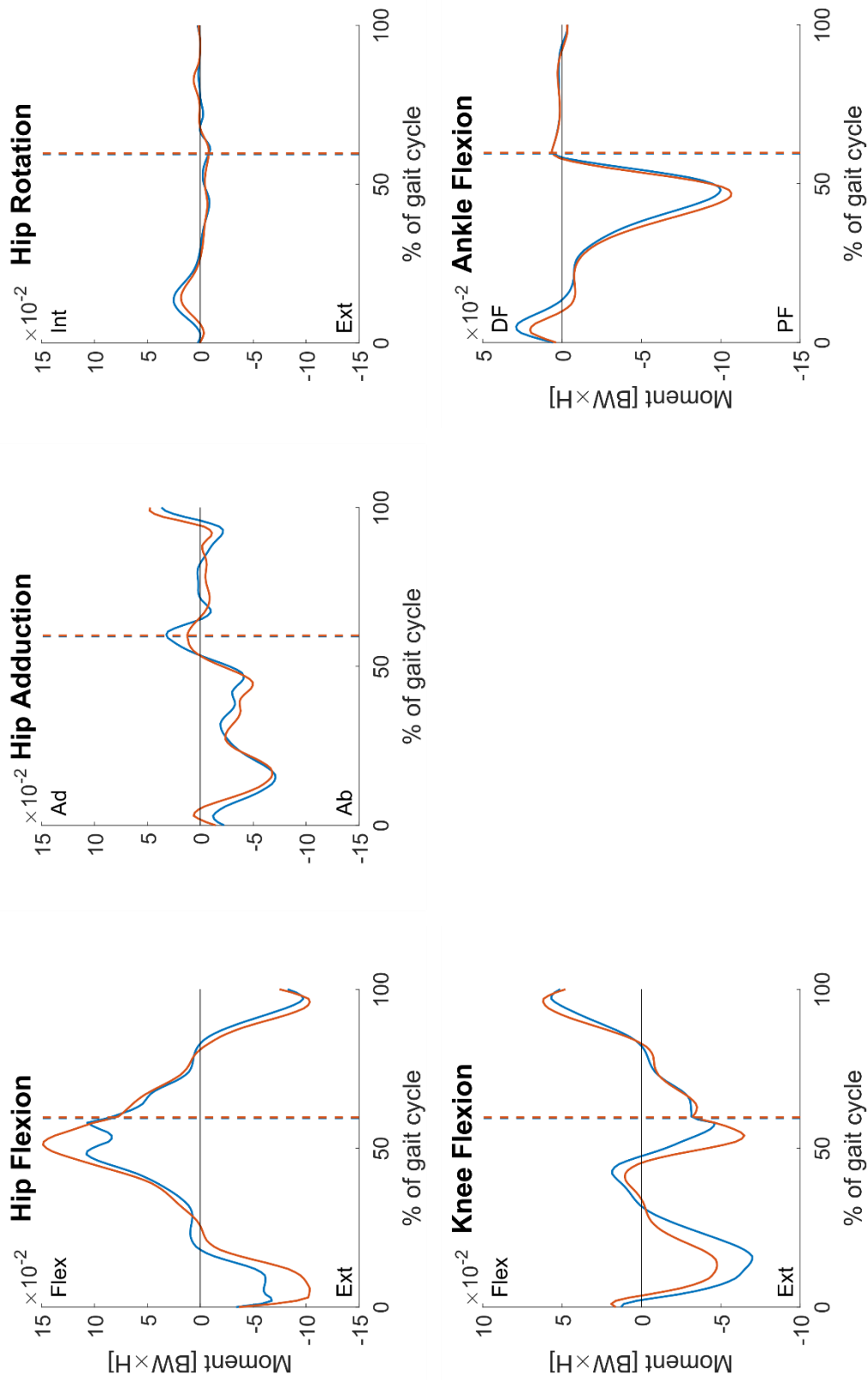
Figure A.3.5: Generalized moment trajectories at the hip, knee and ankle of *p01* for the trials at a fast walking speed; values for each trial are shown in bodyweight × height (BW×H).
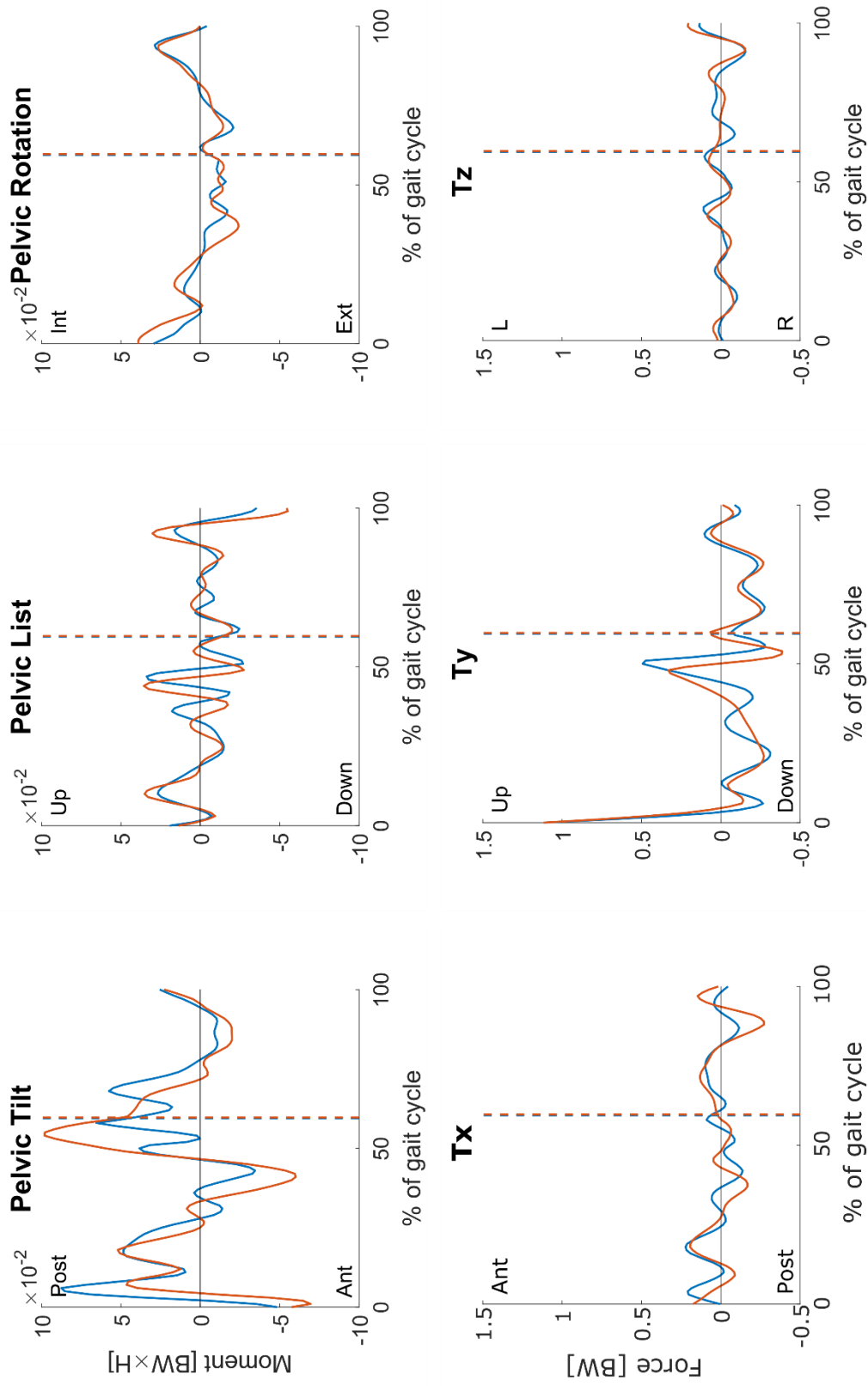
Figure A.3.6: Generalized moment and force trajectories at the ground-pelvis joint of *p01* for the trials at a fast walking speed; values for each trial are shown in bodyweight × height (BW×H) for moments and bodyweight (BW) for forces.
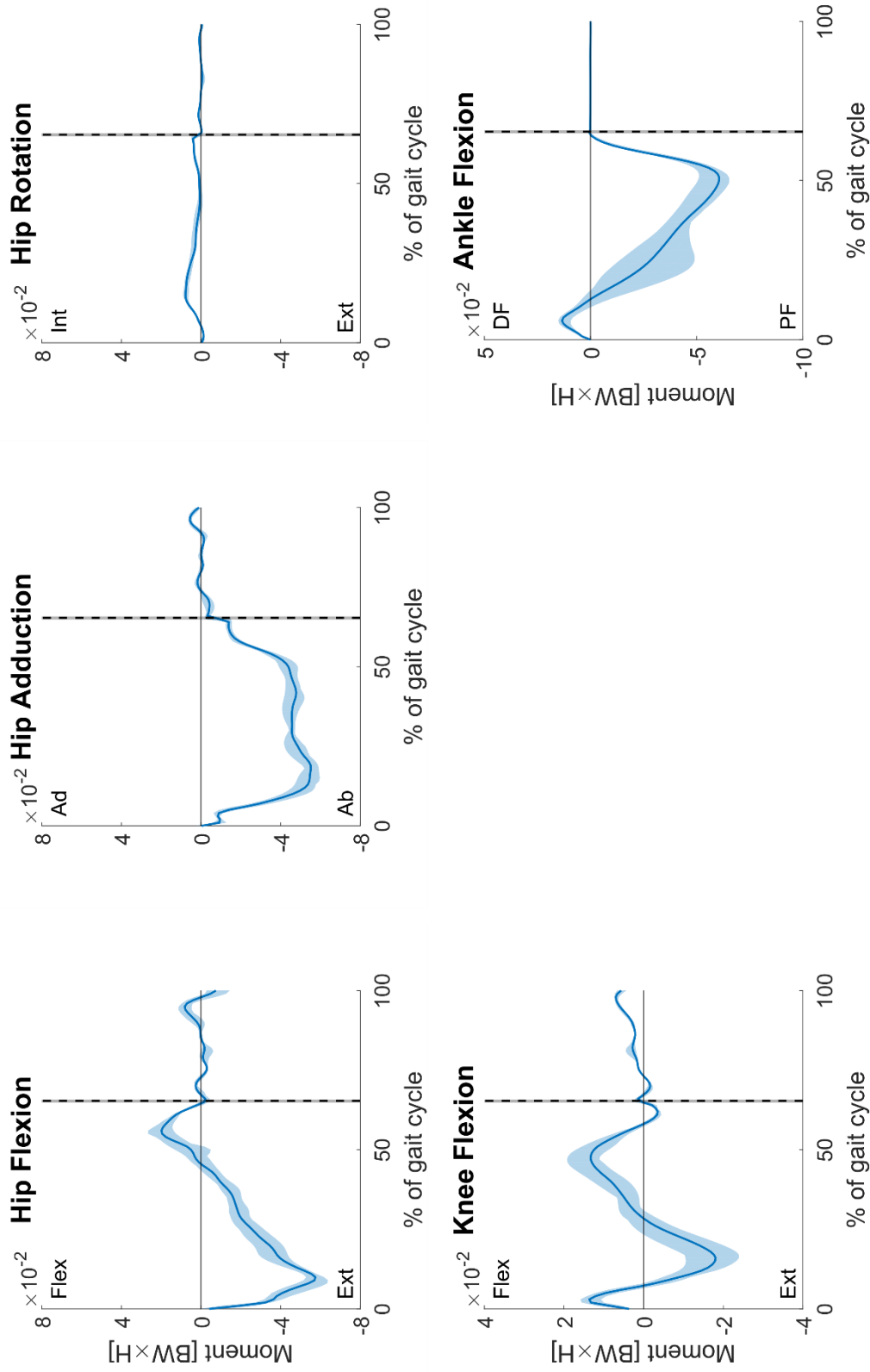
Figure A.3.7: Generalized moment trajectories at the hip, knee and ankle of *p02* for the trials at a self-selected walking speed; mean (solid line) and range (shaded area) values are shown in bodyweight × height (BW×H).
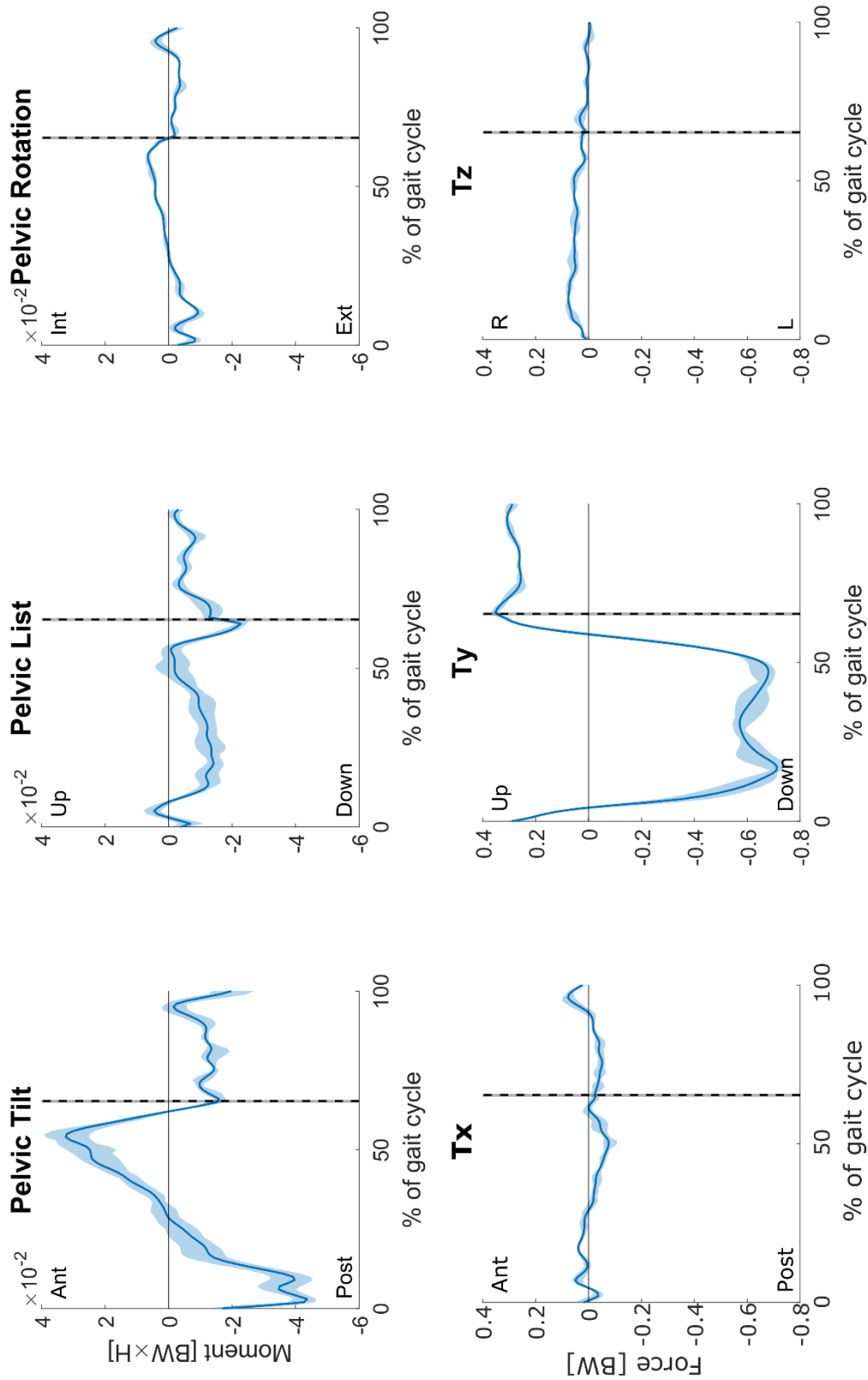
Figure A.3.8: Generalized moment and force trajectories at the ground-pelvis joint of *p02* for the trials at a self-selected walking speed; mean (solid line) and range (shaded area) values are shown in bodyweight × height (BW×H) for moments and bodyweight (BW) for forces.
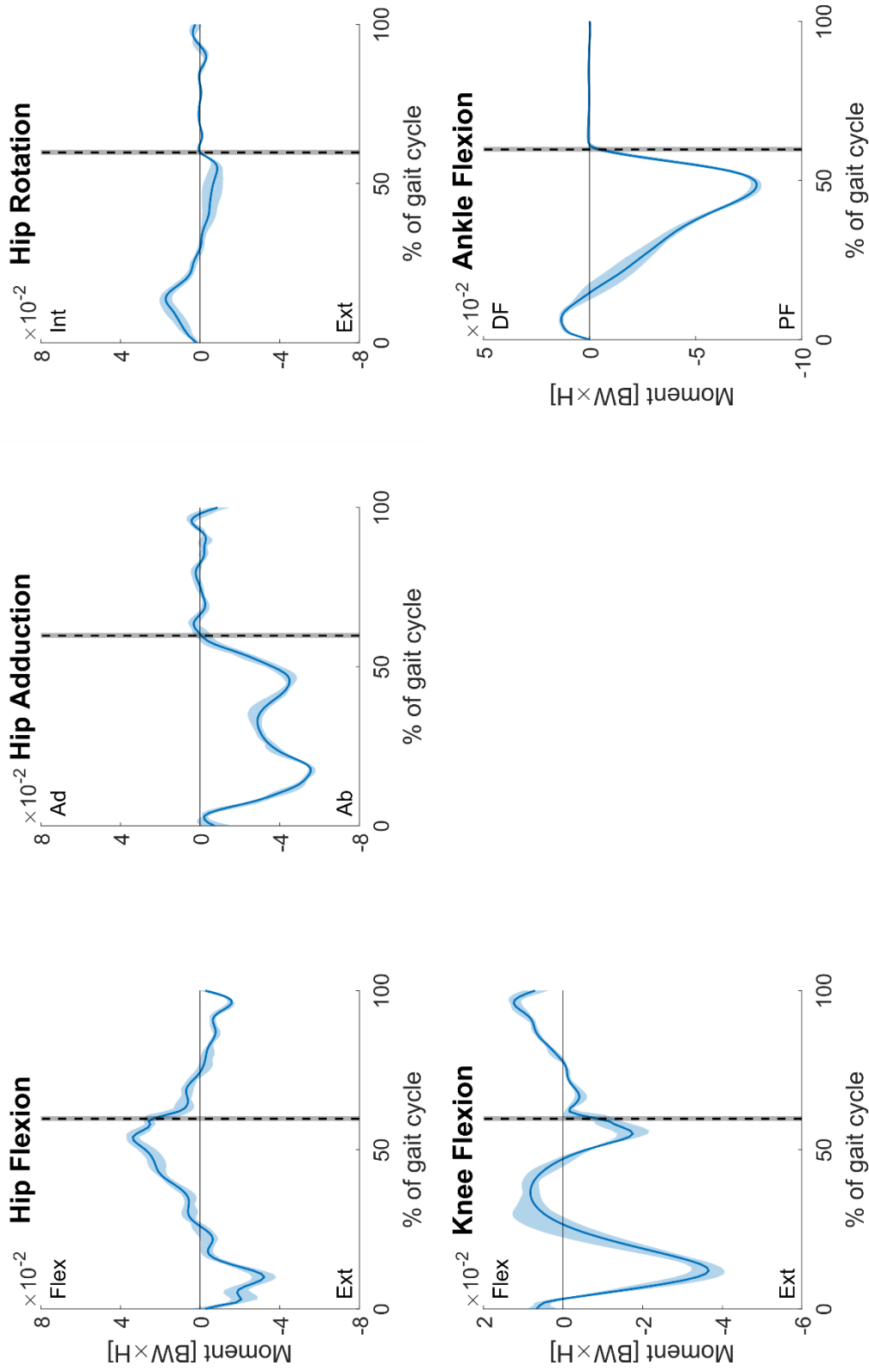
Figure A.3.9: Generalized moment trajectories at the hip, knee and ankle of *p03* for the trials at a self-selected walking speed; mean (solid line) and range (shaded area) values are shown in bodyweight × height (BW×H).
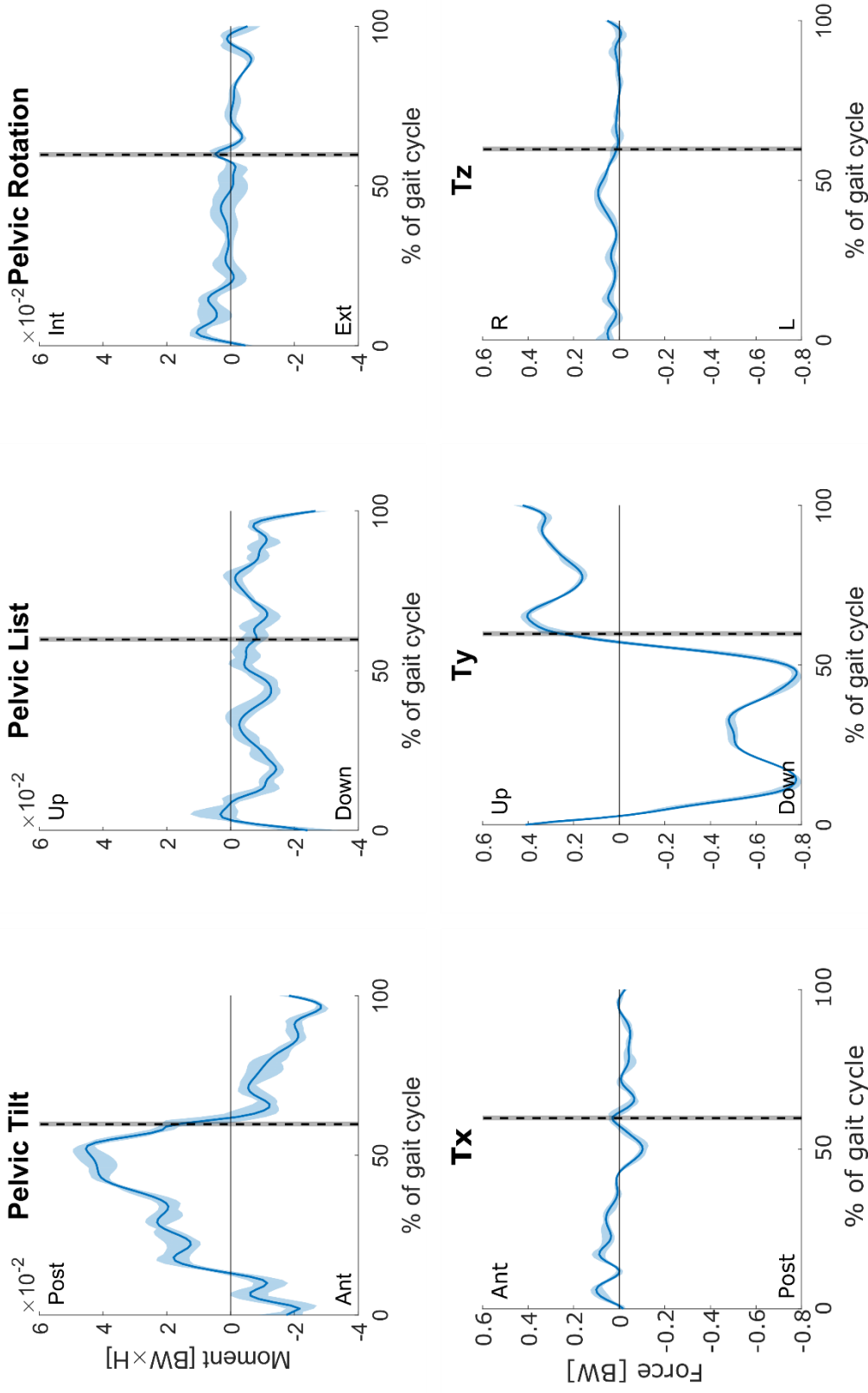
Figure A.3.10: Generalized moment and force trajectories at the ground-pelvis joint of *p03* for the trials at a self-selected walking speed; mean (solid line) and range (shaded area) values are shown in bodyweight × height (BW×H) for moments and bodyweight (BW) for forces.
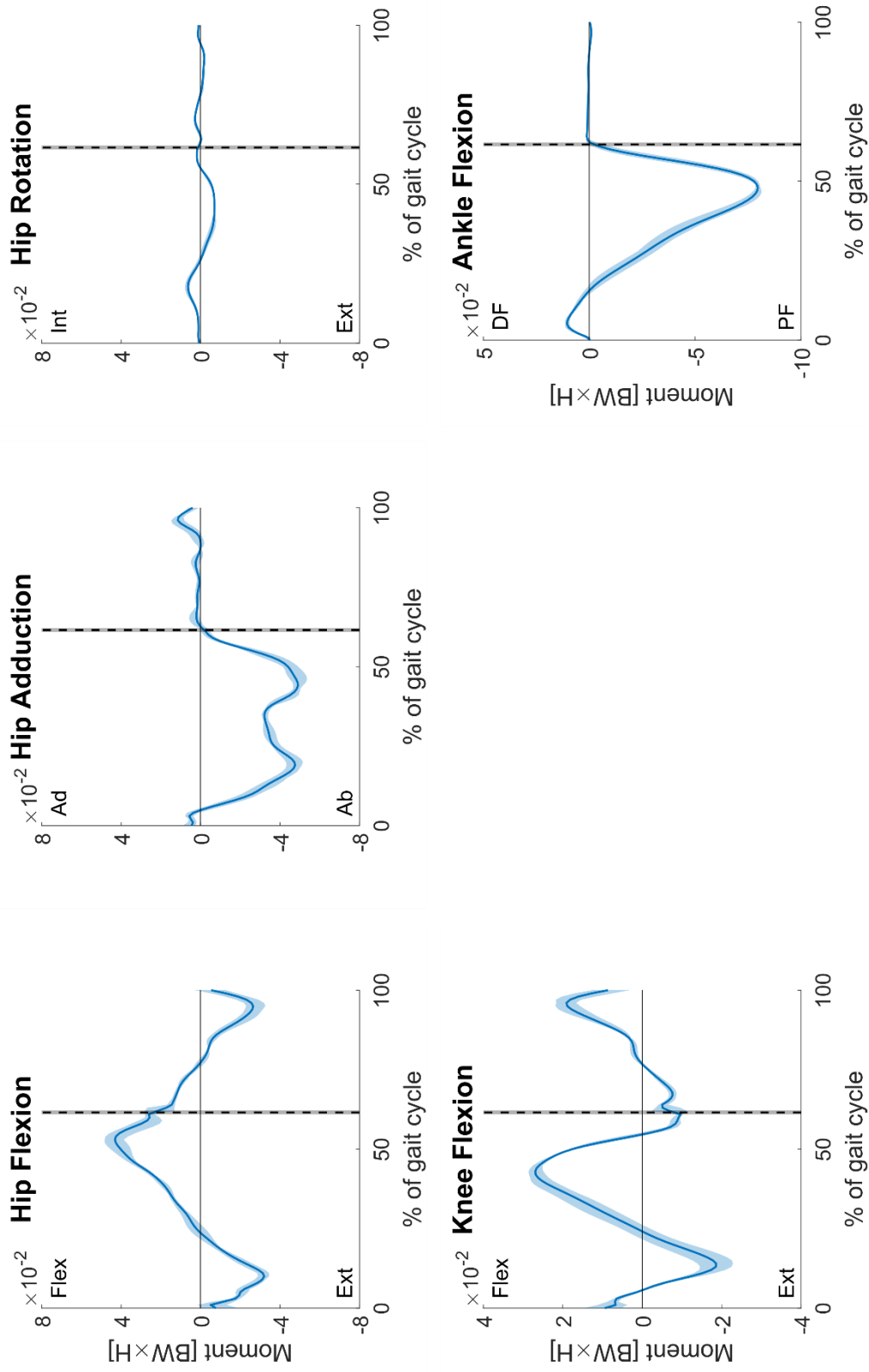
Figure A.3.11: Generalized moment trajectories at the hip, knee and ankle of *p04* for the trials at a slow walking speed; mean (solid line) and range (shaded area) values are shown in bodyweight × height (BW×H).
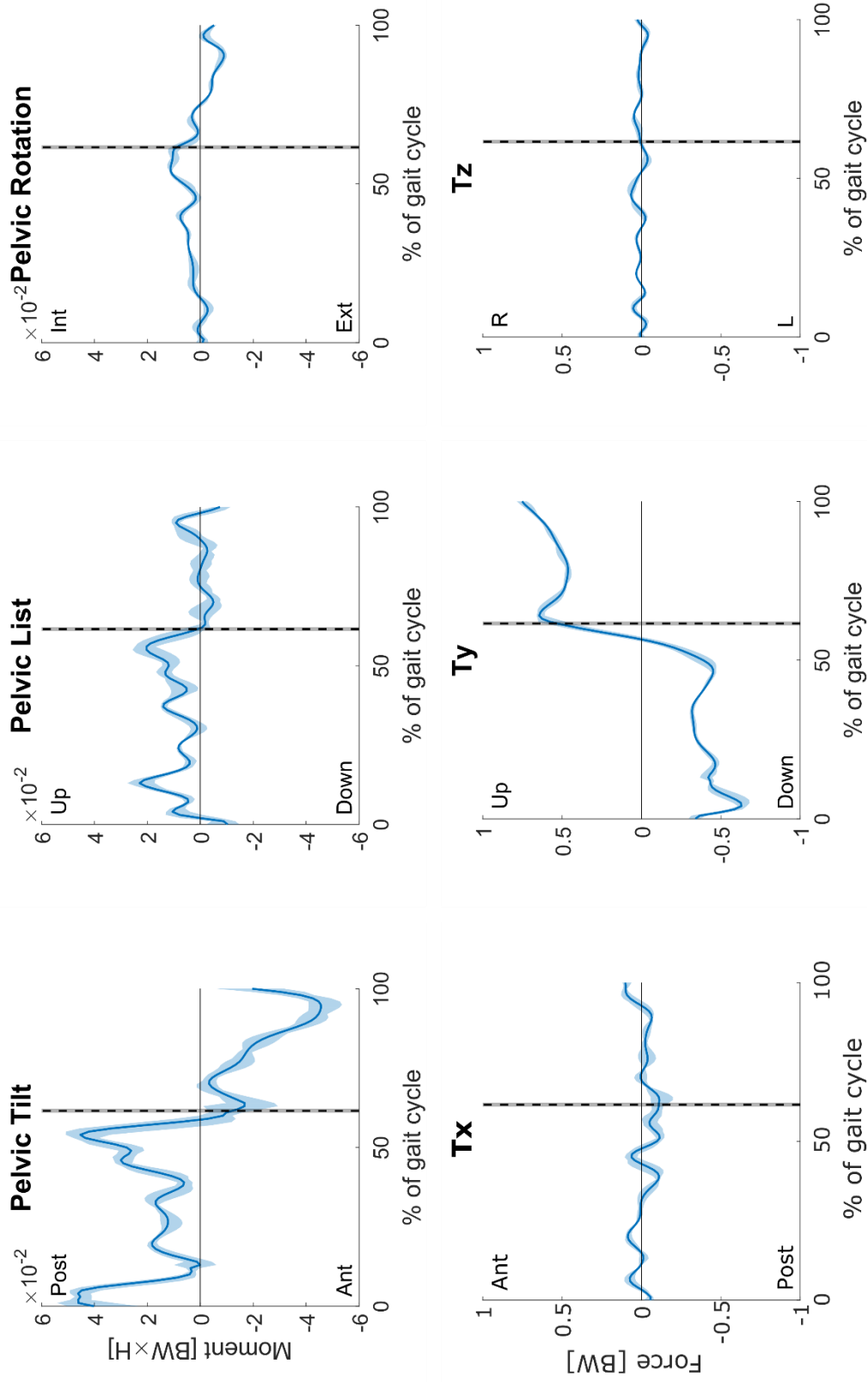
Figure A.3.12: Generalized moment and force trajectories at the ground-pelvis joint of *p04* for the trials at a slow walking speed; mean (solid line) and range (shaded area) values are shown in bodyweight × height (BW×H) for moments and bodyweight (BW) for forces.
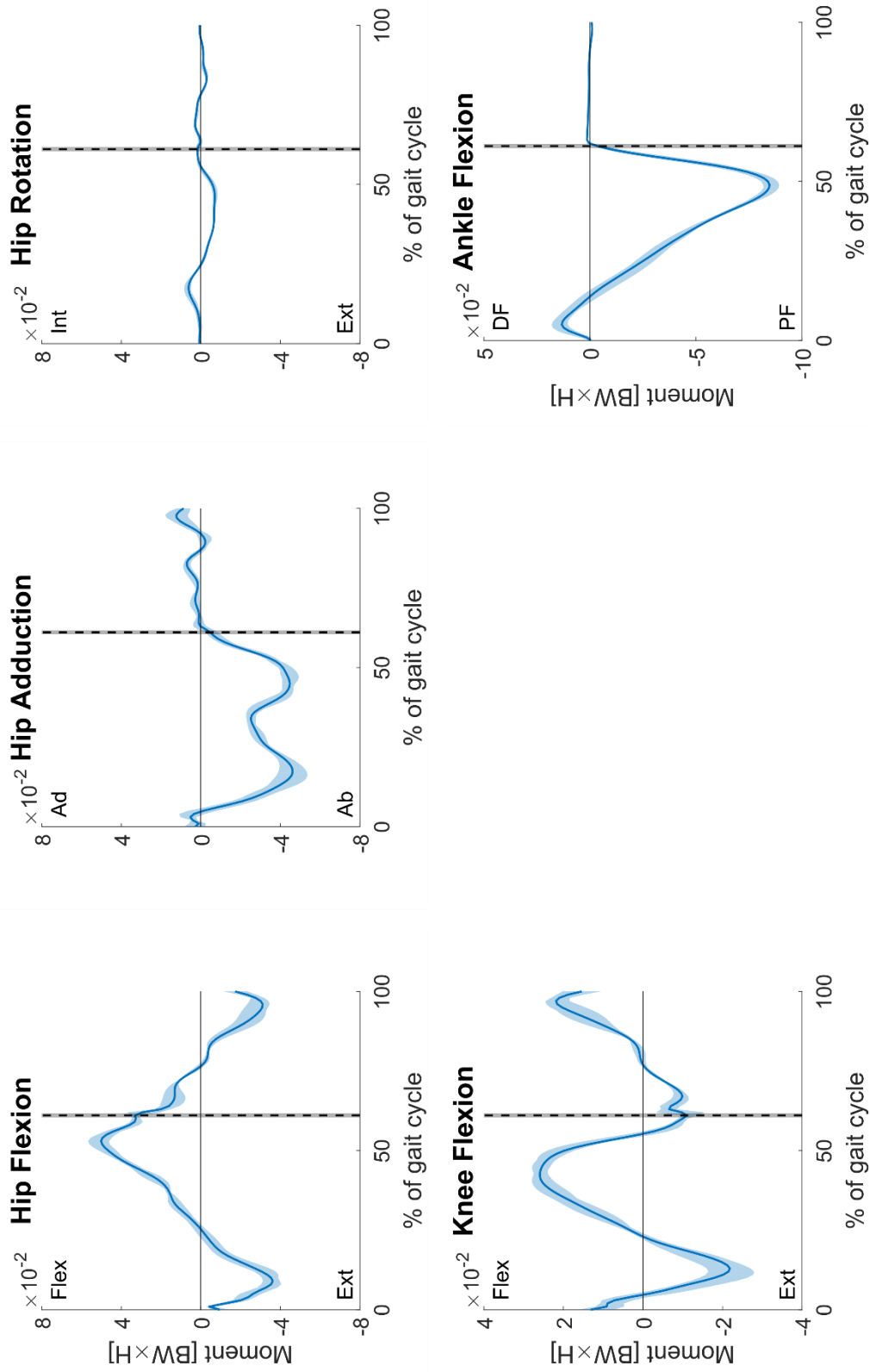
Figure A.3.13: Generalized moment trajectories at the hip, knee and ankle of *p04* for the trials at a self-selected walking speed; mean (solid line) and range (shaded area) values are shown in bodyweight × height (BW×H).
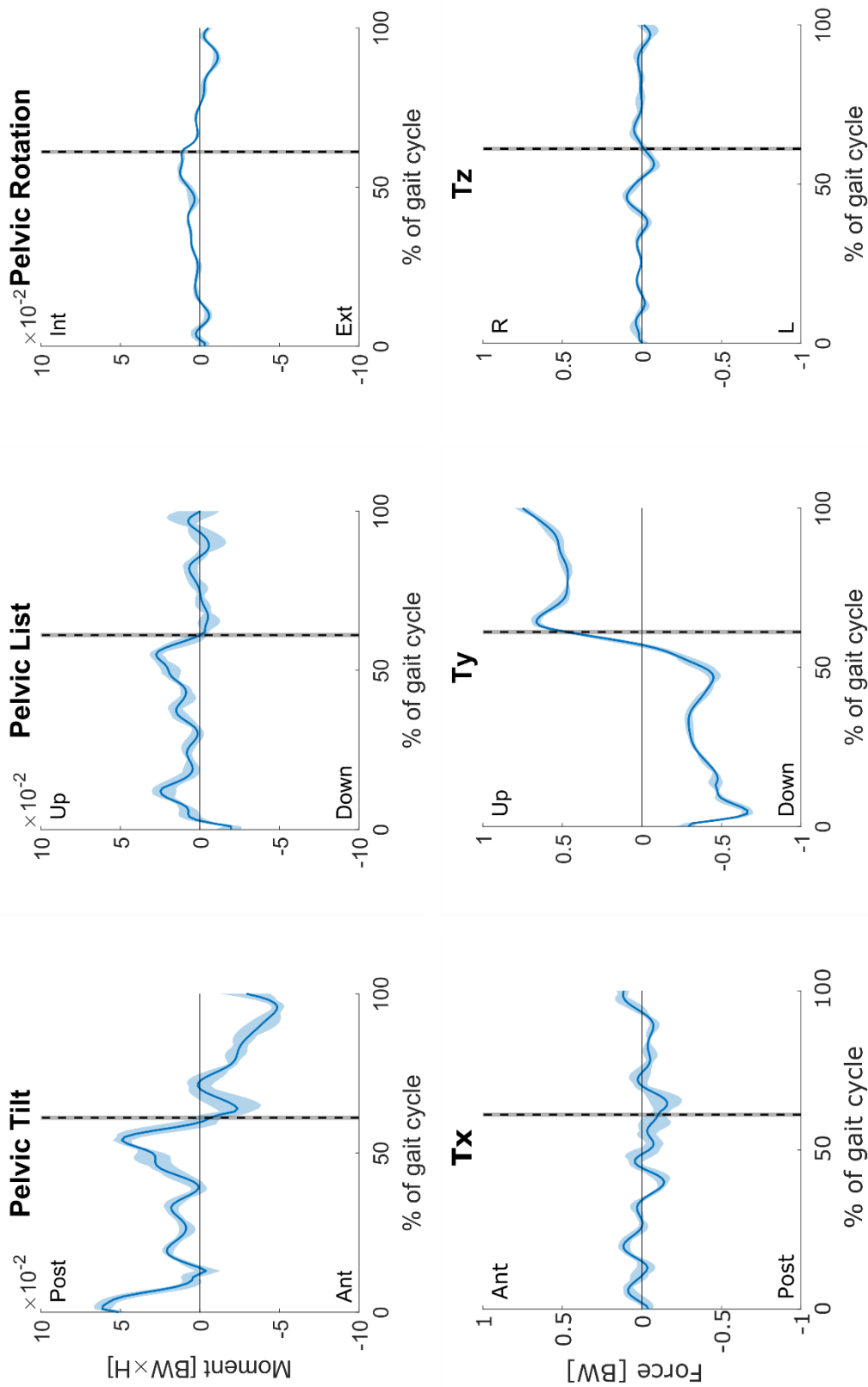
Figure A.3.14: Generalized moment and force trajectories at the ground-pelvis joint of *p04* for the trials at a self-selected walking speed; mean (solid line) and range (shaded area) values are shown in bodyweight × height (BW×H) for moments and bodyweight (BW) for forces.

Figure A.3.15: Generalized moment trajectories at the hip, knee and ankle of *p04* for the trials at a fast walking speed; mean (solid line) and range (shaded area) values are shown in bodyweight × height (BW×H).

Figure A.3.16: Generalized moment and force trajectories at the ground-pelvis joint of *p04* for the trials at a fast walking speed; mean (solid line) and range (shaded area) values are shown in bodyweight × height (BW×H) for moments and bodyweight (BW) for forces.

A.4 Trajectories of joint contact forces
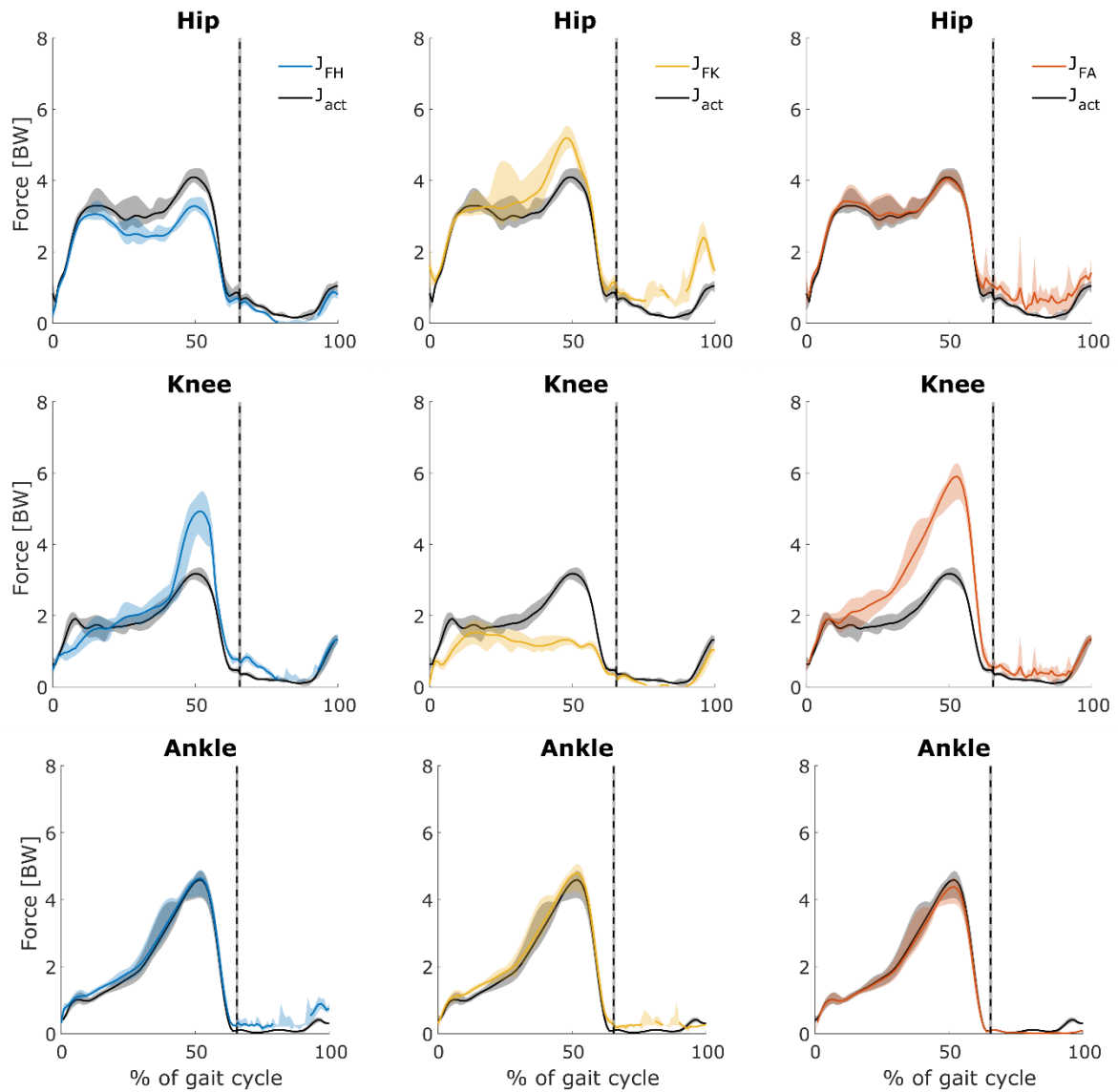
Figure A.4.1: Joint contact force trajectories at the hip (top), knee (middle) and ankle (bottom) of *p01* for the trials at a slow walking speed; mean (solid line) and range (shaded area) values are shown in bodyweight (BW) for the different solutions: J_{act} (black), J_{FH} (blue, left), J_{FK} (yellow, middle) and J_{FA} (red, right).
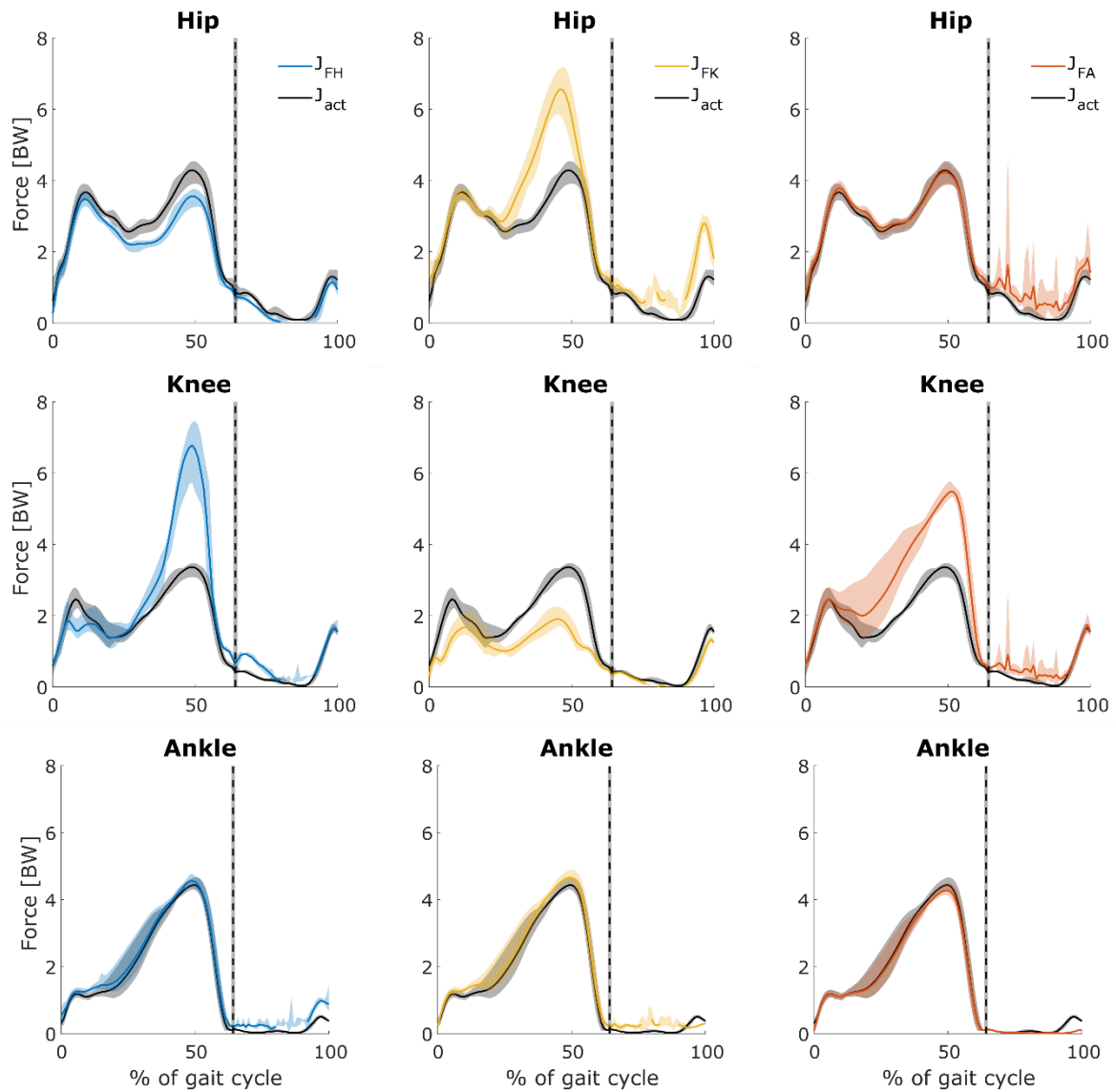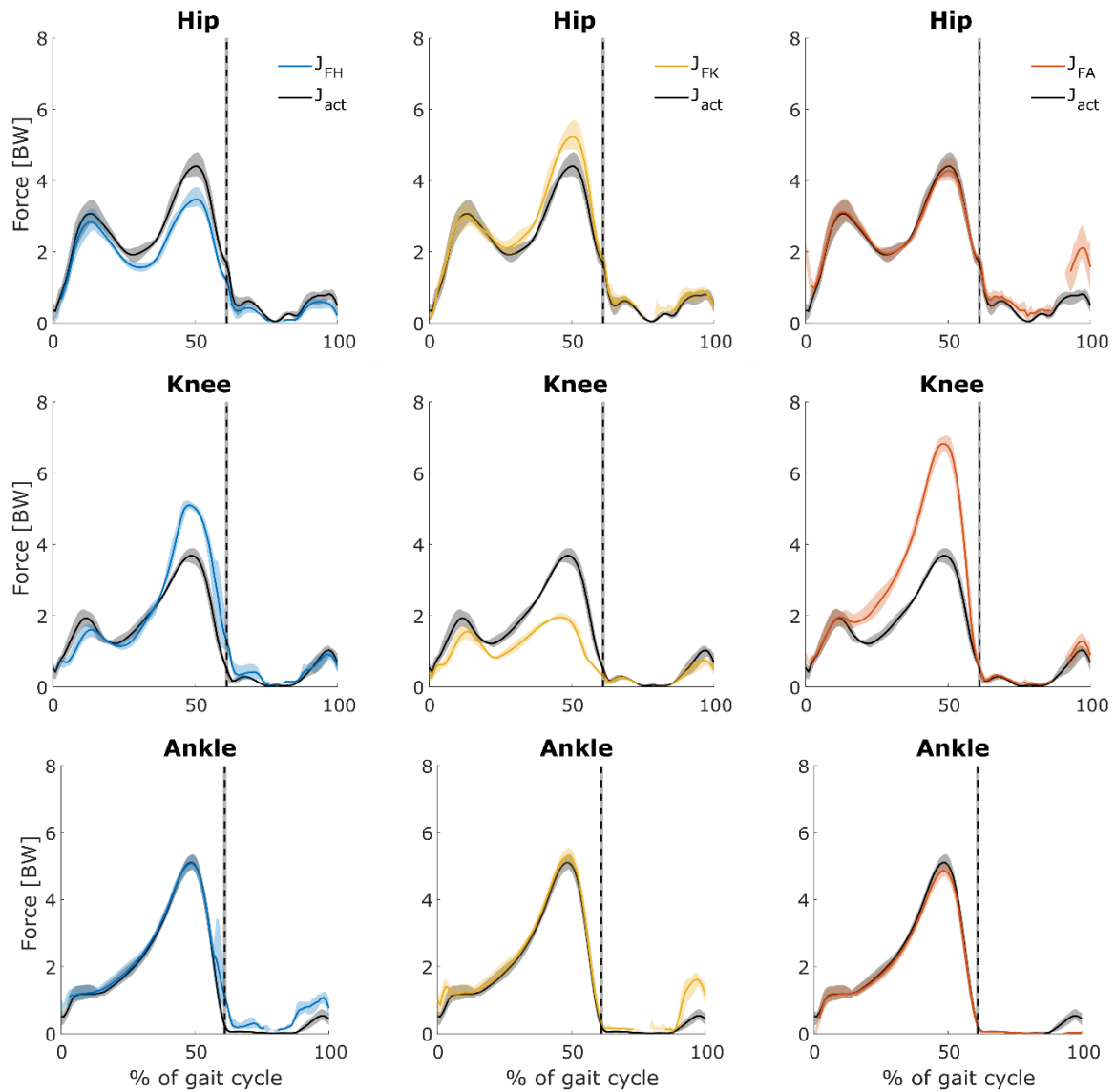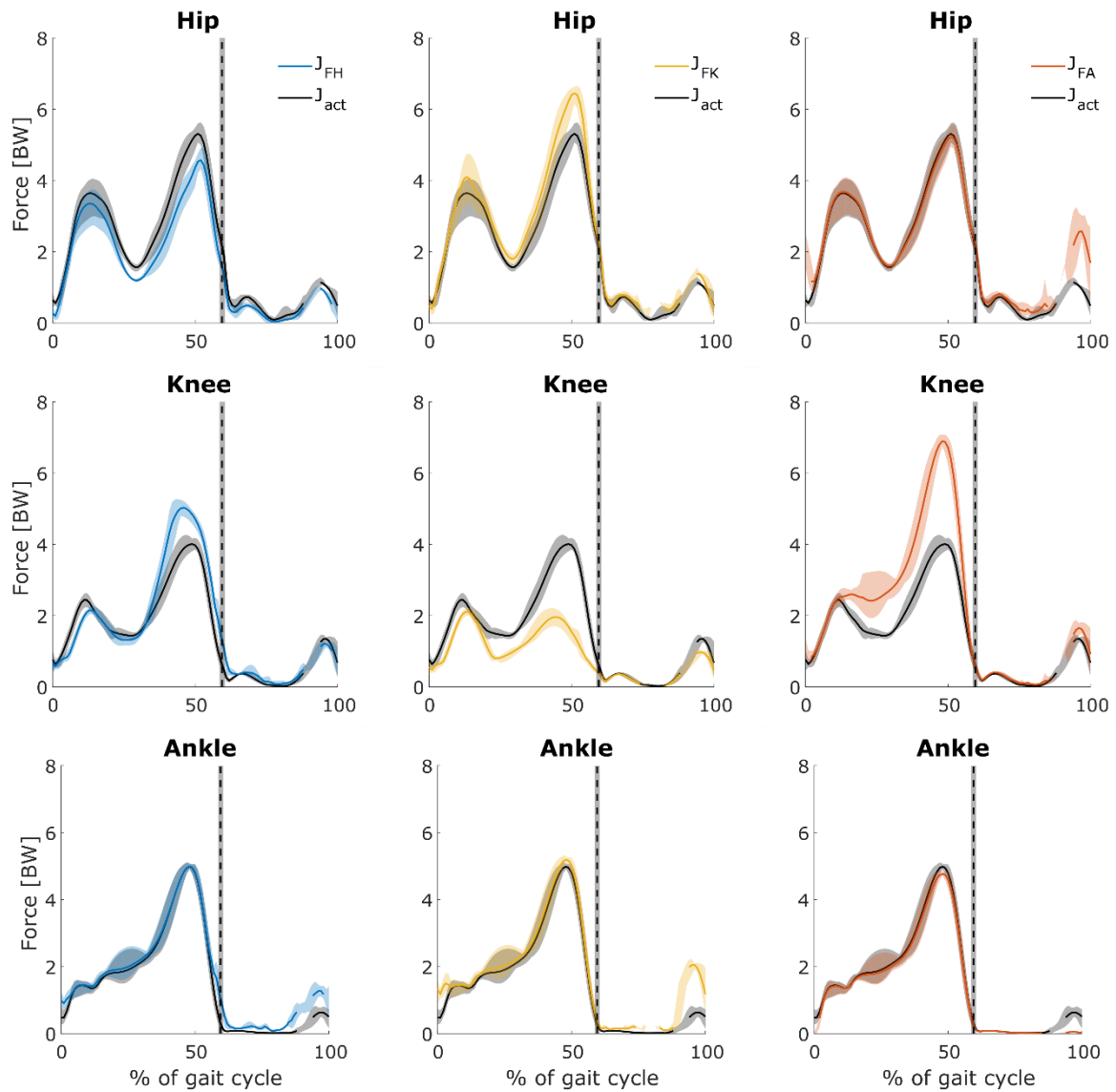
Figure A.4.2: Joint contact force trajectories at the hip (top), knee (middle) and ankle (bottom) of *p01* for the trials at a self-selected walking speed; mean (solid line) and range (shaded area) values are shown in bodyweight (BW) for the different solutions: J_{act} (black), J_{FH} (blue, left), J_{FK} (yellow, middle) and J_{FA} (red, right).
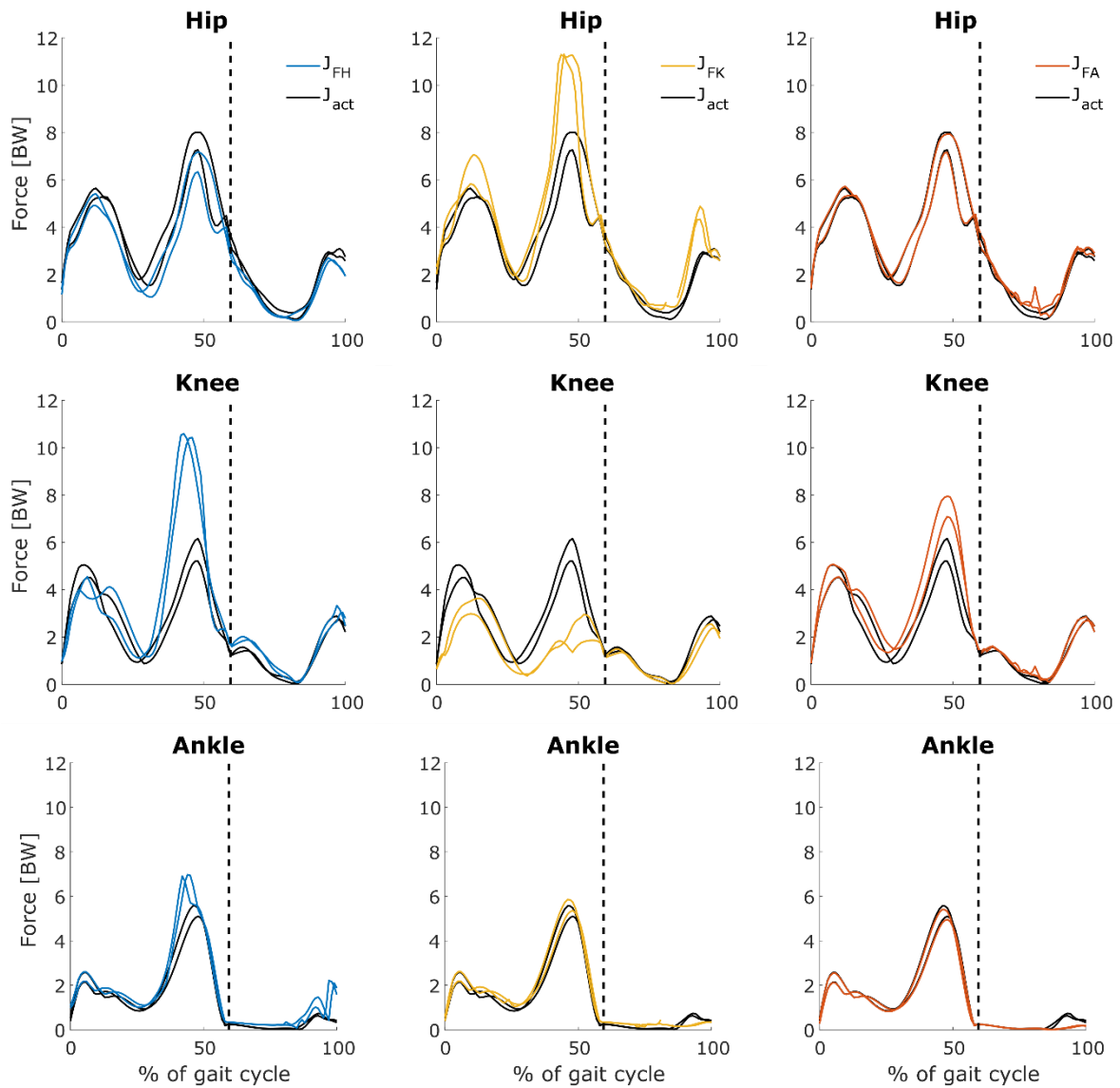
Figure A.4.3: Joint contact force trajectories at the hip (top), knee (middle) and ankle (bottom) of *p01* for the trials at a fast walking speed; values for each trial are shown in bodyweight (BW) for the different solutions: J_{act} (black), J_{FH} (blue, left), J_{FK} (yellow, middle) and J_{FA} (red, right).
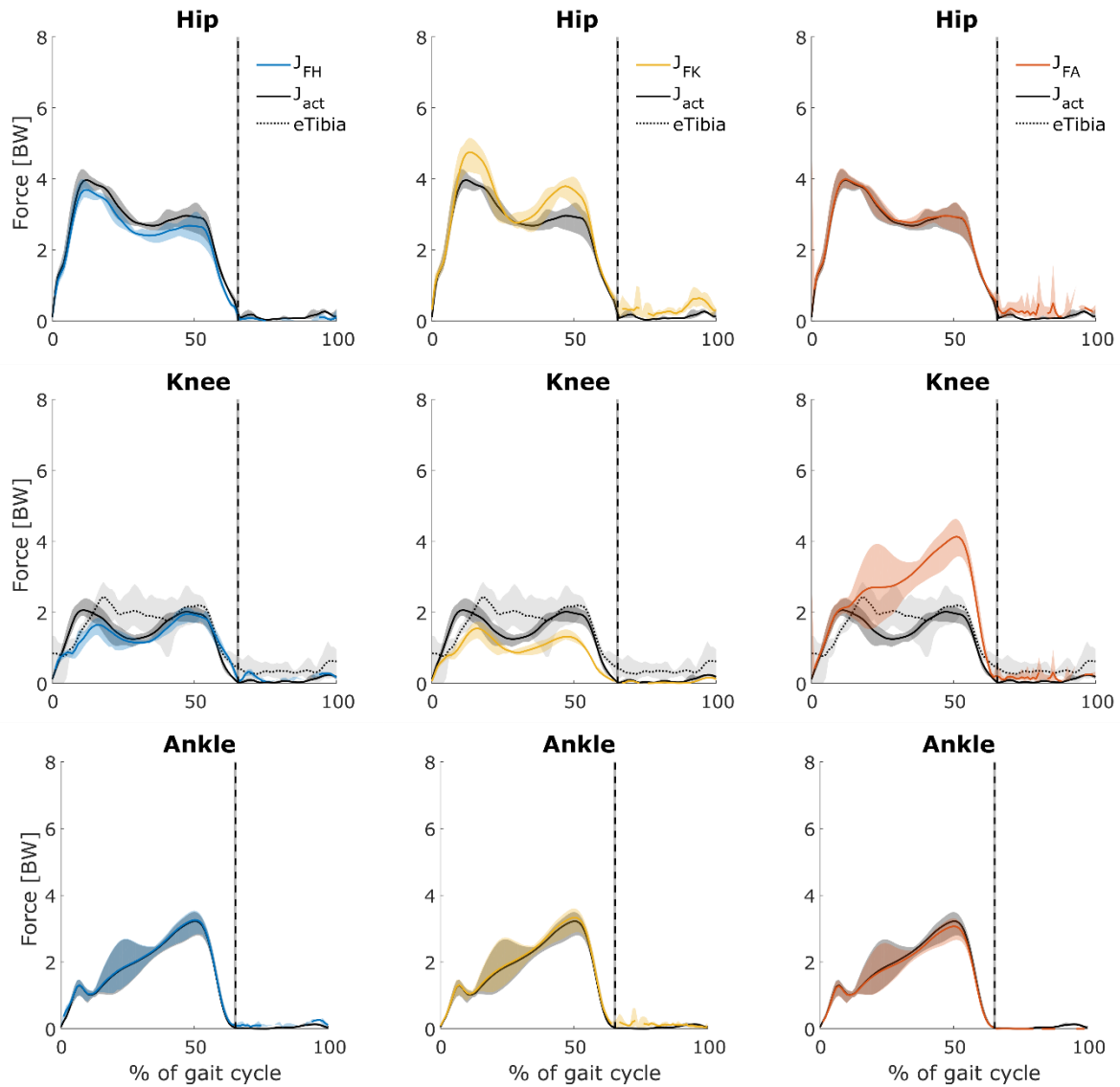
Figure A.4.4: Joint contact force trajectories at the hip (top), knee (middle) and ankle (bottom) of *p02* for the trials at a self-selected walking speed; mean (solid line) and range (shaded area) values are shown in bodyweight (BW) for the different solutions: J_{act} (black), J_{FH} (blue, left), J_{FK} (yellow, middle) and J_{FA} (red, right). Additionally, the mean and range values of the magnitude of force measured by the implant (*eTibia*, dashed) are shown for the knee.
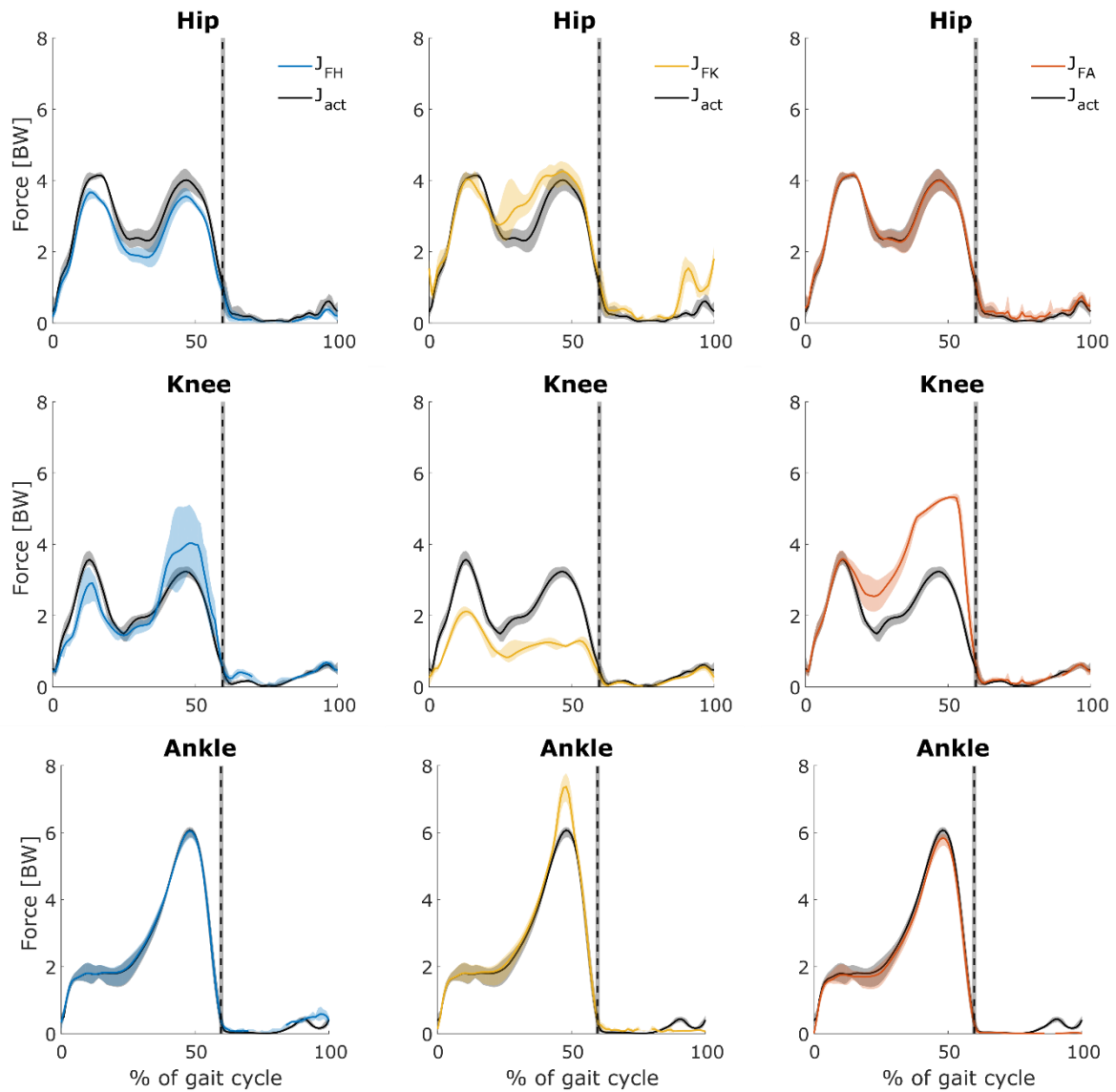
Figure A.4.5: Joint contact force trajectories at the hip (top), knee (middle) and ankle (bottom) of *p03* for the trials at a self-selected walking speed; mean (solid line) and range (shaded area) values are shown in bodyweight (BW) for the different solutions: J_{act} (black), J_{FH} (blue, left), J_{FK} (yellow, middle) and J_{FA} (red, right).
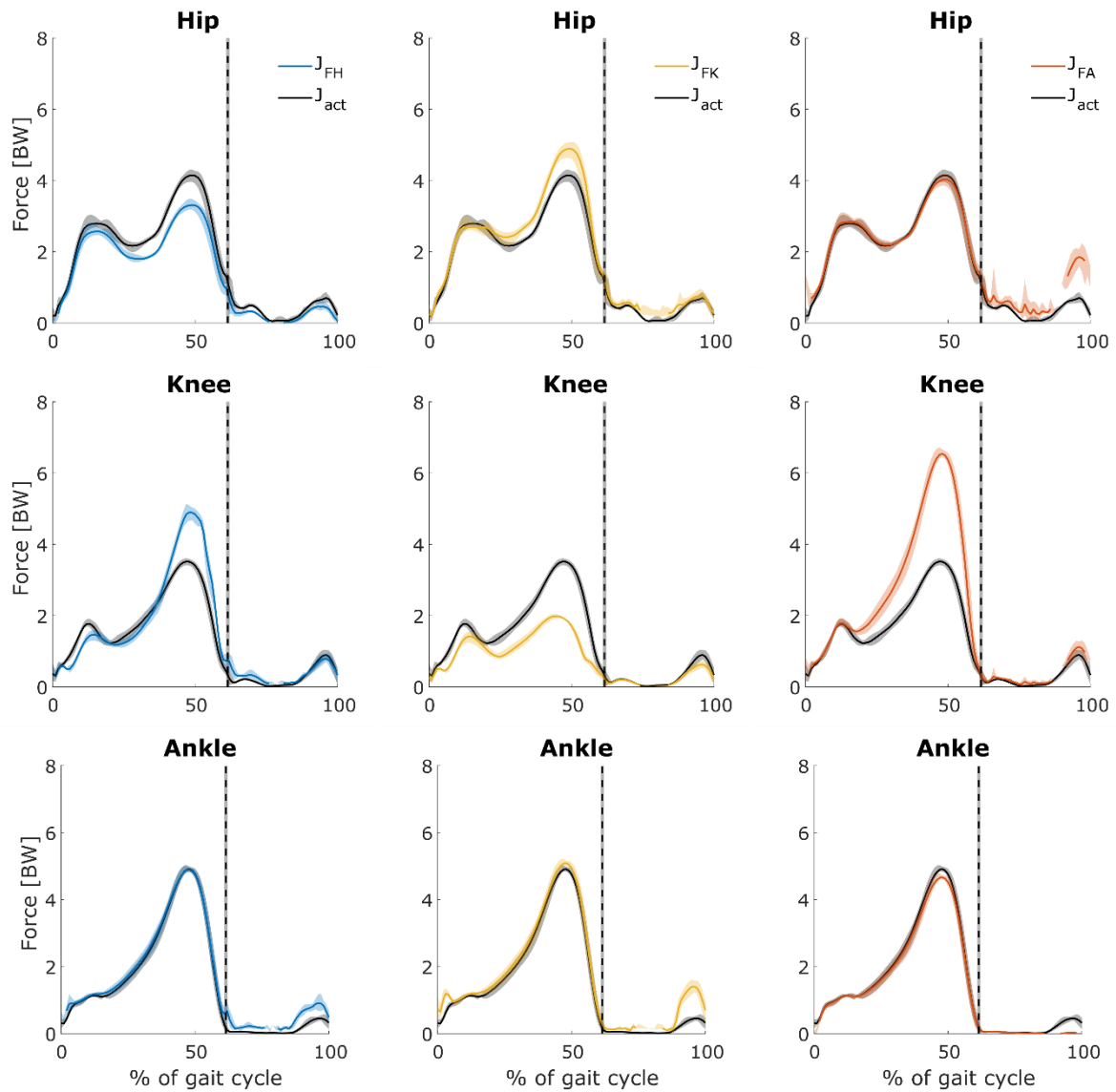
Figure A.4.6: Joint contact force trajectories at the hip (top), knee (middle) and ankle (bottom) of *p04* for the trials at a slow walking speed; mean (solid line) and range (shaded area) values are shown in bodyweight (BW) for the different solutions: J_{act} (black), J_{FH} (blue, left), J_{FK} (yellow, middle) and J_{FA} (red, right).

Figure A.4.7: Joint contact force trajectories at the hip (top), knee (middle) and ankle (bottom) of *p04* for the trials at a self-selected walking speed; mean (solid line) and range (shaded area) values are shown in bodyweight (BW) for the different solutions: J_{act} (black), J_{FH} (blue, left), J_{FK} (yellow, middle) and J_{FA} (red, right).

Figure A.4.8: Joint contact force trajectories at the hip (top), knee (middle) and ankle (bottom) of *p04* for the trials at a fast walking speed; mean (solid line) and range (shaded area) values are shown in bodyweight (BW) for the different solutions: J_{act} (black), J_{FH} (blue, left), J_{FK} (yellow, middle) and J_{FA} (red, right).

A.5 Trajectories of muscle activations

The following section contains the figures that show the trajectories of muscle activation for the different solutions. The results for the Adductor Brevis, Pectineus and Peroneus Brevis muscles are not shown due to the large number of muscles and their relatively small contribution to the joint contact forces.
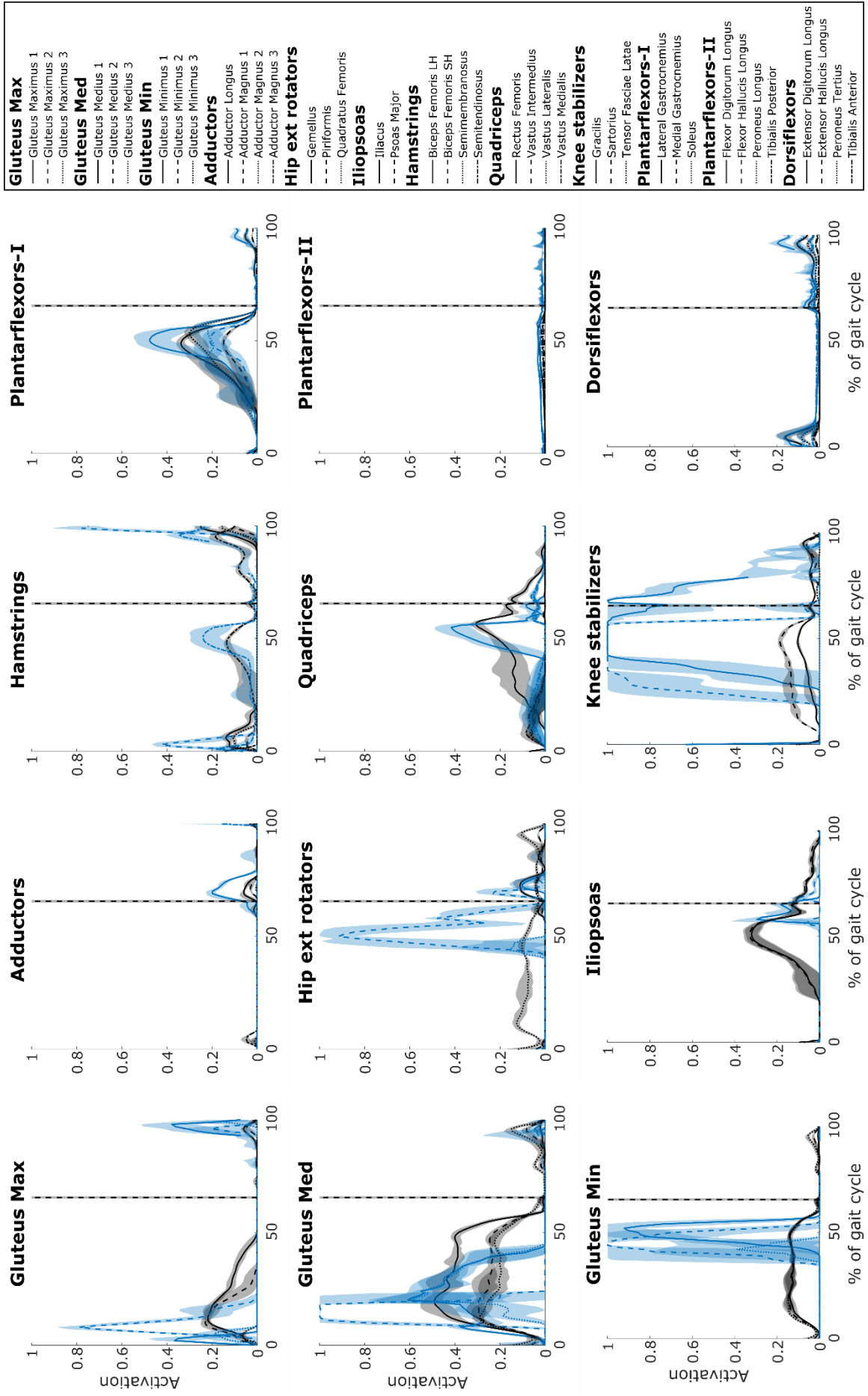
Figure A.5.1: Muscle activation trajectories for the solutions J_{FH} (blue) and J_{act} (black) of *p01* for the trials at a slow walking speed; mean (solid line) and range (shaded area) values are shown for the muscles grouped according to their functionality at the hip (left two columns), knee (middle right) and ankle (right).
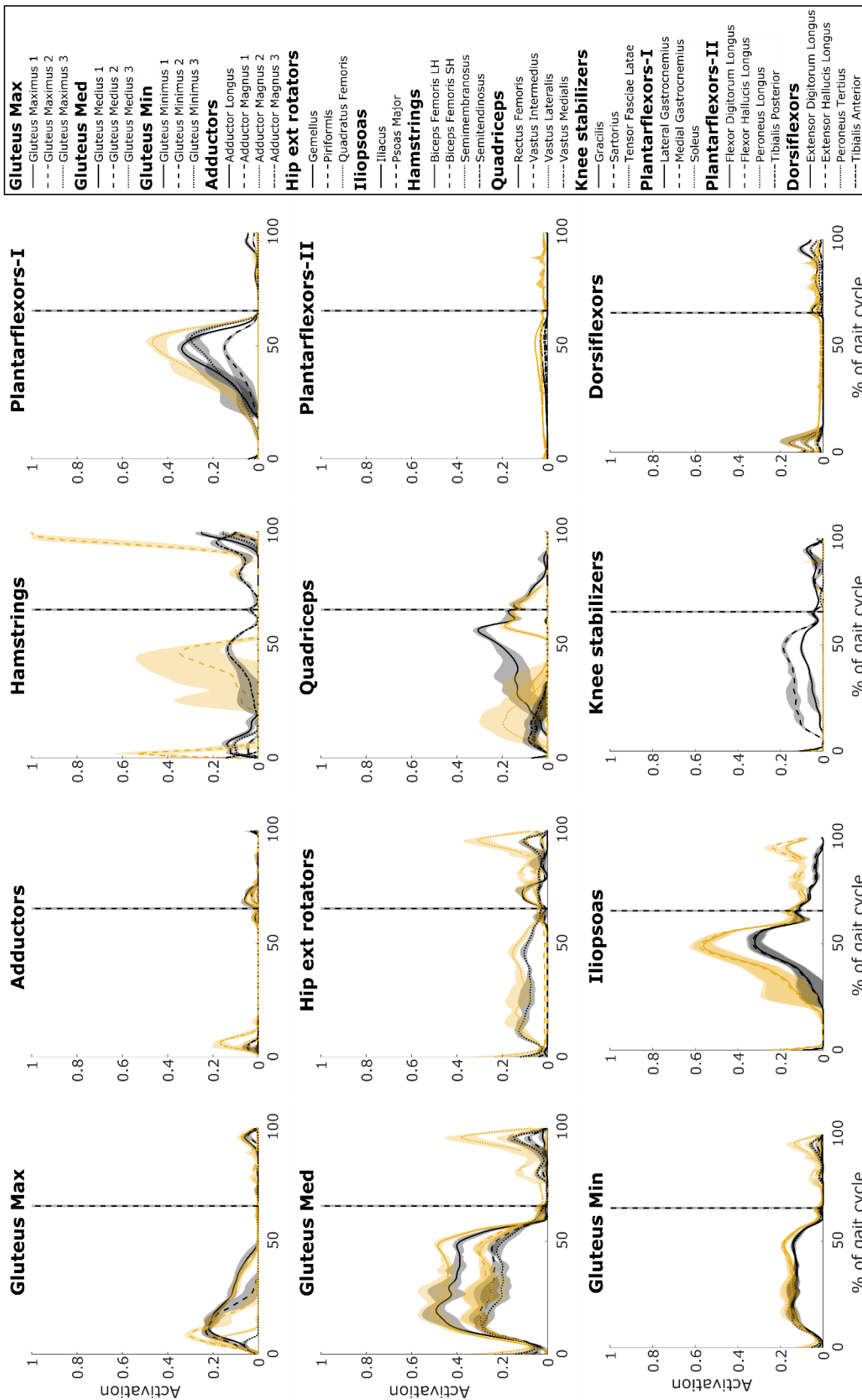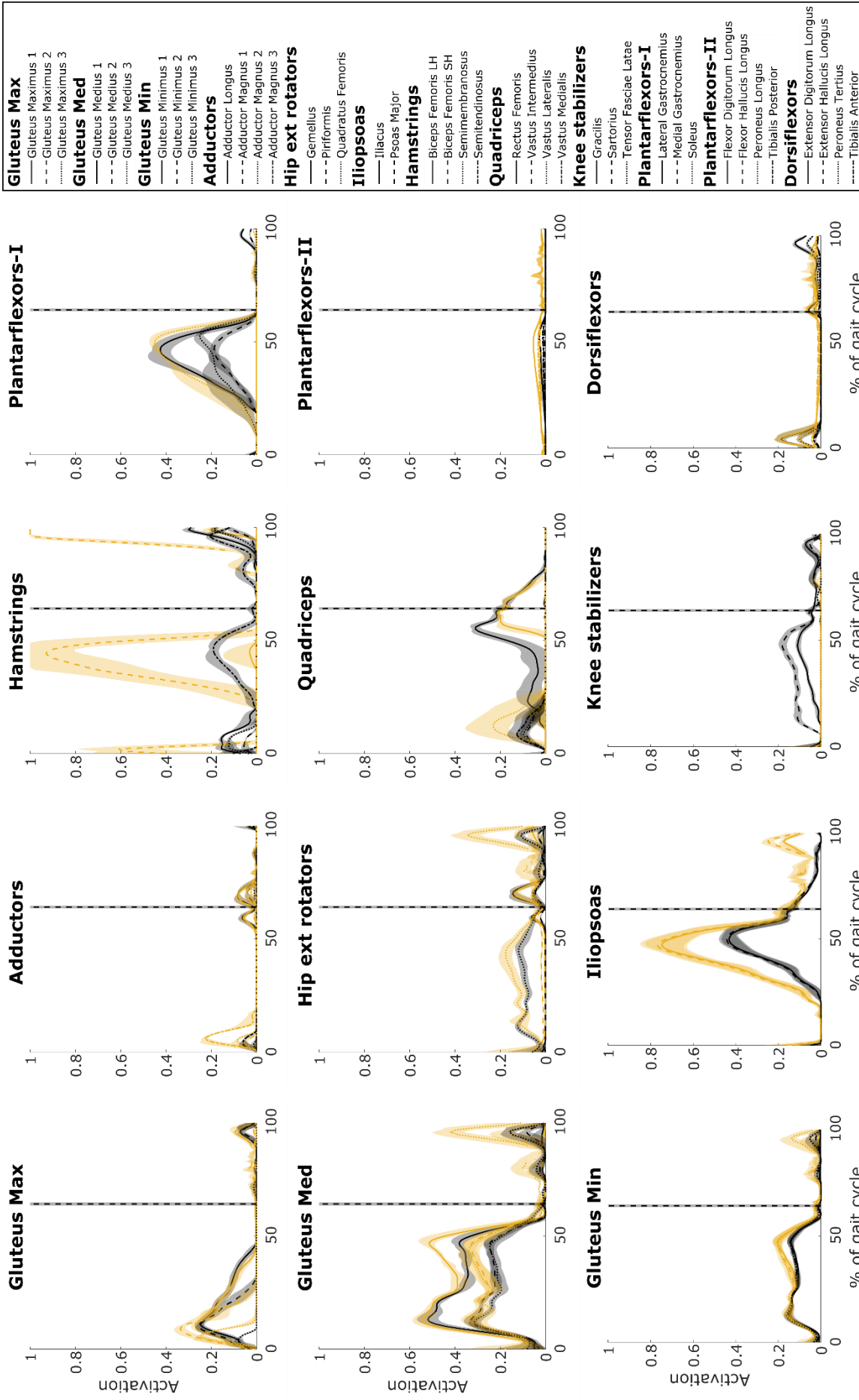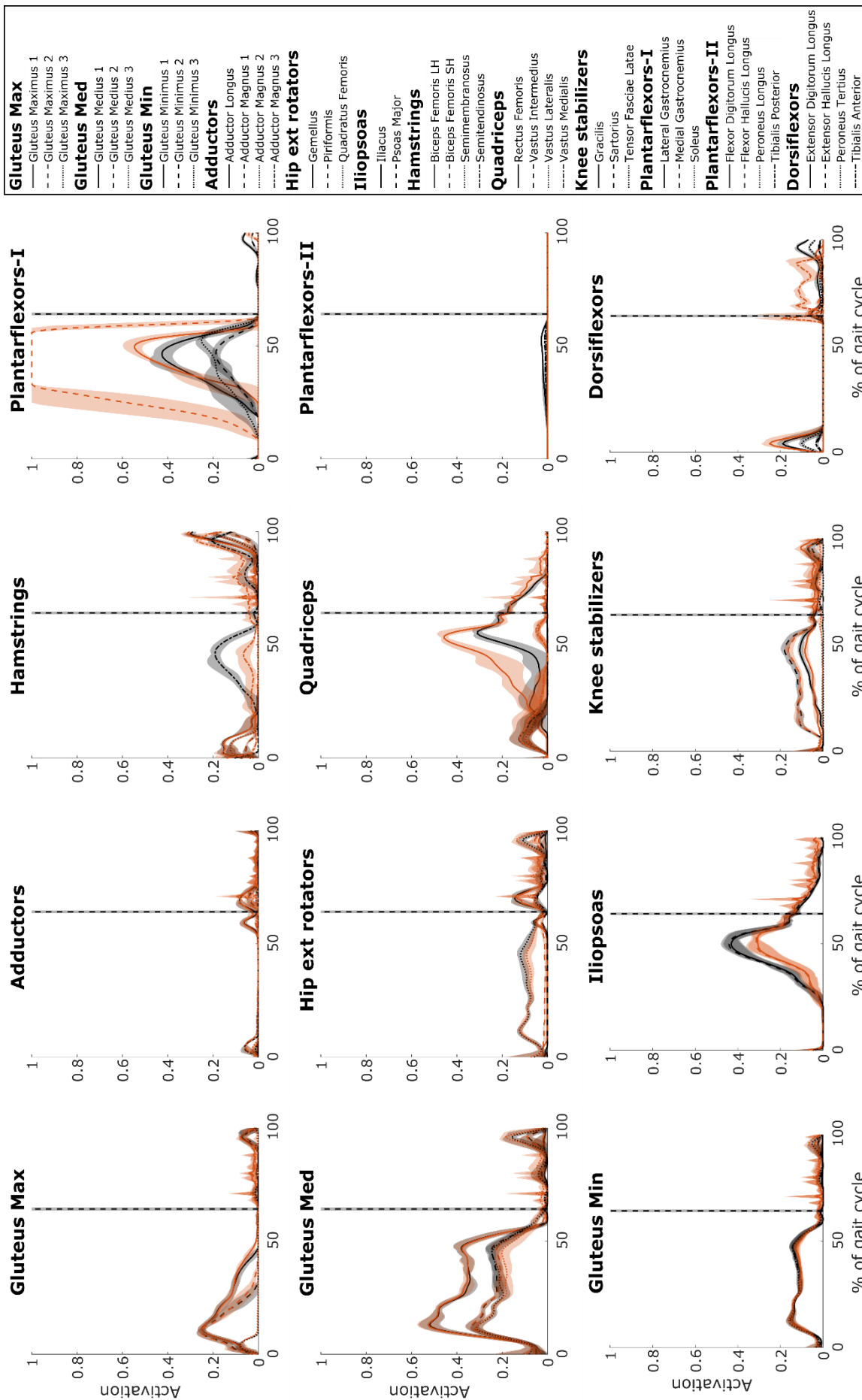
Figure A.5.2: Muscle activation trajectories for the solutions J_{FK} (yellow) and J_{act} (black) of *p01* for the trials at a slow walking speed; mean (solid line) and range (shaded area) values are shown for the muscles grouped according to their functionality at the hip (left two columns), knee (middle right) and ankle (right).
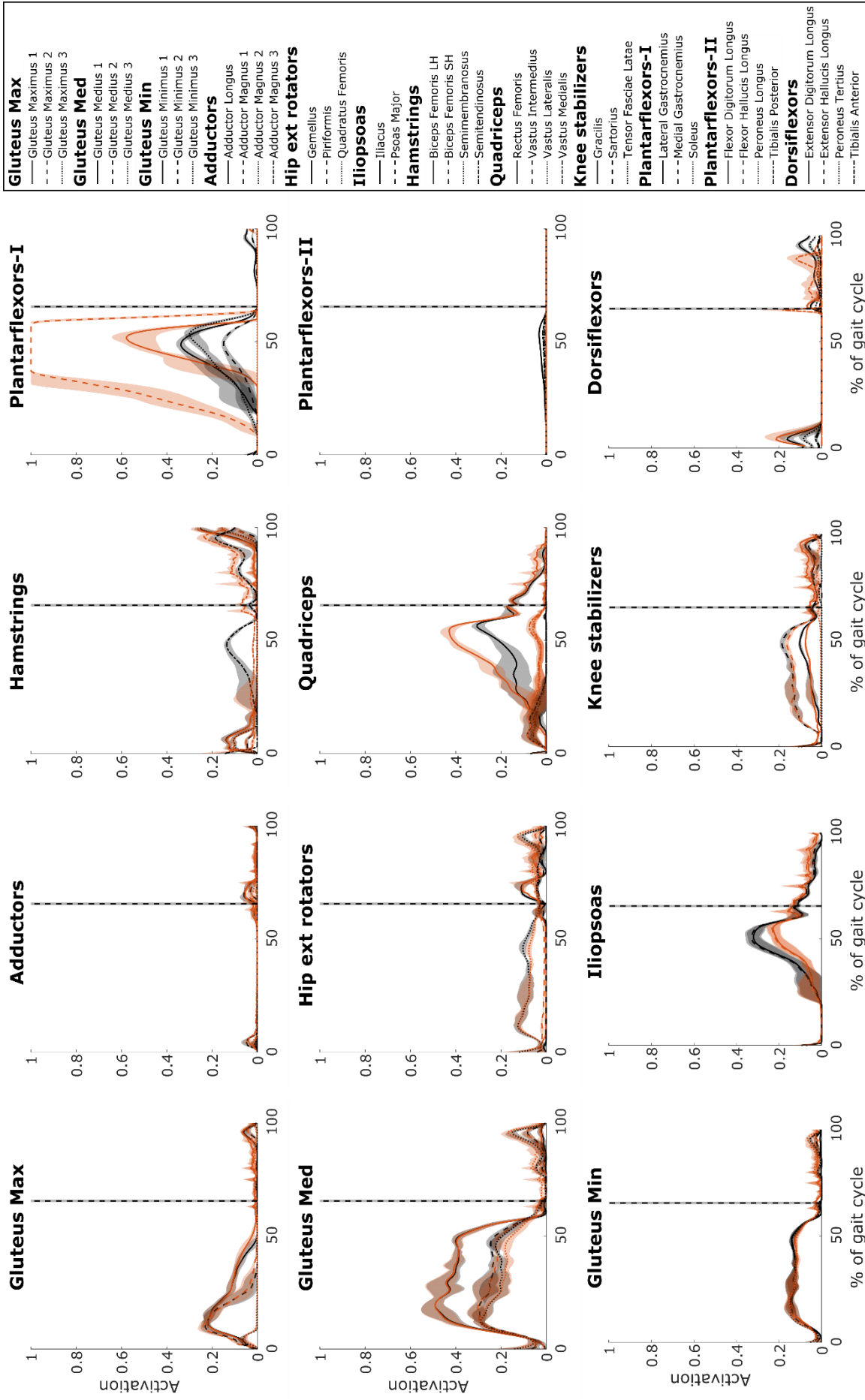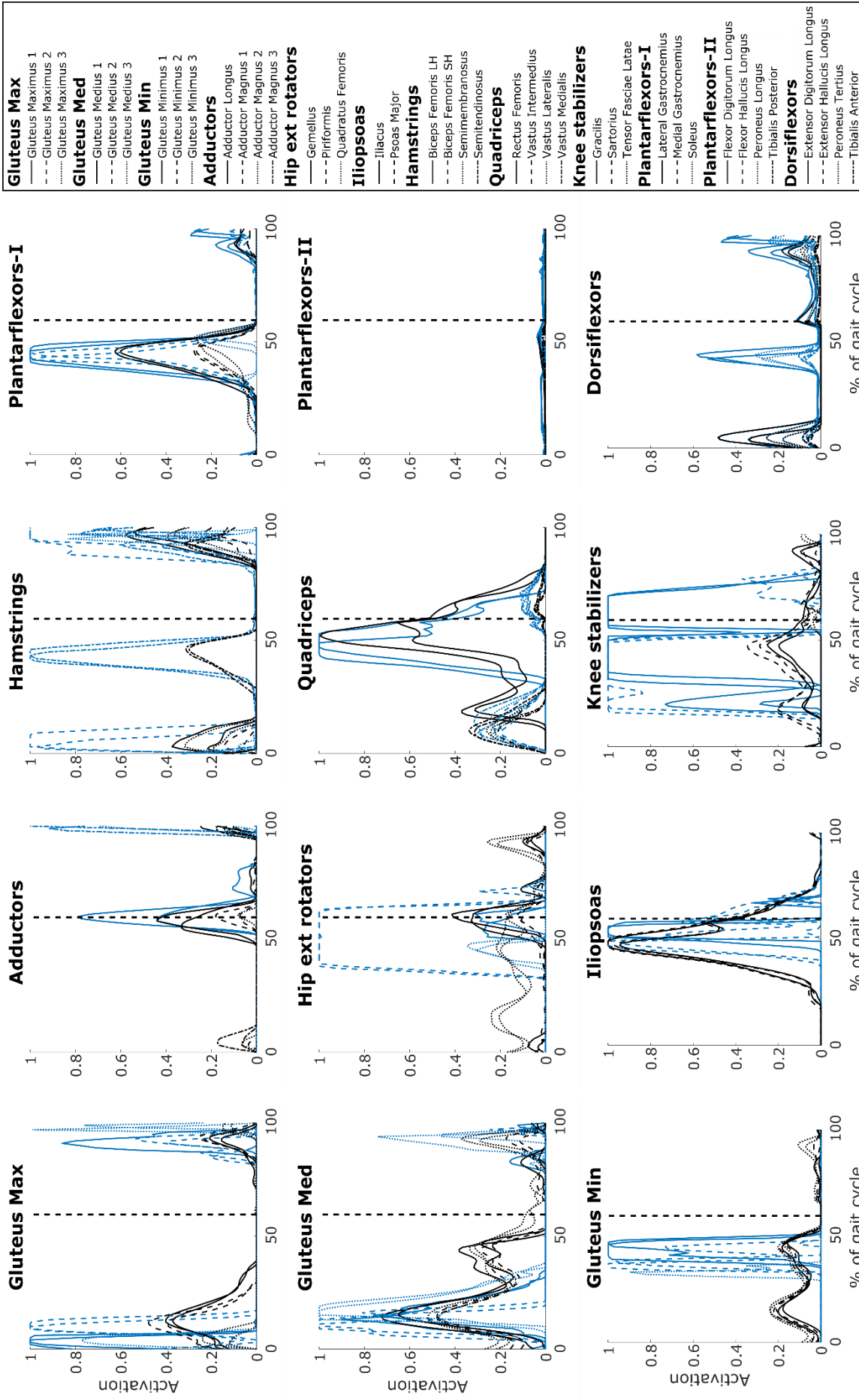
Figure A.5.3: Muscle activation trajectories for the solutions J_{FA} (red) and J_{act} (black) of *p01* for the trials at a slow walking speed; mean (solid line) and range (shaded area) values are shown for the muscles grouped according to their functionality at the hip (left two columns), knee (middle right) and ankle (right).
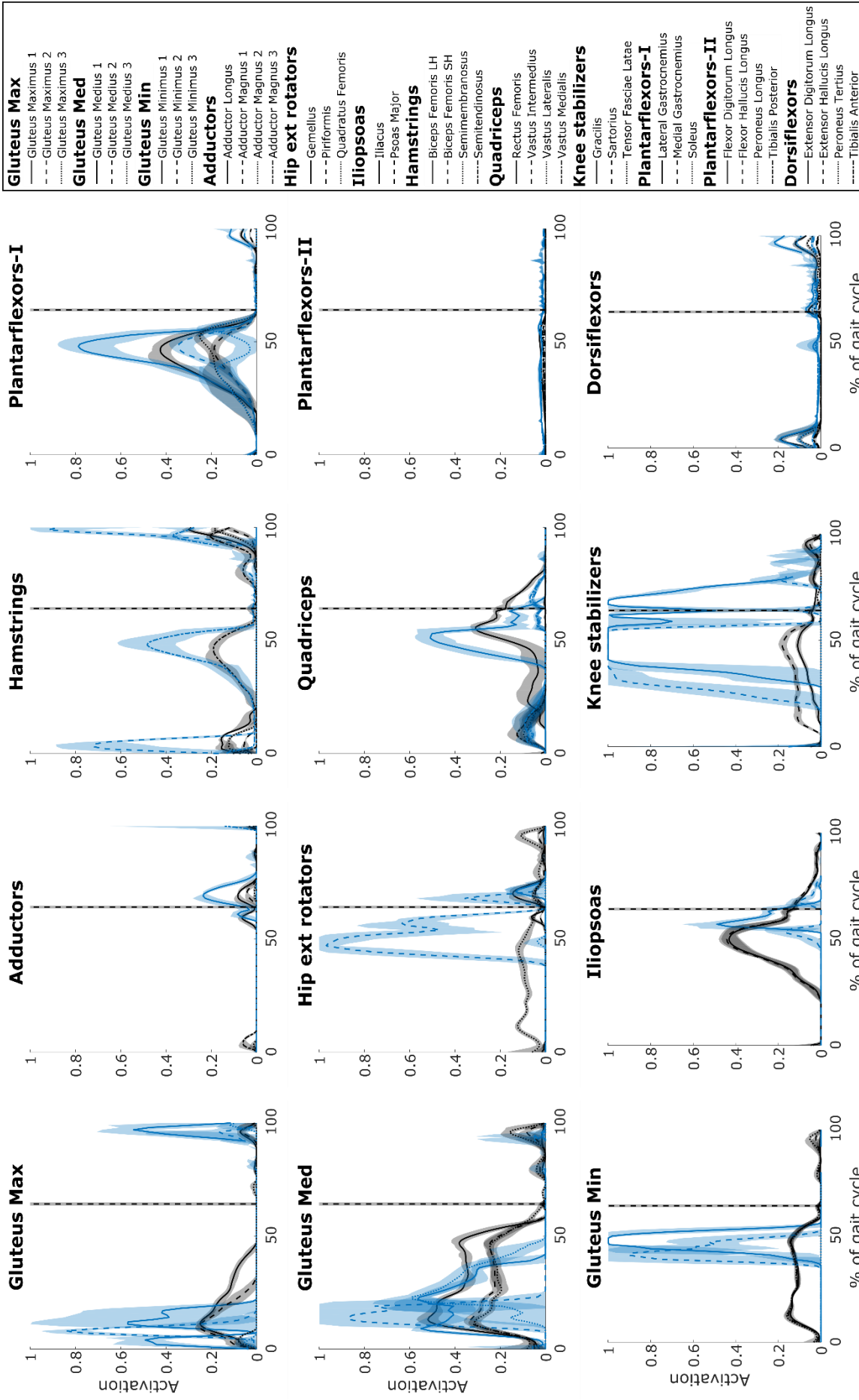
Figure A.5.4: Muscle activation trajectories for the solutions J_{FH} (blue) and J_{act} (black) of *p01* for the trials at a self-selected walking speed; mean (solid line) and range (shaded area) values are shown for the muscles grouped according to their functionality at the hip (left two columns), knee (middle right) and ankle (right).
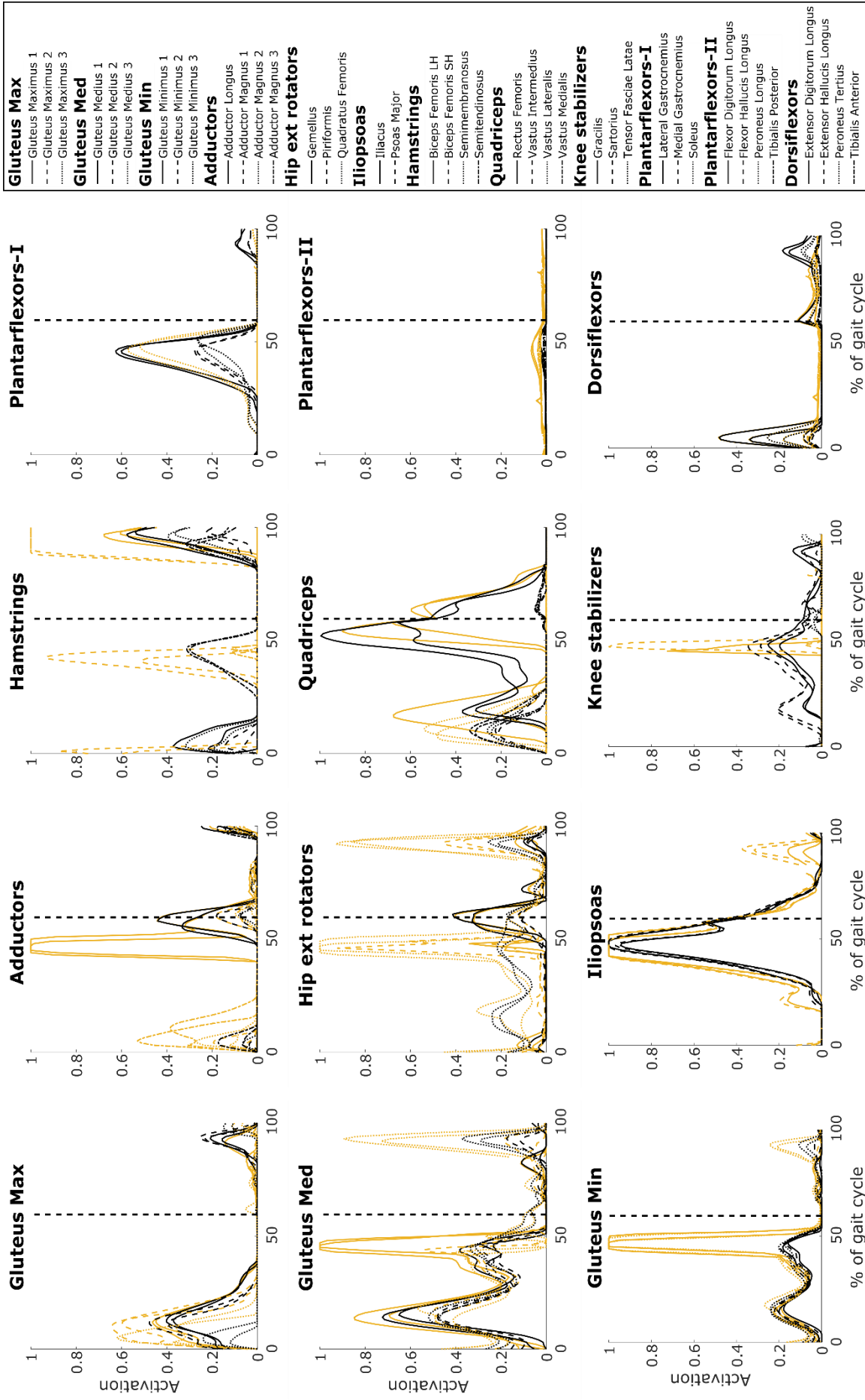
Figure A.5.5: Muscle activation trajectories for the solutions J_{FK} (yellow) and J_{act} (black) of *p01* for the trials at a self-selected walking speed; mean (solid line) and range (shaded area) values are shown for the muscles grouped according to their functionality at the hip (left two columns), knee (middle right) and ankle (right).

Figure A.5.6: Muscle activation trajectories for the solutions J_{FA} (red) and J_{act} (black) of *p01* for the trials at a self-selected walking speed; mean (solid line) and range (shaded area) values are shown for the muscles grouped according to their functionality at the hip (left two columns), knee (middle right) and ankle (right).
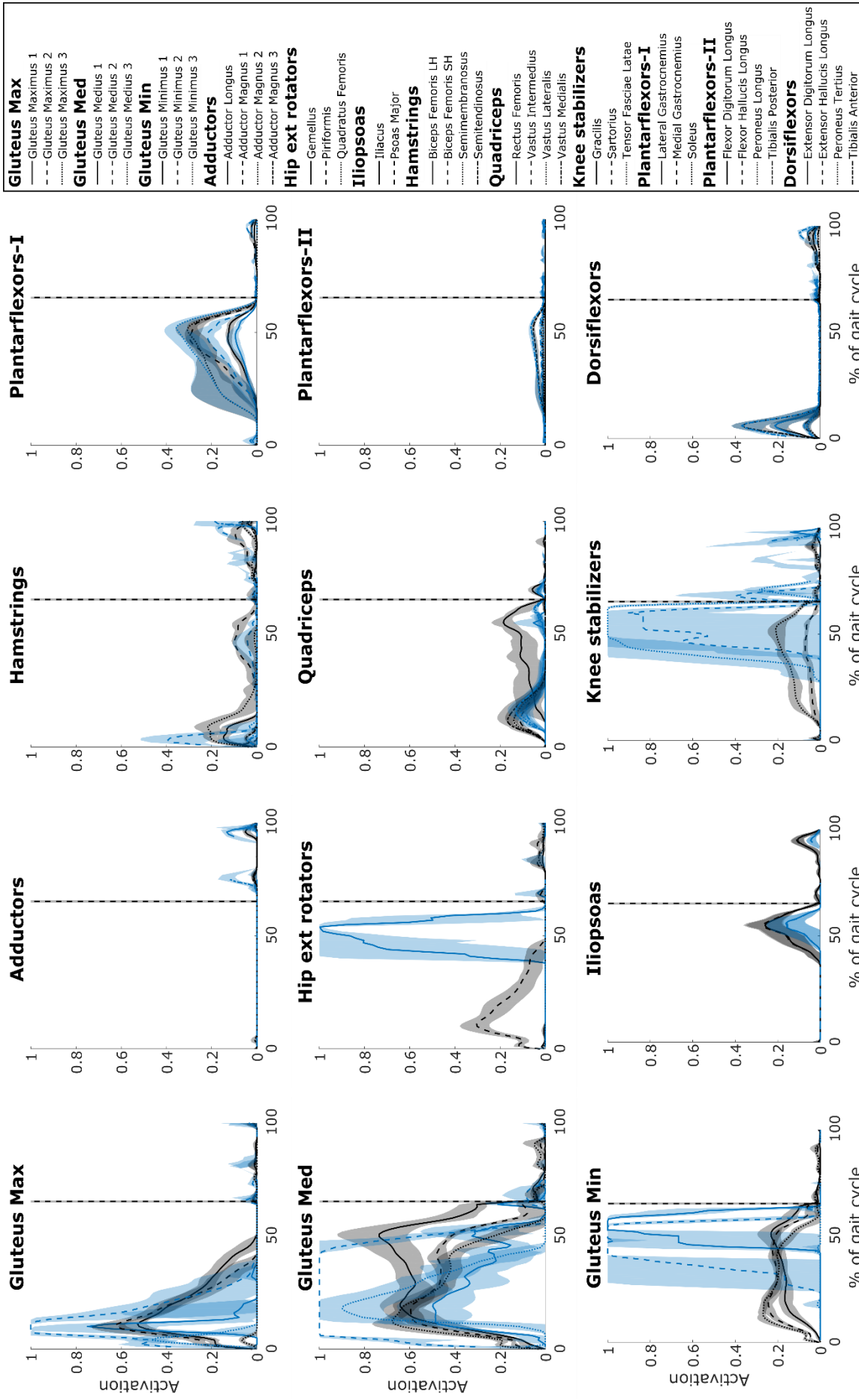
Figure A.5.7: Muscle activation trajectories for the solutions J_{FH} (blue) and J_{act} (black) of *p01* for the trials at a fast walking speed; mean (solid line) and range (shaded area) values are shown for the muscles grouped according to their functionality at the hip (left two columns), knee (middle right) and ankle (right).

Figure A.5.8: Muscle activation trajectories for the solutions J_{FK} (yellow) and J_{act} (black) of *p01* for the trials at a fast walking speed; mean (solid line) and range (shaded area) values are shown for the muscles grouped according to their functionality at the hip (left two columns), knee (middle right) and ankle (right).
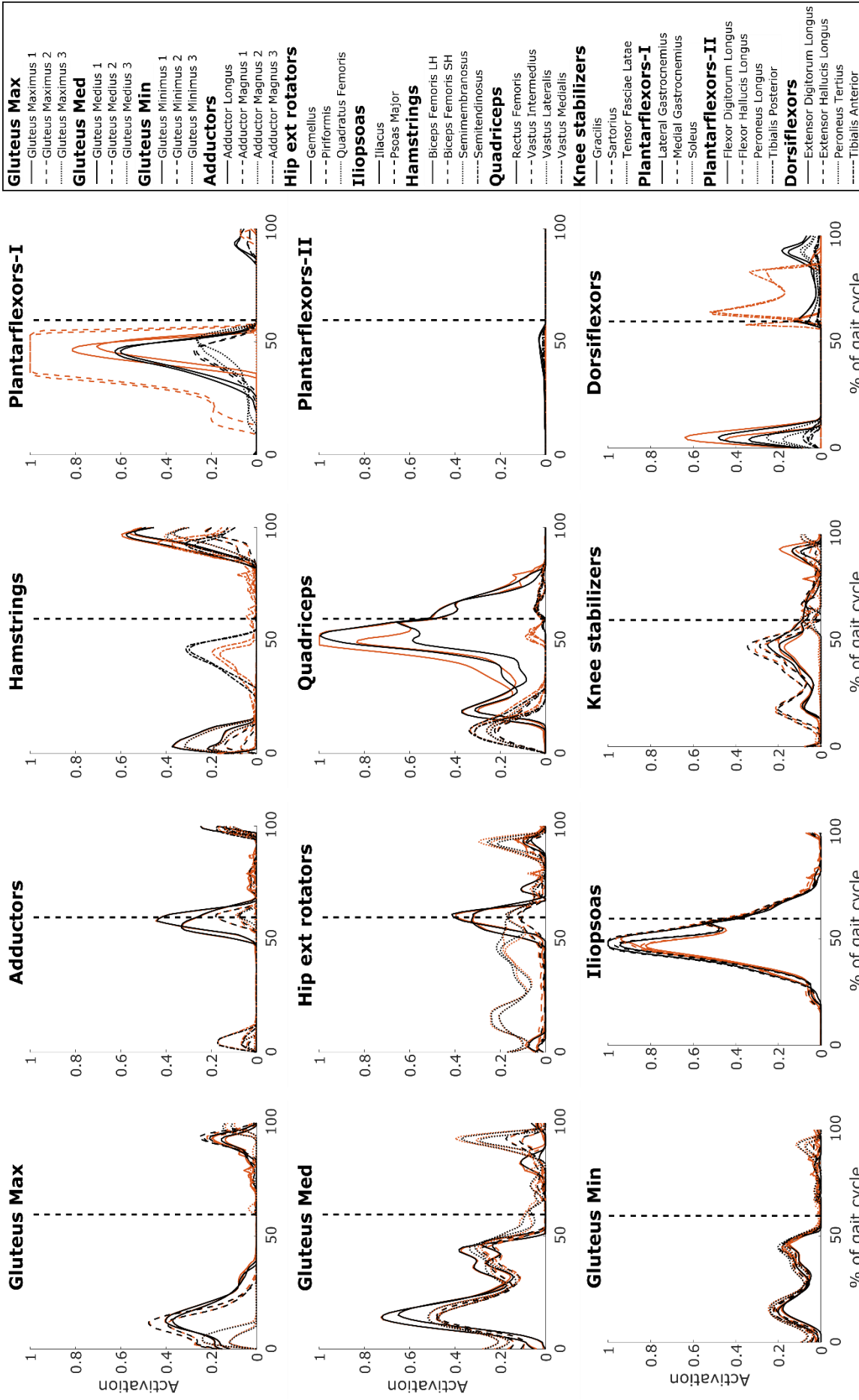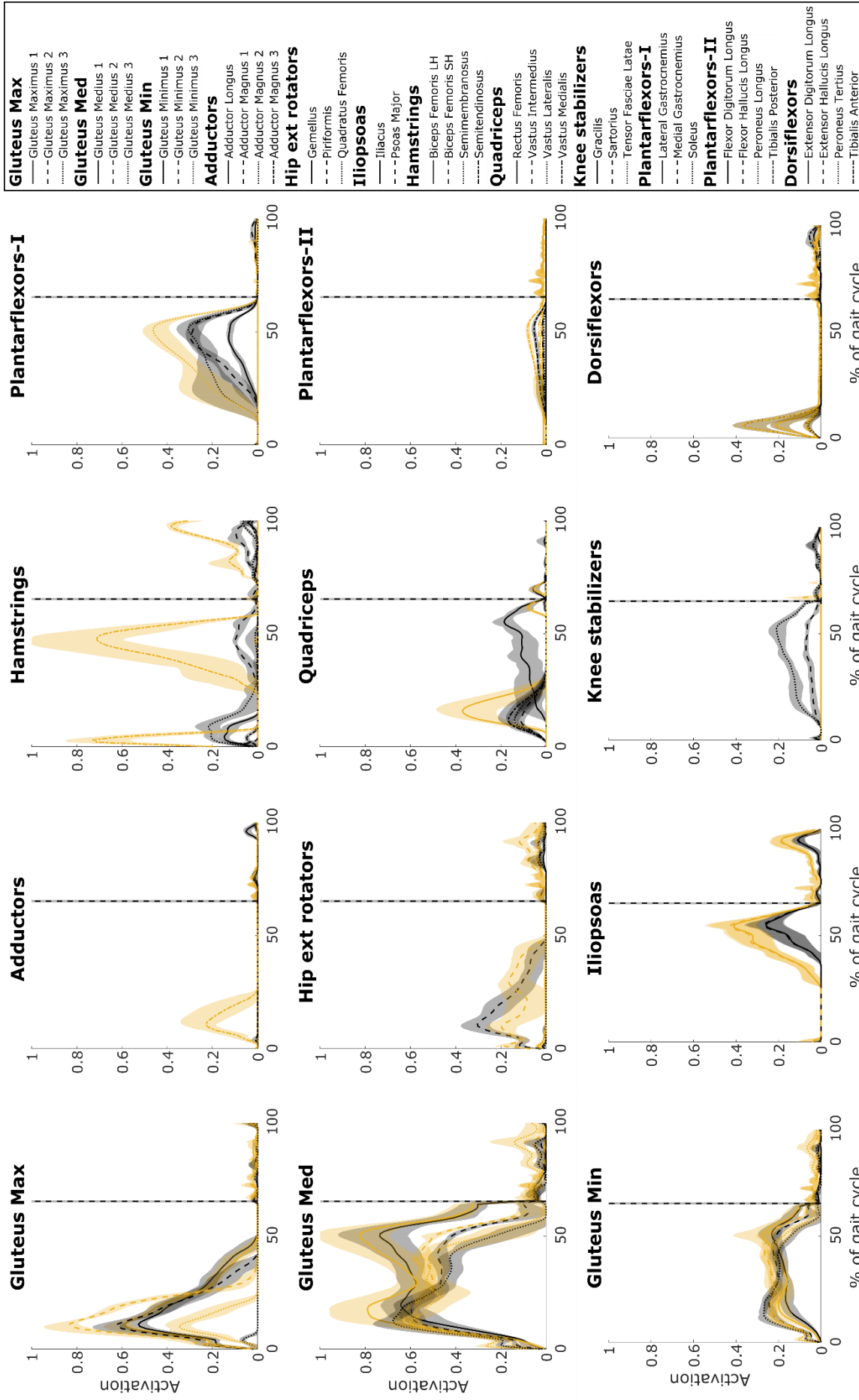
Figure A.5.9: Muscle activation trajectories for the solutions J_{FA} (red) and J_{act} (black) of *p01* for the trials at a fast walking speed; mean (solid line) and range (shaded area) values are shown for the muscles grouped according to their functionality at the hip (left two columns), knee (middle right) and ankle (right).
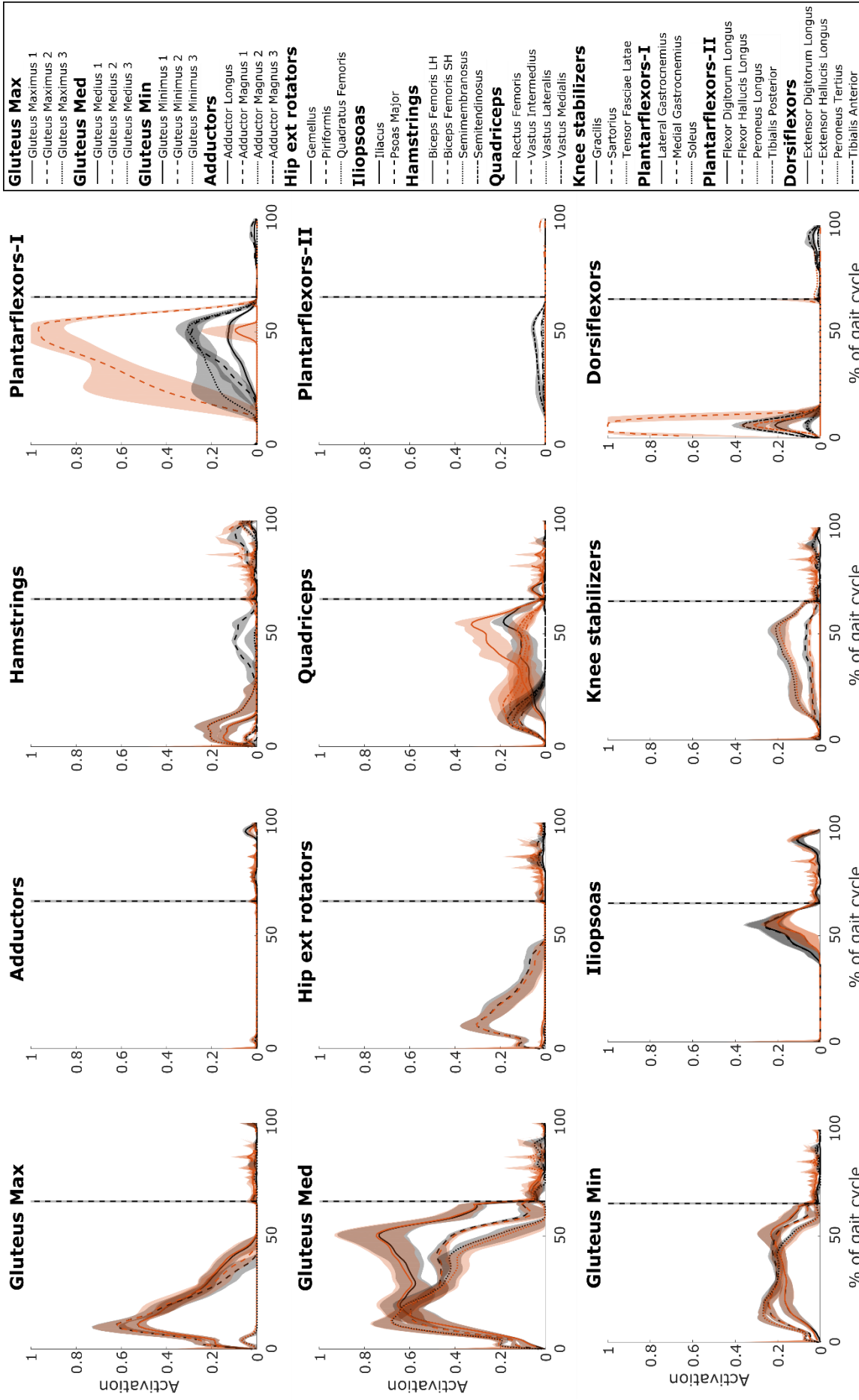
Figure A.5.10: Muscle activation trajectories for the solutions J_{FH} (blue) and J_{act} (black) of *p02* for the trials at a self-selected walking speed; mean (solid line) and range (shaded area) values are shown for the muscles grouped according to their functionality at the hip (left two columns), knee (middle right) and ankle (right).
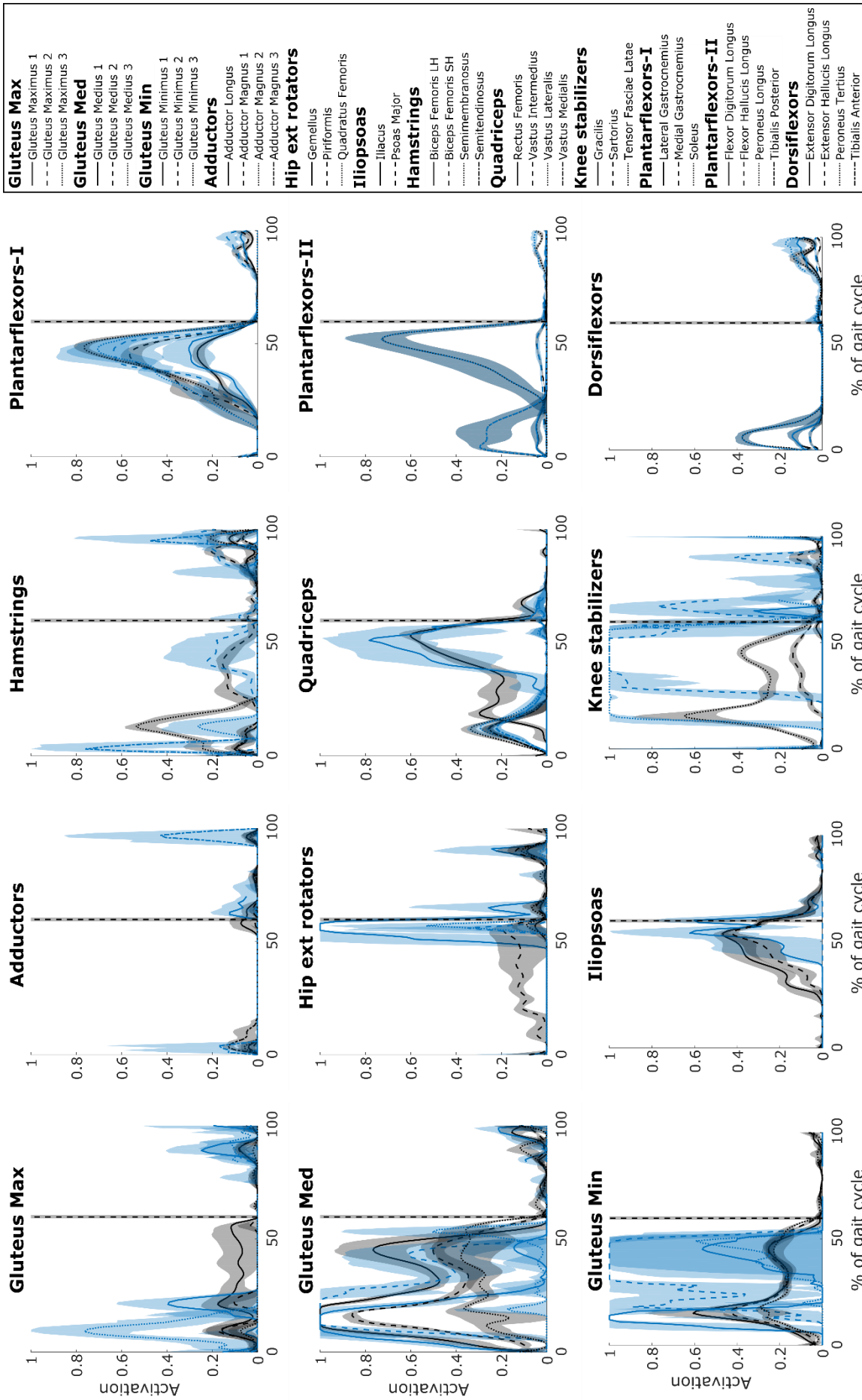
Figure A.5.11: Muscle activation trajectories for the solutions J_{FK} (yellow) and J_{act} (black) of *p02* for the trials at a self-selected walking speed; mean (solid line) and range (shaded area) values are shown for the muscles grouped according to their functionality at the hip (left two columns), knee (middle right) and ankle (right).
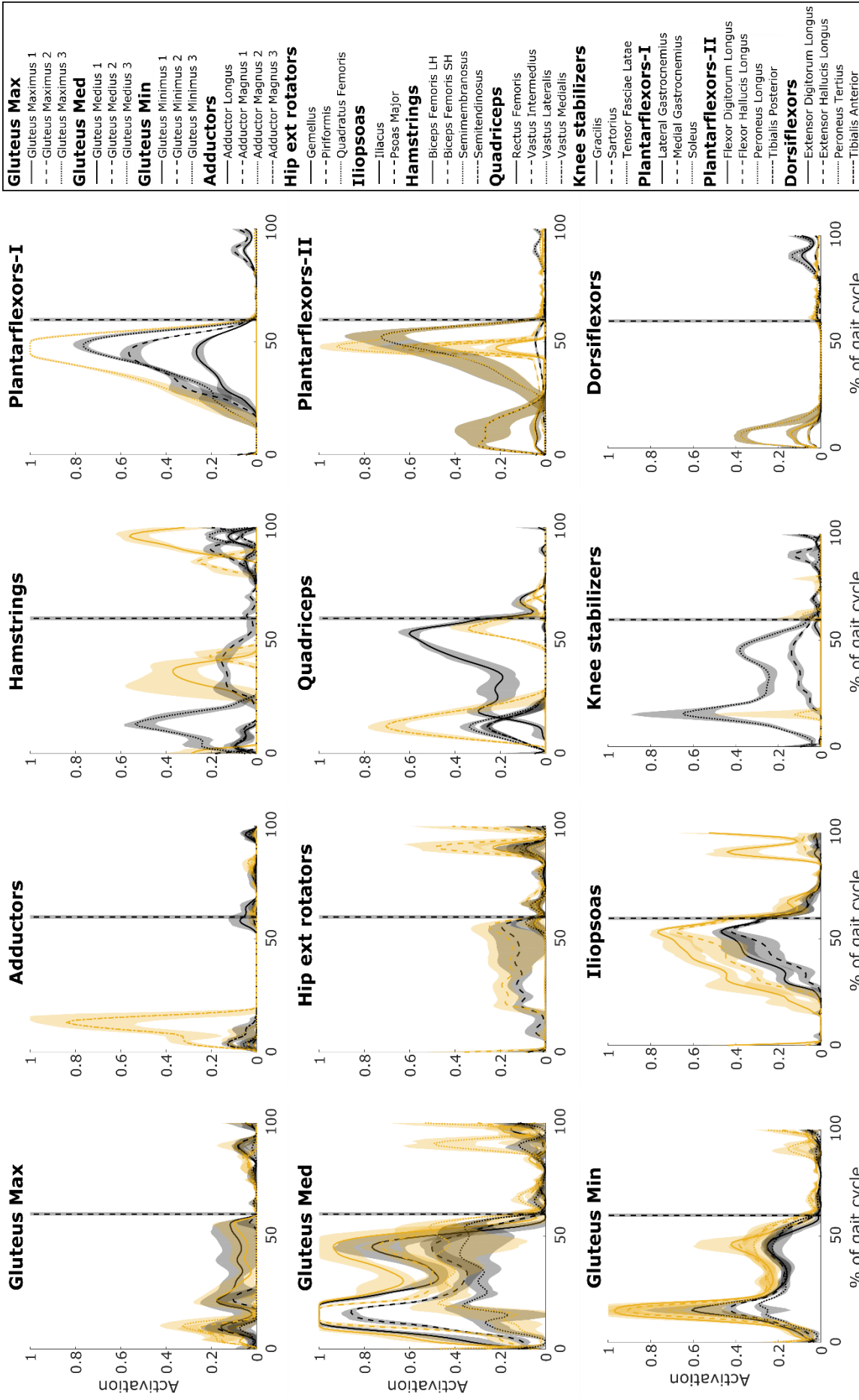
Figure A.5.12: Muscle activation trajectories for the solutions J_{FA} (red) and J_{act} (black) of *p02* for the trials at a self-selected walking speed; mean (solid line) and range (shaded area) values are shown for the muscles grouped according to their functionality at the hip (left two columns), knee (middle right) and ankle (right).

Figure A.5.13: Muscle activation trajectories for the solutions J_{FH} (blue) and J_{act} (black) of *p03* for the trials at a self-selected walking speed; mean (solid line) and range (shaded area) values are shown for the muscles grouped according to their functionality at the hip (left two columns), knee (middle right) and ankle (right).
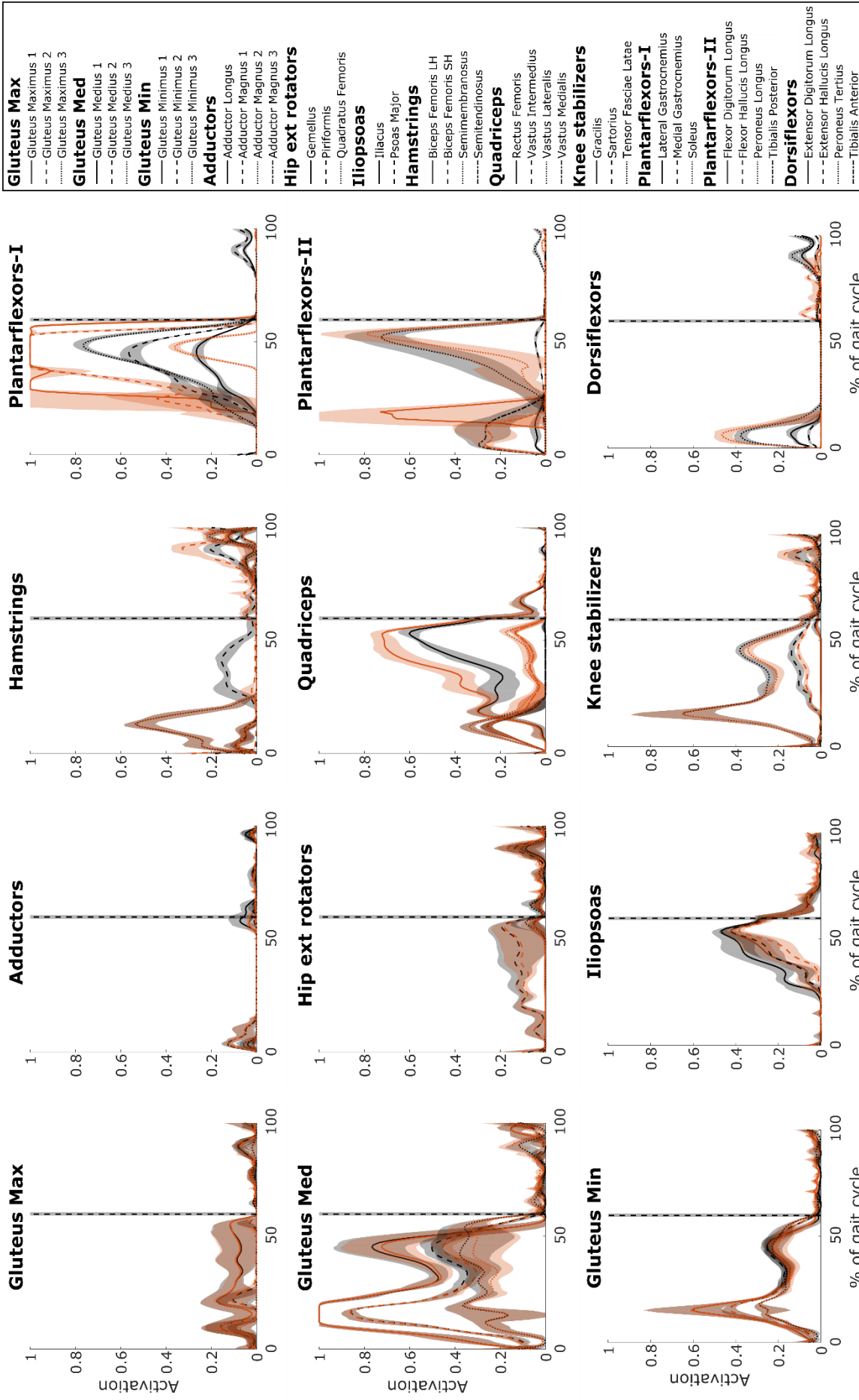
Figure A.5.14: Muscle activation trajectories for the solutions J_{FK} (yellow) and J_{act} (black) of *p03* for the trials at a self-selected walking speed; mean (solid line) and range (shaded area) values are shown for the muscles grouped according to their functionality at the hip (left two columns), knee (middle right) and ankle (right).
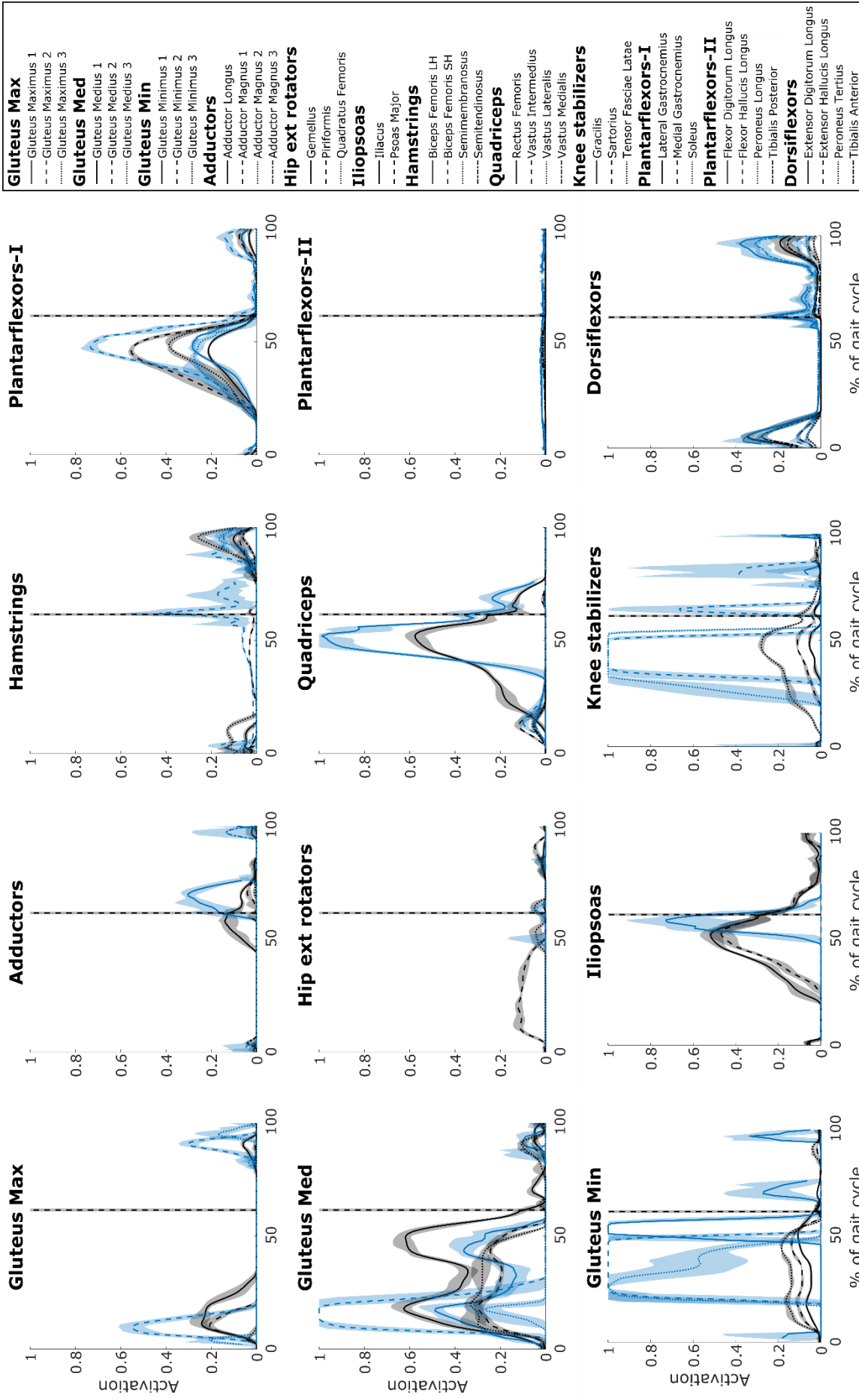
Figure A.5.15: Muscle activation trajectories for the solutions J_{FA} (red) and J_{act} (black) of *p03* for the trials at a self-selected walking speed; mean (solid line) and range (shaded area) values are shown for the muscles grouped according to their functionality at the hip (left two columns), knee (middle right) and ankle (right).

Figure A.5.16: Muscle activation trajectories for the solutions J_{FH} (blue) and J_{act} (black) of *p04* for the trials at a slow walking speed; mean (solid line) and range (shaded area) values are shown for the muscles grouped according to their functionality at the hip (left two columns), knee (middle right) and ankle (right).
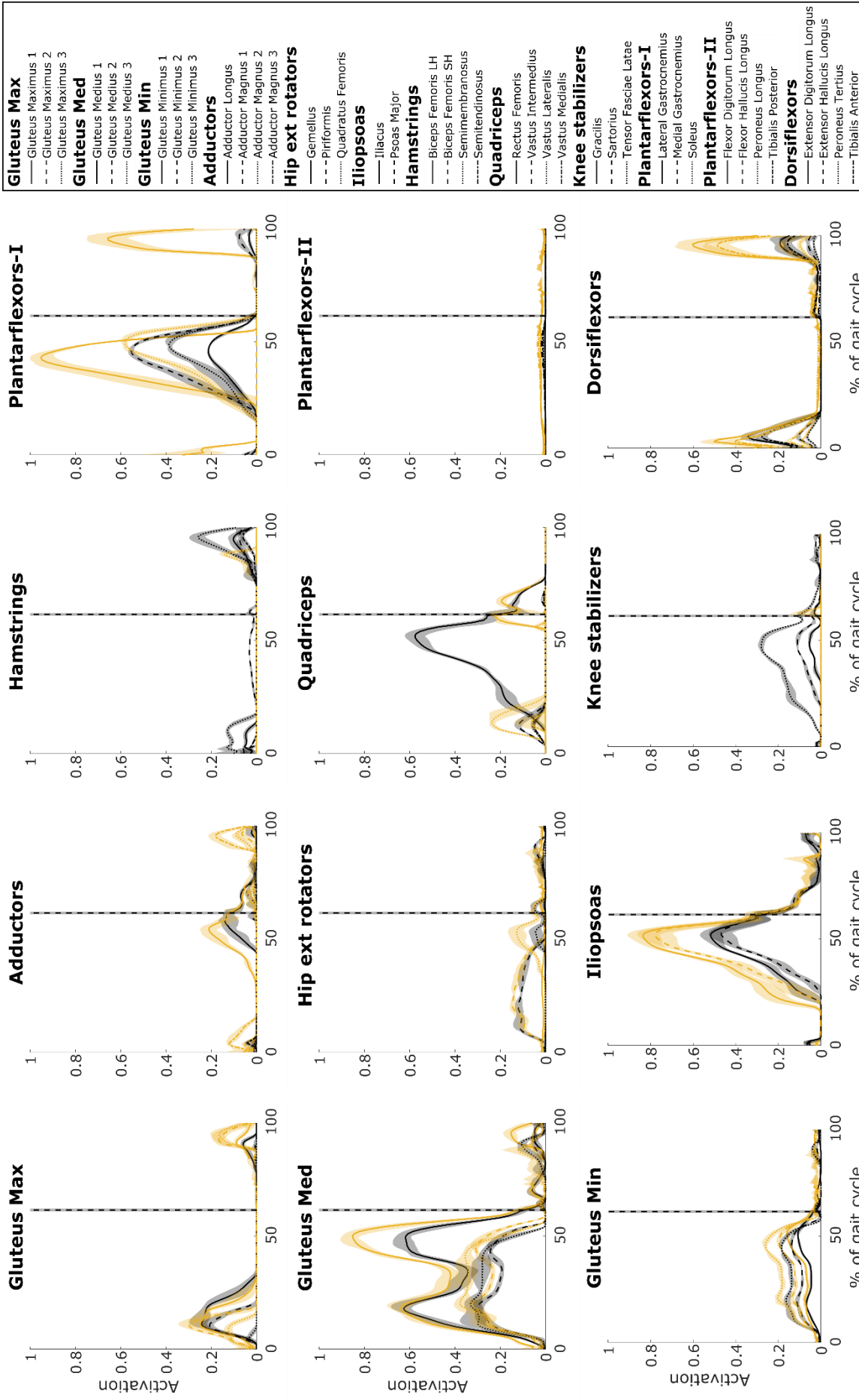
Figure A.5.17: Muscle activation trajectories for the solutions J_{FK} (yellow) and J_{act} (black) of *p04* for the trials at a slow walking speed; mean (solid line) and range (shaded area) values are shown for the muscles grouped according to their functionality at the hip (left two columns), knee (middle right) and ankle (right).
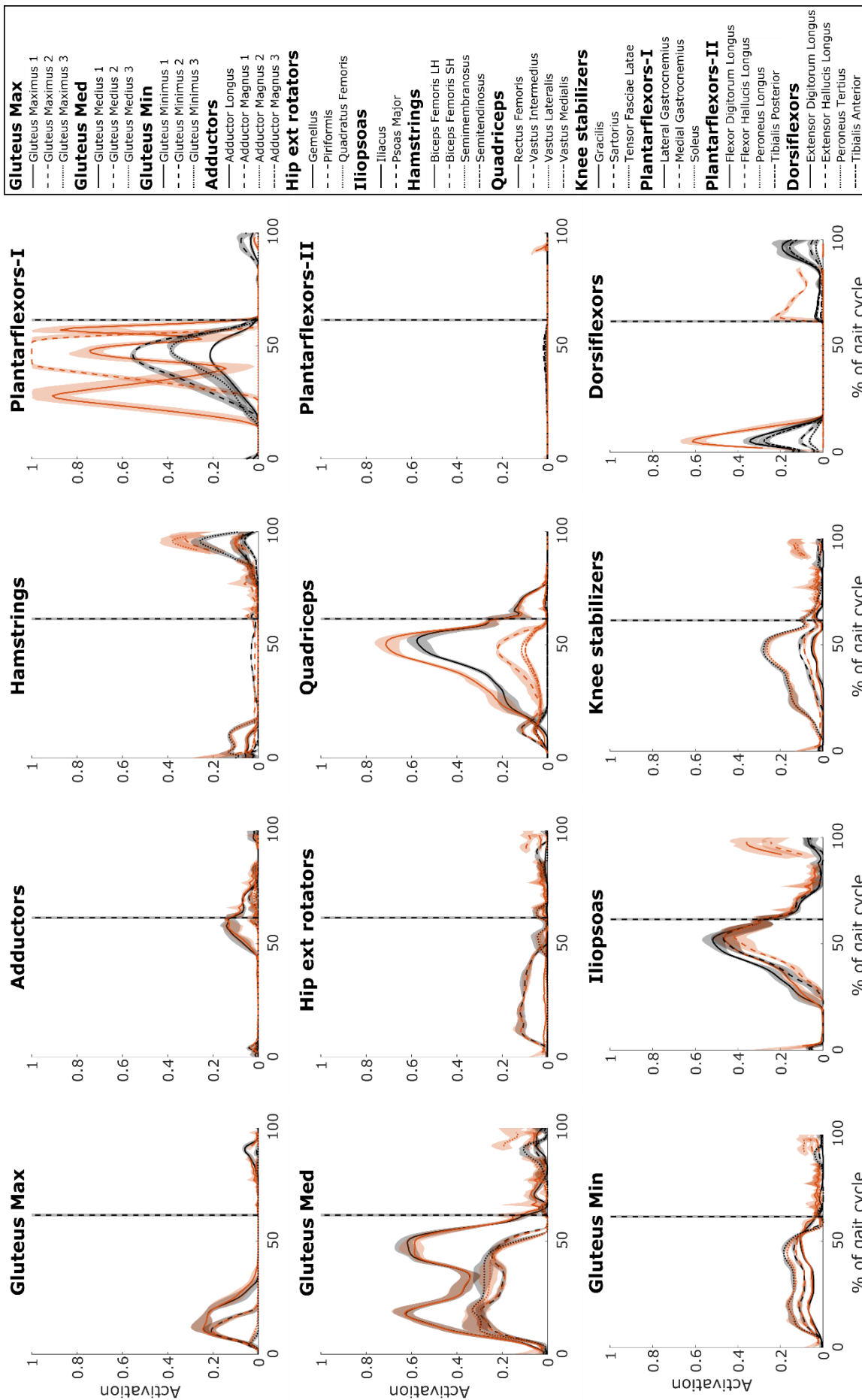
Figure A.5.18: Muscle activation trajectories for the solutions J_{FA} (red) and J_{act} (black) of *p04* for the trials at a slow walking speed; mean (solid line) and range (shaded area) values are shown for the muscles grouped according to their functionality at the hip (left two columns), knee (middle right) and ankle (right).
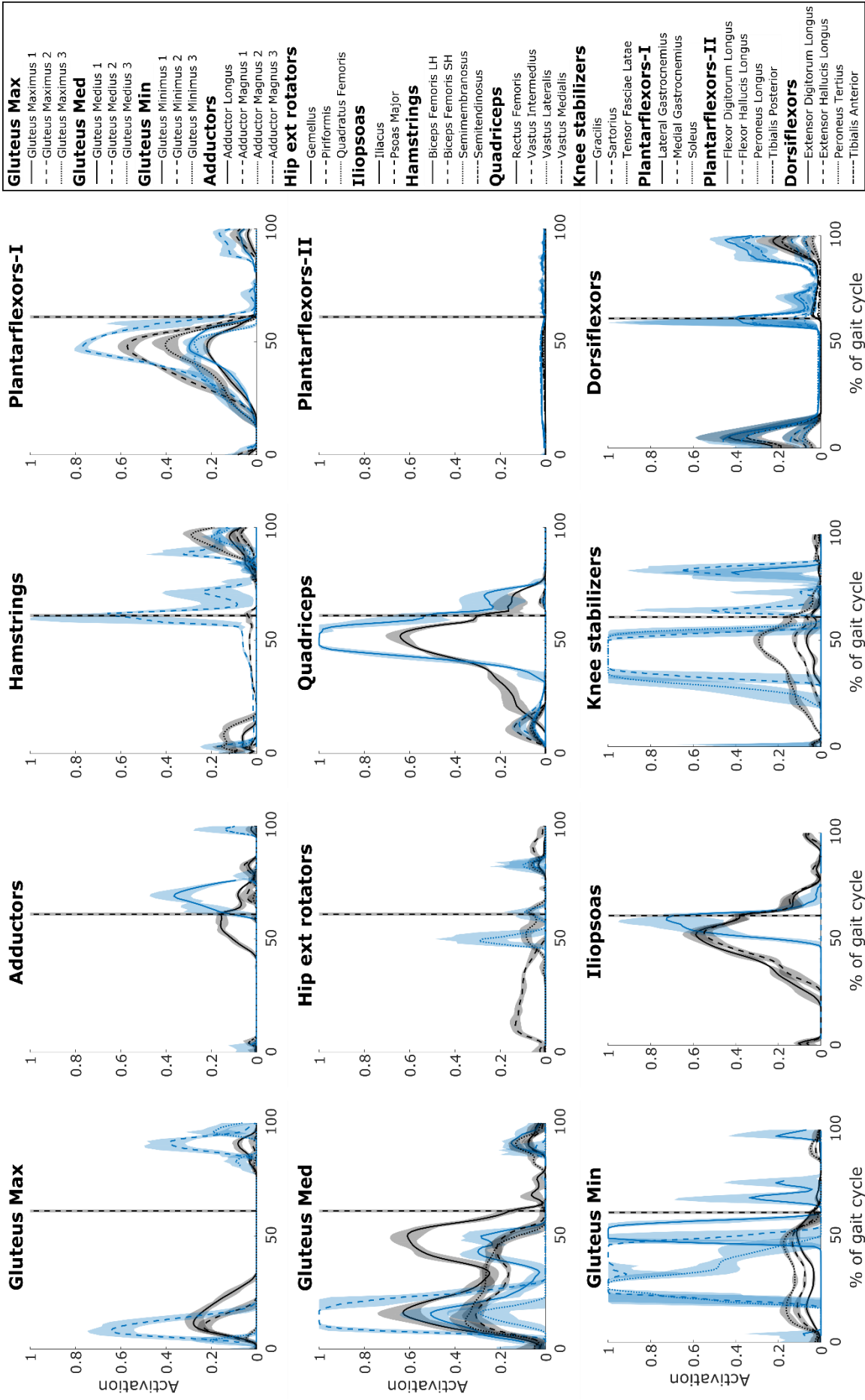
Figure A.5.19: Muscle activation trajectories for the solutions J_{FH} (blue) and J_{act} (black) of *p04* for the trials at a self-selected walking speed; mean (solid line) and range (shaded area) values are shown for the muscles grouped according to their functionality at the hip (left two columns), knee (middle right) and ankle (right).

Figure A.5.20: Muscle activation trajectories for the solutions J_{FK} (yellow) and J_{act} (black) of *p04* for the trials at a self-selected walking speed; mean (solid line) and range (shaded area) values are shown for the muscles grouped according to their functionality at the hip (left two columns), knee (middle right) and ankle (right).
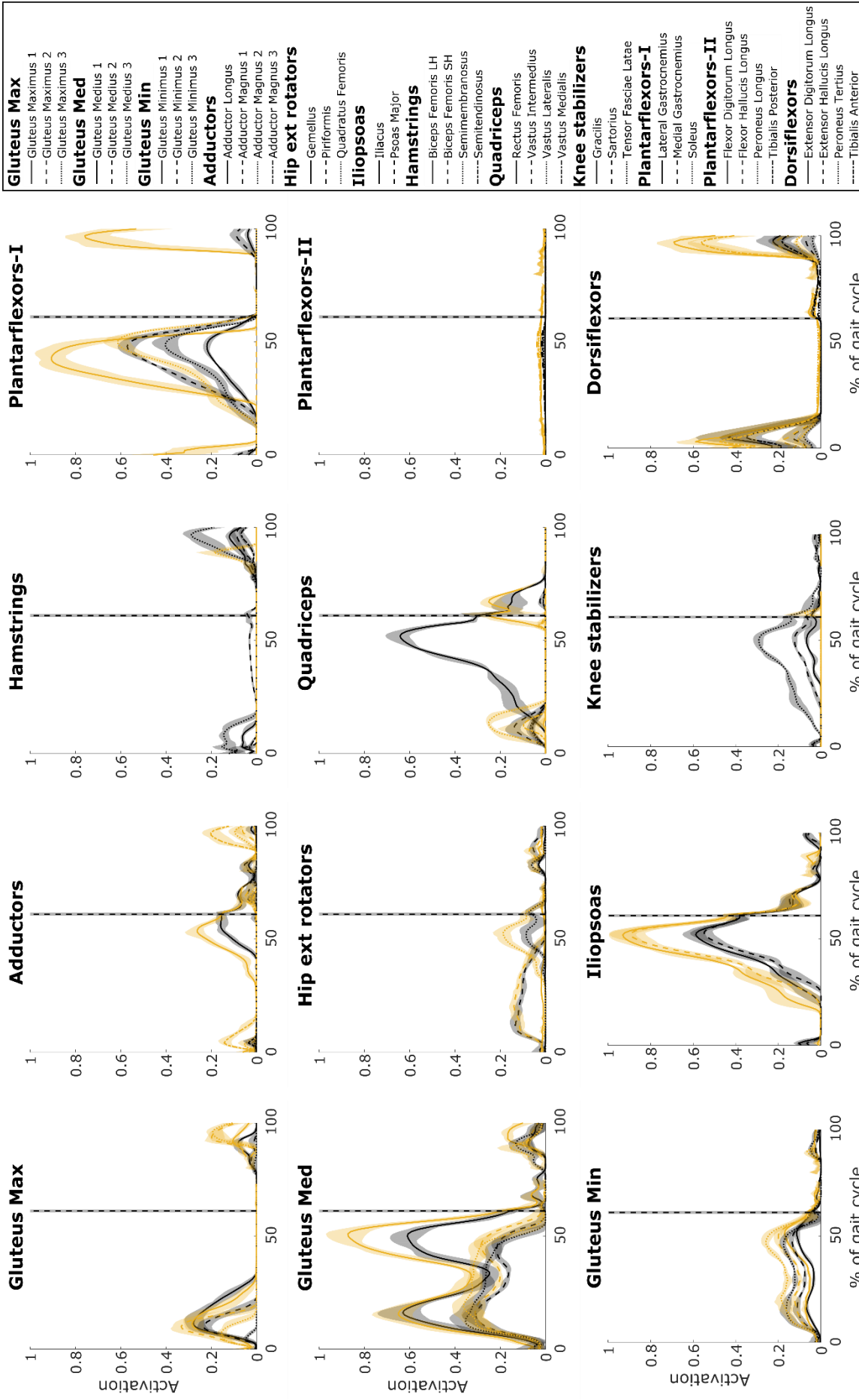
Figure A.5.21: Muscle activation trajectories for the solutions J_{FA} (red) and J_{act} (black) of *p04* for the trials at a self-selected walking speed; mean (solid line) and range (shaded area) values are shown for the muscles grouped according to their functionality at the hip (left two columns), knee (middle right) and ankle (right).
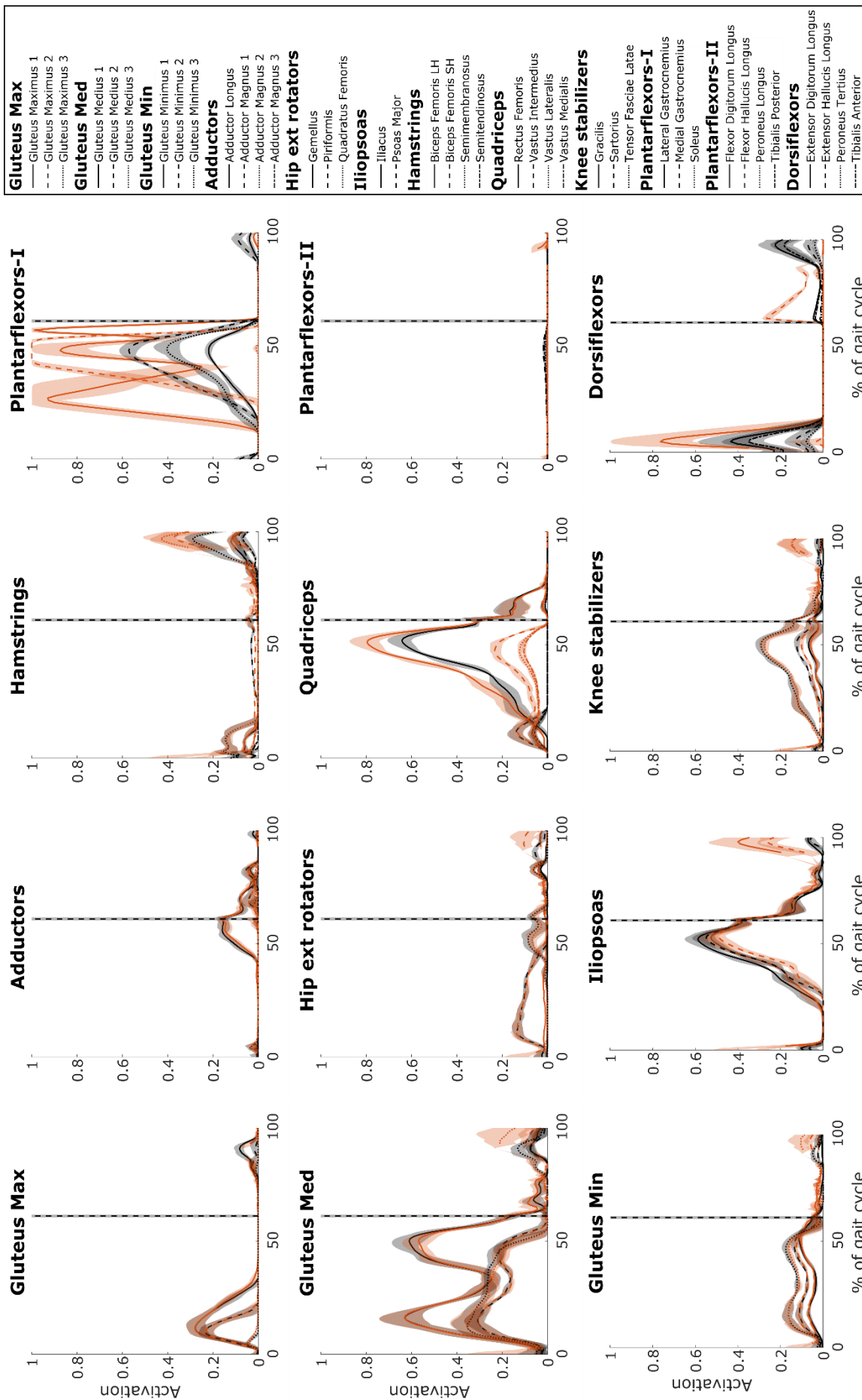
Figure A.5.22: Muscle activation trajectories for the solutions J_{FH} (blue) and J_{act} (black) of *p04* for the trials at a fast walking speed; mean (solid line) and range (shaded area) values are shown for the muscles grouped according to their functionality at the hip (left two columns), knee (middle right) and ankle (right).
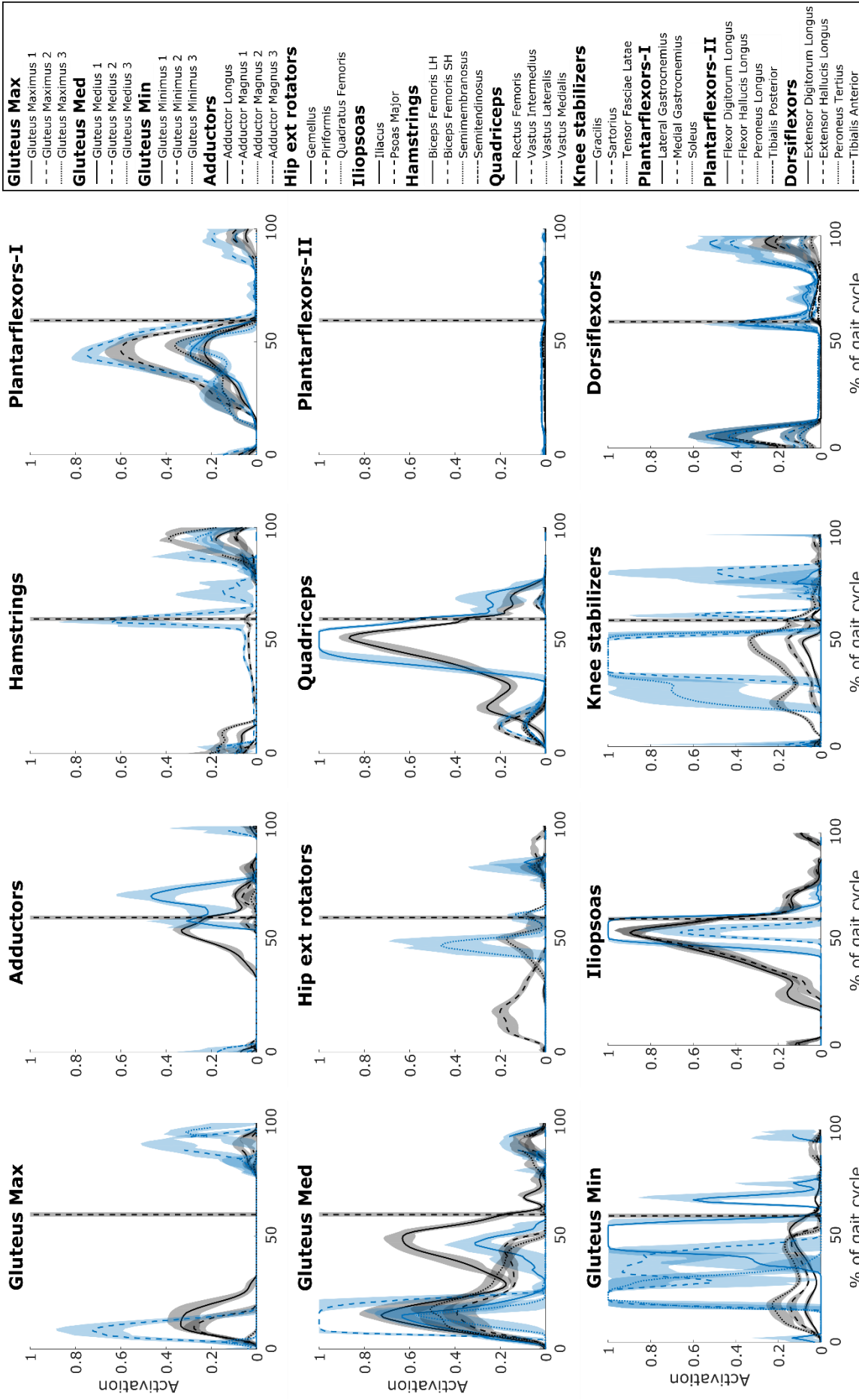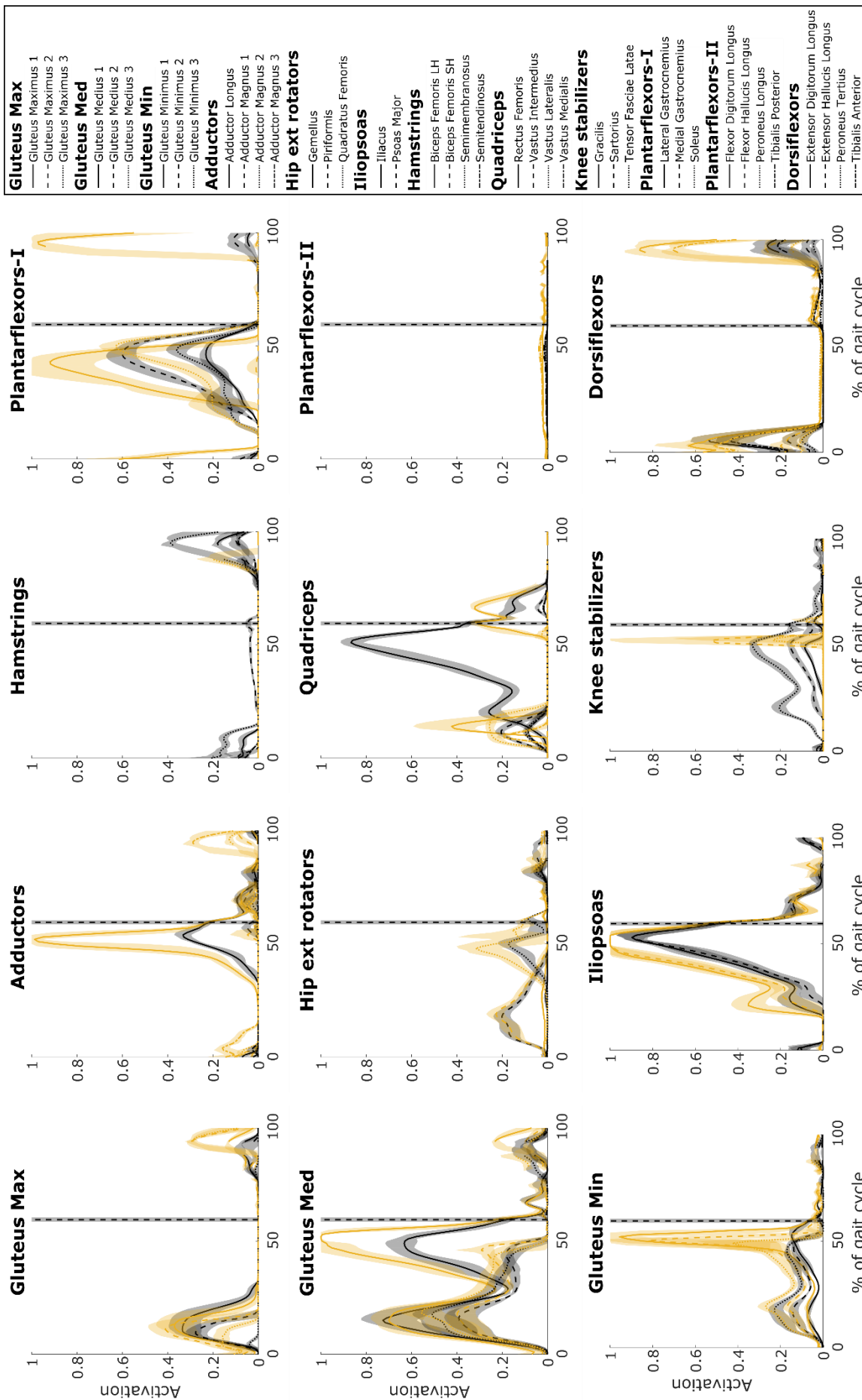
Figure A.5.23: Muscle activation trajectories for the solutions J_{FK} (yellow) and J_{act} (black) of *p04* for the trials at a fast walking speed; mean (solid line) and range (shaded area) values are shown for the muscles grouped according to their functionality at the hip (left two columns), knee (middle right) and ankle (right).

Figure A.5.24: Muscle activation trajectories for the solutions J_{FA} (red) and J_{act} (black) of *p04* for the trials at a fast walking speed; mean (solid line) and range (shaded area) values are shown for the muscles grouped according to their functionality at the hip (left two columns), knee (middle right) and ankle (right).
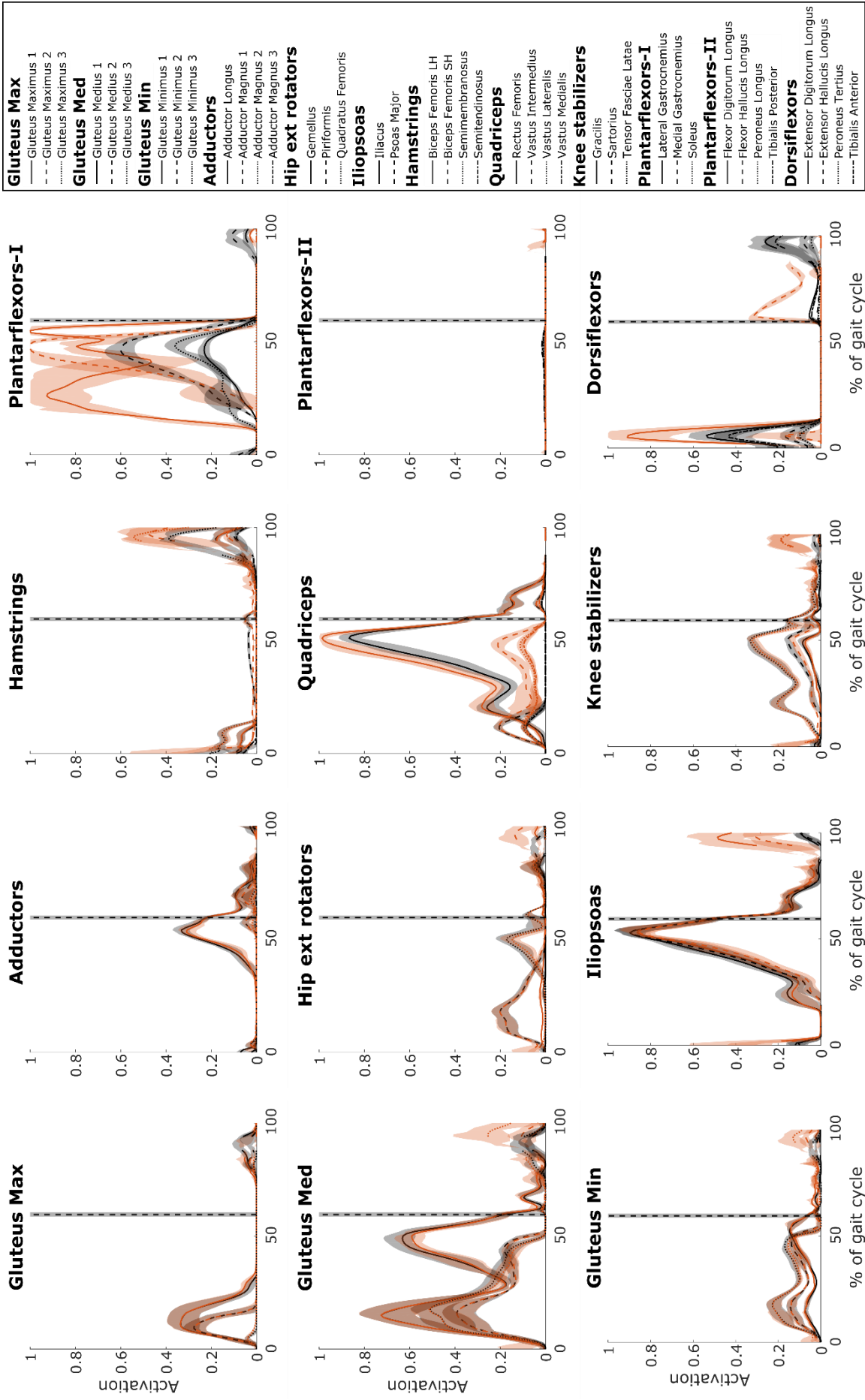
A.6 Table of muscle activation patterns

Table A.6.1: Muscle activations at the time of peak hip, knee and ankle contact force magnitude in the J_{act} solution, given for both the J_{act} and the corresponding J_{Fj} solution. Muscle activation values are averaged over trials at self-selected speed, shown as mean ± standard deviation, and represented by a colour scale (white: no activation, red: full activation). For each muscle, the four rows represent the activation level for the four different participants.

			a at t(Fh_max)		a at t(Fk_max)		a at t(Fa_max)	
			Jact	Jhf	Jact	Jhf	Jact	Jhf
Gluteus Max	Gluteus Maximus 1	p01	0.00 ± 0.00	0.00 ± 0.00	0.00 ± 0.00	0.00 ± 0.00	0.00 ± 0.00	0.01 ± 0.00
		p02	0.03 ± 0.07	0.00 ± 0.00	0.03 ± 0.06	0.02 ± 0.05	0.00 ± 0.00	0.00 ± 0.00
		p03	0.07 ± 0.07	0.00 ± 0.00	0.07 ± 0.07	0.04 ± 0.05	0.08 ± 0.08	0.08 ± 0.08
		p04	0.00 ± 0.00	0.00 ± 0.00	0.00 ± 0.00	0.00 ± 0.00	0.00 ± 0.00	0.00 ± 0.00
	Gluteus Maximus 2	p01	0.00 ± 0.00	0.00 ± 0.00	0.00 ± 0.00	0.00 ± 0.00	0.00 ± 0.00	0.00 ± 0.00
		p02	0.01 ± 0.02	0.00 ± 0.00	0.00 ± 0.00	0.00 ± 0.00	0.00 ± 0.00	0.00 ± 0.00
		p03	0.00 ± 0.00	0.00 ± 0.00	0.00 ± 0.00	0.00 ± 0.00	0.00 ± 0.00	0.00 ± 0.00
		p04	0.00 ± 0.00	0.00 ± 0.00	0.00 ± 0.00	0.00 ± 0.00	0.00 ± 0.00	0.00 ± 0.00
	Gluteus Maximus 3	p01	0.00 ± 0.00	0.00 ± 0.00	0.00 ± 0.00	0.00 ± 0.00	0.00 ± 0.00	0.00 ± 0.00
		p02	0.00 ± 0.00	0.00 ± 0.00	0.00 ± 0.00	0.00 ± 0.00	0.00 ± 0.00	0.00 ± 0.00
		p03	0.00 ± 0.00	0.00 ± 0.00	0.00 ± 0.00	0.00 ± 0.00	0.00 ± 0.00	0.00 ± 0.00
		p04	0.00 ± 0.00	0.00 ± 0.00	0.00 ± 0.00	0.00 ± 0.00	0.00 ± 0.00	0.00 ± 0.00
Gluteus Med	Gluteus Medius 1	p01	0.35 ± 0.04	0.00 ± 0.00	0.35 ± 0.04	0.48 ± 0.04	0.34 ± 0.02	0.33 ± 0.02
		p02	0.70 ± 0.10	0.26 ± 0.15	0.70 ± 0.08	0.80 ± 0.11	0.71 ± 0.09	0.72 ± 0.09
		p03	0.75 ± 0.14	0.14 ± 0.19	0.76 ± 0.14	0.94 ± 0.08	0.69 ± 0.17	0.65 ± 0.18
		p04	0.61 ± 0.05	0.28 ± 0.09	0.61 ± 0.05	0.86 ± 0.06	0.60 ± 0.05	0.56 ± 0.05
	Gluteus Medius 2	p01	0.22 ± 0.03	0.00 ± 0.00	0.22 ± 0.02	0.29 ± 0.03	0.21 ± 0.01	0.19 ± 0.01
		p02	0.41 ± 0.06	0.57 ± 0.33	0.43 ± 0.05	0.50 ± 0.05	0.41 ± 0.04	0.39 ± 0.04
		p03	0.49 ± 0.06	0.46 ± 0.30	0.49 ± 0.06	0.73 ± 0.03	0.46 ± 0.06	0.42 ± 0.05
		p04	0.17 ± 0.01	0.00 ± 0.00	0.20 ± 0.02	0.27 ± 0.02	0.20 ± 0.02	0.18 ± 0.02
	Gluteus Medius 3	p01	0.21 ± 0.04	0.00 ± 0.00	0.21 ± 0.03	0.28 ± 0.04	0.20 ± 0.03	0.15 ± 0.03
		p02	0.26 ± 0.13	0.07 ± 0.17	0.28 ± 0.11	0.35 ± 0.14	0.23 ± 0.08	0.19 ± 0.08
		p03	0.36 ± 0.17	0.03 ± 0.06	0.36 ± 0.17	0.43 ± 0.29	0.35 ± 0.18	0.30 ± 0.17
		p04	0.11 ± 0.04	0.00 ± 0.00	0.16 ± 0.04	0.23 ± 0.05	0.17 ± 0.03	0.15 ± 0.03
Gluteus Min	Gluteus Minimus 1	p01	0.13 ± 0.01	0.99 ± 0.03	0.13 ± 0.01	0.19 ± 0.02	0.13 ± 0.01	0.11 ± 0.01
		p02	0.22 ± 0.03	0.83 ± 0.41	0.22 ± 0.03	0.26 ± 0.04	0.22 ± 0.03	0.22 ± 0.03
		p03	0.25 ± 0.02	0.51 ± 0.48	0.25 ± 0.02	0.42 ± 0.13	0.23 ± 0.03	0.21 ± 0.03
		p04	0.11 ± 0.01	1.00 ± 0.00	0.11 ± 0.01	0.16 ± 0.01	0.11 ± 0.01	0.10 ± 0.01
	Gluteus Minimus 2	p01	0.14 ± 0.01	0.33 ± 0.23	0.14 ± 0.01	0.19 ± 0.02	0.13 ± 0.01	0.11 ± 0.01
		p02	0.21 ± 0.02	0.94 ± 0.16	0.21 ± 0.02	0.26 ± 0.02	0.21 ± 0.02	0.20 ± 0.02
		p03	0.25 ± 0.03	1.00 ± 0.00	0.25 ± 0.03	0.38 ± 0.02	0.24 ± 0.03	0.21 ± 0.02
		p04	0.13 ± 0.01	0.30 ± 0.45	0.13 ± 0.01	0.20 ± 0.01	0.13 ± 0.01	0.12 ± 0.01
	Gluteus Minimus 3	p01	0.13 ± 0.02	0.00 ± 0.00	0.13 ± 0.01	0.18 ± 0.02	0.13 ± 0.01	0.11 ± 0.01
		p02	0.15 ± 0.04	0.00 ± 0.00	0.16 ± 0.04	0.20 ± 0.05	0.14 ± 0.03	0.12 ± 0.03
		p03	0.22 ± 0.05	0.45 ± 0.45	0.22 ± 0.05	0.31 ± 0.06	0.21 ± 0.05	0.19 ± 0.05
		p04	0.16 ± 0.01	0.00 ± 0.00	0.17 ± 0.01	0.26 ± 0.02	0.17 ± 0.01	0.16 ± 0.01
Adductors	Adductor Brevis	p01	0.00 ± 0.00	0.00 ± 0.00	0.00 ± 0.00	0.00 ± 0.00	0.00 ± 0.00	0.00 ± 0.00
		p02	0.00 ± 0.00	0.00 ± 0.00	0.00 ± 0.00	0.00 ± 0.00	0.00 ± 0.00	0.00 ± 0.00
		p03	0.00 ± 0.00	0.00 ± 0.00	0.00 ± 0.00	0.00 ± 0.00	0.00 ± 0.00	0.00 ± 0.00
		p04	0.07 ± 0.02	0.00 ± 0.00	0.06 ± 0.02	0.15 ± 0.02	0.06 ± 0.02	0.04 ± 0.01
	Adductor Longus	p01	0.00 ± 0.00	0.00 ± 0.00	0.00 ± 0.00	0.00 ± 0.00	0.00 ± 0.00	0.00 ± 0.00
		p02	0.00 ± 0.00	0.00 ± 0.00	0.00 ± 0.00	0.00 ± 0.00	0.00 ± 0.00	0.00 ± 0.00
		p03	0.00 ± 0.00	0.00 ± 0.00	0.00 ± 0.00	0.00 ± 0.00	0.00 ± 0.00	0.00 ± 0.00
		p04	0.11 ± 0.02	0.00 ± 0.00	0.09 ± 0.02	0.20 ± 0.03	0.09 ± 0.02	0.07 ± 0.02
	Adductor Magnus 1	p01	0.00 ± 0.00	0.00 ± 0.00	0.00 ± 0.00	0.00 ± 0.00	0.00 ± 0.00	0.00 ± 0.00
		p02	0.00 ± 0.00	0.00 ± 0.00	0.00 ± 0.00	0.00 ± 0.00	0.00 ± 0.00	0.00 ± 0.00
		p03	0.00 ± 0.00	0.00 ± 0.00	0.00 ± 0.00	0.00 ± 0.00	0.00 ± 0.00	0.00 ± 0.00
		p04	0.00 ± 0.00	0.00 ± 0.00	0.00 ± 0.00	0.00 ± 0.00	0.00 ± 0.00	0.00 ± 0.00
	Adductor Magnus 2	p01	0.00 ± 0.00	0.00 ± 0.00	0.00 ± 0.00	0.00 ± 0.00	0.00 ± 0.00	0.00 ± 0.00
		p02	0.00 ± 0.00	0.00 ± 0.00	0.00 ± 0.00	0.00 ± 0.00	0.00 ± 0.00	0.00 ± 0.00
		p03	0.00 ± 0.00	0.00 ± 0.00	0.00 ± 0.00	0.00 ± 0.00	0.00 ± 0.00	0.00 ± 0.00
		p04	0.00 ± 0.00	0.00 ± 0.00	0.00 ± 0.00	0.00 ± 0.00	0.00 ± 0.00	0.00 ± 0.00
	Adductor Magnus 3	p01	0.00 ± 0.00	0.00 ± 0.00	0.00 ± 0.00	0.00 ± 0.00	0.00 ± 0.00	0.00 ± 0.00
		p02	0.00 ± 0.00	0.00 ± 0.00	0.00 ± 0.00	0.00 ± 0.00	0.00 ± 0.00	0.00 ± 0.00
		p03	0.00 ± 0.00	0.00 ± 0.00	0.00 ± 0.00	0.00 ± 0.00	0.00 ± 0.00	0.00 ± 0.00
		p04	0.00 ± 0.00	0.00 ± 0.00	0.00 ± 0.00	0.00 ± 0.00	0.00 ± 0.00	0.00 ± 0.00
	Pectineus	p01	0.00 ± 0.00	0.00 ± 0.00	0.00 ± 0.00	0.01 ± 0.00	0.00 ± 0.00	0.01 ± 0.00
		p02	0.00 ± 0.00	0.00 ± 0.00	0.00 ± 0.00	0.00 ± 0.00	0.00 ± 0.00	0.00 ± 0.00
		p03	0.00 ± 0.00	0.00 ± 0.00	0.00 ± 0.00	0.00 ± 0.00	0.00 ± 0.00	0.00 ± 0.00
		p04	0.07 ± 0.01	0.00 ± 0.00	0.06 ± 0.01	0.13 ± 0.01	0.06 ± 0.01	0.05 ± 0.01

Hip ext rotators	Gemellus	p01	0.00 ± 0.00	0.94 ± 0.10	0.00 ± 0.00	0.01 ± 0.00	0.00 ± 0.00	0.01 ± 0.00
		p02	0.00 ± 0.00	0.83 ± 0.41	0.00 ± 0.00	0.00 ± 0.00	0.00 ± 0.00	0.00 ± 0.00
		p03	0.00 ± 0.00	0.00 ± 0.00	0.00 ± 0.00	0.00 ± 0.00	0.00 ± 0.00	0.00 ± 0.00
		p04	0.00 ± 0.00	0.00 ± 0.00	0.00 ± 0.00	0.00 ± 0.00	0.00 ± 0.00	0.01 ± 0.00
	Piriformis	p01	0.10 ± 0.02	0.04 ± 0.03	0.10 ± 0.02	0.14 ± 0.02	0.10 ± 0.02	0.07 ± 0.02
		p02	0.01 ± 0.04	0.00 ± 0.00	0.01 ± 0.03	0.03 ± 0.05	0.00 ± 0.00	0.00 ± 0.00
		p03	0.12 ± 0.11	0.00 ± 0.00	0.12 ± 0.11	0.15 ± 0.13	0.12 ± 0.11	0.11 ± 0.10
		p04	0.00 ± 0.01	0.00 ± 0.00	0.01 ± 0.01	0.02 ± 0.01	0.01 ± 0.01	0.02 ± 0.01
	Quadratus Femoris	p01	0.00 ± 0.00	0.00 ± 0.00	0.00 ± 0.00	0.00 ± 0.00	0.00 ± 0.00	0.00 ± 0.00
		p02	0.00 ± 0.00	0.00 ± 0.00	0.00 ± 0.00	0.00 ± 0.00	0.00 ± 0.00	0.00 ± 0.00
		p03	0.00 ± 0.00	0.00 ± 0.00	0.00 ± 0.00	0.00 ± 0.00	0.00 ± 0.00	0.00 ± 0.00
		p04	0.08 ± 0.02	0.27 ± 0.11	0.08 ± 0.02	0.17 ± 0.03	0.07 ± 0.02	0.06 ± 0.02
Iliopsoas	Iliacus	p01	0.43 ± 0.03	0.00 ± 0.00	0.43 ± 0.04	0.73 ± 0.07	0.43 ± 0.04	0.30 ± 0.03
		p02	0.18 ± 0.10	0.09 ± 0.07	0.15 ± 0.09	0.34 ± 0.10	0.16 ± 0.06	0.08 ± 0.05
		p03	0.38 ± 0.06	0.18 ± 0.22	0.38 ± 0.06	0.67 ± 0.06	0.39 ± 0.06	0.31 ± 0.06
		p04	0.58 ± 0.05	0.25 ± 0.17	0.55 ± 0.04	0.90 ± 0.06	0.54 ± 0.04	0.47 ± 0.04
	Psoas Major	p01	0.44 ± 0.03	0.04 ± 0.04	0.44 ± 0.04	0.75 ± 0.07	0.44 ± 0.04	0.31 ± 0.03
		p02	0.18 ± 0.11	0.09 ± 0.07	0.16 ± 0.10	0.35 ± 0.11	0.16 ± 0.06	0.08 ± 0.05
		p03	0.26 ± 0.07	0.00 ± 0.00	0.26 ± 0.07	0.48 ± 0.09	0.28 ± 0.07	0.21 ± 0.07
		p04	0.53 ± 0.05	0.00 ± 0.00	0.50 ± 0.05	0.84 ± 0.06	0.49 ± 0.05	0.42 ± 0.04
Hamstrings	Biceps Femoris LH	p01	0.00 ± 0.00	0.00 ± 0.00	0.00 ± 0.00	0.00 ± 0.00	0.00 ± 0.00	0.00 ± 0.00
		p02	0.00 ± 0.00	0.00 ± 0.00	0.00 ± 0.00	0.00 ± 0.00	0.00 ± 0.00	0.00 ± 0.00
		p03	0.00 ± 0.00	0.00 ± 0.00	0.00 ± 0.00	0.00 ± 0.00	0.00 ± 0.00	0.00 ± 0.00
		p04	0.00 ± 0.00	0.00 ± 0.00	0.00 ± 0.00	0.00 ± 0.00	0.00 ± 0.00	0.00 ± 0.00
	Biceps Femoris SH	p01	0.18 ± 0.03	0.48 ± 0.10	0.18 ± 0.02	0.00 ± 0.00	0.17 ± 0.02	0.04 ± 0.01
		p02	0.10 ± 0.02	0.04 ± 0.03	0.11 ± 0.02	0.00 ± 0.00	0.09 ± 0.02	0.00 ± 0.00
		p03	0.12 ± 0.04	0.20 ± 0.16	0.12 ± 0.04	0.08 ± 0.09	0.10 ± 0.03	0.01 ± 0.00
		p04	0.03 ± 0.00	0.06 ± 0.00	0.03 ± 0.00	0.00 ± 0.00	0.03 ± 0.00	0.01 ± 0.00
	Semimembranosus	p01	0.00 ± 0.00	0.00 ± 0.00	0.00 ± 0.00	0.00 ± 0.00	0.00 ± 0.00	0.00 ± 0.00
		p02	0.00 ± 0.00	0.00 ± 0.00	0.00 ± 0.01	0.02 ± 0.04	0.00 ± 0.01	0.00 ± 0.00
		p03	0.00 ± 0.00	0.00 ± 0.00	0.00 ± 0.00	0.00 ± 0.00	0.00 ± 0.00	0.00 ± 0.00
		p04	0.00 ± 0.00	0.00 ± 0.00	0.00 ± 0.00	0.00 ± 0.00	0.00 ± 0.00	0.00 ± 0.00
	Semitendinosus	p01	0.00 ± 0.00	0.00 ± 0.00	0.00 ± 0.00	0.71 ± 0.20	0.00 ± 0.00	0.00 ± 0.00
		p02	0.00 ± 0.00	0.00 ± 0.00	0.00 ± 0.00	0.67 ± 0.17	0.00 ± 0.00	0.00 ± 0.00
		p03	0.00 ± 0.00	0.00 ± 0.00	0.00 ± 0.00	0.00 ± 0.00	0.00 ± 0.00	0.00 ± 0.00
		p04	0.00 ± 0.00	0.00 ± 0.00	0.00 ± 0.00	0.00 ± 0.00	0.00 ± 0.00	0.00 ± 0.00
Quadriceps	Rectus Femoris	p01	0.14 ± 0.05	0.47 ± 0.07	0.14 ± 0.04	0.00 ± 0.00	0.16 ± 0.04	0.39 ± 0.03
		p02	0.13 ± 0.07	0.02 ± 0.05	0.12 ± 0.07	0.00 ± 0.00	0.11 ± 0.06	0.27 ± 0.06
		p03	0.50 ± 0.04	0.64 ± 0.20	0.50 ± 0.03	0.00 ± 0.00	0.52 ± 0.03	0.71 ± 0.05
		p04	0.63 ± 0.04	1.00 ± 0.00	0.61 ± 0.04	0.00 ± 0.00	0.61 ± 0.04	0.77 ± 0.05
	Vastus Intermedius	p01	0.00 ± 0.00	0.00 ± 0.00	0.00 ± 0.00	0.00 ± 0.00	0.00 ± 0.00	0.01 ± 0.01
		p02	0.00 ± 0.00	0.00 ± 0.00	0.00 ± 0.00	0.00 ± 0.00	0.00 ± 0.00	0.10 ± 0.02
		p03	0.00 ± 0.00	0.00 ± 0.00	0.00 ± 0.00	0.00 ± 0.00	0.00 ± 0.00	0.07 ± 0.02
		p04	0.00 ± 0.00	0.00 ± 0.00	0.00 ± 0.00	0.00 ± 0.00	0.00 ± 0.00	0.23 ± 0.02
	Vastus Lateralis	p01	0.00 ± 0.00	0.00 ± 0.00	0.00 ± 0.00	0.00 ± 0.00	0.00 ± 0.00	0.01 ± 0.01
		p02	0.00 ± 0.00	0.00 ± 0.00	0.00 ± 0.00	0.00 ± 0.00	0.00 ± 0.00	0.12 ± 0.02
		p03	0.00 ± 0.00	0.00 ± 0.00	0.00 ± 0.00	0.00 ± 0.00	0.00 ± 0.00	0.10 ± 0.02
		p04	0.00 ± 0.00	0.00 ± 0.00	0.00 ± 0.00	0.00 ± 0.00	0.00 ± 0.00	0.12 ± 0.01
	Vastus Medialis	p01	0.00 ± 0.00	0.00 ± 0.00	0.00 ± 0.00	0.00 ± 0.00	0.00 ± 0.00	0.01 ± 0.01
		p02	0.00 ± 0.00	0.00 ± 0.00	0.00 ± 0.00	0.00 ± 0.00	0.00 ± 0.00	0.08 ± 0.01
		p03	0.00 ± 0.00	0.00 ± 0.00	0.00 ± 0.00	0.01 ± 0.02	0.00 ± 0.00	0.07 ± 0.02
		p04	0.00 ± 0.00	0.00 ± 0.00	0.00 ± 0.00	0.00 ± 0.00	0.00 ± 0.00	0.10 ± 0.01

Group	Muscle							
Knee stabilizers	Gracilis	p01	0.00 ± 0.00	0.00 ± 0.00	0.00 ± 0.00	0.00 ± 0.00	0.00 ± 0.00	0.01 ± 0.00
		p02	0.00 ± 0.00	0.00 ± 0.00	0.00 ± 0.00	0.00 ± 0.00	0.00 ± 0.00	0.00 ± 0.00
		p03	0.00 ± 0.00	0.00 ± 0.00	0.00 ± 0.00	0.00 ± 0.00	0.00 ± 0.00	0.00 ± 0.00
		p04	0.07 ± 0.01	0.00 ± 0.00	0.07 ± 0.01	0.00 ± 0.00	0.07 ± 0.01	0.06 ± 0.01
	Sartorius	p01	0.11 ± 0.01	1.00 ± 0.00	0.11 ± 0.01	0.00 ± 0.00	0.11 ± 0.01	0.08 ± 0.01
		p02	0.07 ± 0.01	0.67 ± 0.52	0.07 ± 0.01	0.00 ± 0.00	0.07 ± 0.01	0.05 ± 0.01
		p03	0.14 ± 0.02	1.00 ± 0.00	0.14 ± 0.02	0.00 ± 0.00	0.13 ± 0.01	0.10 ± 0.01
		p04	0.12 ± 0.01	1.00 ± 0.00	0.12 ± 0.01	0.00 ± 0.00	0.12 ± 0.01	0.10 ± 0.01
	Tensor Fasciae Latae	p01	0.18 ± 0.02	1.00 ± 0.00	0.18 ± 0.01	0.00 ± 0.00	0.18 ± 0.01	0.16 ± 0.01
		p02	0.21 ± 0.03	0.83 ± 0.41	0.20 ± 0.03	0.00 ± 0.00	0.20 ± 0.03	0.18 ± 0.03
		p03	0.38 ± 0.01	1.00 ± 0.00	0.38 ± 0.02	0.00 ± 0.00	0.36 ± 0.03	0.33 ± 0.03
		p04	0.29 ± 0.02	1.00 ± 0.00	0.29 ± 0.02	0.00 ± 0.00	0.29 ± 0.02	0.27 ± 0.02
Plantarflexors-I	Lateral Gastrocnemius	p01	0.18 ± 0.02	0.34 ± 0.05	0.18 ± 0.02	0.00 ± 0.00	0.18 ± 0.01	1.00 ± 0.00
		p02	0.13 ± 0.02	0.09 ± 0.03	0.13 ± 0.02	0.00 ± 0.00	0.13 ± 0.02	0.11 ± 0.13
		p03	0.26 ± 0.02	0.31 ± 0.09	0.27 ± 0.02	0.00 ± 0.00	0.26 ± 0.02	1.00 ± 0.00
		p04	0.21 ± 0.01	0.29 ± 0.01	0.22 ± 0.01	0.80 ± 0.07	0.22 ± 0.01	0.88 ± 0.11
	Medial Gastrocnemius	p01	0.41 ± 0.04	0.78 ± 0.12	0.41 ± 0.04	0.00 ± 0.00	0.40 ± 0.03	0.55 ± 0.03
		p02	0.30 ± 0.05	0.21 ± 0.06	0.31 ± 0.04	0.00 ± 0.00	0.30 ± 0.04	0.97 ± 0.06
		p03	0.56 ± 0.04	0.65 ± 0.18	0.56 ± 0.04	0.00 ± 0.00	0.54 ± 0.03	1.00 ± 0.00
		p04	0.55 ± 0.03	0.74 ± 0.01	0.57 ± 0.03	0.00 ± 0.00	0.57 ± 0.04	1.00 ± 0.00
	Soleus	p01	0.23 ± 0.02	0.04 ± 0.05	0.23 ± 0.02	0.45 ± 0.02	0.23 ± 0.02	0.00 ± 0.00
		p02	0.28 ± 0.06	0.33 ± 0.07	0.28 ± 0.05	0.44 ± 0.07	0.30 ± 0.04	0.00 ± 0.00
		p03	0.73 ± 0.05	0.68 ± 0.13	0.74 ± 0.04	1.00 ± 0.00	0.76 ± 0.03	0.36 ± 0.02
		p04	0.40 ± 0.04	0.27 ± 0.04	0.40 ± 0.04	0.61 ± 0.05	0.41 ± 0.04	0.01 ± 0.01
Plantarflexors-II	Flexor Digitorum Longus	p01	0.00 ± 0.00	0.02 ± 0.00	0.00 ± 0.00	0.02 ± 0.00	0.00 ± 0.00	0.00 ± 0.00
		p02	0.00 ± 0.00	0.01 ± 0.00	0.00 ± 0.00	0.01 ± 0.00	0.00 ± 0.00	0.00 ± 0.00
		p03	0.00 ± 0.00	0.00 ± 0.00	0.00 ± 0.00	0.20 ± 0.05	0.00 ± 0.00	0.00 ± 0.00
		p04	0.00 ± 0.00	0.02 ± 0.00	0.00 ± 0.00	0.02 ± 0.00	0.00 ± 0.00	0.00 ± 0.00
	Flexor Hallucis Longus	p01	0.01 ± 0.00	0.02 ± 0.00	0.01 ± 0.00	0.03 ± 0.00	0.01 ± 0.00	0.00 ± 0.00
		p02	0.02 ± 0.00	0.02 ± 0.00	0.02 ± 0.00	0.03 ± 0.00	0.02 ± 0.00	0.00 ± 0.00
		p03	0.04 ± 0.01	0.04 ± 0.01	0.04 ± 0.01	0.58 ± 0.10	0.04 ± 0.00	0.00 ± 0.00
		p04	0.02 ± 0.00	0.02 ± 0.00	0.02 ± 0.00	0.04 ± 0.00	0.02 ± 0.00	0.00 ± 0.00
	Peroneus Brevis	p01	0.00 ± 0.00	0.02 ± 0.00	0.00 ± 0.00	0.02 ± 0.00	0.00 ± 0.00	0.00 ± 0.00
		p02	0.00 ± 0.00	0.01 ± 0.00	0.00 ± 0.00	0.02 ± 0.00	0.00 ± 0.00	0.00 ± 0.00
		p03	0.23 ± 0.06	0.23 ± 0.06	0.23 ± 0.05	0.43 ± 0.06	0.26 ± 0.05	0.58 ± 0.05
		p04	0.01 ± 0.00	0.02 ± 0.00	0.01 ± 0.00	0.03 ± 0.00	0.01 ± 0.00	0.00 ± 0.00
	Peroneus Longus	p01	0.01 ± 0.00	0.02 ± 0.00	0.01 ± 0.00	0.03 ± 0.00	0.01 ± 0.00	0.00 ± 0.00
		p02	0.01 ± 0.00	0.02 ± 0.00	0.01 ± 0.00	0.02 ± 0.00	0.01 ± 0.00	0.00 ± 0.00
		p03	0.53 ± 0.13	0.54 ± 0.13	0.53 ± 0.11	0.83 ± 0.11	0.60 ± 0.13	0.46 ± 0.16
		p04	0.01 ± 0.00	0.02 ± 0.00	0.01 ± 0.00	0.03 ± 0.00	0.01 ± 0.00	0.00 ± 0.00
	Tibialis Posterior	p01	0.02 ± 0.00	0.02 ± 0.01	0.02 ± 0.00	0.05 ± 0.00	0.03 ± 0.00	0.00 ± 0.00
		p02	0.05 ± 0.01	0.06 ± 0.01	0.05 ± 0.01	0.08 ± 0.01	0.05 ± 0.01	0.00 ± 0.00
		p03	0.00 ± 0.00	0.00 ± 0.00	0.00 ± 0.00	0.42 ± 0.17	0.00 ± 0.00	0.00 ± 0.00
		p04	0.01 ± 0.00	0.02 ± 0.00	0.01 ± 0.00	0.03 ± 0.00	0.01 ± 0.00	0.00 ± 0.00
Dorsiflexors	Extensor Digitorum Longus	p01	0.00 ± 0.00	0.02 ± 0.02	0.00 ± 0.00	0.01 ± 0.00	0.00 ± 0.00	0.00 ± 0.00
		p02	0.00 ± 0.00	0.00 ± 0.00	0.00 ± 0.00	0.00 ± 0.00	0.00 ± 0.00	0.00 ± 0.00
		p03	0.00 ± 0.00	0.00 ± 0.00	0.00 ± 0.00	0.00 ± 0.00	0.00 ± 0.00	0.00 ± 0.00
		p04	0.00 ± 0.00	0.00 ± 0.00	0.00 ± 0.00	0.00 ± 0.00	0.00 ± 0.00	0.00 ± 0.00
	Extensor Hallucis Longus	p01	0.00 ± 0.00	0.02 ± 0.01	0.00 ± 0.00	0.01 ± 0.00	0.00 ± 0.00	0.00 ± 0.00
		p02	0.00 ± 0.00	0.00 ± 0.00	0.00 ± 0.00	0.01 ± 0.00	0.00 ± 0.00	0.00 ± 0.00
		p03	0.00 ± 0.00	0.00 ± 0.00	0.00 ± 0.00	0.00 ± 0.00	0.00 ± 0.00	0.00 ± 0.00
		p04	0.00 ± 0.00	0.01 ± 0.00	0.00 ± 0.00	0.01 ± 0.00	0.00 ± 0.00	0.00 ± 0.00
	Peroneus Tertius	p01	0.00 ± 0.00	0.02 ± 0.00	0.00 ± 0.00	0.01 ± 0.00	0.00 ± 0.00	0.00 ± 0.00
		p02	0.00 ± 0.00	0.00 ± 0.00	0.00 ± 0.00	0.01 ± 0.00	0.00 ± 0.00	0.00 ± 0.00
		p03	N/A ± N/A	N/A ± N/A	N/A ± N/A	N/A ± N/A	N/A ± N/A	N/A ± N/A
		p04	0.00 ± 0.00	0.01 ± 0.00	0.00 ± 0.00	0.01 ± 0.00	0.00 ± 0.00	0.00 ± 0.00
	Tibialis Anterior	p01	0.00 ± 0.00	0.03 ± 0.04	0.00 ± 0.00	0.00 ± 0.00	0.00 ± 0.00	0.00 ± 0.00
		p02	0.00 ± 0.00	0.00 ± 0.00	0.00 ± 0.00	0.00 ± 0.00	0.00 ± 0.00	0.00 ± 0.00
		p03	0.00 ± 0.00	0.00 ± 0.00	0.00 ± 0.00	0.00 ± 0.00	0.00 ± 0.00	0.00 ± 0.00
		p04	0.00 ± 0.00	0.01 ± 0.00	0.00 ± 0.00	0.00 ± 0.00	0.00 ± 0.00	0.00 ± 0.00

Trunk muscles	Erector Spinae	*p01*	0.00 ± 0.00	0.01 ± 0.00	0.00 ± 0.00	0.01 ± 0.00	0.00 ± 0.00	0.01 ± 0.00
		p02	N/A ± N/A	N/A ± N/A	N/A ± N/A	N/A ± N/A	N/A ± N/A	N/A ± N/A
		p03	N/A ± N/A	N/A ± N/A	N/A ± N/A	N/A ± N/A	N/A ± N/A	N/A ± N/A
		p04	N/A ± N/A	N/A ± N/A	N/A ± N/A	N/A ± N/A	N/A ± N/A	N/A ± N/A
	External Oblique	*p01*	0.00 ± 0.00	0.01 ± 0.00	0.00 ± 0.00	0.01 ± 0.00	0.00 ± 0.00	0.01 ± 0.00
		p02	N/A ± N/A	N/A ± N/A	N/A ± N/A	N/A ± N/A	N/A ± N/A	N/A ± N/A
		p03	N/A ± N/A	N/A ± N/A	N/A ± N/A	N/A ± N/A	N/A ± N/A	N/A ± N/A
		p04	N/A ± N/A	N/A ± N/A	N/A ± N/A	N/A ± N/A	N/A ± N/A	N/A ± N/A
	Internal Oblique	*p01*	0.00 ± 0.00	0.01 ± 0.01	0.00 ± 0.00	0.01 ± 0.01	0.00 ± 0.00	0.01 ± 0.00
		p02	N/A ± N/A	N/A ± N/A	N/A ± N/A	N/A ± N/A	N/A ± N/A	N/A ± N/A
		p03	N/A ± N/A	N/A ± N/A	N/A ± N/A	N/A ± N/A	N/A ± N/A	N/A ± N/A
		p04	N/A ± N/A	N/A ± N/A	N/A ± N/A	N/A ± N/A	N/A ± N/A	N/A ± N/A

A.7 Sampled muscle activation patterns for main muscles

The following figures show the muscle activation patterns for the main muscles for each trial of *p02*. The predicted activation patterns from the J_{Fmatch}, J_{act} and J_{FK} and the Metabolica samples were included. The muscles were divided into two groups according to which the figures were organized:

- Muscles that span the knee for which EMG data was available
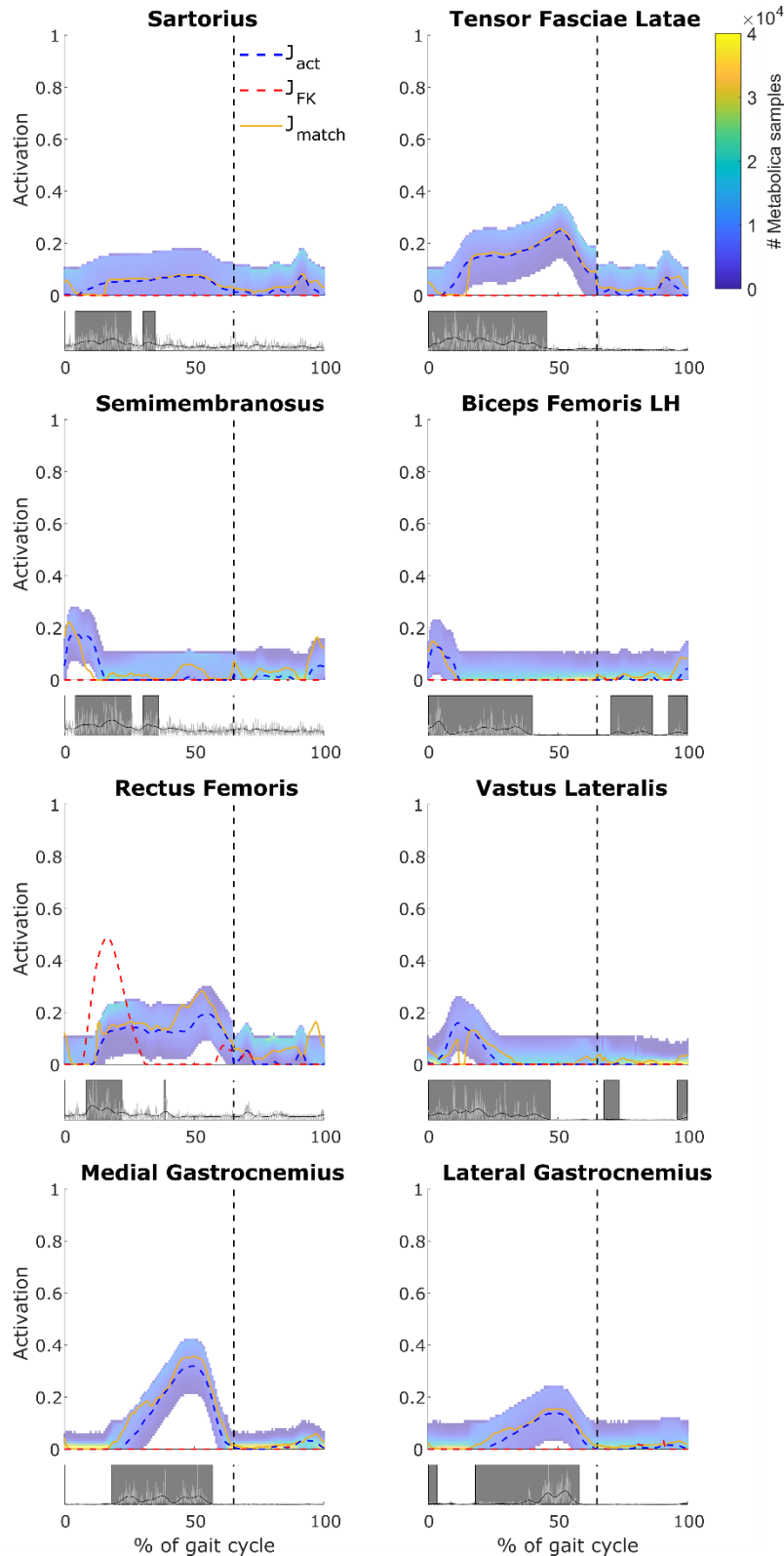- Remaining main muscles
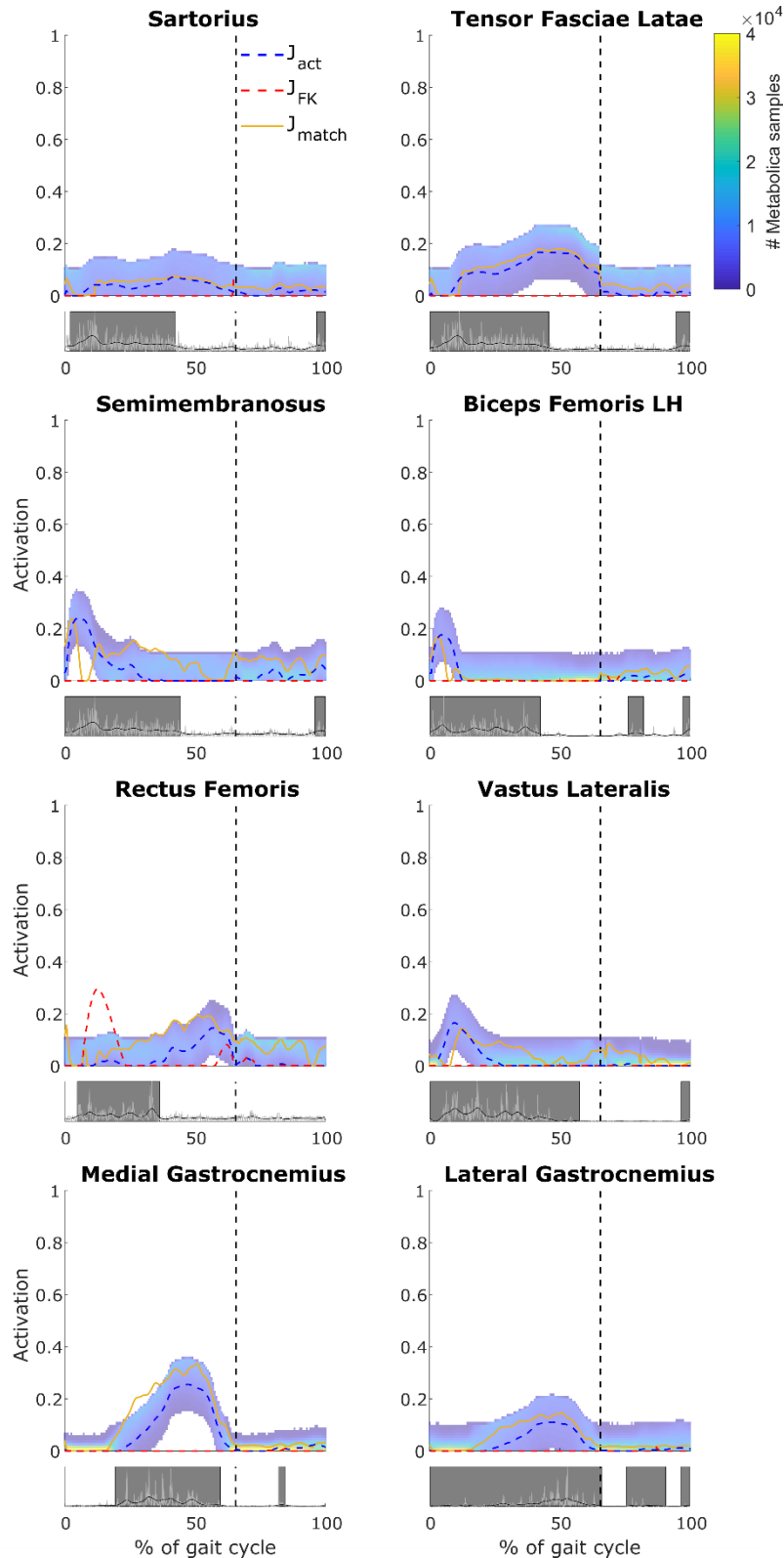
Figure A.7.1: Trial 3, the activation patterns of the muscles that span the knee for which EMG data were available. For each muscle, the top graph shows the J_{act} (blue, dashed), J_{FK} (red, dashed) and J_{Fmatch} (yellow, solid) solutions as lines and the sampled muscle activation patterns as a range for which the colour indicates the number of samples (see colour bar); the bottom graph shows the EMG data: the rectified values in light grey, the envelope in black and the onset timing as dark grey boxes. The vertical axis of the bottom graph was normalized to the maximum value in the rectified EMG data. The vertical dashed lines indicate the time instant when toe off occurred.
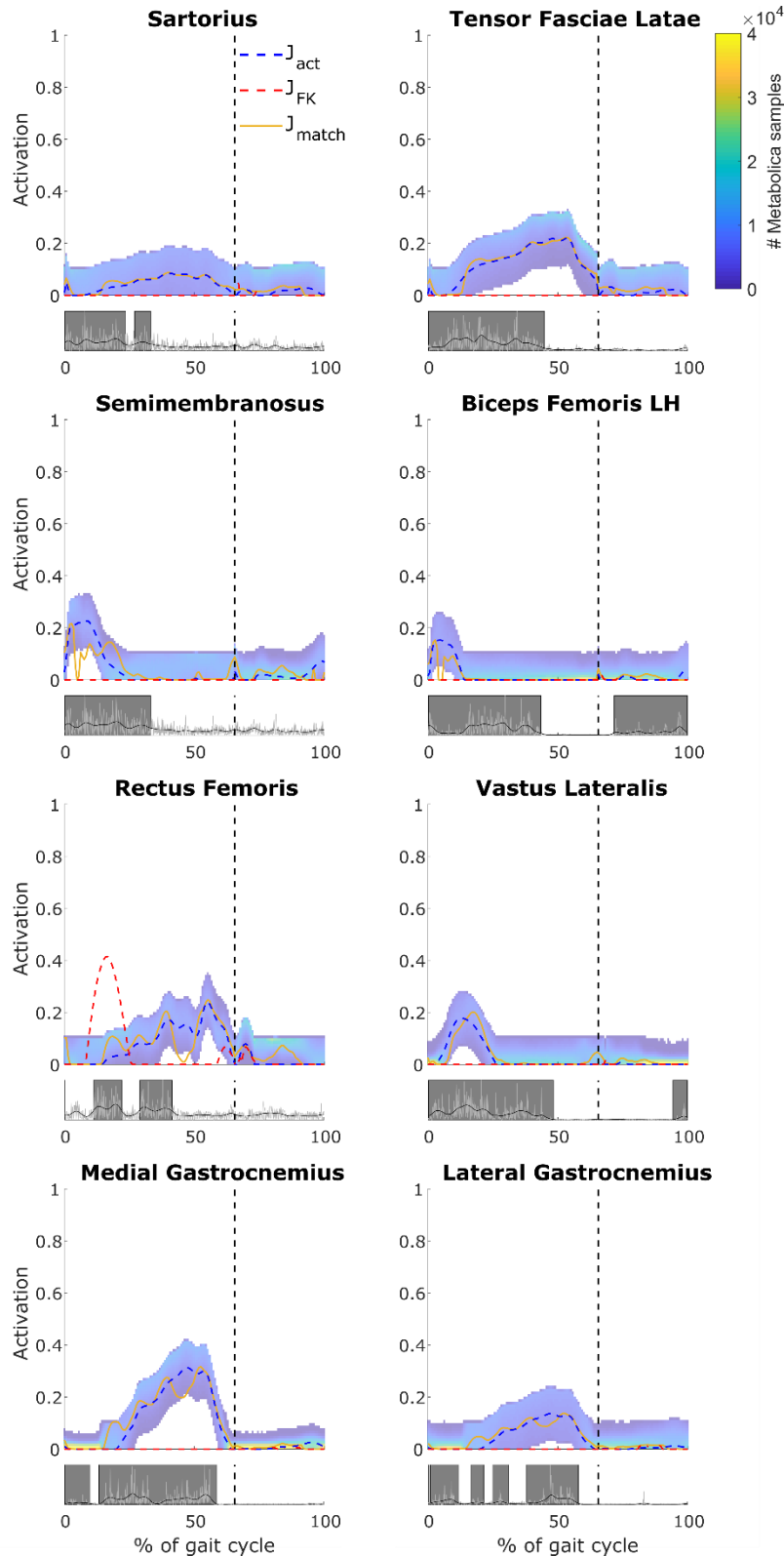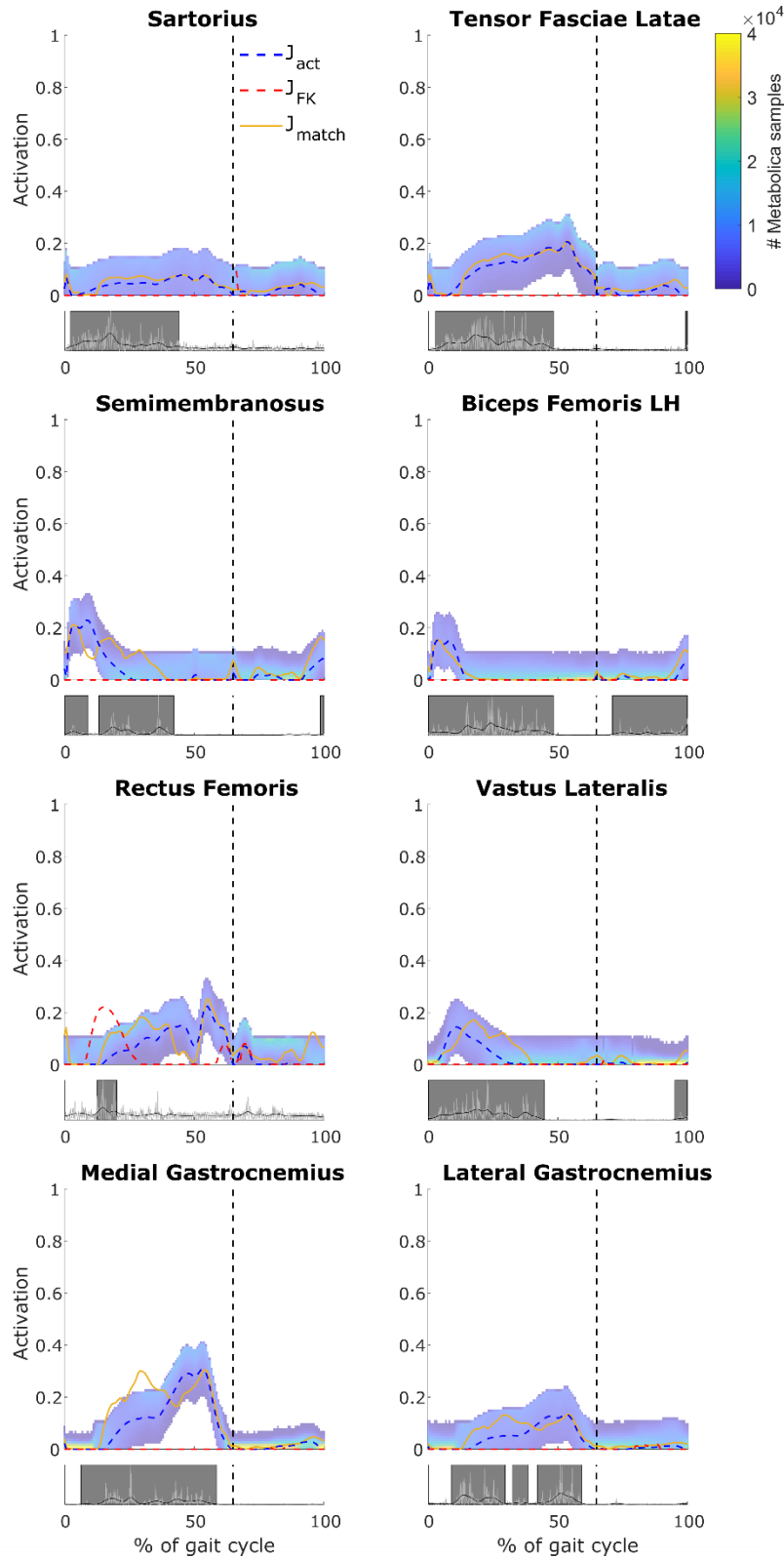
Figure A.7.2: Trial 4, the activation patterns of the muscles that span the knee for which EMG data were available. For each muscle, the top graph shows the J_{act} (blue, dashed), J_{FK} (red, dashed) and J_{Fmatch} (yellow, solid) solutions as lines and the sampled muscle activation patterns as a range for which the colour indicates the number of samples (see colour bar); the bottom graph shows the EMG data: the rectified values in light grey, the envelope in black and the onset timing as dark grey boxes. The vertical axis of the bottom graph was normalized to the maximum value in the rectified EMG data. The vertical dashed lines indicate the time instant when toe off occurred.

Figure A.7.3: Trial 5, the activation patterns of the muscles that span the knee for which EMG data were available. For each muscle, the top graph shows the J_{act} (blue, dashed), J_{FK} (red, dashed) and J_{Fmatch} (yellow, solid) solutions as lines and the sampled muscle activation patterns as a range for which the colour indicates the number of samples (see colour bar); the bottom graph shows the EMG data: the rectified values in light grey, the envelope in black and the onset timing as dark grey boxes. The vertical axis of the bottom graph was normalized to the maximum value in the rectified EMG data. The vertical dashed lines indicate the time instant when toe off occurred.
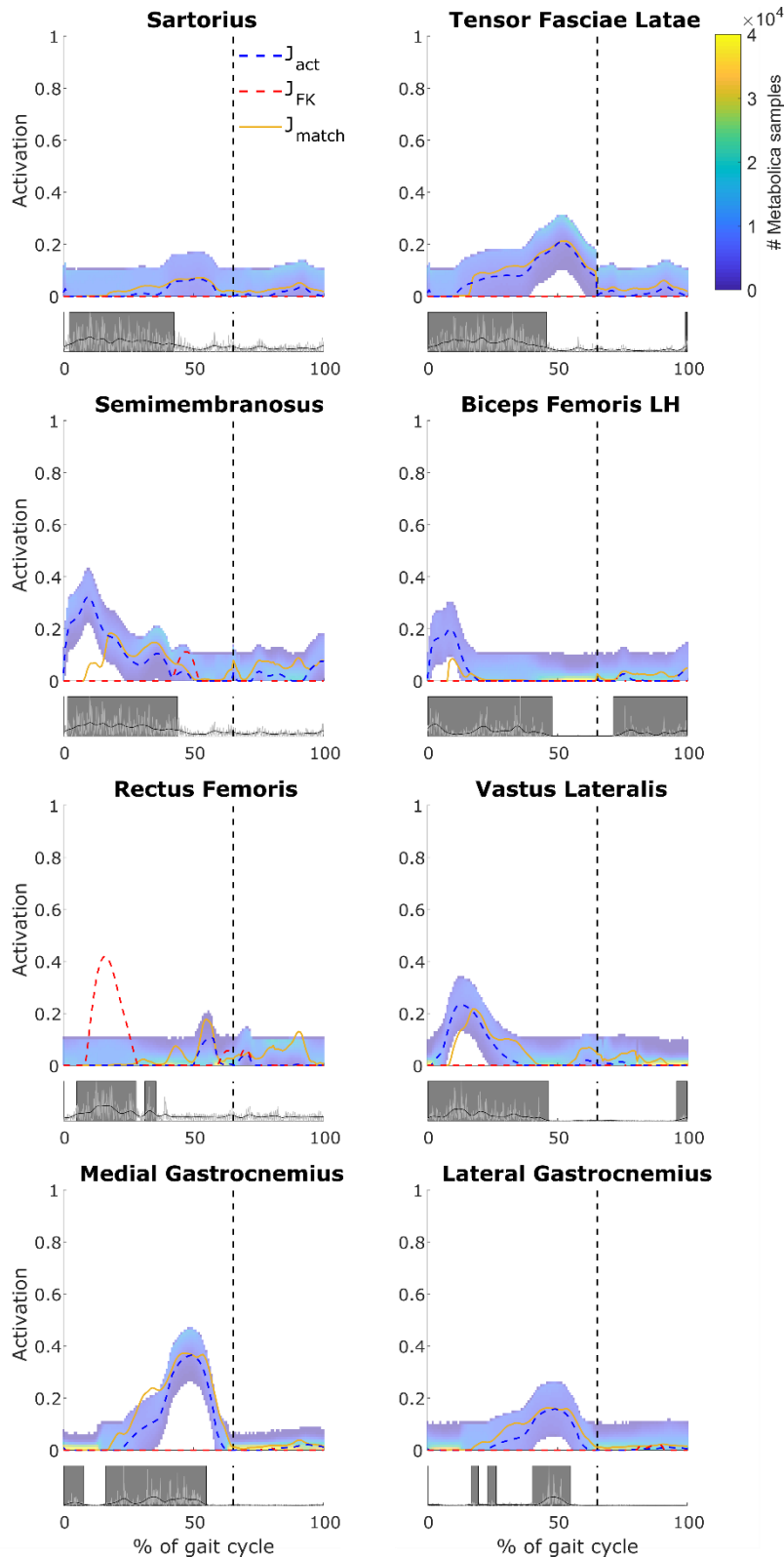
Figure A.7.4: Trial 6, the activation patterns of the muscles that span the knee for which EMG data were available. For each muscle, the top graph shows the J_{act} (blue, dashed), J_{FK} (red, dashed) and J_{Fmatch} (yellow, solid) solutions as lines and the sampled muscle activation patterns as a range for which the colour indicates the number of samples (see colour bar); the bottom graph shows the EMG data: the rectified values in light grey, the envelope in black and the onset timing as dark grey boxes. The vertical axis of the bottom graph was normalized to the maximum value in the rectified EMG data. The vertical dashed lines indicate the time instant when toe off occurred.
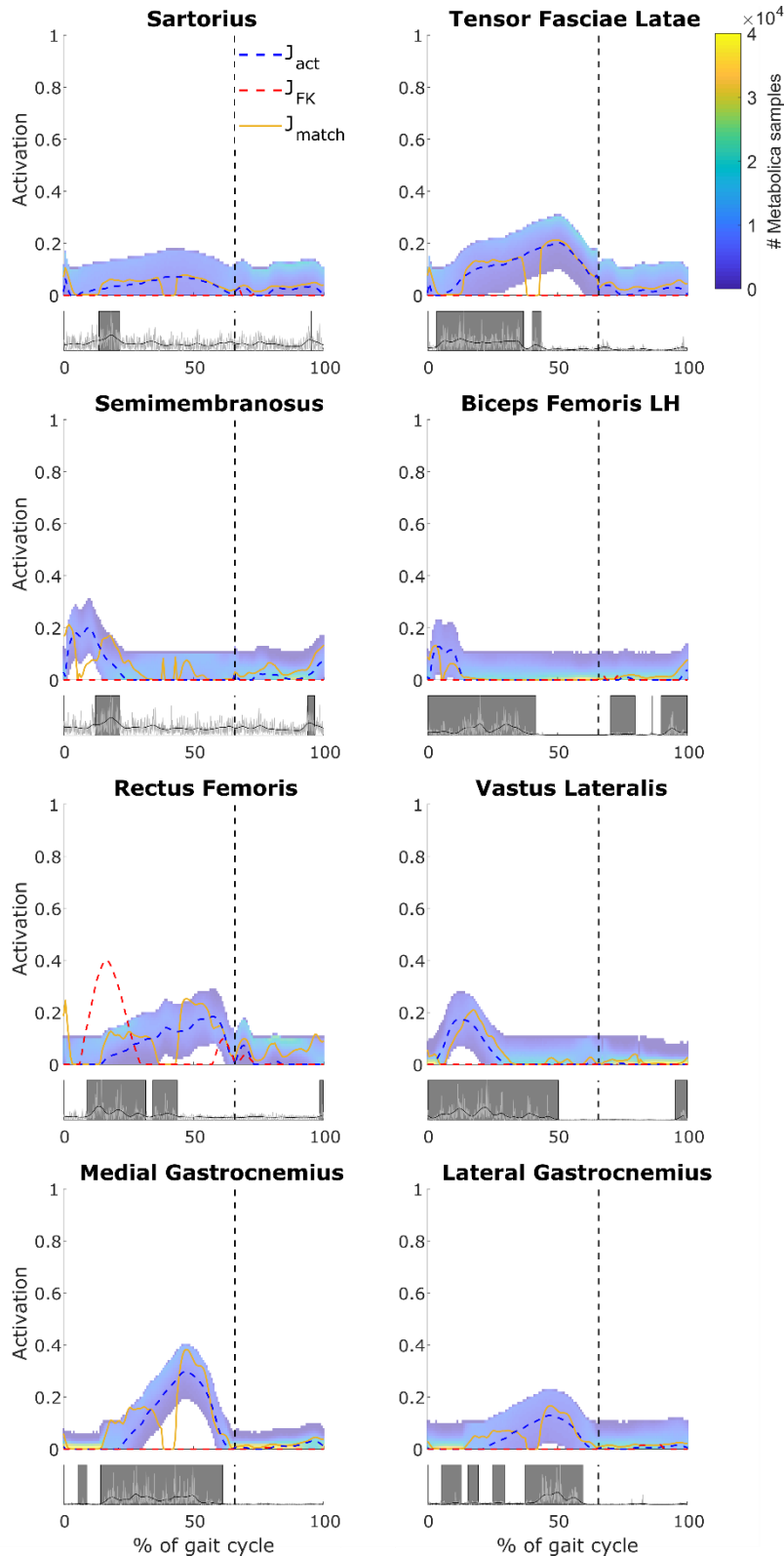
Figure A.7.5: Trial 7, the activation patterns of the muscles that span the knee for which EMG data were available. For each muscle, the top graph shows the J_{act} (blue, dashed), J_{FK} (red, dashed) and J_{Fmatch} (yellow, solid) solutions as lines and the sampled muscle activation patterns as a range for which the colour indicates the number of samples (see colour bar); the bottom graph shows the EMG data: the rectified values in light grey, the envelope in black and the onset timing as dark grey boxes. The vertical axis of the bottom graph was normalized to the maximum value in the rectified EMG data. The vertical dashed lines indicate the time instant when toe off occurred.
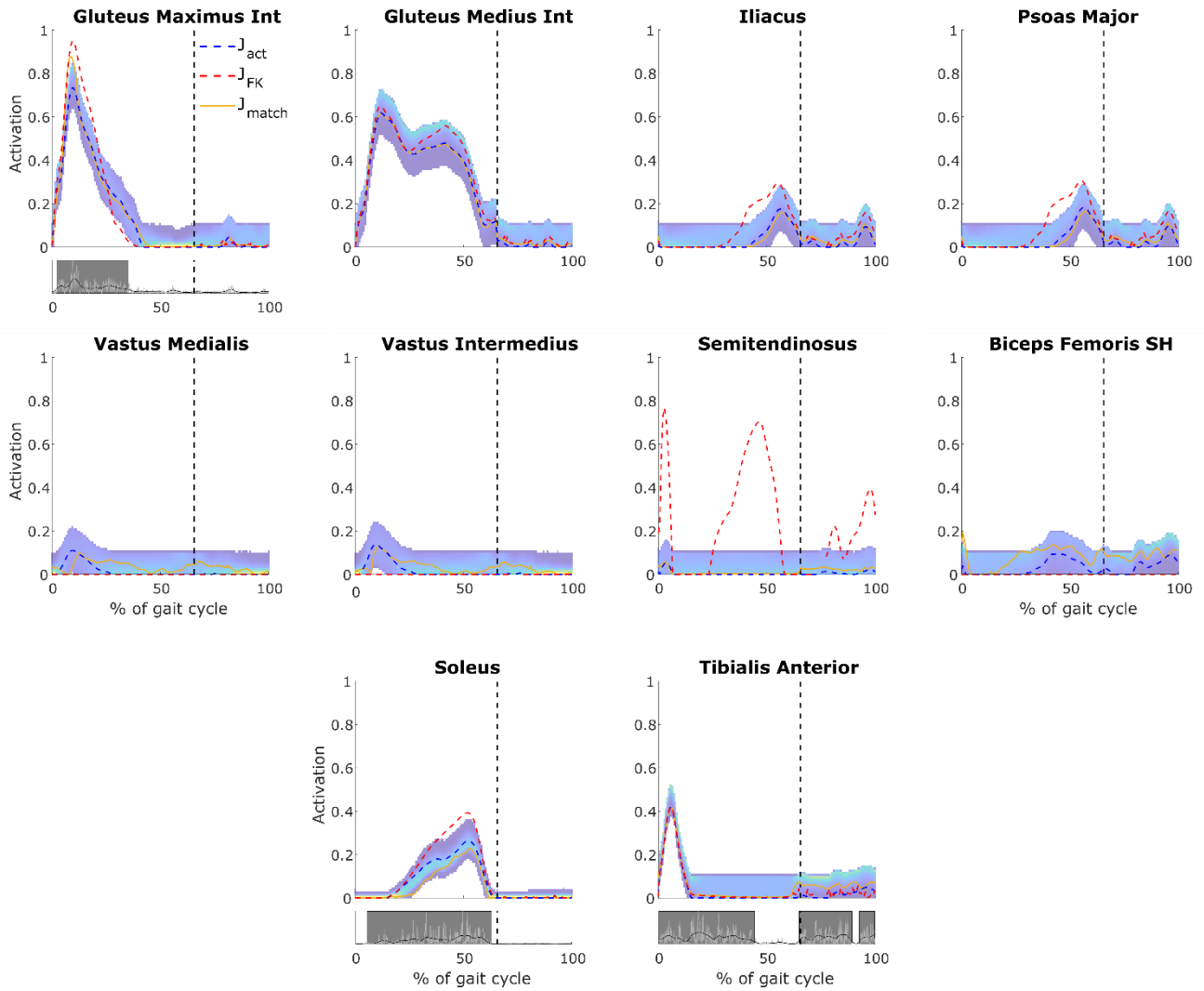
Figure A.7.6: Trial 9, the activation patterns of the muscles that span the knee for which EMG data were available. For each muscle, the top graph shows the J_{act} (blue, dashed), J_{FK} (red, dashed) and J_{Fmatch} (yellow, solid) solutions as lines and the sampled muscle activation patterns as a range for which the colour indicates the number of samples (see colour bar); the bottom graph shows the EMG data: the rectified values in light grey, the envelope in black and the onset timing as dark grey boxes. The vertical axis of the bottom graph was normalized to the maximum value in the rectified EMG data. The vertical dashed lines indicate the time instant when toe off occurred.
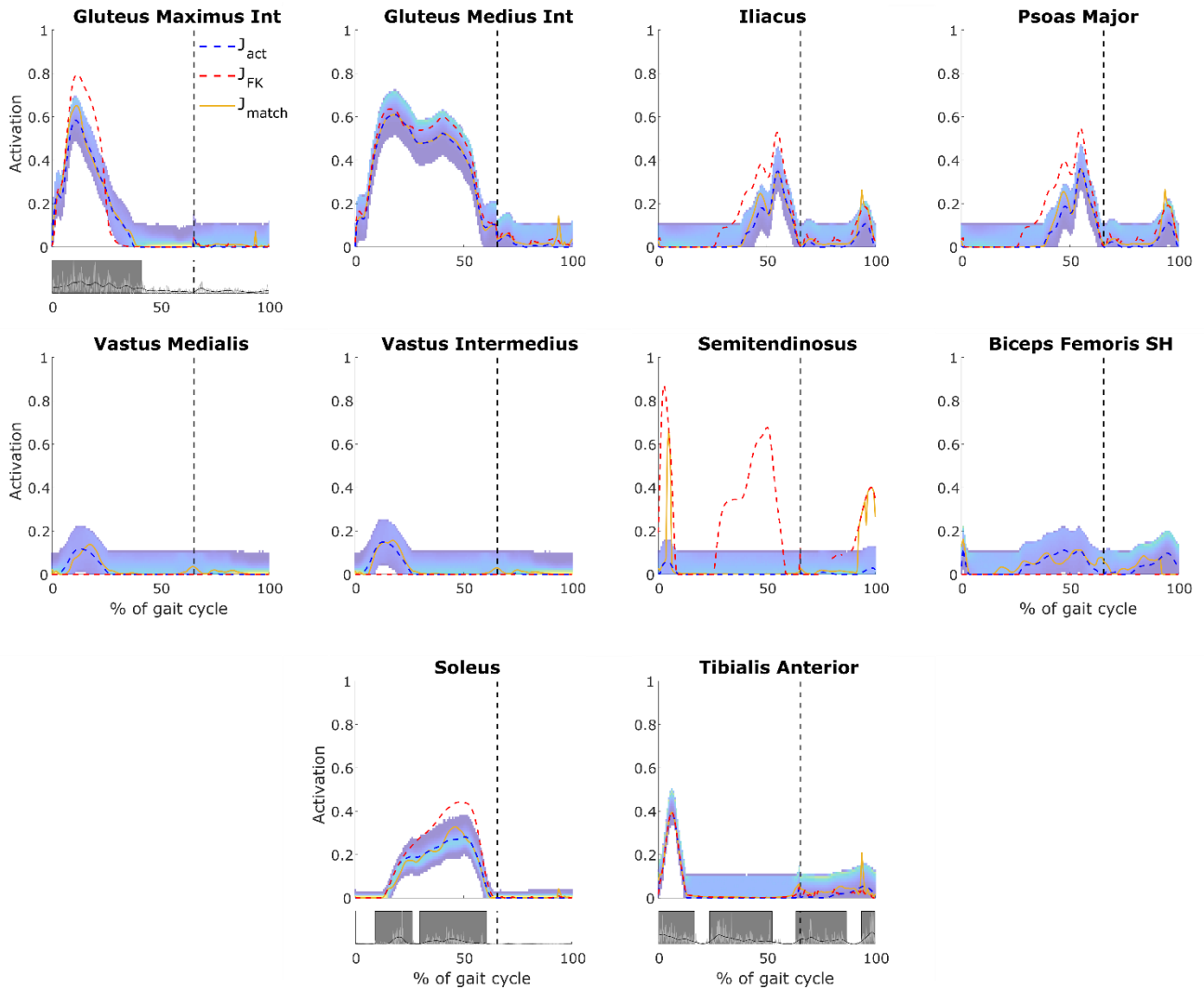
Figure A.7.7: Trial 3, muscle activation patterns. For each muscle, the top graph shows the J_{act} (blue, dashed), J_{FK} (red, dashed) and J_{Fmatch} (yellow, solid) solutions as lines and the sampled muscle activation patterns as a range for which the colour indicates the number of samples (see colour bar); the bottom graph shows the EMG data (if available): the rectified values in light grey, the envelope in black and the onset timing as dark grey boxes. The vertical axis of the bottom graph was normalized to the maximum value in the rectified EMG data. The vertical dashed lines indicate the time instant when toe off occurred.
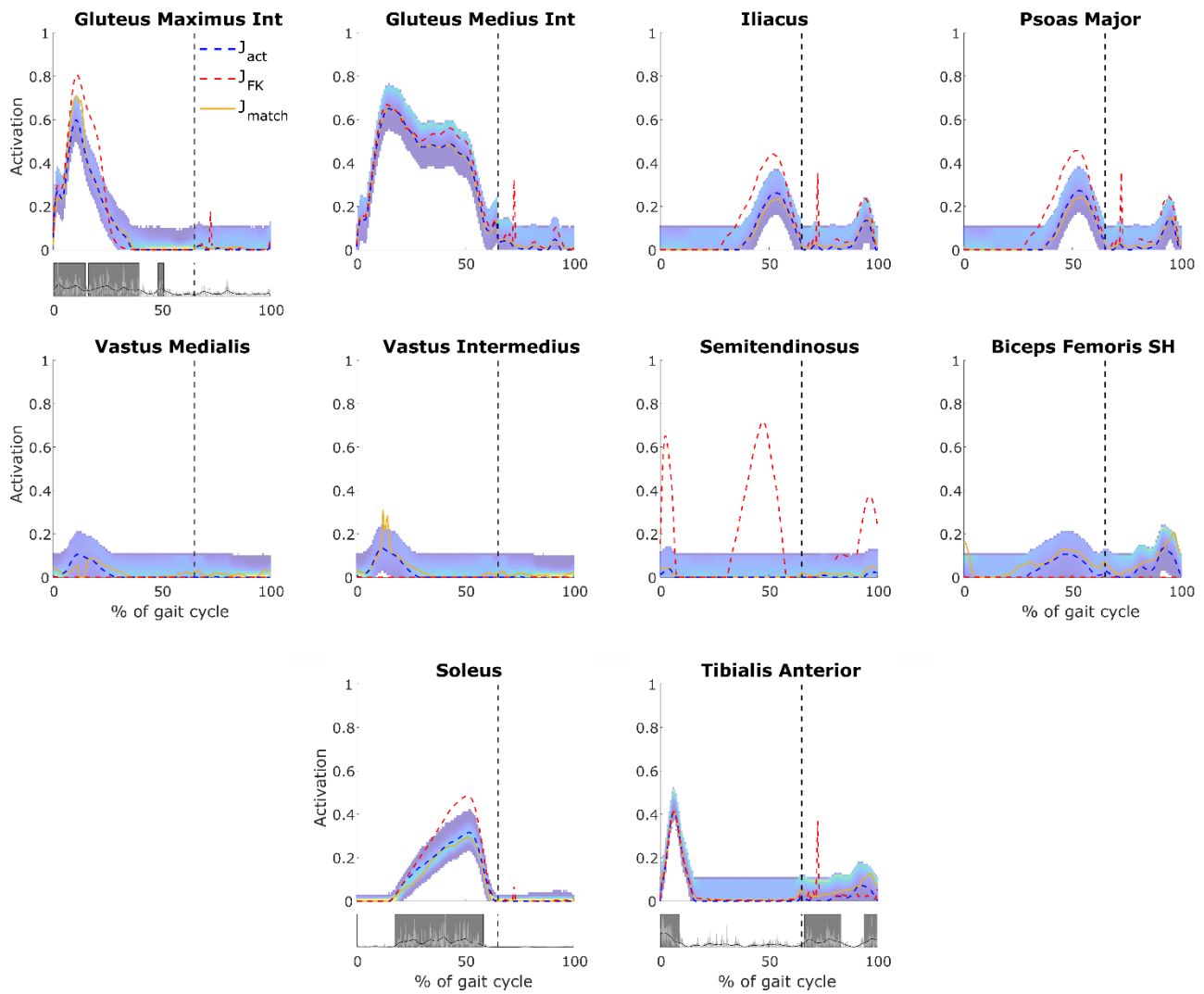
Figure A.7.8: Trial 4, muscle activation patterns. For each muscle, the top graph shows the J_{act} (blue, dashed), J_{FK} (red, dashed) and J_{Fmatch} (yellow, solid) solutions as lines and the sampled muscle activation patterns as a range for which the colour indicates the number of samples (see colour bar); the bottom graph shows the EMG data (if available): the rectified values in light grey, the envelope in black and the onset timing as dark grey boxes. The vertical axis of the bottom graph was normalized to the maximum value in the rectified EMG data. The vertical dashed lines indicate the time instant when toe off occurred.

Figure A.7.9: Trial 5, muscle activation patterns. For each muscle, the top graph shows the J_{act} (blue, dashed), J_{FK} (red, dashed) and J_{Fmatch} (yellow, solid) solutions as lines and the sampled muscle activation patterns as a range for which the colour indicates the number of samples (see colour bar); the bottom graph shows the EMG data (if available): the rectified values in light grey, the envelope in black and the onset timing as dark grey boxes. The vertical axis of the bottom graph was normalized to the maximum value in the rectified EMG data. The vertical dashed lines indicate the time instant when toe off occurred.
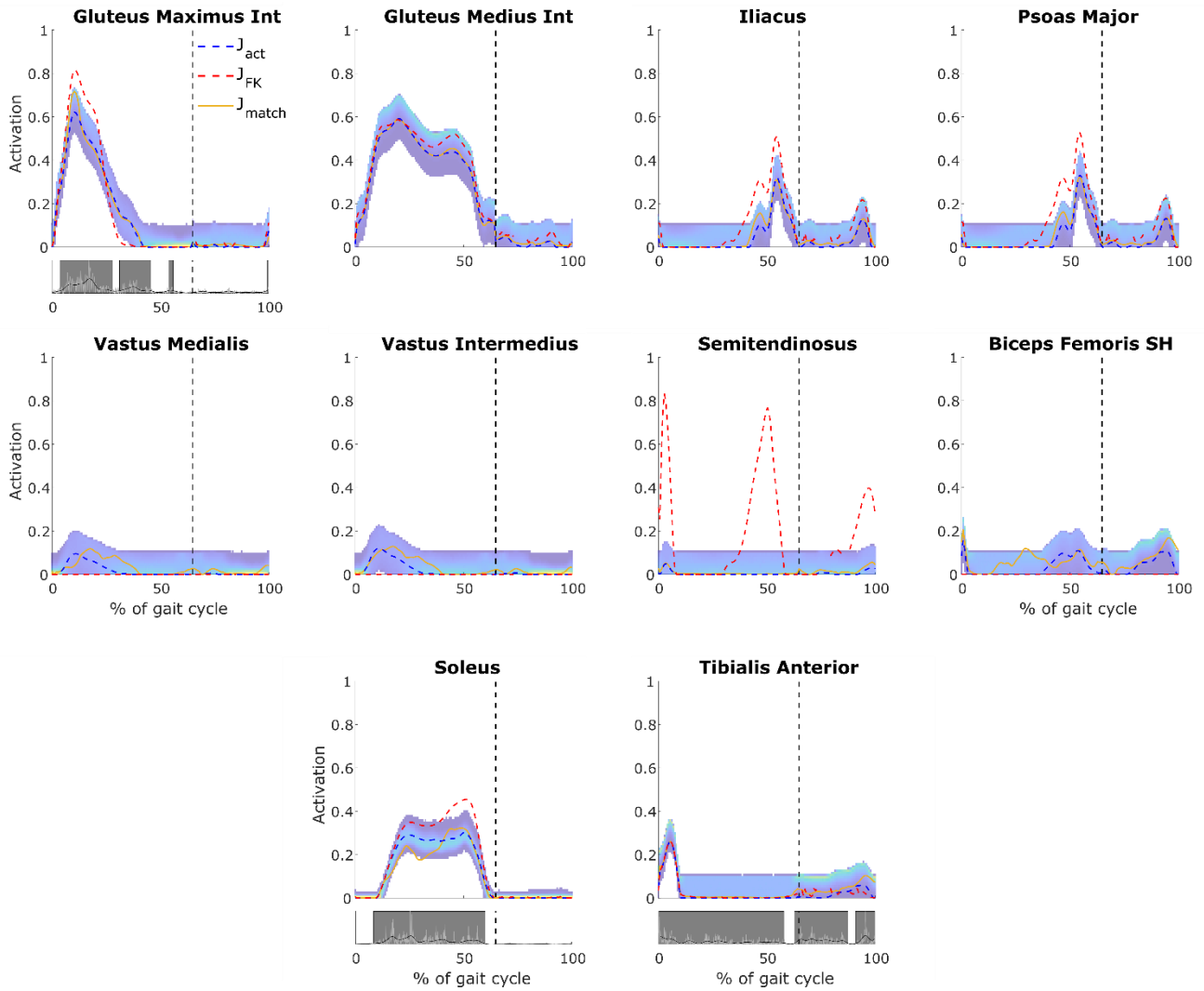
Figure A.7.10: Trial 6, muscle activation patterns. For each muscle, the top graph shows the J_{act} (blue, dashed), J_{FK} (red, dashed) and J_{Fmatch} (yellow, solid) solutions as lines and the sampled muscle activation patterns as a range for which the colour indicates the number of samples (see colour bar); the bottom graph shows the EMG data (if available): the rectified values in light grey, the envelope in black and the onset timing as dark grey boxes. The vertical axis of the bottom graph was normalized to the maximum value in the rectified EMG data. The vertical dashed lines indicate the time instant when toe off occurred.
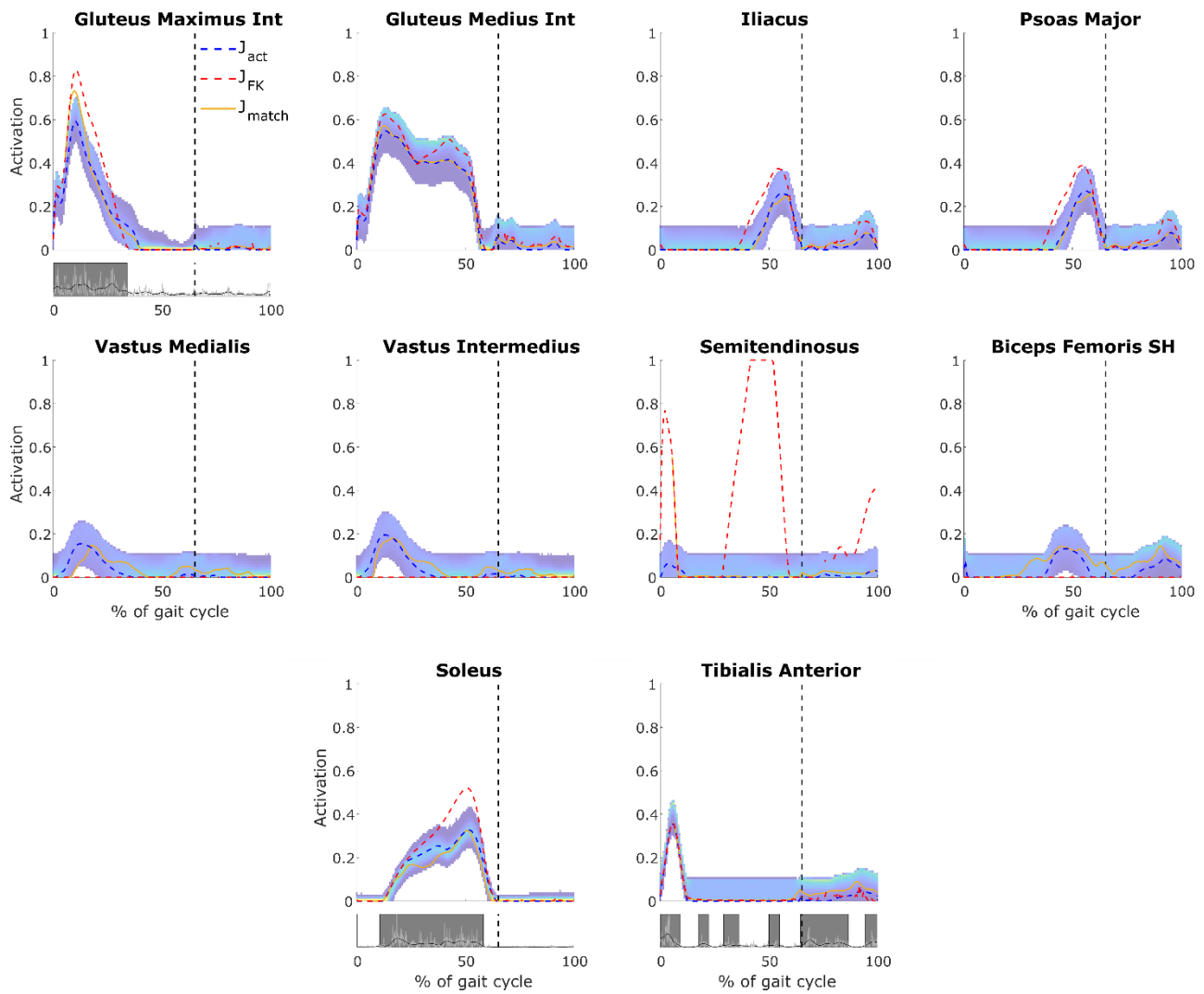
Figure A.7.11: Trial 7, muscle activation patterns. For each muscle, the top graph shows the J_{act} (blue, dashed), J_{FK} (red, dashed) and J_{Fmatch} (yellow, solid) solutions as lines and the sampled muscle activation patterns as a range for which the colour indicates the number of samples (see colour bar); the bottom graph shows the EMG data (if available): the rectified values in light grey, the envelope in black and the onset timing as dark grey boxes. The vertical axis of the bottom graph was normalized to the maximum value in the rectified EMG data. The vertical dashed lines indicate the time instant when toe off occurred.
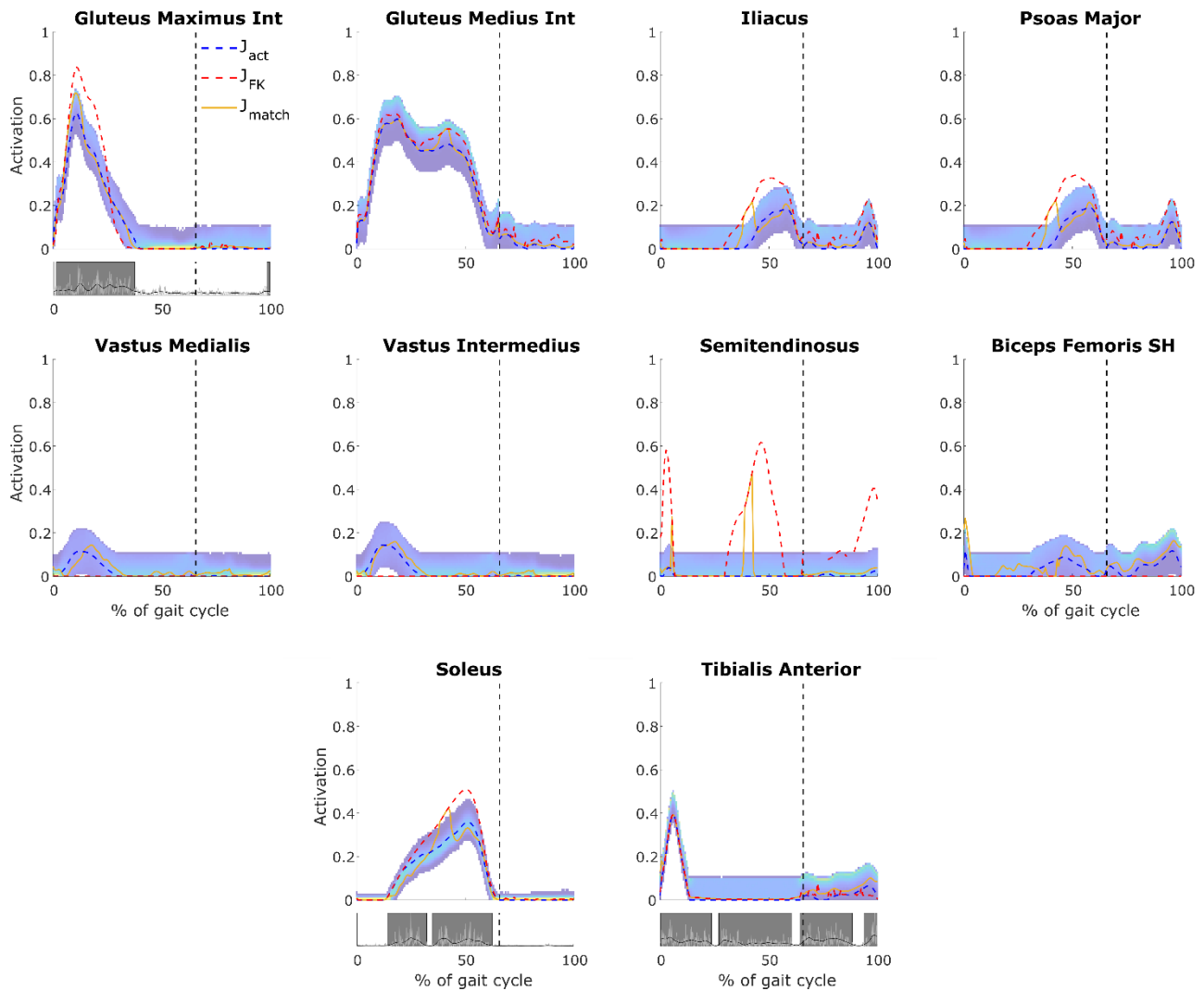
Figure A.7.12: Trial 9, muscle activation patterns. For each muscle, the top graph shows the J_{act} (blue, dashed), J_{FK} (red, dashed) and J_{Fmatch} (yellow, solid) solutions as lines and the sampled muscle activation patterns as a range for which the colour indicates the number of samples (see colour bar); the bottom graph shows the EMG data (if available): the rectified values in light grey, the envelope in black and the onset timing as dark grey boxes. The vertical axis of the bottom graph was normalized to the maximum value in the rectified EMG data. The vertical dashed lines indicate the time instant when toe off occurred.